PROCESSING OF LAMELLAR STRUCTURED LIQUIDS

by

Grace Ellie Cunningham

A thesis submitted to the University of Birmingham for the degree of
DOCTOR OF ENGINEERING

Formulation Engineering Centre for Doctoral Training
School of Chemical Engineering
College of Engineering & Physical Sciences
University of Birmingham
June 2024

Abstract

In today’s society where health and sustainability are two key consumer trends, global FMCG companies like Unilever are driven to innovate, adapt, and adopt responsible practices. Aligning with consumer expectations enhances Unilever's market position and supports long-term business sustainability. Therefore, this thesis aims to improve insights into the hair conditioner manufacturing process to reduce energy and resource consumption while ensuring the desired product microstructure (a lamellar gel network) can be manufactured efficiently every time.

Hair conditioner improves manageability and enhances the appearance and shine of hair - a key indicator of hair health. Consumers expect a thick, opaque cream product that spreads evenly over hair and provides detangling and conditioning through deposition of beneficial ingredients. These physical and rheological properties are achieved through a lamellar gel network (LGN) microstructure - a product of the ingredients used and the manufacturing process. Insights into the influence of processing conditions on the LGN microstructure are limited due to the complexity of the product limiting the availability of process monitoring and characterisation techniques.

In this thesis, rheological mapping using a rheometer and 3D-printed scaled-down geometries to imitate the batch manufacturing vessel, was applied to generate viscosity-time profiles for LGNs at various speeds, times, and temperatures. Samples were characterised by their rheological properties and power requirements, comparing yield stress to qualitatively assess process optimisation strategies. Shorter mixing times, ending after the peak viscosity was reached, produced higher yield stress products, presenting energy-saving opportunities.

The importance of monitoring viscosity during LGN mixing was highlighted, informing further studies on the application of mixer-viscometer approaches to partially-filled batch vessels (25% to 100% liquid height to impeller length). The torque curve method and Couette analogy were applied to torque-speed data for various fluids, including LGNs. However, changes in fluid contact with the impeller as a function of speed, geometry, and fluid rheology showed no measurable relationships, limiting the application of mixer-viscometer techniques due to the consequent impact on torque measurement.

Finally, data-driven models were investigated to predict online viscosity from torque for mixing systems at three scales (0.045 L, 2 L. 50 L). A random forest regression model used mixer diameter, speed, fill level and torque as inputs, and apparent viscosity as the output. The model indicated signs of over-fitting, likely due to an uneven dataset favouring lower viscosity values. Despite this, the work provides an initial contribution towards applying soft sensors to predict online viscosity during manufacture of formulated products.

This research provides Unilever with valuable techniques for monitoring microstructure formation using rheological approaches to enable process and product optimisation, aiding in achieving their net-zero targets and enhancing product superiority.

Acknowledgements

I would like to express my gratitude to my supervisors, Prof. Mark Simmons and Dr. Jonathan O'Sullivan, for their invaluable guidance, support, and encouragement throughout the course of this EngD. Their expertise, insightful feedback and patience have been vital to the completion of this thesis. Thanks also go to Dr. Richard Greenwood for creating a wonderful group to be a part of and providing a sense of reality when things could get overwhelming.

Thanks go to EPSRC and Unilever for sponsoring this project; I am extremely appreciative of all the opportunities that have been presented to me as a result of being part of the Centre for Formulation CDT at the University of Birmingham. I am also thankful to everyone at Unilever who supported this research, either practically by helping with experiments, or through insightful discussion and helpful inputs.

To my fellow researchers, your friendship, collaboration, and solidarity in knowing that we were all navigating the successes and challenges of pursuing a doctorate together gave me a great sense of comfort, inspiration and motivation.

My deepest thanks go to my family, especially my parents, Kay and Robert, and my husband, Emin, for their unwavering support and encouragement, always celebrating the highs with me and getting me through the lows. Your belief in me was the motivation I needed to complete this degree. Thank you for supporting me in the decision to pursue this doctorate and continuing to support me throughout.

Table of Contents

List of Tables

List of Figures

List of Symbols

Symbol	**Definition**	**Units**	**Notes**
c	Wall clearance	m	Clearance between close-clearance impeller and vessel wall, used specifically in Eq.6-5
C_b	Impeller off-bottom clearance	m	Distance from bottom of tank to impeller
D	Impeller diameter	m	
E	Energy	Joules (J)	
Fr	Froude number	Dimensionless	
G’	Storage Modulus	Pa	Represents the elastic portion of a material's viscoelastic behavior
G’’	Loss Modulus	Pa	Represents the viscous component of a material's viscoelastic behavior
h	Height of close-clearance impeller	m	Used specifically in Eq. 6-5
H	Liquid Height	m	In a mixing vessel
H/T	Liquid height to tank diameter ratio	-	
K	Consistency Index	-	Used in power law equation and other rheology models
K_P	Laminar power constant	-	
L	Length of impeller	m	Used in Couette analogy (Eq. 5-10)
M	Torque	N m (Newton metre)	
M_0	Torque measured with empty vessel	N m (Newton metre)	
N	Rotational speed	s^{-1}	May also be RPS (rotations per second), rad s-1, m s-1

n	Flow Index	-	Used in power law equation and other rheology models
n_b	Number of blades		For close clearance impeller system used specifically in Eq. 6-5
P	Power	Watts (W)	
P_{NN}	Power consumption of non-Newtonian fluid	Watts (W)	
P_N	Power consumption of Newtonian fluid	Watts (W)	
Po	Power number	Dimensionless	
p	pitch	m	*pitch (ribbon height in one 360° turn), used specifically in Eq.6-5*
R_e	Radius of outer cylinder (mixing vessel)	m	Used in Couette analogy (Eq. 5-10)
R_i	Equivalent Coutte (cylinder) radius of mixer geometry	m	Used in Couette analogy (Eq. 5-10)
Re	Reynolds number	Dimensionless	
r	Radius	m	
r^*	Optimal radius	m	Radius at which shear rate is nearly independent of flow index of fluid
S_b	Impeller submergence	m	Distance from top of liquid to bottom of impeller
T	Temperature	°C	
T	Tank Diameter	m	
t	Time	s (seconds)	Units of time may vary and will be stated in the text
v	Velocity of the fluid (impeller tip speed for stirred vessel)	m s-1	

w	Blade width	m	For close clearance impeller blade, used specifically in Eq.6-5
γ (Gamma)	Shear Rate	s-1	
γ_{av}	Average Shear Rate	s-1	Used for non-Newtonian fluids to represent the average shear rate
η (Eta)	Apparent Viscosity	Pa s (Pascal seconds)	Used for non-Newtonian fluids
η_0	Zero shear viscosity	Pa s	Relevant for the Cross rheology model (Table 2-2)
η_∞	Infinite shear viscosity	Pa s	
Θ (Theta)	Mixing time	s (seconds)	Time required to achieve homogeneity in the vessel
μ (Mu)	Dynamic Viscosity	Pa s	Used for Newtonian fluids
ρ (Rho)	Density	kg m^{-3}	
τ (Tau)	Shear stress	Pa (Pascals)	
τ_0	Yield stress	Pa	Yield stress marks end of elastic region and beginning of plastic deformation
Ω	Angular velocity	rad s^{-1}	

CHAPTER 1: INTRODUCTION

1.1 Context

When Lady Gaga said ‘I just wanna be myself, and I want you to know, I am my hair’, she summarised how many people feel about their hairstyle being the ultimate expression of freedom (Germanotta and Khayat, 2011). But in achieving our personal style, we put our hair through damaging routines, such as bleaching, colouring, chemical treatments, heat styling, brushing. Modern lifestyles put further strain on our hair’s health – less frequent washing, application of styling products, and environmental pollution can all leave our hair looking frizzy and dull (Rocafort, 2017; Yang, 2017; Gavazzoni Dias, 2015). Trends in the beauty and personal care sector increasingly show a preference towards health (healthy scalp, dandruff treatment, improving the microbiome), with shiny hair being a key indicator of this (Sandler, 2022; Mintel, 2023).

Hair conditioner is an important hair care product which is used to reduce the static charge after shampooing, improve manageability, aid detangling and deposit beneficial ingredients on to the hair to improve shine and reduce the visual impact of damage (Rocafort, 2017). As with all formulated products, the microstructure of hair conditioner is integral to its in-use performance and rheology and is determined by a combination of both the formulation and the manufacturing process (Figure 1-1) (Lister and Bogle, 2019; O'Sullivan and Lett, 2015).

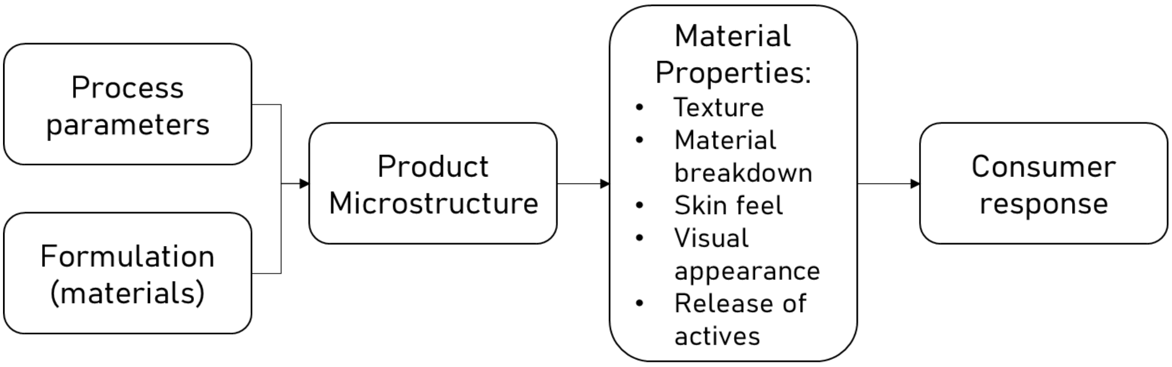

Figure 1-1. Relationship between material properties and consumer response and their impact on product microstructure, determined through both formulation and processing parameters (adapted from Norton *et al.* (2008))

There are three primary conditioning ingredients in a hair conditioner: cationic surfactants, such as behentrimonium chloride (BTAC), fatty alcohol (cetyl or stearyl alcohol), and silicones or oils. Cationic surfactants provide both wet and dry conditioning, whilst silicones mostly provide dry conditioning properties (Rocafort, 2017).

In suitable ratios and under specific processing conditions, cationic surfactants and fatty alcohols (FA), in combination with water, form a lamellar gel phase, L_β; where solid-state surfactant and FA are arranged in bilayers, alternating with interlamellar water. The lamellar gel phase is the defining component of the multiphase lamellar gel network (LGN), which includes further components such as a bulk water phase, oil phase ingredients stabilised by surfactant molecules, and unincorporated fatty alcohol crystals.

The LGN structure is responsible for delivering many of the attributes expected of a hair conditioner. It has a naturally opaque appearance due to its multiphase nature, as well as a slippery and oily texture and enhanced delivery of cosmetic benefit ingredients onto the hair due to the lamellar arrangement of solid-state surfactants. Perhaps most importantly the interconnected system of lamellar gel phase imparts a high yield stress, and highly shear-thinning properties, so the conditioner is able to spread easily over the hair to distribute ingredients and detangle hair (Iwata, 2017a).

In order to achieve the desired LGN structure, the surfactant, FA and water are heated to a temperature above the melting point of the surfactants, homogenised and cooled to below the Krafft point. When the system is cooled to below the solubility limit, the surfactants phase separate from the solution and various crystalline structures can form dependant on the critical packing parameter, CPP (Nakama, 2017). When a ratio of FA and surfactant is used that gives a CPP close to 1, the molecules form lamellar bilayers (Fairhurst *et al.*, 2008), (Ribiero *et al.*, 2004), (Wunsch *et al.*, 2016), (Yamagata and Senna, 1999). Efficient mixing is necessary for two key reasons. Firstly, the surfactant and fatty alcohol must be completely homogenised to ensure the required ratio/arrangement of molecules is achieved in the lamellar bilayers (α-gel arrangement). The surfactant must be evenly distributed to ensure repulsion and swelling between the layers, which is key to forming a gel phase rather than the alternative coagel phase, which precipitates out of solution (Davies and Amin, 2020). Secondly, the shear applied during the homogenisation dictates whether vesicles or bilayers are formed (Ito *et al.*, 2011). The manufacturing process is typically performed in a jacketed, temperature-controlled batch mixing vessel. Multiple impellers are employed to address the range of mixing requirements and fluid properties encountered throughout the process, *e.g.*, close clearance impeller to aid bulk mixing of high viscosity fluids and heat transfer, and rotor-stator mixers to provide emulsification of the oil phase ingredients into the aqueous phase.

The challenge of controlling mixing is not just confined to LGNs and it forms one of the most important operations in formulated product manufacture (Taifouris *et al.*, 2019). The transformation of raw materials into products increases the value of the constituent parts by up to two orders of magnitude (Centre for Process Innovation, 2018). However, it was predicted in 1992 that the cost to all process industries of poorly understood mixing was in the region of $1 to 10 billion (Nienow *et al.*, 1992). Thus, optimisation and understanding of mixing processes is integral to reducing production cost to enable price differentiation. Consumers have a plethora of brands and products to choose from, so manufacturers must differentiate themselves through either price, use of natural and organic ingredients, or superior performance, to win a share of the $12.7 billion global market (est. for 2022) (IMARC Group, 2022). Furthermore, FMCG manufacturers, such as Unilever, have set ambitious targets to reduce their greenhouse gas (GHG) emissions, most recently aiming to achieve Net Zero by 2039 across Scope 1,2 and 3 emissions (Unilever, 2024). They aim to achieve this by reformulating products with more environmentally-friendly ingredients, decarbonising the manufacturing process, and working with third party manufacturers to reduce their carbon emissions. Utilising raw materials and energy in the most effective way and optimising the manufacturing process will contribute to achieving these targets.

Therefore, it is highly beneficial for a global FMCG manufacturer such as Unilever to characterise the mixing stage of their manufacturing processes. An increased understanding of how processing parameters impact the formation of the lamellar gel network structure across different scales will aid in scaling-up formulations with new environmentally friendly ingredients in the most efficient manner, reducing research and development resource requirements (time, raw materials and energy).

In general, hair conditioner and its manufacturing process scale-up have received limited research focus due to the complexity of the fluid (structure and rheology) restricting the availability of mixing characterisation techniques. Understanding around the generation of the LGN structure is also relatively new information in the cosmetic formulation industry (Iwata, 2017a). Thus far, previous studies sponsored by Unilever in the Beauty and Personal Care area have focused on understanding isotropic fluids such as shampoos and bodywashes, which are more simple surfactant systems with less complex rheological behaviour (Espinoza *et al.*, 2018; Ryan *et al.*, 2018; Haroon *et al.*, 2020; Mihailova *et al.*, 2018). They also have the added benefit of being optically transparent when applying flow visualisation techniques (*e.g.*, particle image velocimetry) (Ryan *et al.*, 2017; Espinoza *et al.*, 2018). A relatively simple technique which can be applied to understand mixing processes is the measurement of torque on the mixer shaft, which allows for (i) calculation of the power number and determination of the mixing regime, (ii) correlation to viscosity to monitor the evolution of the microstructure as a function of processing parameters, and (iii) determination of scale-up parameters. This can be applied to manufacture of hair conditioners, where a large increase in the viscosity is seen as a result of the structure formation. It will also further understanding of the key scale-up parameters for LGNs, which to the authors' knowledge has not been reported previously.

Therefore, this work will focus on using torque measurements during the batch mixing process to understand how product microstructure formation and processing parameters are related, as well as how torque measurements can be utilised for in process understanding.

1.2 Relevance to Unilever

The industrial sponsor of this work was Unilever – a fast-moving consumer goods (FMCG) company with a presence in over 190 countries and a € 60.1 billion turnover in 2022 (Unilever, 2023c). Unilever are responsible for manufacturing some of the world's most well-known brands. 14 of these are defined as 'one billion euro plus' brands, with a turnover over € 1 billion in 2022, e.g. Dove, Sunsilk, Axe[1], Hellmann's, Lifebuoy, Knorr, Omo[2], Rexona[3], and Comfort. Unilever's products are used by over 3.4 billion people every day and are present in at least 98% of UK households (Unilever, 2023c). The beginnings of Unilever can be traced back to the development of Sunlight Soap, launched by the Lever Brothers in the UK in 1883. The purpose of this product was to bring cleanliness to ordinary people and improve health and hygiene. These key ideas evolved throughout time into the company's modern purpose which is 'to make sustainable living commonplace' (Unilever, 2023b). Unilever have ambitious targets for reducing their impact on the environment and have targets to achieve zero emissions in operations by 2030 (Unilever, 2023a).

The company is divided in to five business groups: beauty & wellbeing, personal care, home care, nutrition, and ice cream, underpinned by the business need to manufacture complex, multiphase products, where the microstructure is carefully designed to ensure the product achieves its intended purpose during application.

---

[1] Lynx in the UK
[2] Persil in the UK
[3] Sure in the UK

Employing new technologies and product structures allows for greater innovation of products and consumer benefits. For example, Unilever recently relaunched their Dove body wash featuring ‘Renewing MicroMoisture’ technology, which employs microdroplets to boost and retain moisture. This technology enabled new product claims such as ‘visibly reducing dryness by 50% after every shower’, ensuring product superiority compared to competitors (Mueller, 2023). This example highlights the continual need for innovation in the formulated product industry, especially for global companies such as Unilever.

This work will contribute towards Unilever’s net zero targets by furthering understanding of mixing processes and enabling optimisation of the manufacturing process, *e.g.*, by reducing time and energy needed to achieve the same quality product. It will also improve understanding of the impact of processing parameters on the LGN structure, so that if new ingredients need to be introduced, there are robust methods in place to characterise the structure formation. This project aligns with Unilever’s overall strategy by developing a greater understanding of how to generate the optimal product microstructure, and hence superior consumer experience, whilst employing the least energy to minimise GHGs.

1.3 Objectives

The purpose of this project is to further understand the manufacturing and scale-up of lamellar structured liquids, and how mixing efficiency and flow characteristics are affected by evolving rheology, fill level and scale. Whilst the study has primarily focused on lamellar structured liquids, this work is generally applicable to the manufacture of all structured liquids.

The main objectives of this thesis are:

1.) To study the effects of processing conditions on the formation and final microstructure of LGNs using a rheological approach

2.) To determine the impact of mixing geometry on the formation and final microstructure of LGNs

3.) To understand how torque measurements are affected by different processing conditions (fluid rheology, fill level, speed, scale) and how this affects online viscosity measurement

4.) To develop tools which enable online measurement of viscosity in partially filled vessels with close-clearance agitators (helical ribbons) to enable process optimisation

1.4 Thesis Layout

This thesis consists of seven chapters; an introduction, literature review, four results chapters, and finally conclusions and future work. The thesis follows an alternative format, where each results chapter is presented as an individual, published peer-reviewed research paper, including an introduction and background to the study, specific materials and methods, followed by discussion and conclusions. Additional context has been provided between the chapters to show the progression of thoughts throughout the project. Further information such as supporting data, short studies and method development can be found in the appendix. The chapters are as follows:

5.) **Chapter 1** provides a background and introduction to the work, and its industrial relevance.
6.) **Chapter 2** contains a review of the current literature in two sections. The first section (a) has been published as a review article and explores the use, structure and rheology of hair conditioner, as well as the current manufacturing process and scale-up approach. The second part (b) covers more fundamental aspects and critique of techniques for measuring rheology, monitoring mixing and model development.
7.) **Chapter 3** is the first results chapter. This study details the use of a rheometer with cup and vane geometry as a manufacturing vessel for a simple lamellar structured liquid. The processing time, temperature and impeller speed were varied, and the in-situ viscosity of the incipient lamellar structured liquid compared, along with the final rheological properties of the samples. A potential relationship between the peak viscosity during processing and the specific energy input to achieve this was discovered.
8.) **Chapter 4** is the second results chapter, which builds on the previous work by investigating the impact of impeller geometry on the formation of lamellar structured liquids, as well as the previously investigated processing parameters: temperature, time and impeller speed. The geometries used were a commercially available specialised rheometer geometry (helical rotor), as

well as two scaled-down, 3D-printed versions of industrially relevant agitators (anchor and helical ribbon). One of the key findings of this work was the consistent power per unit volume (P/V) value required to achieve the peak viscosity during mixing, regardless of mixing time, speed, and geometry, suggesting power per unit volume should be investigated further as a scale-up parameter for lamellar structured liquids.

9.) Following on from the key findings of the previous chapter, **Chapter 5** focuses on the understanding of how torque measurements are affected by process parameters such as speed, fluid rheology, and batch fill levels, and consequently whether typical mixer-viscometer techniques such as the torque curve method and Couette analogy can be applied to partial batch fill levels, with a view to developing an online viscosity soft sensor for use during formulated product batch manufacture.

10.) Chapter 5 established that typical mixer-viscometer techniques were not suitable for partial fill levels. In **Chapter 6**, the application of data-driven machine learning models was investigated for inferring viscosity from torque-speed data during batch processing.

11.) **Chapter 7** summarises the main conclusions of this work and the achievements compared to the objectives set. It also provides some ideas around future areas of research on this topic.

1.5 Publications, conferences, presentations, and awards

1.5.1 Publications

12.) Cunningham, G.E., Alberini, F., Simmons, M.J.H.; O’Sullivan, J.J. (2021). Understanding the effects of processing conditions on the formation of lamellar gel networks using a rheological approach. *Chemical Engineering Science, 242.* (Chapter 3)

13.) Cunningham, G.E., Deshpande, S., Simmons, M.J.H., O’Sullivan, J.J. (2023). Investigation of Industrially Relevant Rheometer Geometries for Improved Scale-Up of Lamellar Structured Liquids. *IFSCC Magazine, 26, (March), pp. 55-62* (Chapter 4)

14.) Cunningham, G.E., Deshpande, S., Simmons, M.J.H.; O’Sullivan, J.J. (2023). Investigating mixer-viscometer techniques for partially filled stirred tanks. *Chemical Engineering Science, 282.* (Chapter 5)

15.) Cunningham, G.E.; Simmons, M.J.H., O’Sullivan, J.J. (2024). Exploring Formulation, Manufacture and Characterisation Techniques of Lamellar Gel Networks in Hair Conditioners: A Review. Submitted to Advances in Colloid and Interface Science 23rd June 2024. (Chapter 2)

1.5.2 Conferences

Oral Presentations

- Cunningham, G.E.; Alberini, F., Deshpande, S.; Simmons, M.J.H., O’Sullivan, J.J. Investigating the effects of process variable on torque measurements to improve the scale-up of structured liquids. *Mixing XXVII – North American Mixing Forum,* online, 2022

- Cunningham, G.E., Alberini, F., Simmons, M.J.H., O'Sullivan, J.J. Mixing rheometry approach for investigating the manufacture of lamellar gel networks, *IChemE Fluid Mixing SIG Student Conference,* online, 2022
- Cunningham, G.E., Deshpande, S., Simmons, M.J.H., O'Sullivan, J.J. Investigation of Industrially Relevant Rheometer Geometries for Improved Scale-Up of Lamellar Structured Liquids. *32nd International Federation of Societies of Cosmetic Chemists Congress*, London, 2022
- Cunningham, G.E., Greenwood, R.W., Simmons, M.J.H., O'Sullivan, J.J., Developing an online viscosity soft sensor for partially filled vessels, *Mixing 17 – 17th European Conference on Mixing*, Porto, 2023

Poster Presentations

- Cunningham, G.E., Greenwood, R., Simmons, M.J.H., O'Sullivan, J.J. Neural Net Regression for Viscosity Soft Sensor with Evolving Batch Fill Level, *IChemE SIG Catalysis – Factories of the Future,* Birmingham, 2023

1.5.3 Awards

- Formulation Engineering CDT Award for STEM engagement and outreach (2019-2020)
- Winner of IChemE Fluid Mixing Process Special Interest Group student research competition (16th September 2022, University College London and online)

CHAPTER 2: LITERATURE REVIEW

CHAPTER 2, PART A: EXPLORING FORMULATION, MANUFACTURE AND CHARACTERISATION TECHNIQUES OF LAMELLAR GEL NETWORKS IN HAIR CONDITIONERS: A REVIEW

Adapted from Cunningham, G.E.; Simmons, M.J.H., O'Sullivan, J.J. (2024). Exploring Formulation, Manufacture and Characterisation Techniques of Lamellar Gel Networks in Hair Conditioners: A Review. Submitted to Advances in Colloid and Interface Science on 23rd June 2024.

2.1 Introduction

Surfactants are amphiphilic molecules that reduce the interfacial tension between fluids (typically air-liquid or liquid-liquid). For this reason, they have found applications in nearly every formulated liquid product where cleansing is the primary function, enhancing wetting, spreading and soil removal. Most recently, formulation scientists have turned to surfactants for their ability to generate complex microstructures which can provide new consumer benefits (Lai, 2005; Nakama, 2017). Due to their amphiphilic nature, surfactants assemble into a variety of different microstructures when dissolved. The geometry and morphology of the microstructure produced is dependent on the type of surfactant(s), solvent, temperature, concentration, and the method of assembly (processing conditions). Above the critical micelle concentration (CMC) and the Krafft temperature (the temperature at which surfactants become soluble), surfactants will begin to form micellar solutions. With increasing concentration, structural transitions to various lyotropic liquid crystal structures are observed. The structure depends on the critical packing parameter (CPP) and hydrophilic-lipophilic balance (HLB) for the surfactant, and the interfacial curvature (Miyake and Yamashita, 2017; Ghosh *et al.*, 2020).

Liquid crystal phases such as the lamellar phase, L_α, reversed hexagonal phase, H_{II}, and bi-continuous cubic phase, have garnered particular attention in recent years for their promising encapsulation properties (Huang and Gui, 2018). Potential applications that have been investigated include controlled drug release in the pharmaceutical industry (Guo *et al.*, 2010), unlocking the formulation of previously unstable actives in the cosmetic industry, (Yang *et al.*, 2023) and the development of low-calorie food products (Heertje *et al.*, 1998; Rezende Maciel *et al.*, 2016).

The lamellar gel phase, L_β, is a unique surfactant structure that is formed when a high concentration of surfactants (above the solubility limit) are cooled to below their Krafft point so that the surfactant tails are in a solid state, compared to lamellar liquid

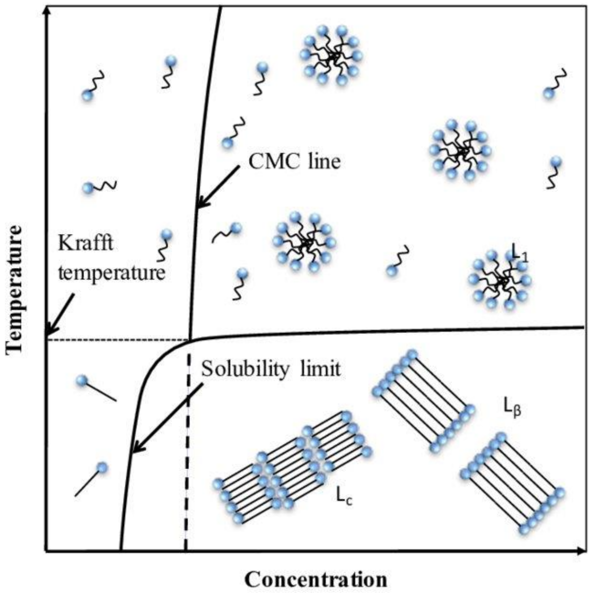

Figure 2-1. Iwata shows the lamellar gel phase, L_β, is an exception to conventional surfactant solutions which are present at concentrations above than CMC and Krafft temperature (from Iwata (2017b))

crystal, L_α, where tails are molten and flexible (Figure 2-1) (Iwata, 2017a; Iwata, 2017b).

For the gel phase to form on cooling rather than the hydrated solid or coagel phase (L_c), repulsive forces between the bilayers must be great enough to allow swelling to occur between the bilayers. This imparts a viscoelastic, gel-like behaviour to the system (Nakama, 2017; Wang and Maragoni, 2014; Eccleston, 1997). In cosmetic applications, typically a combination of fatty alcohol (cetostearyl alcohol) and high HLB surfactants (sodium docecyl sulphate (SDS), behentrimonium chloride (BTAC), behentrimonium methosulphate (BTAMS), cetyltrimonium chloride (CTAC), stearamidopropyl dimethylamine (SAPDNMA), *etc.)* are used to achieve this structure (Eccleston, 1997; Awad *et al.*, 2011; Nakarapanich *et al.*, 2001; Iwata and Aramaki, 2013; Minguet *et al.*, 2010; Iwata, 2017a).

The lamellar gel phase, L_β, is the key component of the multiphase lamellar gel network (LGN), first described by Junginger (1984), depicted in Figure 2-2. Other components of the LGN can include a bulk aqueous phase, hydrated solid crystals of amphiphiles (*e.g.,* fatty alcohol) which have not been incorporated in to the lamellar

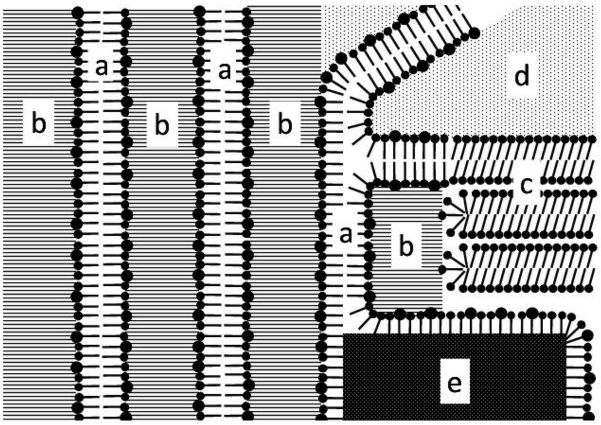

Figure 2-2. Schematic representation of a lamellar gel network. a) a-gel composed of surfactant and fatty alcohol, b) interlamellar water, c) hydrated fatty alcohol crystals, d) bulk aqueous phase, e) stabilised oil phase (from (Iwata, 2017a))

gel phase, and oil phase ingredients, which are stabilised by a monolayer of surfactant and fatty alcohol (Figure 2-2) (Iwata, 2017a; Junginger, 1984).

The LGN structure imparts desirable attributes mostly related to the rheological behaviour and texture, as well as high stability and compatibility with a broad range of ingredients compared to traditional emulsions. Iwata (2017a) summarises the key advantageous characteristics of LGN based creams:

- A desirable texture is achievable with a relatively low concentration of surfactants (minimum of 5 wt. %). As the surfactants are interconnected in a 3D network, the system is elastic at rest (possesses a yield stress), yet readily flows above the yield stress (extremely shear-thinning). This combination of rheological behaviour signifies a rich and creamy texture to the consumer.
- The bilayers of surfactant have greater surface area contact with the substrate, providing better deposition of actives, and improved tactile perception for the consumer.
- The LGN is very stable compared to other colloidal systems or emulsions, again due to the interconnectivity of the lamellar gel phase.
- It is compatible with formulations which include oil-soluble, water-soluble, and insoluble materials. Oil-soluble materials can be included in the bilayers, or as a separate phase, stabilised by the network. Water-soluble materials can be included in the interlamellar or bulk water phase, and insoluble materials can be dispersed throughout the network.

In summary, the targeted microstructure of hair conditioners, and other cosmetic and pharmaceutical cream products is an LGN. The amphiphilic molecules in this system are below their Krafft temperature, in a solid state (lamellar gel phase), which gives the system greater mechanistic strength than the liquid crystal phase (L_α). The interconnected, multiphase system imparts benefits when formulating a stable product, and with desirable rheological properties.

Whilst LGNs are common and valuable surfactant structures for formulating cream-based pharmaceutical and cosmetic products, little information exists regarding how the effects of processing history affect the formation of the microstructure during manufacture, and the resulting properties of the product, namely rheology and in-use performance. The aim of this review is therefore to critically evaluate the existing literature on the relationship between formulation, manufacturing, microstructure and in-use performance, with a focus on use of lamellar gel networks in hair conditioners and to propose opportunities for future research.

2.2 Hair Conditioner

The purpose of a hair conditioner is to enhance the appearance and feel of hair, adding shine, reflectance, fullness, and lubrication to improve manageability and maintain hairstyles (D'Souza and Rathi, 2015; Boullion, 1988). The need for hair conditioners stems from two key aspects of modern hair care. Firstly, in modern times, people may wash their hair every two to three days. Shampoo, a viscous liquid formulation containing surfactants, is used to cleanse the hair and scalp by removing unwanted dirt such as sebum, dandruff, residues from hair care products and environmental particulates (Thompson *et al.*, 2023). Advances in shampoo technology mean they are extremely effective in removing dirt, including sebum. However, sebum is a natural conditioner for the hair, and removing it completely can leave the hair tangled, frizzy, without shine, and susceptible to damage during styling (Alessandrini and Piraccini, 2016). Secondly, in the digitally connected world, trends in fashion and celebrity are shared globally and instantly using social media platforms. Consumers are using dyes, chemical treatments, and heat styling more often to achieve the styles they desire, resulting in damage to the hair (Swift and Brown, 1972; Rocafort, 2017). Thus, hair conditioners have become an essential part of the modern hair care regime, to *(i)* replace the beneficial properties of sebum, *(ii)* neutralise the negative charge left after shampooing. *i.e.,* reduce static electricity, in turn reducing hydrophilicity, and *(iii)* help to realign the hair cuticle with the shaft. All of these actions impart desirable attributes to the hair, such as shine, lubrication, and volume, improving the appearance of damaged hair (D'Souza and Rathi, 2015; Boullion, 1988; Bolduc and Shapiro, 2001; Fernandes *et al.*, 2023).

The main functions of hair conditioner are often separated into two parts – wet and dry conditioning (Yang, 2017). To enable wet conditioning and detangling, the key ingredients in the formulation are cationic surfactants and fatty alcohols (Fernandes *et al.*, 2023). In the concentrations used and in combination with water, these ingredients form the LGN microstructure previously described (Iwata, 2017a). This 3D connected structure presents unique advantages such as: (i) a high yield stress and shear-thinning rheological behaviour which is highly suited for formulating rinse-off treatments, (ii) superior stability compared to traditional emulsions, and (iii) excellent deposition of active ingredients on to the substrate (*e.g.,* hair and/or skin) (Iwata, 2017a; Moraes *et al.*, 2018; Eccleston, 1997). The key ingredients for dry conditioning action are traditionally silicones, and more recently natural oils such as almond and coconut oil, as well as fatty alcohols (Yang, 2017; Rocafort, 2017). Formulation and microstructural aspects will be discussed in more detail in the subsequent sections.

2.2.1 Formulation

For cosmetic applications, the typical primary constituents of a lamellar gel network are non-ionic or ionic surfactants, fatty amphiphiles, and water (Eccleston, 1989). Hair is a composite biomaterial composed of 65-95% proteins, as well as lipids, water, and other minor compounds. The main constituent of hair is keratin, a fibrous protein rich in tyrosine, glycine and cysteine amino acids, which have many negatively charged groups(Fernandes *et al.*, 2023). This makes the hair fibres naturally negatively charged, and this is enhanced further if the protective lipid layer is removed due to shampooing or damage exposing more of the hair substrate. This renders the hair fibre more hydrophilic, attracting moisture from the atmosphere and leading to capillary bridging between fibres, increasing friction, reducing manageability, and thus increasing likelihood of further damage (Yang, 2017; Bhushan, 2008). Therefore, cationic surfactants are normally included in hair conditioner formulations to neutralise the negative charge, which reduces hydrophilicity and increases lubrication, reducing friction and helping to minimise the effects of physical damage (Boullion, 1988; Bhushan *et al.*, 2005). A list of commonly used surfactants is given in Table 2-1.

The type of surfactant used provides different levels of conditioning for the consumer, and also alters the properties of the lamellar gel phase. Iwata and Aramaki (2013) investigated the differences in rheology, wet conditioning performance, and dry friction in formulations prepared with two different behentrimonium-based surfactants with different counterions: behentrionium methosulfate (BTAMS) and behentrimonium chloride (BTAC) (Figure 2-3).

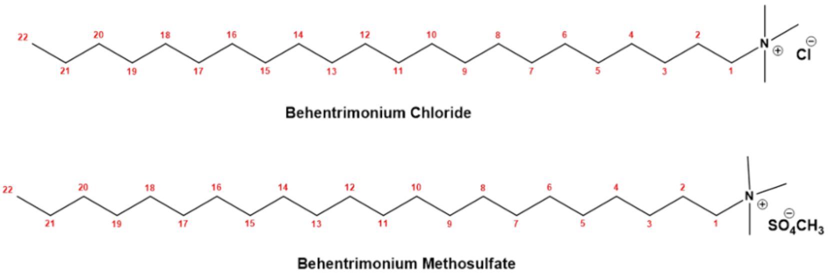

Figure 2-3. Schematic representation of Behentrimonium Chloride (BTAC) and Behentrimonium Methylsulfate (BTAMS) (from Meachum (2023))

The counterions affect the binding interactions within the LGN. The methylsulfate counterion in BTAMS is more tightly bound to the quaternary ammonium headgroup than the chloride counterion. This leads to reduced electrostatic repulsive forces between neighbouring surfactant molecules in the lamellar bilayer, which makes the bilayer in BTAMS systems more rigid. Consequently, the BTAMS system has less swelling capacity, and increasing the water concentration in the formulation results in lower overall mechanical properties, as the water only contributes to the bulk water phase instead of swelling the gel phase.

As well as the primary cationic surfactant, long-chain fatty alcohols are included as a secondary surfactant. Their purpose is multifaceted: as well as being texture and rheology modifiers, acting as bodying agents, adding slip and thickening the formulation, they are emollients and provide wet and dry conditioning to the hair (Rocafort, 2017; Suzuki, 2017). The most common choice is a combination of cetyl (C-16) and stearyl (C-18) alcohol. The combination of chain lengths is required to form a stable lamellar gel phase. Pure cetyl or stearyl alcohol are unstable in the α-gel unit structure of the lamellar bilayer and will separate upon cooling below the melting point to β (orthorhombic) or γ (monoclinic) crystals and phase separate (Eccleston *et al.*, 2000; Fukushima *et al.*, 1977). Not only does the combination of chain lengths improve packing in the α-gel structure, Fukushima *et al.* (1977) and Awad *et al.* (2011) showed how the melting enthalpy of the mixture is reduced, often to below ambient temperature, reducing the likelihood of transition to *β*- or *γ*- crystals.

For dry hair conditioning, the main ingredients are silicones, and sometimes other natural oils. The aim is to deposit the material on to the surface of the hair to reduce hydrophilicity and increase lubrication. Silicones are naturally hydrophobic, which allows for effective deposition onto undamaged, hydrophobic hair, but deposition onto damaged, and therefore more hydrophilic, hair is limited. Therefore, modified silicones with amino groups have been developed to improve deposition (Yang, 2017). The success of natural oils for lubrication is limited by poorer deposition and higher surface tension. Nevertheless, trends are moving towards silicone-free formulations for sustainability reasons (Goussard *et al.*, 2022), since silicones are derived from fossil fuels, require large amounts of energy to produce, and are not biodegradable (Grabenhofer, 2022; Peeters, 2020).

All of these key ingredients exist only in small percentages in the formulation (< 5 wt. %) (Table 2-1). Other functional ingredients such as solvents, humectants, rheology modifiers, pH adjusters, preservatives and emotive ingredients such as fragrances and appearance modifiers appear at even smaller concentrations (< 2 wt. %).

Table 2-1. Examples of hair conditioner ingredients and inclusion levels

Ingredient	**Example**	**Percentage in formulation**
Water	-	Up to 90%(Yang, 2017)
Cationic surfactant	Behenyl trimethyl ammonium chloride (BTAC) (Yang, 2017), (Yang & Okada, 2014), (Iwata & Aramaki, 2013), (Hough et al., 2013), (Ozkan, *et al.*, 2020) Behenyl trimethyl ammonium methyl sulfate (BTAMS) (Yang, 2017), (Yang & Okada, 2014), (Iwata & Aramaki, 2013), (Hough *et al.*, 2013) Stearamidopropyl dimethylamine (TAS) (Yang, 2017), (Labarre *et al.*, 2023) Cetyltrimethyl ammonium chloride (CTAC) (Yang, 2017), (Nakarapanich *et al.*, 2001)	0.5-3.5%(Yang, 2017),(Yang & Okada, 2014),(Iwata & Aramaki, 2013),(Ozkan *et al.*, 2020)
Fatty alcohol	Cetostearyl alcohol(Yang &Okada, 2014)*,* (Ozkan *et al.*, 2020)*,* (Labarre *et al.*, 2023)*,* (Nakarapanich *et al.*, 2001), (D'Souza & Rathi, 2015) *(combination of cetyl alcohol (C-16) and stearyl alcohol (C-18), of which cetyl alcohol = 1.2-2.2% and stearyl alcohol = 3.7-5.5% (of total formulation))*	0.5-10%(Yang, 2017), (Labarre *et al.*, 2023)
Lubricants	Aminosilicone(Iwata & Aramaki, 2013), (Ozkan *et al.*, 2020), (D'Souza & Rathi, 2015) PDMS (dimethicone) (Labarre *et al.*, 2023) Jojoba oil(Bhushan, 2008) Coconut oil(Bhushan, 2008)	0-10%(Yang, 2017), (Iwata & Aramaki, 2013),(Labarre *et al.*, 2023)
Benefit Ingredients/ Actives	Panthenol(Bhushan, 2008) Glycerin(Yang, 2017) Vitamin E Nicotinate(MakingCosmetics, Inc., 2023), (Rocafort, 2017)	0.05-1%(Nakarapanich *et al.*, 2001),(Yang, 2017)
Preservatives	Methylparaben(Yang, 2017) Phenoxyethanol(Yang, 2017) Methylisothiazolinone(Yang, 2017)	0.4-1%(Iwata & Aramaki, 2013),(Yang, 2017)
Fragrance	Fragrance(Rocafort, 2017)	0.1-1% (Yang, 2017),(Iwata & Aramaki, 2013)
Polymers/ Rheology Modifiers	Hydroxyethyl cellulose(Yang, 2017) PEGs(Yang, 2017) Hydrolysed proteins(D'Souza & Rathi, 2015) Collagen derived polypeptides(D'Souza & Rathi, 2015) Polyvinylpyrrolidone (PVP) (D'Souza & Rathi, 2015)	0-2%(Yang, 2017)

Ingredient	Example	Percentage in formulation
Colours/ Appearance Modifiers	Mica(Rocafort, 2017) Dyes(Rocafort, 2017)	0-0.5%(Yang, 2017)
pH adjusters	Citric acid(Yang, 2017) Lactic acid(Yang, 2017)	0-1%(Yang, 2017)

2.2.2 Rheology

The rheological behaviour of personal care products is integral to their functionality and consumer acceptance and is closely linked to the microstructure of the system (Ozkan *et al.*, 2020; Laba, 1997). The ability to characterise personal care product rheology becomes crucial in gauging consumer perception and potentially supplanting resource-intensive consumer panels (Ozkan *et al.*, 2020). Furthermore, a comprehensive understanding of how non-Newtonian rheological behaviours affect the manufacturing process is integral to their successful production. The interconnected nature of the LGN gives the structure a yield stress, shear-thinning behaviour, and viscoelastic nature (Davies and Amin, 2020; Datta *et al.*, 2020; Iwata, 2017a; Iwata and Aramaki, 2013; Stokes and Telford, 2004). These properties are important to understand during manufacture and in determining high performance in consumer usage. The examination of shear rates and associated rheological features at distinct processing and consumer usage stages is crucial for achieving optimal product performance. This spans manufacturing stages such as pumping and mixing and extends to in-use behaviour and consumer experience, stability and storage (Steffe, 1996). Figure 2-4 illustrates typical shear rate ranges, as a function of apparent viscosity, for some of the key flow processes in hair conditioner manufacture and use.

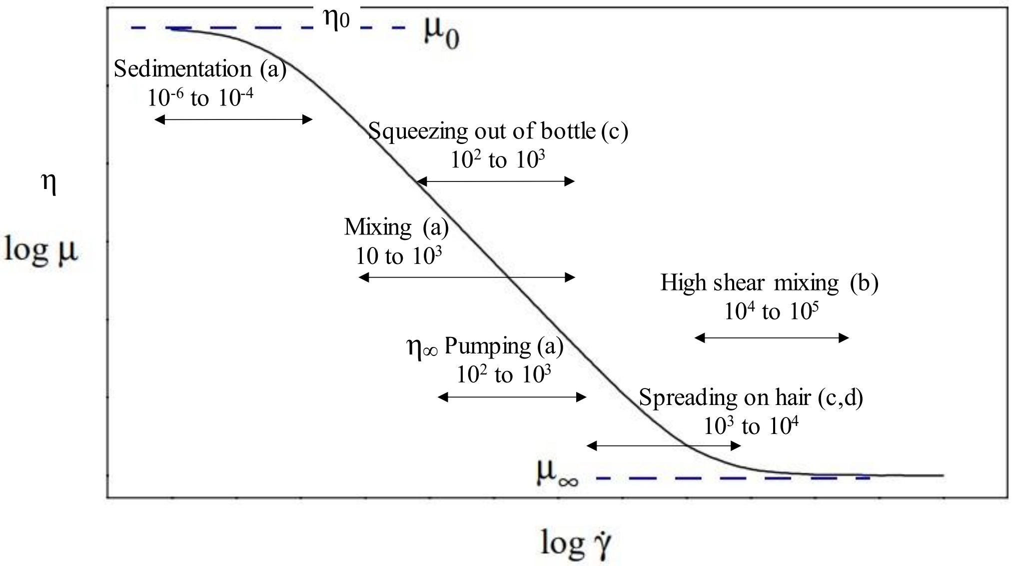

Figure 2-4. Typical flow curve of non-Newtonian, shear-thinning fluid showing typical shear rate regions (s^{-1}) of consideration for processing and consumer use of hair conditioner a) Alderman (1997), b) Espinoza *et al.* (2018), c) Formulaction (2016), d) Iwata and Aramaki (2013)

Initially, at rest, or at extremely low shear rates, strong interactions between colloidal scale particles cause the system to exhibit a high Newtonian viscosity plateau – the zero-shear viscosity, η_0. As the shear rate increases, the shear forces disrupt these interactions. For example, polymer chains become aligned with the flow rather than entangled, or aggregates of large particles are broken up. Eventually, the system reaches a second low Newtonian plateau corresponding to the infinite shear viscosity η_∞, where the internal microstructure cannot be broken down further by shear.

In chronological order, the first process stage to consider during the manufacture of the product is mixing. This occurs at both moderate shear rates (10^2 to 10^3 s^{-1}) during the initial stages of manufacture, followed by high shear rates (10^4 to 10^5 s^{-1}) during latter stages. High shear mixing is required to homogenise the oil and water phases effectively and to distribute later stage ingredients into the product once the viscosity has increased due to the emulsification (Hough *et al.*, 2013). Shear rate has been shown to impact the structure of the LGN, thus it is important that all of the product receives the same uniform mixing treatment (Coppola *et al.*, 2005; Ito *et al.*, 2011).

Hair conditioner, both during manufacture and in its final product form, shows a yield stress, shear-thinning rheological behaviour which is often described by the Herschel-Bulkley model (discussed further in later sections). It is well-established in the literature that mixing of shear-thinning fluids with a single, central impeller, such as a Rushton turbine or Scaba impeller, can lead to the formation of a cavern. This is where the area directly around the impeller is well-mixed, due to the reduced viscosity of the fluid at high shear rates, but the surrounding high viscosity fluid is not (Pakzad *et al.*, 2013; Kazemzadeh *et al.*, 2017; Bonnot *et al.*, 2007). Therefore, multiple impeller systems, including a close clearance scraper such as an anchor or helical ribbon, have been employed to aid bulk mixing and move the fluid towards the high shear regions. Alternatively, high shear rotor-stator mixers can be placed in-line, *e.g.*, in a recirculation loop to improve mixing efficiency (Ahmed *et al.*, 2018).

After manufacture, the final product is transported to filling and packing lines, where it is dispensed into bottles (van der Burgh, 2023). This pumping and dispensing action occurs at moderate to high shear rates, where the fluid is in its shear-thinning region. The shear-thinning behaviour can cause some difficulties in controlling pumping and dispensing (Holland and Bragg, 1995). Furthermore, if the system is left at rest between manufacturing and transportation to the filling lines, pumping equipment must be able to overcome the yield stress or zero-shear viscosity plateau to initiate fluid movement. Fortunately, hair conditioner also shows thixotropic behaviour, *i.e.*, its viscosity returns to the original at-rest value after shear stops, as its structure reforms over time (Datta *et al.*, 2020). Otherwise, pumping and filling could permanently disrupt the product structure which has been carefully manufactured in the previous stage.

For a desirable consumer experience, hair conditioner should have a thick texture and a piled appearance when dispensed into the palm – behaving more like a solid than a liquid, *i.e.*, exhibiting viscoelastic behaviour (Iwata and Aramaki, 2013). Viscoelasticity is characterised by the magnitude of the storage and loss moduli, where the storage modulus is the elastic component which quantifies a material's ability to store energy within its structure, whilst the loss modulus is the viscous component, which refers to the energy dissipated by the system (Larson, 1999). Again, thixotropy is important, as once the consumer has applied shear to dispense the product from the pack, it must immediately reform to behave as a solid.

Next, when hair conditioner is applied to wet hair, it should offer a thick, luxurious texture, and during rinsing, it should impart a slippery, soft feel (Iwata and Aramaki, 2013). Davies & Amin (2020) found that a high yield stress value correlated with better wet lubrication and deposition. Interparticle interactions, *e.g.,* the network of lamellar bilayers, cause the material to exhibit solid-like behaviours at low shear conditions. The yield stress is considered as the point at which a material transitions from behaving as an elastic solid, to flowing like a liquid (Larson, 1999). Furthermore, a higher degree of shear-thinning typically suggests better lubrication, and this is correlated with the formation of a thin coating which maintains separation between surfaces (Centre for Industrial Rheology, 2014).

Finally, Figure 2-4 shows that for the shear rates which are relevant for separation and sedimentation of multiphase colloidal systems (10^{-6} to 10^{-4}); hair conditioner should ideally be in the Newtonian zero-shear viscosity plateau, or below its yield stress value to prevent separation from occurring and to maintain a stable product.

Measuring Rheology of LGNs

Small angle oscillatory shear (SAOS) measurements using a rotational rheometer are a standard technique for characterising viscoelastic samples. A plot of the storage modulus (G') and loss modulus (G") versus the strain amplitude or frequency can provide insights into the structure of the material. For example, in Figure 2-5a (amplitude sweep), the profile is typical of a gel, where elastic behaviour is initially dominant, and G' and G" are independent of strain rate (linear viscoelastic region, LVER) up until a critical strain rate, at which point the storage modulus decreases considerably resulting in viscous behaviour dominating at high strain rates (G">G'). The LVER typically exists up to a limit of ~10% oscillation strain for LGNs (Datta *et al.*, 2020; Colafemmina *et al.*, 2020; Youssry *et al.*, 2008). Subsequent frequency sweeps are typically carried out at 1% amplitude to ensure it is within the LVER (Figure 2-5b). For structured, solid-like materials, the storage modulus G' is often nearly independent of frequency in the LVER, whilst a higher dependency of G' on frequency indicates the material is more fluid-like. In Figure 2-5b, G' and G" show a weak dependence on frequency.

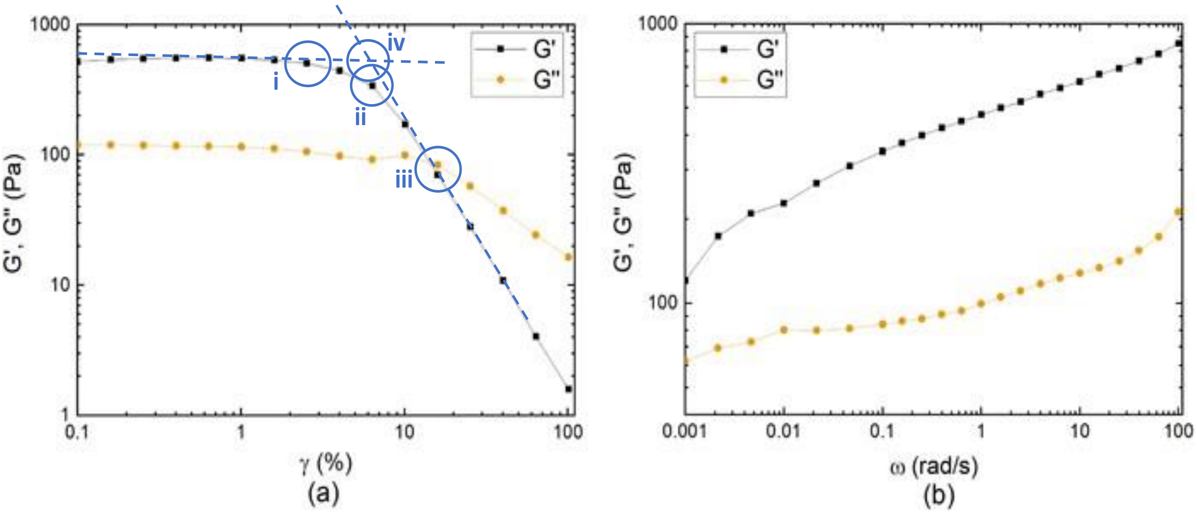

Figure 2-5. Storage and loss moduli in (a) an amplitude sweep at a fixed angular frequency of 1 rad/s and in (b) an angular frequency sweep at a fixed shear strain amplitude of 1%, which lies within the LVER indicated in (a). Marked with various methods for determining yield stress: i) last point in linear viscoelastic region, ii) last point before second linear slope starts, iii) cross-over point of G' and G'', iv) extrapolated point where two linear lines meet (Datta *et al.*, 2020)

Applying oscillation measurements to a manufacturing context, high frequencies simulate short time scales, and low frequencies simulate long-term stability or at rest conditions.

The 'bump' in G" before the cross-over of G' and G" is an important feature (Figure 2-5a) attributed to the formation of a weak intermediate structure. The structure is able to withstand deformation up until a critical strain value, after which it breaks up and begins to align with the flow and behave in a viscous manner (Youssry *et al.*, 2008; Hyun *et al.*, 2002). This phenomena was first described by Payne for filled rubber systems, is therefore often referred to as the Payne effect (Payne, 1962). Youssry *et al.* (2008) found that a strain overshoot occurred for LGNs which contain multilamellar vesicles (MLVs), where the feature coincides with the breakdown of the MLVs to smaller structures. MLVs are structures made up of concentric lamellar bilayers. Amplitude sweeps can also be used to determine the yield stress of LGNs.

However, care must be taken as different points on the curve are regarded as the yield stress value by different researchers. Davies & Amin (2020) utilised the last measured point before the storage modulus drastically reduces, *i.e.,* point ii on Figure 2-5a to determine the yield stress values for hair conditioner samples, whilst others use the last point in the LVER (point i). The cross-over point (point iii) is generally considered to be higher than the true yield stress value, but is commonly used as it is easier to define (Öhrlund, 2018). Another commonly used method is to extrapolate the two linear lines and take the cross-over point of these lines as the yield stress. This removes the ambiguity around selecting the point on the graph for method i and ii (Cyriac *et al.*, 2016).

Another important rheology measurement for LGNs is the flow curve, *i.e.,* a plot of apparent viscosity versus shear rate. LGNs have most commonly been fitted to the Herschel-Bulkley and Cross models (Stokes and Telford, 2004; Simoes *et al.*, 2020; Rezende Maciel *et al.*, 2016) (Table 2-2). The Herschel-Bulkley model is often well-fitted over the range of shear rates a typical rheometer can measure, however the Cross model is more representative of the rheology over a very large shear rate range since it models the low shear and infinite shear plateau regions. The flow curve can also be simplified to a power law model by concentrating on shear rates above the yield stress value of the fluid. It is important to measure the viscosity over a range of shear rates, as different shear rates are relevant for each part of the process, from manufacturing to consumer use (Figure 2-4).

Table 2-2. Empirical Rheology Models used for description of LGNs

Model	**Equation**	**Use**
Ostwald-de Waele (Power Law)	$\tau = K\dot{\gamma}^n$ *Where* τ *is shear stress,* K *is the consistency index,* n *is the flow behaviour index*	Describes power law region of non-Newtonian flow curve, can be applied to shear-thinning (n<1) or shear-thickening (n>1)
Herschel-Bulkley	$\tau = \tau_0 + K\dot{\gamma}^n$ *Where* τ *is shear stress,* τ_0 *is yield stress,* K *is the consistency index,* n *is the flow index*	Can be applied to a wide range of properties. Typically fluids which show a yield stress, followed by power-law flow above the yield stress (normally shear-thinning)
Cross	$\eta = \frac{\eta_0 - \eta_\infty}{1 + (K\dot{\gamma})^n} + \eta_\infty$ *Where* η *is apparent viscosity,* η_0 *is the zero-shear viscosity,* η_∞ *is the infinite shear viscosity*	Describes transition from zero-shear viscosity plateau to power-law shear-thinning region, followed by the infinite shear viscosity plateau
Whilst *K* and *n* are conventionally used as symbols for the consistency index and flow behaviour index across all models, they will not have the same value when data is fitted to the same fluid, so values for different fluids should not be compared from data fitted to different models.		

Due to the heterogeneous nature of LGNs, wall slip can occur during rheology measurements caused by depletion of the dispersed phase at the solid geometry wall, leaving the lower viscosity continuous phase remaining where high velocity gradients develop (Barnes, 1995). This often manifests itself as a drastic reduction in viscosity and can therefore be commonly mistaken for a yield stress or erroneously low viscosity values. To compensate for this, roughened or profiled geometries, or vanes can be employed. This aids prevention of depletion at the wall as particles can fit into the recesses of the roughened geometries (Figure 2-6).

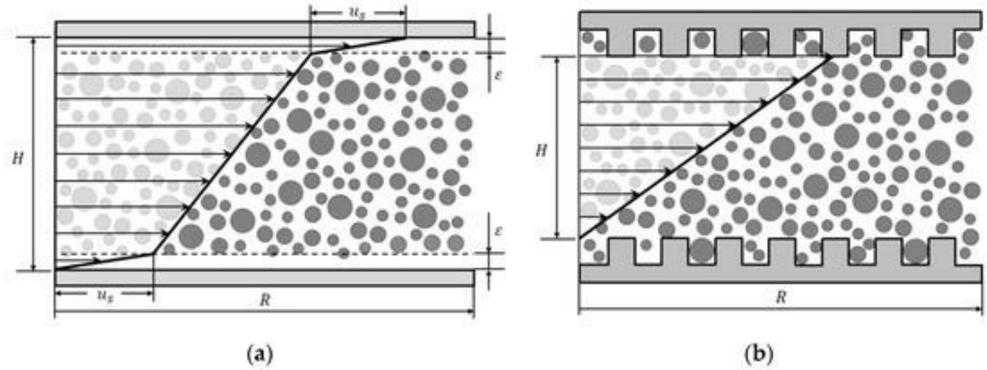

Figure 2-6. Schematic of the velocity profile in a parallel-plate system with a) particle-depleted areas at the wall (slip), b) grooved surface to prevent wall slip (Pawelczyk *et al.*, 2020)

2.2.3 Additional characterisation methodologies

The microstructure of colloidal systems impacts the in-use performance and consumer acceptance of the product, including its rheological behaviour. Thus, to design superior products, it is necessary to characterise the microstructure.

Microscopy enables the visualisation of the morphology, size, and arrangement of structures within colloidal systems such as emulsions and surfactant systems (Ahmadi *et al.*, 2020b). It is commonly used to investigate changes in microstructure due to pH, temperature, and shear (Muller *et al.*, 1999; Barry and Saunders, 1970). Optical (light) microscopy is suitable for probing macroscopic level features from millimetre to µm, whilst Electron microscopy enables the structure of colloidal, multiphase materials to be probed at a much higher resolution from 10 µm to 0.1 nm (Yamashita and Sakamoto, 2017). Cross-polarised light microscopy is commonly used to detect anisotropic liquid crystal structures, *e.g.,* the hexagonal or lamellar phase (Yamashita and Sakamoto, 2017). These structures are birefringent, and exhibit brightness under cross-polarised light. Multilamellar vesicles (MLVs) present as Maltese crosses (Duerr-Auster *et al.*, 2007) (Figure 2-7).

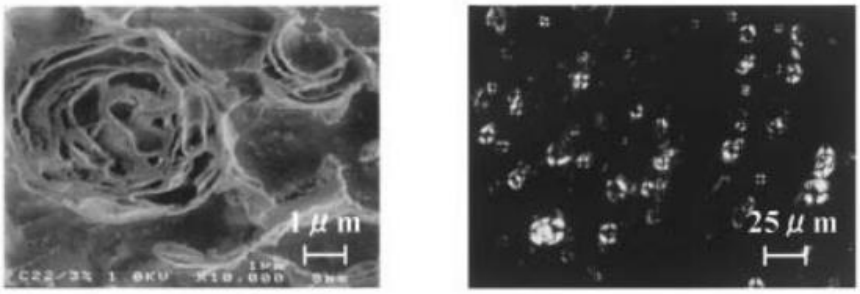

①Cyro-SEM image with LPB ②Polarization microscope image with LPB

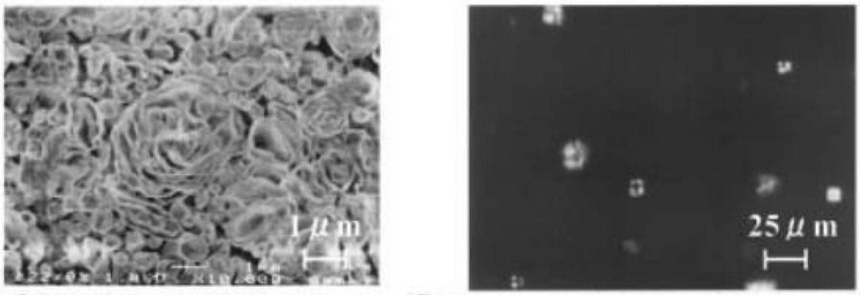

③Cyro-SEM image without LPB ④Polarization microscope image without LPB

Figure 2-7. Cryo-SEM and Polarization Micrographs of Cationic Assemblies of 0.06 mol/L BTAC, 0.18 mol/L $C_{22}OH$, with and without 0.1 mol/L LPB in water (Nagahara *et al.*, 2007)

Transmission electron microscopy (TEM) and scanning electron microscopy (SEM) are the main types of electron microscopy used. TEM works by passing a high energy electron beam through an ultra-thin sample, and the electrons which are transmitted are used to create high-resolution images of the specimen's internal structure and composition. SEM passes a beam of electrons across the surface of the sample, and the emitted electrons are used to build images of the sample's surface topography. For liquid samples, sample preparation can include rapid freezing through use of liquid nitrogen (-196 °C) and etching (*i.e.*, active sublimation of superficial water) to reveal aspects of the microstructure, which adds complexity to the technique, and therefore limited use of the technique is present in literature. Figure 2-8 shows two examples of cryo-SEM micrographs of a lamellar structured hair conditioner manufactured under different conditions. The differences in structure of the two samples are evident, with the sample prepared at high deformation rates showing a more structured system, with interconnected layers of lamellar sheets, whilst the sample at low deformation rates has a more amorphous structure (Hill, 2004).

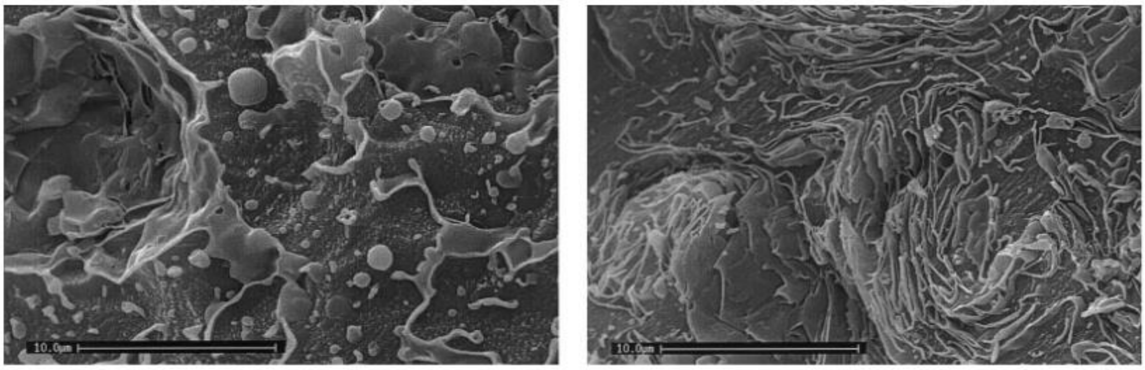

Figure 2-8. Cryo-SEM micrographs of a lamellar structured hair conditioner manufactured under low deformation rates (left) and high deformation rates (right) (Hill, 2004)

Nagahara, *et al.*, (2007) also used cryo-SEM along with DSC, calorimeter polarisation and X-ray diffraction to examine differences in microstructure and resulting in-use performance of a hair treatment when amido propyl betaine laurate (LPB) was included in the formulation. Differences were seen in both the polarised optical and cryo-SEM micrographs (Figure 2-7). The cryo-SEM shows a more visual representation of the microstructure and scales, whilst polarised optical microscopy must be interpreted by a trained expert with domain knowledge of the system.

Since optical microscopy is not efficient in differentiating between different lamellar phases, differential scanning calorimetry (DSC) is employed. In DSC, the heat changes in a sample are measured as it is subjected to a controlled temperature program, *i.e.,* heating or cooling, which provides information about phase transitions, such as melting, crystallisation, glass transition temperatures and chemical reactions. DSC is therefore useful in determining the purity of samples, studying stability and determining if a lamellar structure is in the liquid crystal phase, L_α or gel phase, L_β. Eccleston (1985) utilised DSC to examine stability variations in ternary systems (cetrimide, fatty alcohol, water) and oil-in-water emulsions.

Ternary systems, representing the emulsion continuous phases, display immediate semisolid properties post-preparation. The ternary system and oil-in-water emulsion prepared with cetostearyl alcohol maintained their semisolid state over 30 days, exhibiting consistent DSC curves with a crystal-gel network transition at ~14°C and gel network-liquid crystalline transitions at ~45°C. In contrast, unstable pure alcohol systems become mobile, causing emulsion separation, with apparent viscosities decreasing and DSC transitions occurring well above 25°C – the stability test temperature. These findings highlight the importance of the stable viscoelastic gel network phase, with specific transition temperatures, for achieving and maintaining multiphase formulation stability. Wunsch *et al.,* (2016) used DSC and x-ray scattering to investigate the effect of surfactant on the thermal behaviours of fatty alcohols. Ternary creams (water, fatty alcohol, and CTAC) showed a single transition at ~70°C, from the L_β to the L_α phase, on heating and cooling. However, a DSC prepared with solid fatty alcohol in a CTAC solution showed additional transitions even after the second heating, highlighting the presence of fatty alcohol impurities due to the lack of mixing (Figure 2-9).

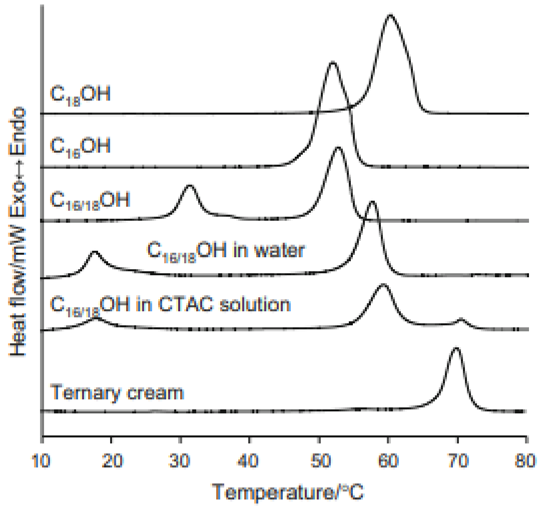

Figure 2-9. Thermal behaviour of long-chain alcohols: pure ($C_{16}OH$ and $C_{18}OH$) and in 50/50 mixture ($C_{16/18}OH$), flooded with water ($C_{16/18}OH$ in water) or surfactant with a mass fraction of 6^ ($C_{16/18}OH$ in CTAC solution), and in a homogenised ternary cream. Second heating at 5°C min^{-1} (Wunsch *et al.*, 2016)

2.3 Lamellar Gel Network Manufacturing Process

There is little discussion in the literature of how LGNs, and more specifically hair conditioners, are manufactured, as processing information is typically held as commercially confidential. However, some information can be found in the patent literature. In general, the key processing steps for producing a lamellar gel network are heating the ternary system comprised of main surfactant, co-surfactant (fatty alcohol) and water, to above the melting temperature of the fatty alcohols, homogenising, and then cooling to ambient temperature.

Yang and Okada (2014) detail a method of manufacture of a hair conditioning treatment. To summarise, a premix which consists of some of the oil phase ingredients, *i.e.,* the cationic surfactant and long-chain fatty alcohol is prepared in a vessel to a temperature between 65-85°C. In a second vessel, the aqueous carrier phase, consisting mostly of water, is prepared to a temperature between 55-75°C, and cooler than the melting point of the premix ingredients. The two phases are mixed using a higher shear mixer such as a liquid whistle, (*e.g.,* a Sonolator, Sonic Corp, USA) in a continuous manufacturing approach or a Becomix Universal homogeniser in a batch mixing vessel to form an emulsion (Yang and Okada, 2014). A similar process is described by Hough *et al.* (2013). An oil phase containing the surfactant and long-chain fatty alcohol is prepared by melting them together at a temperature of 85°C. The aqueous phase, water, is heated to 40°C. The phases are combined using a homogeniser and the mixture is subsequently cooled to ambient temperature by the injection of a second ambient water stream (Hough *et al.*, 2013).

2.3.1 Manufacturing Equipment

Personal care and cosmetic products, such as hair conditioners, can be manufactured in a batch or continuous mode. In batch mixing, sequential addition of raw materials into the vessel under controlled process parameters causes the formation of the microstructure of the product. To handle the rheologically evolving system and significant increase in viscosity, batch mixing vessels are typically equipped with multiple agitator types (Franco *et al.*, 2005; Espinosa-Solares *et al.*, 2002) (Figure 2-10).

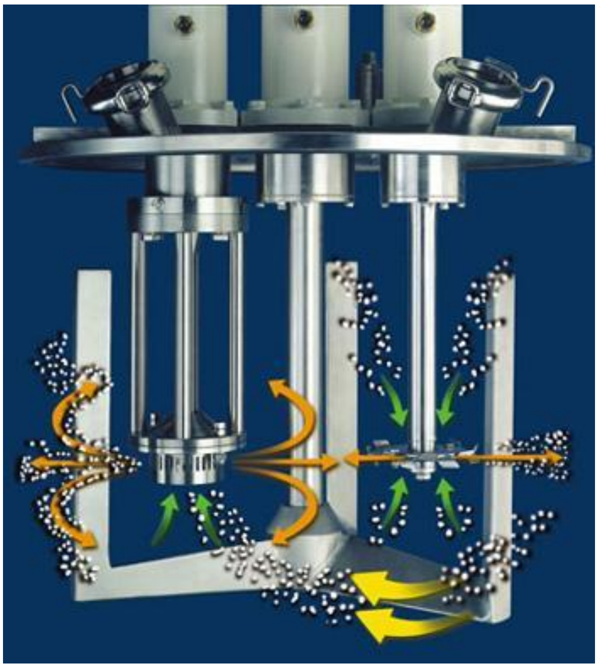

Figure 2-10. Schematic of example multi-agitator mixer used in processing of rheologically evolving systems, including a close-clearance anchor scraper, high-shear rotor stator and disperser (adapted from (Ghanem *et al.*, 2014))

This normally includes a close clearance agitator such as an anchor or helical ribbon, which is specifically designed for high viscosity fluids (10 to 100 Pa s), aids heat transfer and enhances bulk mixing (Pedrosa and Nunhez, 2000; Brito-de La Fuente *et al.*, 1997). Close clearance impellers are for example used in saponification reactions, for the manufacture of lithium greases, where extremely high viscosities and non-Newtonian behaviour are present throughout the process (Franco *et al.*, 2005), and frequently in food applications where again high yield stress, high viscosity fluids and suspensions are commonplace (Mokhefi, 2024). Espinosa-Solares *et al.* (2001) also noted how a helical ribbon acts as a baffle to prevent vortex formation in lower viscosity fluids. Secondly, an impeller to promote higher shear radial and/or axial mixing, such as a propeller or turbine, is situated offset to the centrally positioned close clearance agitator. Kazemzadeh *et al.* (2017) investigated the mixing efficiency of various combinations of Scaba impellers, Rushton turbines, and pitched blade agitators in combination with anchors for yield-pseudoplastic fluids. The combination of a Scaba, pitched blade, and anchor was found to provide the most efficient mixing. In cases where powders are included in the formulation, a sawtooth impeller may be used as an offset mixing element (Chara and Kysela, 2019; Paul *et al.*, 2003). Finally, to promote efficient incorporation of ingredients, emulsification and droplet breakup, a rotor-stator mixer (*e.g.,* a Silverson or YTRON) may be used either a dip-in type within the vessel (*i.e.*, offset to the centrally positioned mixing element) or inline as part of a recirculation loop (Hall *et al.*, 2011). Due to the use of close clearance impellers, vessels for personal care manufacture are typically not baffled, however, the inclusion of thermowell temperature probes within the vessel have the dual function of acting as baffles to some extent. Examples from literature include the Becomix universal homogeniser and Ekato Unimix (Yang and Okada, 2014).

Alternatively, continuous manufacturing offers some advantages over traditional batch manufacture for fast-moving consumer goods, namely (Koo, 2021):

- Higher efficiency – all of the ingredients are always moving through the system, and less downtime is required for cleaning between batches.
- Higher production volumes – a higher volume can be produced in a shorter time frame and with a smaller equipment footprint.

For continuous manufacturing, an inline mixer such as a Sonolator liquid whistle can be used for a range of home and personal care products (Yang and Okada, 2014) (Figure 2-11). A Sonolator is operated by pumping multiple liquid phases through a specially designed orifice and blade configuration.

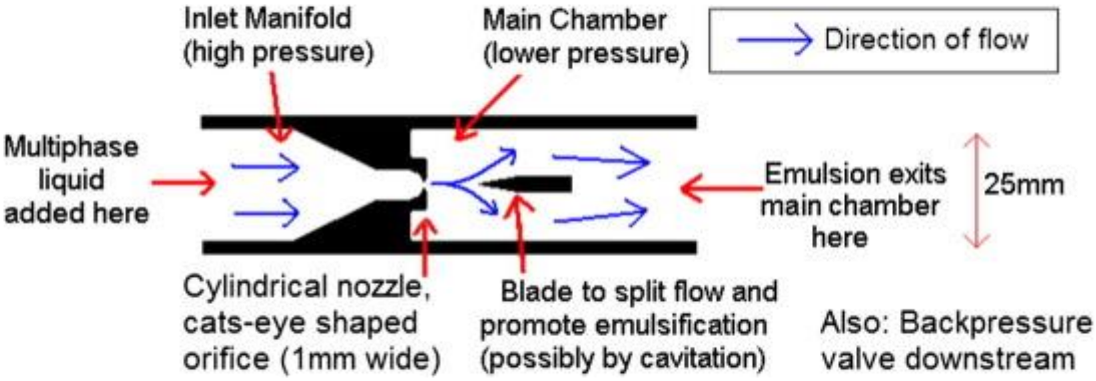

Figure 2-11. Schematic of sonolator whistle (Ryan *et al.*, 2017)

The materials undergo ultrasonic cavitation, resulting in the breakup of the liquid into small droplets, forming a homogenised or emulsified outlet stream. It was originally thought that the mechanism of droplet breakup was due to the high pressures experienced in the orifice, as well as cavitation around the orifice and blade (John *et al.*, 2020). However, some studies suggest that the turbulence through the orifice is sufficient, and the mixture is homogenised before reaching the blade (Ryan *et al.*, 2017; John *et al.*, 2020). Liquid whistles have found other novel applications (John *et al.*, 2020), for example, hydrodynamic cavitation in a Sonolator was used to improve ozone mass transfer in water disinfection (Chand *et al.*, 2007). Ultrasonic cavitation was also proven to be a useful technology for formulating pharmaceutical nano-emulsions, providing superior energy efficiency and low equipment contamination compared to existing available technologies (Sivakumar *et al.*, 2014).

After the initial homogenisation stage, whether batch or continuous, the product is a highly viscous, structured material. The proceeding stages of manufacture comprise the inclusion of low concentration, possibly temperature sensitive ingredients such as fragrance, benefit ingredients, pH adjusters and preservatives, *etc.* Ensuring efficient mixing of small quantities of material into a high viscosity system can be difficult. Static mixers, which are pipe inserts that disrupt flow and encourage distributive mixing, can be useful for laminar mixing applications (Mihailova *et al.*, 2015), particularly in continuous manufacturing.

Nevertheless, batch processing remains popular as it offers several advantages for the consumer goods industry:

- Better control over product quality; raw material variability is high and difficult to control in continuous processing, but less noticeable and more easily rectifiable in batch.
- Greater flexibility in the types and volumes of products which can be manufactured, which allows faster innovation and room for market personalisation.
- Better traceability and lower chance of contamination across batches.

Furthermore, continuous processing requires higher initial capital investment, take longer commission, and add operational complexity (*i.e.,* more complex start-up and shut-down procedures).

2.3.2 Effects of Processing Parameters on Structure Formation

Impact of Temperature During the Mixing of Oil and Aqueous Phases

Temperature can be varied in different ways during LGN manufacture. The temperature of the oil phase, aqueous phase, and temperature when they are combined can be varied to yield different outputs in terms of product microstructure and thus rheology. The temperature profile and/or cooling rate after the homogenisation of the aqueous and oil phases also plays a significant role in final product structure and characteristics. This will be discussed in subsequent sections.

The temperature of the oil phase is normally dictated by the melting point of the cationic surfactant and fatty alcohol. Ensuring that all of the components are above their melting point is essential for effective mixing and structure formation. At commercial manufacturing scale (> 5 tonnes), efficient mixing is important to maintain good heat transfer throughout the vessel. A high temperature gradient between the jacket vessel and the contents could cool the mixture before the lamellar gel phase has formed, leading to the presence of hydrated crystals of fatty alcohol which are not incorporated into the gel phase (Iwata, 2017). Temperature also impacts whether the lamellar phase forms as vesicles or lamellar sheets. Ito *et al.* (2011) showed how at higher temperatures (>70°C) and shear rates (>1 s^{-1}), lamellar systems form multilamellar vesicles (Figure 2-12).

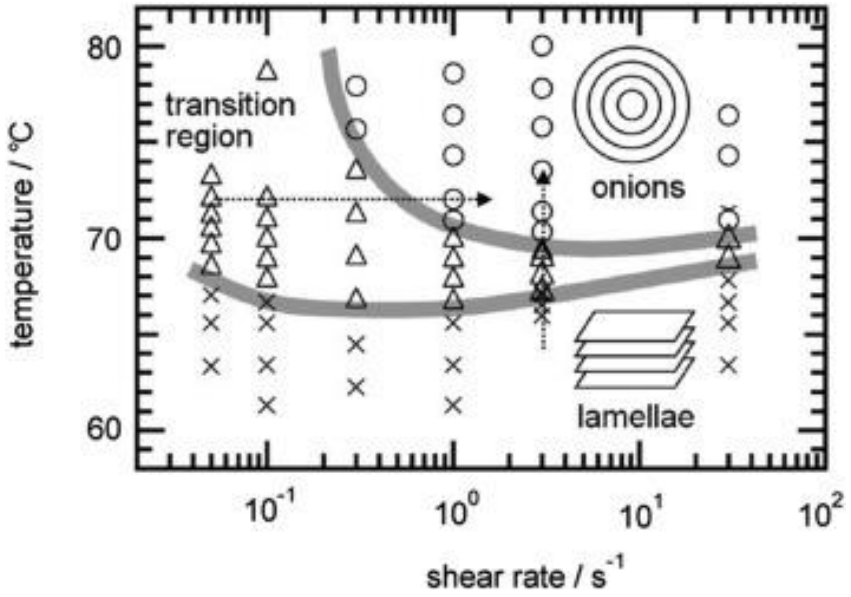

Figure 2-12. Temperature-shear rate phase diagram of 48% $C_{16}E_7$ in deuterium oxide (D_2O) showing lamellar to multilamellar packed vesicle ('onion') transition. Cross, triangle, and circle indicate lamellar, transition zone, and onion, respectively (Ito *et al.*, 2011)

Hough *et al.* (2013) also describe how temperature should not be “too high” as to prevent vesicle formation, but not “too cold” that the oil phase solidifies. Thus far, no studies have investigated the effects of mixing time, mixer speed, and temperature during the homogenisation stage of LGN manufacture on the final structural and rheological properties of the product. The Krafft temperature of the surfactants, which commonly coincides with the melting point of the surfactant tails is an important temperature to consider as this is when the lamellar phase transitions from liquid crystal, L_α, to gel phase, L_β. Furthermore, most shear-temperature studies have been carried out on binary systems (*e.g.,* surfactant and water, (Ito *et al.*, 2011; Hatakeyama *et al.*, 2023), and not ternary systems, so it would be interesting to see the effects of concentration in different ternary systems. Finally, the concept of adding surfactants as solids and heating them in solution is not discussed in literature, nor is the order of addition of surfactant, fatty alcohol, and water, or the effect of temperature during addition of minor materials after the initial homogenisation stage.

Impact of Shear during the Mixing of the Oil and Aqueous Phases

Studies have shown that shear has an impact on the formation of multilamellar vesicles in contrast to lamellar bilayers. It has been observed for multiple binary systems that above a critical shear rate, multilamellar vesicles are the dominant microstructure observed (Coppola *et al.*, 2005; Ito *et al.*, 2011). The mechanism by which this occurs developed by Zilman and Granek is widely accepted (Zilman and Granek, 1999). They suggest that if lamellar sheets are subject to shear forces greater than the typical undulation in the system from bilayers colliding, the lamellar buckles and curls up, eventually leading to concentric spherical layers, *i.e.,* a multilamellar vesicle. This is also assumed to be the mechanism for ternary systems. Ajayi *et al.*, (2021) found that increasing shear/mixing speed resulted in diminished rheological properties and wet conditioning performance. This suggests that too high a speed leads to the formation of vesicles and reduced rheological and conditioning performance. The manufacture of a single formulation over a wider range of mixing speeds, shear rates, or energy densities, would help to confirm this hypothesis.

Whilst the impact of shear on the formation of vesicles or sheets in binary systems has received some research attention, the type of mixer, *e.g.*, batch vs continuous, high shear vs moderate, and the duration of each type of mixing could all impact the overall structure formation and rheological properties. This should be further investigated, and the properties of the system linked to in-use performance.

Impact of Cooling Rate after Homogenisation

The cooling step after the oil phase and aqueous phase have been mixed impacts structure formation as it induces crystallisation of the surfactant and fatty alcohol in to the L_β phase as the system is cooled below the Krafft temperature (Colafemmina *et al.*, 2020). Colafemmina *et al.,* investigated the effect of cooling rate on the structure and rheology of a CTAC, cetearyl alcohol and water mixture. They found that quench cooling (40 °C/min) compared to slow cooling (5 °C/min) produced a sample where a higher percentage of materials were converted to the L_β phase (100% compared to 90%), the *d*-spacing was higher (31.4 nm compared to 28.5nm), and the bending rigidity was five times higher; resulting in an elastic modulus and viscous modulus four times higher for the quench cooled sample (Colafemmina *et al.*, 2020). This is thought to be because once the initial structure is formed at high temperatures, the system, at the concentrations of fatty alcohols and surfactants in this study, favours a fully swollen L_β phase, and the rapid cooling action "freezes" this in place, without allowing other lamellar phases to be formed. Cooling rate appears to have a significant effect on the conversion of materials into the lamellar gel phase, yet research so far appears to be limited to this study. In the future, the full range of cooling rates (e.g., between 5 °C/min and 40 °C/min) could be studied. This would also inform process optimisation where the balance of achieving fast cooling rates at manufacturing scale is balanced with the improvements in product quality. Similarly, it would be interesting to characterise a bulk product which has seen a range of cooling rates due to poor heat transfer at large scale, or in general assess the effects of scale on heat transfer and product quality. Different methods of cooling should also be investigated, *e.g.*, jacket cooling, natural cooling, passing through a heat exchanger, quench cooling via addition of cool materials, *etc.*

2.4 Areas for Future Research

Although numerous advances have been made in the understanding of the microstructure and formation of LGNs, there is still more research to be done on understanding the impacts of processing variables during commercial manufacture to keep up with consumer needs and wants. Across FMCG industries, trends towards sustainability and targets for achieving Net Zero remain prevalent, driven by consumers' increasing awareness of the social and environmental impact of products and potential economic benefits (Laursen, 2023; Martins and Marto, 2023). Sustainability of FMCGs can be improved through packaging innovation, sustainable sourcing, circular economy, carbon neutrality. Two key focus areas for improving sustainability are sustainable sourcing, *e.g.*, replacing fossil fuel derived, non-biodegradable, or unsustainably grown plant-based materials (Martins and Marto, 2023). This presents challenges in formulation that require fundamental understanding of microstructure formulation (Goussard *et al.*, 2022). Secondly, large global companies are setting targets to be carbon neutral or negative within the next 5-20 years (Unilever, 2023d). Within this, targets to reduce emissions from operations play a significant role. In manufacturing this can be achieved by reducing operating temperatures, water usage, energy consumption, *etc.* (Bom et al., 2019).

Digital tools such as process analytical technology and machine learning techniques could also prove useful in enhancing our understanding of how product structure is generated under different conditions. Mowbray *et al.,* (2022) showed how machine learning models can be applied to monitored process variables (temperature, pressure, flowrates, pH) to predict the end viscosity of consumer goods manufactured in batch.

2.5 Conclusions

In the context of cosmetic and pharmaceutical cream-based products, the lamellar gel phase (L_β) has emerged as a key microstructure. This phase, formed by cooling surfactants below the Krafft point, imparts viscoelastic, gel-like behaviour to the system. Specifically focusing on hair conditioners, the LGN structure, and the lamellar gel phase play crucial roles in achieving desirable attributes such as a rich and creamy texture, superior stability, and effective deposition of actives on the hair. The formulation of hair conditioners involves carefully selecting surfactants, fatty alcohols, and other key ingredients to create the desired microstructure.

Understanding the rheological properties of these LGNs is imperative for formulating effective consumer products. The interconnected nature of the lamellar gel network imparts unique rheological behaviours, including a yield stress, shear-thinning, and viscoelasticity, which contribute to high-performance consumer experiences. Techniques such as small angle oscillatory shear testing and flow curve analysis provide valuable insights into the rheological characteristics of LGNs. Characterising the microstructure of LGNs through advanced techniques such as microscopy, electron microscopy, and DSC offers insights into their formation and behaviour at smaller length scales. Furthermore, exploring the effects of processing parameters, such as mixing efficiency, temperature, and cooling rates, contributes to a comprehensive understanding of LGN structure formation. The temperature and shear rates during mixing can impact the purity of the lamellar gel phase, and whether it is in a vesicle or bilayer formation. This in turn impacts the rheological properties and in-use performance of the hair conditioner. The importance of innovating for sustainability has also been considered, as well as the use of digital tools to enable greater understanding of the effect of processing conditions on microstructure, rheology and in-use performance.

In summary, the review aims to enhance the understanding of the relationship between formulation, manufacturing, microstructure, and in-use performance of LGNs with a focus on hair conditioners. The formation of the lamellar gel network (LGN) structure is essential for achieving desired attributes in hair conditioners, such as texture, stability, and effective actives deposition. Understanding the rheological properties, including yield stress, shear-thinning, and viscoelasticity, is crucial for formulating high-performance products. This review discusses current research into the impact of processing variables on LGN structure formation and highlights areas for future research.

CHAPTER 2, PART B: MIXING LITERATURE REVIEW

2.6 Introduction

Mixing is a fundamental unit operation critical for achieving homogeneity in chemical, biological and physical processes, facilitating other process objectives such as mass, momentum and heat transfer. Stirred vessels are among the most common mixing systems, present across industries such as pharmaceuticals, chemicals, food and consumer good production. The design of stirred tanks considers factors such as tank shape geometry and dimensions, impeller type, fluid properties, and desired mixing outcome. The typical configuration of a mechanically stirred tank is given in Figure 2-13.

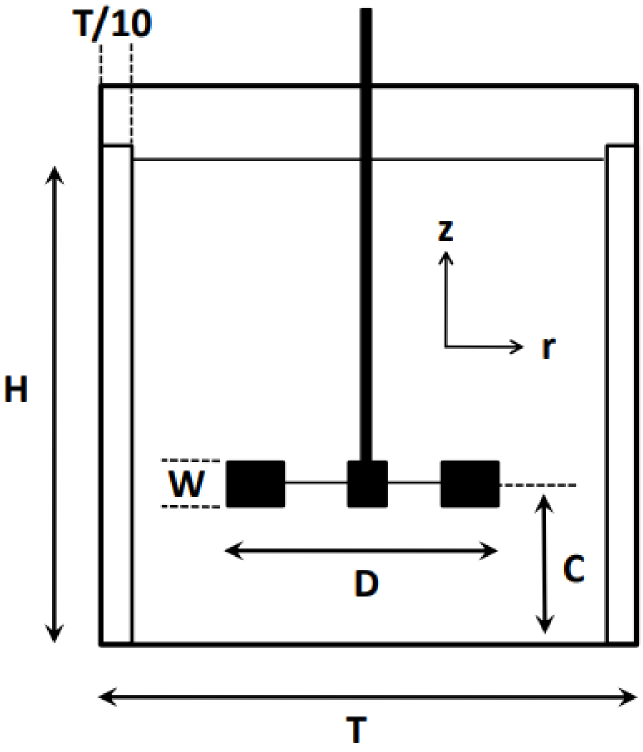

Figure 2-13. Typical stirred tank configuration and dimensions

Where: D = impeller diameter (m), T = tank diameter (m), W = impeller width (m), H = fill height (m), C_b = impeller off-bottom clearance (m).

Typical ratios for the above dimensions are:

- Impeller diameter/tank diameter, D/T, ~0.3 to 0.5
- Fill height/tank diameter, H/T, ~1
- Baffle width/tank diameter, ~0.1
- Impeller clearance/tank diameter C_b/T, ~0.2 to 0.25

The use of standard ratios provides a framework for designing efficient and scalable mixing systems. Radial flow impellers, such as flat-blade turbines, direct flow outwards, axial flow impellers, such as propellors, direct flow parallel to the impeller shaft. For more viscous fluids, close-clearance impellers such as anchors and helical ribbons are employed to aid tangential flow.

Dimensionless numbers are used in mixing to simplify the complex relationships between variables. They can be used to analyse the performance of the system, such as determining the flow regime, power consumption, and vortex formation, and to aid in scale-up. Important dimensionless numbers for mixing are given in Table 2-3.

Table 2-3. Important Dimensionless Groups for Mixing

Dimensionless number	**Equation**	**Notes**
Reynolds, *Re*	$\frac{\rho N D^2}{\mu}$	Ratio of viscous to inertial forces. Used to determine whether flow is in the laminar, transitional or turbulent regime.
Power, *Po*	$\frac{P}{\rho N^3 D^5}$	Power consumption of mixers. Po vs Re plots showing power consumption versus mixing regime often used to characterise performance of impellers.
Froude, Fr	$\frac{v^2}{g\ D}$	Used for unbaffled tanks to evaluate vortex formation.
Flow, *Fl*	$\frac{Q}{N D^3}$	Expressing mixer efficiency (fluid movement) as a function of impeller size and speed.

Where: ρ = density (kg m^{-3}), N = impeller speed (s^{-1}), D = impeller diameter (m), μ = fluid viscosity (Pa s), P = impeller power consumption (W), v = fluid velocity (m s^{-1}), g = gravitational force (m s^{-2}), Q = volumetric flow rate (m^3 s^{-1}).

Dimensionless groups in combination with the defined tank geometry variables can be further used to predict other important mixing parameters such as mixing time, power input per unit mass, *etc*. For example, the Grenville and Nienow for mixing time in the turbulent regime, when H ≠ T (Eq. 2-1).

$$\theta_m = 5.2\frac{Po^{-\frac{1}{3}}}{N}\left(\frac{T^{1.5}H^{0.5}}{D^2}\right) \tag{2-1}$$

Where: θ_m = dimensionless mixing time (-), Po = dimensionless Power number (-; defined in Table 2-3), T = tank diameter (m), H = liquid fill height (m), D = impeller diameter (m), N = impeller speed (s^{-1}).

2.6.1 Mixing at Partial Fill Levels

The manufacture of microstructured formulated liquid products is typically carried out in batch mixing vessels with multiple impellers to manage the evolving viscosity of the product as the microstructure is generated. Traditional batch mixing systems are operated using a liquid height, *H*, to tank diameter, *T*, ratio (H/T) equal to or greater than unity (Motamedvaziri, 2012). However, in batch mixing processes across the pharmaceutical, fine chemical, personal care and food industry, it is also necessary to ensure sufficient mixing when H/T < 1 in order to achieve process objectives (Pieralisi *et al.*, 2016) such as:

- Ensuring components are well mixed during the addition of raw materials into the vessel to achieve the final desired composition.
- Ensuring dispersions or suspension remain homogeneous when discharging a vessel into a filling line or packaging.
- Recovering expensive products from the vessel.
- Minimising waste products.

Motamedvaziri (2012) investigated the effect of H/T and impeller submergence, S_b, on the impeller performance for single liquid phase and solid-liquid suspensions. The work focussed on flat-bottomed cylindrical, baffled vessel equipped with a single disk turbine agitator. Four different scales were investigated (5L, 12L, 20L and 170L). Velocity profiles were determined using particle image velocimetry, colorimetry was used to determine mixing times and a strain-gauge torque transducer was used to characterise the power draw. The key findings were that a critical impeller submergence to impeller diameter, *D*, ratio (S_b/D) exists. Below this critical value, the observable flow pattern transitions from the normal double-loop recirculation flow for a turbine agitator to a single-loop recirculation flow, the power number drops significantly, and vortex formation occurs, with increased air entrainment leading to impeller flooding. Furthermore, the change in flow regime resulted in a substantial decrease in the average velocity and intensity of turbulence near the bottom of the tank. Operating ranges for the different flow regimes were quantified for various impeller off-bottom clearances (C_b/T), impeller submergences (S_b/D), agitator speeds, *N*, and liquid height to tank diameter ratios (H/T).

Similarly, Banerjee (2013) investigated the effect of fill height ratio on power number and blend time for Rushton turbine and retreat turbine in baffled, partially baffled, and unbaffled tanks at H/T= 0.3 -1 (Banerjee, 2013). Power number decreased as a function of fill ratio and extent of baffling (from fully to none). Vortex formation occurred at similar speeds for each fill height in unbaffled systems. For baffled systems, the speed for vortex formation decreased with fill height ratio. Both authors found that dimensionless blending time was constant for H/T between 0.7 and 1; below this value there was erratic behaviour.

Delbridge *et al.* (2023) characterised the power draw, mixing and flow dynamics of a novel Allegro™ bioreactor. The power curves for H/T from 0.6-1.1 were determined, as the authors identified that in industrial applications, bioreactors are typically operated at a range of fill heights. Reducing H/T to 0.8 only caused a minor decrease in power number, Po. At H/T = 0.7, power number increased unexpectedly. At H/T = 0.6, Po increased again, particularly at low Reynolds numbers, but then drastically decreased above Re = 11 000, which was attributed to air entrainment. Similar results were reported by Simmons *et al.* (2007) who noted that for a pitch blade turbine, hydrofoil, and elephant ear impeller, the turbulent power number was independent of fill height unless surface aeration occurred.

Robinson & Cleary (2012) used computational fluid dynamics (CFD) to examine differences in mixing between variants of a helical ribbon mixer: a single helical ribbon (SHR), double helical ribbon (DHR) and a single helical ribbon combined with a central screw (CSR) (Figure 2-14). For the SHR, they also looked at the transport and mixing of a volume of fluid which initially filled a quarter of the tank. The results showed how the rotation of the impeller pushes fluid to downwards at the boundary of the tank and is then pushed back upwards near the centre shaft. Smaller recirculation loops exist around the ribbon blades.

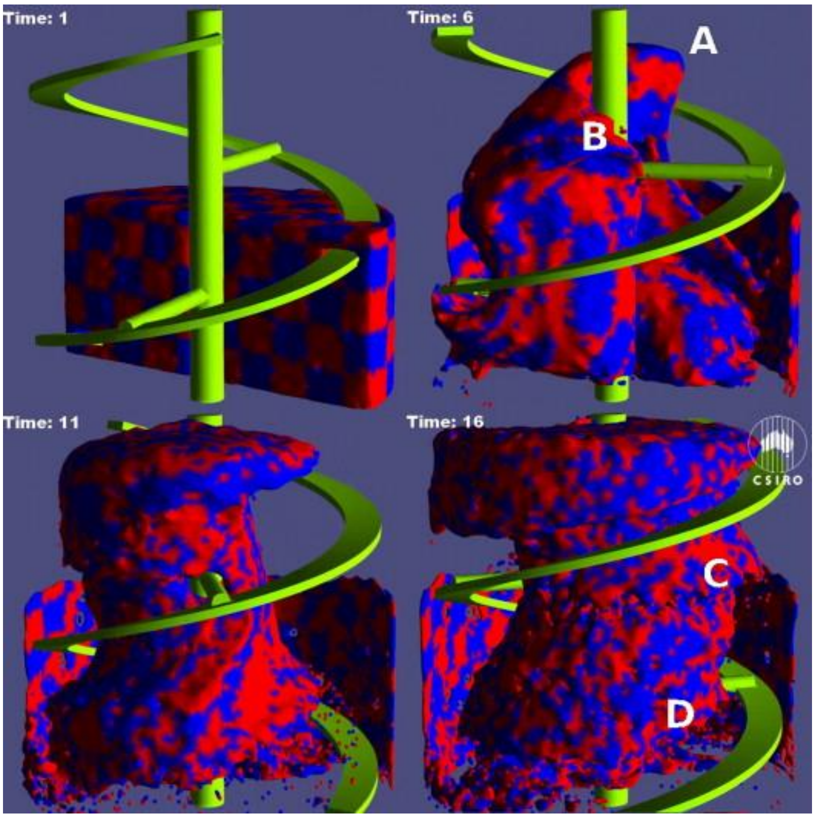

Figure 2-14. Transport and mixing of a representative volume of fluid initially covering a lower quarter of the (SHR) single helical ribbon tank. The fluid volume is coloured by an arbitrary checkerboard pattern in order to show the movement of the fluid (Robinson and Cleary, 2012).

Alberini *et al.* (2024) characterised a Flexel-Levmixer (cubic single-use bioreactor with a bottom impeller) at liquid fill heights from 17% to 81% H/T using the power number, torque, and particle image velocimetry (PIV). Torque and power number were grouped into zones based on liquid fill heights, where increasing speed determined differing responses in torque and power number for different fill heights. Vortex formation and air entrainment were shown to be key reasons for this. PIV was used to further examine the flow regimes and velocity profiles at different fill heights and speeds.

Overall, the research into mixing at partial fill levels, particularly in systems with close clearance agitators such as helical ribbons and anchors is very limited and the effect of fill level on flow patterns and mixing efficiency is highly system dependent.

2.6.2 Monitoring Mixing

Numerous techniques have been developed for monitoring mixing throughout the years, some with limited success due to limitations to very specific applications. For example, a large proportion of techniques cannot be directly applied to industrial systems (flow visualisation techniques which require optically transparent fluids and systems), require specific physical properties of the fluid (*e.g.,* conductivity), or by their nature interrupt the flow in the system (probe-based measurements). Thus, choosing an appropriate monitoring technique to characterise flow regimes remains a challenge (Brown *et al.*, 2004). A summary of some available techniques for online measurement, examples, advantages and limitations are given in Table 2-4.

Table 2-4. Online Monitoring Techniques for Mixing, their Operating Principle, Example, Advantages and Limitations

Technique	Operating Principles	Uses	Advantages	Disadvantages
Power and Torque Measurement	Measuring the force required to turn the impeller, either through electrical power (Cazacliu, 2008) or a strain gauge located on impeller shaft (Delaplace *et al.*, 2000a).	• Changes in mixing dynamics • Determining power curve and mixing regime • Optimising process and product quality • Scale-up	• Easily applied to industrial systems • Simple and low cost • Non-invasive	• Electrical power measurement not accurate or precise due to losses to system • Does not provide detailed velocity information, more of a general picture
Point Property Measurement	Measuring a specific physical or chemical property of the system at a certain location in the vessel, e.g., pH, conductivity (Ng and Assirelli, 2007), optical properties (light-scattering) (Pizzino *et al.*, 2009)	• Determining critical impeller speeds for solids suspension • Identifying process stages through changes in properties	• Simple and inexpensive • Robust, suitable for high temperature and pressure environments	• Disrupt flow • Multiple probes often required • Process contacting probes may need to be constructed from resistant materials • Susceptible to fouling • Measurements sensitive to temperature, pH, other physical properties not being measured

Technique	**Operating Principles**	**Uses**	**Advantages**	**Disadvantages**
Tomographic Techniques (Mosorov, 2015)	Cross-sectional images of a specific property distribution. Techniques such as: • Electrical resistance tomography (Machin *et al.*, 2018) • Magnetic resonance imaging (Mihailova *et al.*, 2015) • X-ray tomography	• Determining mixing endpoints • Monitoring flow patterns • Identifying dead zones, caverns, *etc.* (Pakzad *et al.*, 2008)	• Non-invasive • Can be used on multiphase systems (gas-solid-liquid)	• Specific material properties required dependent on technique • X-ray tomography poses safety hazard • X-ray and MRI expensive • Large space required for setup (Bowler *et al.*, 2020) • Limited to macro-scale visualisation

Technique	Operating Principles	Uses	Advantages	Disadvantages
Spectroscopic Techniques (Abatzoglou, 2015)	Spectroscopy works by analysing the interaction between electromagnetic radiation and matter, examples include: - Near Infrared - Laser induced fluorescence - Raman Calibration models (typically using Partial Least Squares or Principal Components Analysis) are developed and applied to determine chemical composition	- Determining chemical composition - Monitoring homogeneity in continuous pharmaceutical processes (Wahl *et al.*, 2013)	- Simple - Can be non-invasive (flow cells *etc.*)	- NIR limited to non-aqueous environments due to -OH band in spectra hiding other details - Chemometric techniques and calibration models required to fully interpret measurements - Susceptible to fouling - Local measurement might not be representative of bulk at larger scales
Image Analysis (Brown *et al.*, 2004)	Optical image analysis is based on distinguishing between components of different colours, e.g.: - Liquid dye tracer - Acid-base transition (Lamberto *et al.*, 1996)	- Mixing time - Flow patterns	- Simple and low cost - Non-intrusive - Widely used	- Sometime dependent on human subjectivity - Require optically transparent system - Only characterising material at surface

One of the simplest techniques conceptually for visualising flow patterns is light sheet visualisation. Reflective tracer particles are introduced into the bulk fluid, and a narrow light sheet is applied to the system, illuminating the tracer particles. The light sheet may be positioned radially or axially, and quantitative velocity data can be determined using the shutter speed of the camera. This technique can only be applied to transparent mixing systems and fluids.

Particle Tracking Velocimetry (PTV) and Particle Image Velocimetry (PIV)

Particle Tracking Velocimetry (PTV) is one such flow visualisation technique where the trajectories of individual particles in a three-dimensional space is traced. A similar technique is Particle Image Velocimetry (PIV) which instead focuses on the mean displacement of a small group of particles. In both cases, tracer particles are suspended in the flow. It is particularly important that the seeded particles accurately follow the fluid motion. A laser light sheet is used to illuminate the region of interest, and successive images of the system are taken with a high-speed camera, capturing the movement of the particles over extremely short time periods. Specialist software is then used to track the motion of the particles from one frame to another (Adrian, 1991).

In PIV, the velocity fields of the flow, turbulence, vorticity, and flow patterns can be determined from further analysis. Advantages are high temporal (1 μs to ms) and spatial resolution (~10μm – 100 μm), dependent on camera type, suitability over a wide range of scales and fluid rheological properties (assuming an optically transparent model fluid is available), and a useful technique for validation of CFD models. Table 2-5 highlights some key applications.

Table 2-5. Uses of Particle Image Velocimetry

Use Area	Application	Example
Range of Scales	Micro-mixing	Mixing in T-shaped microreactors using micro-PIV (Hoffmann *et al.*, 2006)
	Wind tunnels	Large-scale tomographic PIV in wind tunnel experiments (Scarano *et al.*, 2015)
Complex rheology	Highly viscous, shear-thinning fluids	Validation of CFD studies of highly viscous shear thinning fluids with complex impeller design (Cortada-Garcia *et al.*, 2018)
	Investigating effect ultrasound on fluids of various rheology	Effect of fluid rheology, acoustic intensity and transducer size on flow behaviour/velocity induced by ultrasound (O'Sullivan *et al.*, 2018)
Validating CFD	CFD validation of pumps	(Zou *et al.*, 2016)
	CFD validation of rotor-stator mixers	(Mortensen *et al.*, 2018)

Nevertheless, the need for an optically transparent system (equipment and fluid) limits application in some industrial areas. This is predominantly because producing model transparent fluids which match the complex rheological behaviour of multiphase, structured products remains a challenge. On the other hand, 3D printing has widened the variety and complexity of mixing systems able to be manufactured (Kasparek and Novakova, 2022).

Positron Emission Particle Tracking (PEPT)

Positron emission particle tracking (PEPT) is a non-invasive flow visualisation technique pioneered at the University of Birmingham (Parker *et al.*, 1993). The location of a radioactive positron-emitting tracer particle is determined through triangulation of the back-to-back gamma rays which are emitted through electron-positron annihilation (Barigou, 2004). This allows for flow visualisation in ‘real’ systems, including opaque fluids and equipment, whereas other conventional techniques such as particle image velocimetry (PIV) and laser doppler velocimetry (LDV) require optically transparent systems.

First, a suitable tracer particle is determined. In granular flow systems, this may be an actual particle of interest (Al-Shemmeri *et al.*, 2021); in a fluid-based system, it is important that the particle is neutrally buoyant. The particle is labelled using a positron emitting isotope, *e.g.,* Fluorine-18, Gallium-68, Carbon-11 or Sodium-22 (Langford *et al.*, 2016). The particle is placed in the system under investigation, which is placed inside a detector system. Typically the detectors have been configured as two parallel screens, but the availability of modular systems has allowed for greater flexibility in the geometry of systems which can be studied (Leadbeater and Parker, 2011). Simultaneous detection of a photon on the parallel screens suggests that the gamma-rays are from the same positron-electron annihilation event, and thus a trajectory (known as a line of response, LoR) can be constructed. The intersection of multiple LoRs can then be used to determine the location of the tracer particle.

Not all LoRs correspond to true annihilation events, and false LoRs can be generated by secondary radiation, scatter, or background noise. Algorithmic approaches are utilised to triangulate the location of the tracer particle and remove errors due to false events. The original and still most widely used algorithm is the Birmingham method, developed by Parker and Hawkesworth (Parker *et al.*, 1993). Windows-Yule *et al.* (2022) provide a detailed comparison of other PEPT methodologies developed since.

Once the x-y-z location of the particle with respect to time has been determined, further calculations can be applied to derive important information such as velocity, dispersion, shear rate, occupancy, *etc*. (Bakalis *et al.*, 2006; Sindall *et al.*, 2017; Martin *et al.*, 2007). These derived properties rely on the assumption that the time averaged path of a single particle in the system is representative of the ensemble-averaged behaviour of all the particles in the system – given that the particle has been followed for a long enough period of time for it to have chance to reach the entire area of the system (Windows-Yule *et al.*, 2020). In larger systems, this means that multiple experiments will be required, or very long mixing times will be required. However, the half-life of the most commonly-used tracer (Fluorine-18) has a half-life of 109 minutes which limits the length of experiments as detection events decrease as radioactivity decays (Parker and Fan, 2008). The probability of successful detection is also impacted by the distance and materials the gamma rays must travel through (Ingram *et al.*, 2007). This again poses a challenge for larger vessels full of multiphase fluid product. However, the motion of water in a dishwasher (Pérez-Mohedano *et al.*, 2015) and the motion of textiles in a washing machine (Mac Namara *et al.*, 2012) have been characterised using PEPT.

2.6.3 Power and torque measurement

For characterising mixing in stirred tanks, the power draw of the impeller is one of the most fundamental measurements (Brown *et al.*, 2004). The power draw cannot, however, be readily calculated from the power input supplied to the impeller by the motor using a wattmeter or ammeter, due to lack of information about mechanical losses to the system due to bearings etc. and variation and noise in the electrical signal (Ascanio *et al.*, 2004). Therefore, it is typically not employed for technical purposes. An alternative to electrical measurement of power is the measurement of torque, which is the moment of force required to rotate an object. It is directly related to the power draw of the impeller as a function of the angular velocity (Eq. 2-2):

$$P = M\Omega \tag{2-2}$$

Where: P = power (W), M = torque (N m), Ω = angular velocity (rad s^{-1}*).*

Torque and power measurement have found application in many industries for different purposes, e.g.:

- Integration of power with time provides the energy input into the system, allowing for control of processes by stopping the mixing stage at a predetermined total energy input. Useful for any processes where the structure formation and product quality is impacted by energy input, *e.g.,* bread dough (Perez Alvarado *et al.*, 2016)
- Torque can be correlated with viscosity, thus can be used to identify changes in rheology throughout the process, and linked to structural changes (Cunningham *et al.*, 2021). Examples of this include ensuring homogeneity and complete

hydration of concrete raw materials to ensure a better performing product (Cazacliu, 2008).

- Studying changes in power draw to determine critical impeller speed for particle suspension (Raghava Rao *et al.*, 1988), or distinguishing between different flow regimes (dispersion, cavity formation, flooding) in gas-liquid systems (Khopkar *et al.*, 2005).

Torque can be measured using a range of equipment, but they are ultimately based on two main principles: strain gauges or a combination of load cells and dynamometers (Brown *et al.*, 2004; Ascanio *et al.*, 2004). Table 2-6 describes the operating principles, advantages, and disadvantages of these two approaches.

The overall advantages of measuring torque and power to characterise mixing systems are the relatively simple and low-cost installation of instrumentation onto the vessel, the ability to measure in ‘real’ industrial systems, including opaque, multi-phase fluids/systems, and the possibility of transferring results across scales. The drawbacks are ensuring accurate measurement by accounting for losses to the system and zero drift and noise.

Table 2-6. Torque Measurement Operating Principles

Equipment/Technique	Principle	Advantages	Disadvantages
Air bearing system /dynamometer (Cortada-Garcia *et al.*, 2017; Ascanio *et al.*, 2004; Nienow and Miles, 1969)	The rotating impeller imparts a mechanical force to the fluid in the vessel, and eventually to the tank itself. As the vessel is mounted on an air bearing system, it can freely rotate and eventually rotates in the same direction and speed as the impeller. A load cell and arm located on the rotating table is used to measure the force required to stop the vessel from rotating. The power draw of the impeller can the be calculated as: $P = 2\pi NFx$ Where P(W) is the power required to drive the impeller, N (rev s^{-1}) is the impeller speed, F (N) is the force measured by the load cell, r (m) is the radial distance from the impeller shaft to the centre of the load cell	• Best suited to lab and pilot scale measurement • Able to cover a wide torque range • High precision measurement	• Industrial size vessels cannot be supported • Cannot determine individual torque for multiple impeller systems

Equipment/Technique	**Principle**	**Advantages**	**Disadvantages**
Strain gauges (Alberini *et al.*, 2023)	Strain gauge torquemeters operate using a four element Wheatstone bridge electrical circuit affixed to the shaft. When torque is exerted on the shaft, the circuit twists in the direction of rotation, leading to shear strain. This causes one pair of strain gauges to elongate, whilst the other is compressed. The resistance of the circuit is affected, and the electrical output corresponds to the torque applied (Schicker and Wegener, 2002; Ascanio *et al.*, 2004).	• Independent measurements for multiple impellers is possible with multiple strain gauges on each shaft • Minimal losses due to friction • Low cost • Wide measurement range and linearity over a wide range • Short response time	• Mounting on to shaft can be complicated and correct installation is critical to performance – overcome by the use of telemetry or slip rings • Considerable amount of instrumentation required • Susceptible to zero drift

Mixer-Viscometer Approaches

One of the advantages of monitoring torque during mixing processes, is that the force required to turn the agitator is directly correlated to the viscosity of the system in the laminar mixing regime, thus viscosity can be inferred from torque measurements. For Newtonian fluids, the power consumption of a mixing system can be evaluated by a plot of the Power number (Po) versus the Reynolds number (Re) (defined in Table 2-3).

In the laminar regime, Po is proportional to Re:

$$Po = K_P Re^{-1} \tag{2-3}$$

Where K_p is the laminar power constant.

Metzner and Otto expanded this relationship to non-Newtonian fluids by assuming the Newtonian viscosity term in the Reynolds number can be equated to the apparent non-Newtonian viscosity at a corresponding effective shear rate (Metzner and Otto, 1957). For example, for a power law fluid:

$$\mu = \eta = K(\dot{\gamma}_{av})^{(n-1)} \tag{2-4}$$

Where μ is the Newtonian viscosity (Pa s), η is the apparent non-Newtonian viscosity (Pa s) at the effective shear rate, $\dot{\gamma}_{av}$ (s^{-1}), K is the consistency index (Pa s^n) and n is the flow index (-).

The effective shear rate is related to the impeller speed by:

$$\dot{\gamma}_{av} = k_{\gamma} N \tag{2-5}$$

Where N = impeller speed (s^{-1}) and k_γ is the shear rate constant, also known as the Metzner-Otto constant.

Many different approaches have been developed for determining the Metzner-Otto constant and transforming torque-speed data into viscosity-shear rate data, such as the power curve and torque curve method (Castell-Perez and Steffe, 1990), the slope method (Rieger and Novak, 1973) and the Couette analogy (Ait-Kadi *et al.*, 2002). A more detailed review of the techniques and their applications is given in Chapter 4.

CHAPTER 3:UNDERSTANDING THE EFFECTS OF PROCESSING CONDITIONS ON THE FORMATION OF LAMELLAR GEL NETWORKS USING A RHEOLOGICAL APPROACH

Adapted from Cunningham, G.E.; Alberini, F.; Simmons, M.J.H.; O’Sullivan, J.J. (2021). Understanding the effects of processing conditions on the formation of lamellar gel networks using a rheological approach. *Chemical Engineering Science, 242, 116752*.

3.1 Introduction

The basis of many cosmetic and pharmaceutical cream products, such as hair conditioner, facial creams, moisturisers and topical medications, is an oil-in-water emulsion, stabilised by ionic or non-ionic surfactants and long-chain fatty alcohols (FA) (Junginger, 1984). When these ingredients are combined, a multiphase colloidal structure known as a lamellar gel network (LGN) is formed. The key component of the LGN is the lamellar gel phase, L_β, which consists of hexagonally packed, solid-state amphiphilic molecules (surfactant and FA) arranged in regularly spaced, planar bilayers, swollen by interlamellar aqueous phase. The remainder of the bulk aqueous phase is in dynamic equilibrium with this interlamellar phase (Junginger, 1984). The lamellar gel phase can exist as an interconnected system of planar sheets, or spherical multilamellar vesicles (Iwata, 2017a). Other oil phase ingredients, generally included in cosmetic and pharmaceutical formulations, exist as droplets surrounded by a single layer of amphiphilic molecules (Iwata, 2017a).

The multiphase nature of the LGN structure imparts several properties which make it highly desirable for formulating cosmetic and pharmaceutical cream products, in terms of opaque appearance, slippery and oily texture, rheological properties, emulsion stability and delivery of active ingredients (Iwata, 2017a). As the amphiphilic molecules exist in their solid-state in an LGN, when applied to the skin, this imparts an oily tactile feel. This is further enhanced by the bi-continuous arrangement of the layers, whereby a greater amount of amphiphiles have contact with the skin than in typical emulsions. The amphiphiles used in LGNs are typically water-insoluble (hence more hydrophobic than typical oil-in-water surfactants). Therefore, the amphiphiles can be used to deliver cosmetic benefit in rinse-off cosmetic products (Iwata and Aramaki, 2013).

Perhaps the most important aspect of the lamellar gel network is the bulk rheological properties it imparts. The system is a highly viscous, shear-thinning material which possesses a high yield stress due to the interconnected lamellar gel phase (Datta *et al.*, 2020). The rheology of the system is highly dependent on the type, concentration and ratio of FA and surfactant used (Nakarapanich *et al.*, 2001), which has been the subject of considerable research effort (Awad *et al.*, 2011; Fukushima and Yamaguchi, 1983; Iwata and Aramaki, 2013; Nakarapanich *et al.*, 2001). However, the method of preparation as well as the formulation has considerable impact on the final structure and resultant rheological properties (Colafemmina*, et al.,* 2020; Eccelston, 1997).

In typical colloidal systems, the surfactant concentration is kept below the solubility limit to prevent precipitation, and the intended storage and usage temperature of the product is higher than the Krafft point to allow a higher concentration of surfactant than the critical micelle concentration in the system (Nakama, 2017). However, a lamellar gel phase, L_β, is formed when the total surfactant concentration is above the solubility limit and the system is below the Krafft point (Davies and Amin, 2020). Lamellar gel networks can therefore be prepared by heating the ternary phase ingredients (FA, surfactant and water) to a temperature above the melting point of the FA, homogenising, and cooling to room temperature (Davies and Amin, 2020; Wunsch *et al.*, 2016; Yang, 2017). When the mixture is heated to above the Krafft point, the surfactants are in a stable, spherical micellar solution. When the system is cooled to below the solubility limit, the surfactants phase separates from the solution and forms various crystalline structures dependant on the critical packing parameter, CPP, a property based on the geometry of the surfactant which determines the type of micellar aggregate formed (Nakama, 2017). When a ratio of FA and surfactant is used that gives a CPP close to 1, the molecules form lamellar bilayers, which can hold large amounts of water between them, mainly due to the repulsive forces between the layers, *i.e.,* lamellar gel phase, L_β (Fairhurst *et al.*, 2008; Ribiero *et al.*, 2004; Wunsch *et al.*, 2016; Yamagata and Senna, 1999). If the system is purely cetostearyl alcohol with no additional surfactant, then the system will still form lamellar bilayers, but with much tighter packing, and only a small amount of water between layers – this is known as lamellar coagel phase, L_c. Finally, if the temperature is above the melting point of the hydrocarbon chains of the amphiphiles, the system transitions from a gel state to a lamellar liquid crystal state, where packing of the surfactants is looser and the overall behaviour of the system is more liquid like (Davies and Amin, 2020).

There are some discussions in the literature regarding the effects of thermal profile, temperatures, and shearing effects on the final properties of LGNs. Iwata suggested that, on a commercial manufacturing scale, insufficient mixing, or cooling the mixture too quickly before the lamellar gel phase has formed (perhaps due to a high temperature gradient between the product within the vessel and the coolant in the jacket of the vessel), can lead to a higher percentage of hydrated crystals of FA which are not incorporated in to the gel phase (Iwata, 2017a). This reduces stability of the gel network, and affects the shear-thinning properties, as the hydrated FA crystals are hydrogen-bonded and do not slip over each other. Fukushima and Yamaguchi (1983), Ito *et al.* (2011) and Partal *et al.,* (2001) found that applying increasing shear onto a lamellar structure forces the bilayers to form vesicles, as the 'infinite' sheets cannot accommodate the flow. Colafemmina *et al.,* (2020) investigated the effects of different cooling rates on the final structural and rheological properties of a LGN using rheology, small-angle X-ray scattering (SAXS) and diffusion NMR. They found that cooling the system rapidly (40°C/min) in contrast to cooling slowly (5°C/min) produced a more favourable structure and rheological properties *i.e.,* higher yield stress. However, there remains relatively little insight on the relationship between processing variables, such as: thermal profile, mixing time, mixing intensity, shear rate, and scale of manufacture on the physicochemical and rheological properties of the final LGN and this requires further investigation (Colafemmina *et al.*, 2020; Davies and Amin, 2020; Yang, 2017; Ito *et al.*, 2011; Ballman and Mueller, 2008).

Whilst research publications regarding manufacturing of lamellar gel networks is limited, there are some patent applications from several global personal care and cosmetic companies (Unilever (Hough *et al.*, 2013), Procter & Gamble (Yang and Okada, 2012; Yang and Okada, 2014), L'Oreal (Grollier and Richoux, 1990)) disclosing manufacturing methods and process parameters such as: processing temperatures and temperature profiles, suitable fatty alcohol and surfactant combinations, order of addition of ingredients, mixing intensity, energy input, suitable equipment. In summary, the oil-phase ingredients (*i.e.*, fatty alcohol and surfactant) are prepared to a temperature above the melting point of the components (typically ~85°C) and combined with the aqueous phase which is prepared at a lower temperature to ensure that when combined, the temperature of the mixture is 57-70°C. After mixing, the product is cooled either via jacket cooling or addition of ambient materials (Flanagan, 2013; Grollier & Richoux, 1993; Venkateswaran, *et al.*, 2009; Zhong & Toshiyuki, 2009).

The formation of a LGN inherently involves a large increase in viscosity of the system as the microstructure is generated (Iwata and Aramaki, 2013). It would therefore be highly beneficial to measure the rheology of the incipient LGN in situ to investigate the effects of varying different process conditions from which the structure can be inferred. This can be achieved by using a mixing rheometry approach, in which torque requirements are measured throughout the process, and an analytical approach such as the Couette analogy, or an empirical method such as the Metzner-Otto approach which are used to convert torque-speed data to apparent viscosity measurements (Bousmina, *et al.,* 1999; Metzner & Otto, 1957). By utilising a rheometer with a cup geometry to represent the manufacturing vessel, albeit at a much smaller scale, this is easily achieved. Different geometries such as helical ribbons, anchors, paddles and vanes have been used to follow the apparent viscosity of a system as it evolves, and to measure power consumption (Ait-Kadi *et al.*, 2002). Franco *et al.* (2005) used a torque measuring device paired with an anchor agitator and high shear device to follow the manufacture of lubricating greases and characterise the power consumption of each stage, using the Metzner-Otto approach. Chavez-Montes *et al.,* (2003) and Choplin *et al.* (2009) both used a rheometer with adapted mixing geometries to investigate the changing rheological properties of ice-cream and cosmetic lotions, respectively. A similar approach was used by Gaiani et al. to follow the dissolution behaviour of phosphocaseinate at different temperatures and times, using a vane attachment. The viscosity profile was matched to the measured particle size of the phosphocaseinate to determine the time taken for different phases of the dissolution process *i.e.,* wetting, swelling and dissolution (Gaini *et al.*, 2006).

The work presented in this chapter describes how the rheological properties of an incipient LGN evolve as a function of time when different processing conditions, namely vane speed, processing time, and processing temperature, are employed. A ternary system of cetostearyl alcohol (FA) (7.06 wt%), behentriominum surfactant (BTAC) (2.35 wt%) and water was chosen to study. Cetostearyl alcohol is a popular commercially available fatty alcohol used in the formulation of many personal care and cosmetic products, and BTAC is a quaternary ammonium salt most commonly used in the formulation of hair conditioners. This formulation has been studied elsewhere, is known to generate a lamellar structure, and is representative of the rheology of a fully formulated cosmetic or personal cream product (Davies and Amin, 2020). The relationship between the processing conditions and the final product quality will be explored, in terms of final rheological properties of the product, and process optimisation, in terms of power consumption.

3.2 Materials and Methods

3.2.1 Materials

The fatty alcohol (FA) used as part of this study was a commercially available blend of cetyl alcohol (30 wt. %) and stearyl alcohol (70 wt. %) (cetostearyl alcohol) sourced from Godrej Industries (India). The surfactant used was behentrimonium trimethyl ammonium chloride (BTAC), supplied by Clairant International Ltd. (Germany). This surfactant is provided at 70 wt. % purity, where the remaining 30 wt. % is comprised of dipropyl glycol, which acts as a processing aid. Glycerine (Palmera G995E; >99.5% purity; supplied by KLK Oleo) was used for the purpose of calibrating the vane geometry (viscosity @ 25°C: 0.95 Pa s). Distilled water was used for all experiments.

3.2.2 Preparation of lamellar gel network (LGN) samples

A Discovery HR-III stress-controlled rheometer (TA Instruments, UK) with a four-bladed vane spindle geometry was used for the preparation of the LGNs (dimensions of the geometry are shown in Figure 3-1).

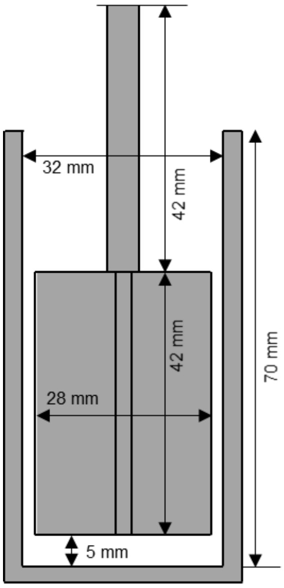

Figure 3-1. Dimensions of rheometer geometry with four-bladed vane attachment and associated cup

The samples were prepared and processed in the rheometer in the following stages.

Preparation stage. 7.06 wt. % (of total formulation) of FA and 90.59 wt. % of distilled water was added to the rheometer cup with a targeted total batch size of 34g. The cup was installed in the rheometer and the mixture heated to a temperature of 70°C, with the vane at a shear rate of 200 s^{-1}. Once at 70°C, the sample was stirred for 5 min, and then cooled to the temperature required for the structuring stage.

Structuring stage. Once at the appropriate defined temperature, 2.35 wt. % of BTAC was added to the rheometer cup and stirred for the desired time and at the defined vane speed; values of these parameters are given in Table 1. The reference conditions for this study were a temperature of 60°C, shear rate of 200 s^{-1}, and time of 30 min.

Cooling stage. After the structuring stage, the sample was cooled at a rate of 5 °C min^{-1} to a final target temperature of 30°C whilst continuing to mix at a shear rate of 200 s^{-1}.

Table 3-1. Investigated variable of vane speed, temperature, and time for the structuring stage of LGN preparation

LGN	$\mathbf{LGN_{ref}}$	$\mathbf{LGN_{T=67°C}}$	$\mathbf{LGN_{\gamma=400}}$	$\mathbf{LGN_{t=20}}$	$\mathbf{LGN_{T=63°C}}$	$\mathbf{LGN_{T=57°C}}$	$\mathbf{LGN_{\gamma=600}}$	$\mathbf{LGN_{t=40}}$	$\mathbf{LGN_{\gamma=400;t=20}}$	$\mathbf{LGN_{t=10}}$	$\mathbf{LGN_{\gamma=600;t=10}}$	$\mathbf{LGN_{\gamma=50}}$
Vane speed (s^{-1})	200	200	400	200	200	200	600	200	400	200	600	50
Temperature (°C)	60	67	60	60	63	57	60	60	60	60	60	60
Time (minutes)	30	30	30	20	30	30	30	40	20	10	10	30

3.2.3 Calibration of vane geometry using Couette analogy and Metzner-Otto correlation

The vane geometry (*cf.*, Figure 3-1) used in this work is a commercially available attachment for the DHR-3 rheometer (TA Instruments, UK), thus apparent viscosity can be read directly from the rheometer software and does not need to be calculated from torque-speed data (Trios, TA instruments, UK). However, it was decided to calculate the stress and strain constants via the Couette analogy and Metzner-Otto concept for reference purposes, and to utilise the Metzner-Otto concept for power consumption calculations (Choplin & Marchal, 2010; Metzner & Otto, 1957). The shear stress constant (k_τ) and the shear rate constant ($k_{\dot{\gamma}}$) relate torque and rotational speed measurements to stress and shear rate as shown below:

$$\tau = k_\tau T \tag{3-1}$$

$$\dot{\gamma} = k_{\dot{\gamma}} N \tag{3-2}$$

Where: τ is shear stress (Pa), $\dot{\gamma}$ is shear rate (s^{-1}), T is torque (N m), and N is rotational speed (rps).

The constant, $k_{\dot{\gamma}}$, which relates shear rate to rotational speed is also known as the Metzner-Otto constant (Metzner and Otto, 1957). Metzner-Otto theorised that for non-Newtonian fluids in the laminar regime, there exists an average shear rate from which the apparent viscosity can be determined. The aim of the Couette analogy is to determine the equivalent dimensions of a Couette cylinder for a non-conventional geometry which provide the same torque measurement at the same rotational speed (Ait-Kadi *et al.*, 2002). Once the equivalent internal radius of the Couette cylinder has been determined analytically, the shear stress and shear rate can be calculated based on the rheological behaviour of the fluid (most commonly applied to power-law fluids). The final rheological characteristics of a LGN can be described using a power law model (Ahmadi *et al.*, 2020a):

$$\eta = K\dot{\gamma}^{n-1} \tag{3-3}$$

Where η is the apparent viscosity (Pa s), $\dot{\gamma}$ is the shear rate (s^{-1}), and K and n are the consistency (Pa s^n) and flow (-) indices, respectively.

The Couette analogy approach described by Ait-Kadi *et al.* (2002) has been utilised in this work to determine the shear stress constant (k_τ) and the shear rate constant ($k_{\dot{\gamma}}$) by calibration with a fluid with known power law characteristics; in this case, glycerine

(>99.5% purity), a Newtonian fluid, where n=1. The values calculated for the stress and strain constants are given below (Table 3-2).

Table 3-2. Stress constant and strain constant calculate from data, Couette analogy and Metzner-Otto concept

Constant	Calculated from rheometer data for non-Newtonian fluid	Couette analogy	Metzner-Otto
k_τ (-)	17867	16141	N/A
k_γ (-)	76.7	69.1	76.0

The stress and strain constant values calculated using the different methods are in satisfactory agreeance. Figure 3-2 shows a flow curve for an example lamellar gel network measured using both the vane geometry and cross-hatched parallel plates, which are the conventional geometry used for measuring rheology of lamellar gel networks. The similarity of the flow curves measured using the two different geometries further proves that the stress and strain constants for the vane are accurate.

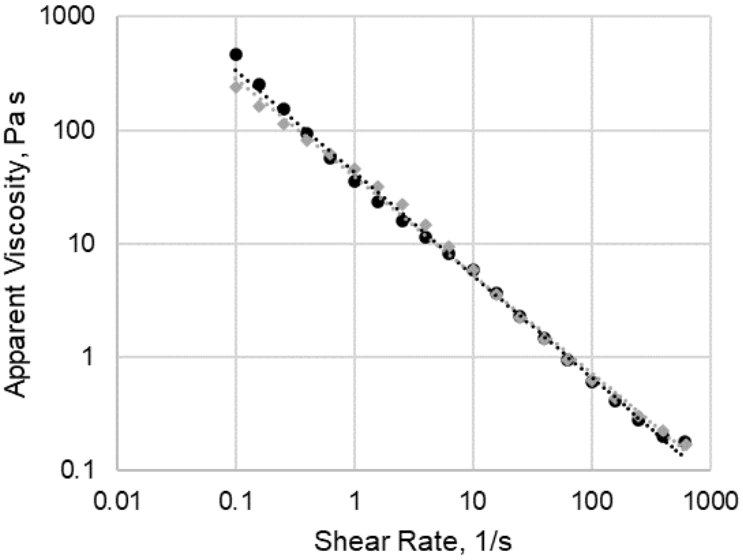

Figure 3-2. Flow curve of LGN_{ref} measured using vane geometry and cross-hatched parallel plates

3.2.4 Power consumption determination

By applying the Metzner-Otto concept and assuming instantaneous torque measurement, instantaneous power consumption can easily be calculated using Equation 3-4 (*W*; Watts). From a plot of power *vs*. time, it is then possible to calculate the energy input for the process through integration of the area under the curve (Franco *et al.*, 2005). This has been done to calculate the energy input required to achieve the maximum viscosity, as well as for the entire process.

$$\dot{P} = 2\pi N(M - M_0) \qquad (3\text{-}4)$$

$$E = 2\pi \mathrm{N} \int_0^t (M - M_0)dt \qquad (3\text{-}5)$$

Where: $\dot{P}$ *is power consumption (W), E = energy (J), M is the torque measured with fluid present (N m),* M_o *is the torque measured on the impeller with empty vessel (N m), N is rotational speed (RPS), t is time (s).*

3.2.5 Corrective factor to compare samples prepared at different shear rates

For LGNs prepared at different rotational speeds, a corrective factor has been applied to data to enable direct comparison between samples, taking in to account the shear-thinning behaviour of the system. Torque-speed measurements were taken for a reference Newtonian fluid (glycerine at 25°C) and the instantaneous power consumption calculated using the method described previously. Knowing the viscosity of the Newtonian system, and the power consumption for Newtonian and non-Newtonian fluid, the apparent viscosity of the non-Newtonian fluid (η; Pa s) can be determined from Equation 3-6.

$$\mathrm{P}_{NN}\mu = \mathrm{P}_{N}\eta \tag{3-6}$$

Where P_N and P_{NN} are the power consumption for the Newtonian and non-Newtonian fluid, respectively.

To estimate the apparent viscosity at the reference shear rate of 200 s^{-1} instead, N can be taken as the equivalent reference vane speed (2.61 rps) in Equation 3-6. This provides an insight in the apparent viscosity of the system at the reference shear rate so that it is possible to determine the effects of varying vane speed, as well as directly comparing the viscosity across samples prepared at different mixing speeds.

3.2.6 Rheological characterisation of LGN samples

Characterisation of all samples was carried out using the Discovery DHR-3 rheometer (TA instruments) equipped with cross-hatched parallel plates to minimise slip. All measurements were carried out at 25°C on samples aged for at least 24 h. The yield stress was measured using an oscillation amplitude sweep method, 24 h after preparation. Amplitude sweep measurements were carried out at a frequency of 0.1 Hz, and a strain of 1 – 2 000%. The yield stress was determined from a plot of storage modulus (*G'*) against oscillation stress; taken as the stress value which corresponds to the onset of the loss modulus (Davies and Amin, 2020). Flow curves of the samples were obtained using a rotational shear rate sweep from 0.1 – 1 000 s^{-1}. Flow curve data was fitted to a power-law model in the shear rate range 10 – 250 s^{-1}.

3.2.7 Statistical analysis

All samples were prepared in triplicate, and an average of the viscosity profile is presented in this study. Standard deviation of the maximum viscosity value and final viscosity value for samples were calculated to investigate replicability. The average standard deviation for the maximum viscosity value was 5.24% and for the final viscosity value was 5.89%. Yield stress measurements were also completed in triplicate and an average and standard deviation is presented in the text. Student's t-test ($\alpha = 0.05$) were utilised to compare samples against the reference conditions.

3.3 Results and Discussion

3.3.1 Analysis of effects of process conditions of formation of LGNs

Analysis of rheological mapping profile for the preparation of LGN at reference conditions

An example of an apparent viscosity-time plot for LGN_{ref} is shown in Figure 3-3, with key parts of the curve labelled and attributed to different parts of the process to aid in comparison with other LGNs prepared at different conditions. The process starts at point *a* (t = 0s), where water and FA is being agitated at 200 s^{-1}. The temperature is at 70°C for the first 300 s, and then reduced to 60°C, the temperature being investigated for the structuring stage. During the preparation stage, the mixture is an unstable emulsion of FA liquid crystals and water (Yamagata and Senna, 1999). The viscosity remains constant as both the microstructure and the processing conditions are in steady state. At point *b* (t = 420 s), BTAC is introduced into the cup. There is an initial jump in the viscosity due to solid particulates having been introduced. The figure then shows an increase in viscosity from *b* to *c,* where the BTAC is melting and beginning to combine with the FA and water, which lasts for ~300 s. From *c* to *d* the viscosity continues to increase to the maximum value at *d* (0.99 Pa s, 1340 s). Between these stages a plateau in the apparent viscosity can be seen (t = 950 s to t = 1150 s).

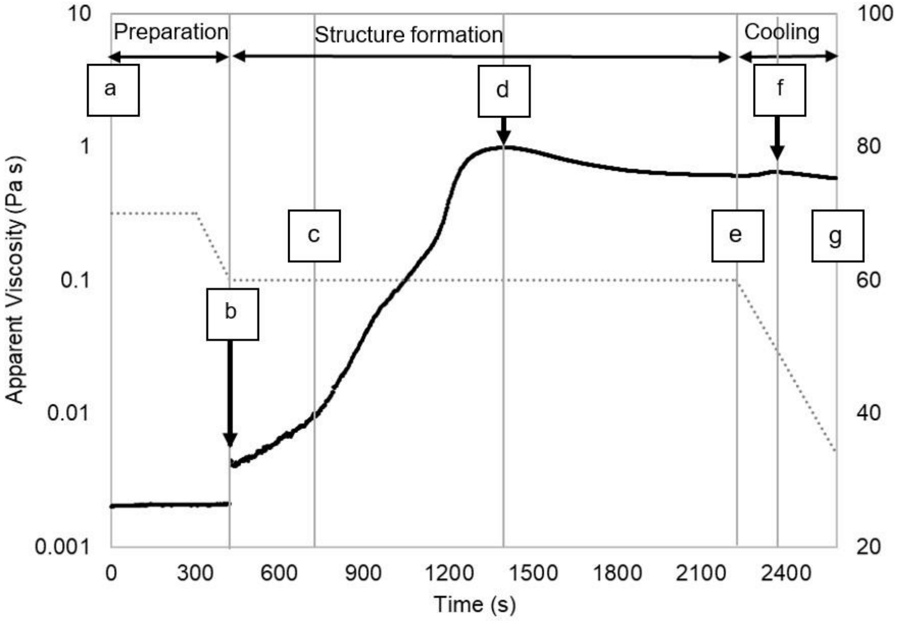

Figure 3-3. Viscosity-time profile of lamellar structured liquid (LGNref) prepared at reference conditions (structuring stage: temperature 60°C, vane speed 200/s, time 30 minutes)

Work by Gentile *et al.* (2012); (2014) on shear-induced transitions from lamellar sheets to multilamellar vesicles (MLVs) in single surfactant aqueous systems ($C_{12}E_3/D_2O$) showed a similar plateau at an intermediate time when the system was subjected to much lower shear rates. This was attributed through rheo-SALS and other techniques to be caused by an intermediate aggregate structure being formed. A similar transition could be occurring in this system and this idea is supported by the presence of MLVs in the final products (Gentile *et al.*, 2014; Gentile *et al.*, 2012). The overall viscosity gradient from *b* to *d* is 6.1 x 10^{-2} Pa s min^{-1}. After the peak at *d,* the viscosity then slightly reduces and levels out around t = 2000 s at a viscosity value of

0.61 Pa s. The cooling stage commences at *e* (t = 2220 s). A lower second peak in viscosity is seen at *f* (0.64 Pa s) at a temperature ~51°C, before the viscosity continues to slightly decrease to a final value of 0.58 Pa s at *g*. The second peak in viscosity could correlate to the transition of the lamellar liquid crystal structure to a lamellar gel phase, where the hydrocarbon chains reach a temperature below their melting point, the surfactant packing becomes more ordered, and more swelling occurs. Ribiero *et al.* (2004), performed DSC on different semisolid O/W creams containing cetyl alcohol and non-ionic surfactant, and observed a broad endotherm around 55°C, which they constituted towards the transition to and swelling of the lamellar gel phase.

Effects of temperature on the formation of LGNs

The effect of processing temperature on the viscosity of the incipient LGN was explored by varying the temperature during the structuring stage and maintaining the time and vane speed at the reference conditions of 30 min and 200 s^{-1}, respectively. Temperatures of 57°C, 60°C, 63°C and 67°C were investigated. The viscosity profiles for these samples are given in Figure 3-4.

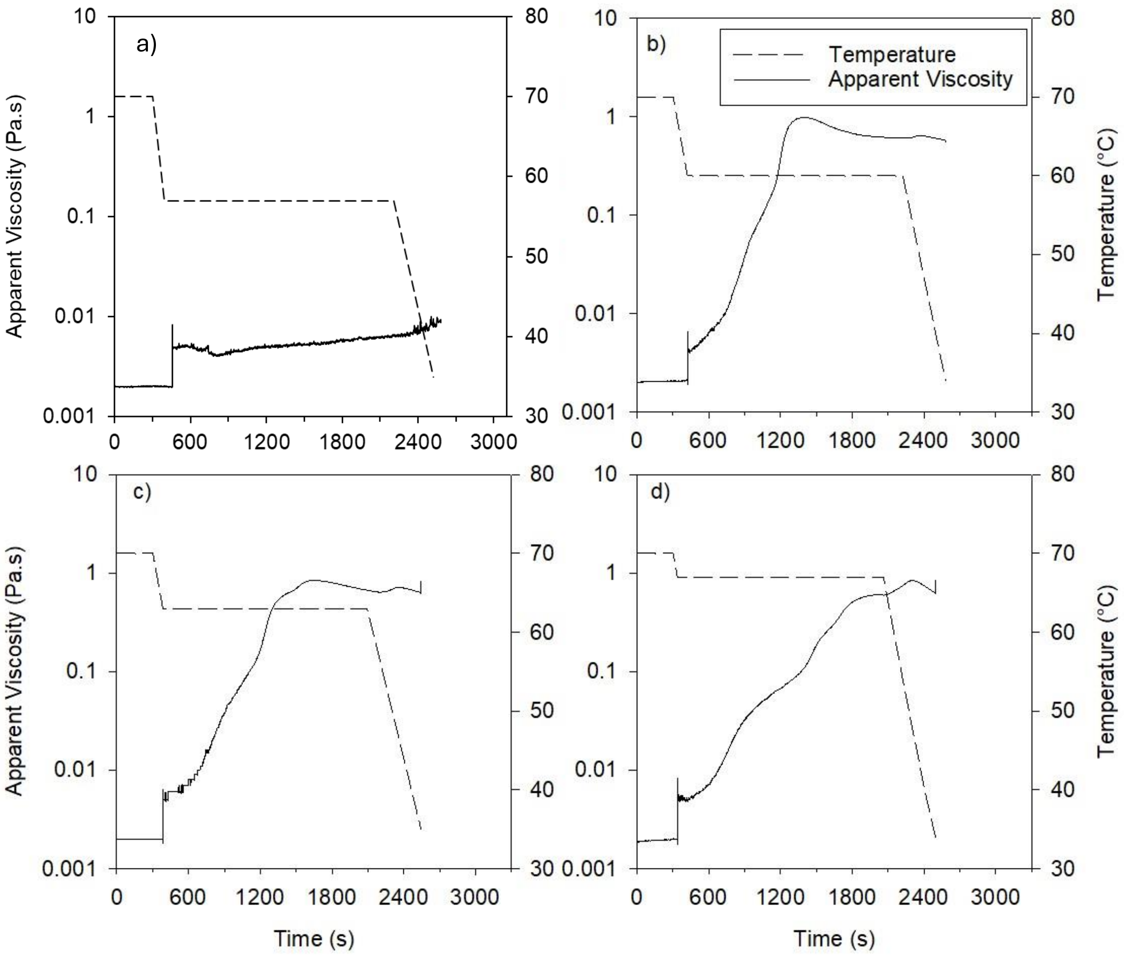

Figure 3-4. Apparent viscosity-time plots for LGNs prepared at different structuring stage temperatures. a) $LGN_{T=57}$ b) LGN_{ref} c)$LGN_{T=63}$ d)$LGN_{T=67}$; (dashed line = temperature profile; solid line = apparent viscosity)

For a processing temperature of 57°C (Figure 3-4a), the viscosity of the system does not increase significantly in comparison to the other investigated temperatures. This behaviour was ascribed to insufficient temperature to melt the BTAC in solution (melting point = 52-64°C; dependent on purity) (Clairant Corporation, 2018), thus the required emulsification with the FA did not occur and the lamellar structure was not formed. This was evident due to the inhomogeneous nature of the prepared sample (*i.e.*, presence of not melted solid particulates) which did not possess sufficient structure for yield stress characterisation. Figure 3-4b shows the viscosity profile for LGN_{ref}, which was prepared at a processing temperature of 60°C. This viscosity profile is previously discussed in Section 3.3.1 (*cf.,* Figure 3-3). A comparable trend was observed for $LGN_{T=63°C}$ (Figure 3-4c) in terms of viscosity profile, where certain distinct differences were exhibited. The viscosity gradient from *b* to *d* was less steep for $LGN_{T=63°C}$ (4.2 x 10^{-2} Pa s min^{-1}) than the reference conditions (6.1 x 10^{-2} Pa s min^{-1}), with the peak viscosity at *d* (0.86 Pa s) occurring at 1650s, 250s later than for LGN_{ref}. The viscosity profile for $LGN_{T=67°C}$ (Figure 3-4d) shows a slightly different trend to LGN_{ref} and $LGN_{T=63°C}$. The peak viscosity (0.79 Pa s) occurs considerably later for $LGN_{T=67°C}$ and occurs during the cooling stage rather than the structuring stage (~ 2380s) when the temperature has reduced to 47.5°C. This behaviour is thought to be associated with a combination of elevated temperatures reducing the magnitude of the viscosity response, and that lower processing temperatures form LGNs at a faster rate as seen through the rate of change of viscosity in comparison to the other investigated temperatures (Figure 3-4c,d). The peak in viscosity at around 50°C for $LGN_{T=67°C}$ again corresponds to the temperature seen for the transition to a swollen gel phase from the lamellar liquid crystal phase (Ribiero, *et al.*, 2004; Wunsch, *et al.,* 2015). Nevertheless, no significant differences ($p > 0.05$) were seen for the final viscosity values (0.59 ± 0.03 Pa s) and yield stress measurements (105 ± 3 Pa) across the samples prepared at 60 - 67°C. However, when the temperature was increased to 67°C, there was a slight reduction in the consistency index (Table 3-3). Overall, the effect of processing temperature is on the rate of attaining a given microstructure rather than differences in the final achieved microstructure for the formulation utilised in this study.

Table 3-3. Properties of LGNs prepared at different structuring stage temperatures

LGN	Viscosity gradient *b* to *d* (Pa s min s^{-1})	Peak viscosity value, *d*, (Pa s)	Time of peak viscosity, *d*, (s)	Final Viscosity value (Pa s)	Yield stress (Pa)	Consistency index, K (Pa s^n)	Flow index, n (-)	Average R^2 for fitting flow curve to Eq. 3-3.
$LGN_{T=57}$	-	-	-	-	-	-	-	
LGN_{ref}	6.1 x 10^{-2}	0.99± 0.03	1400	0.58 ± 0.02	108 ± 3	75.5 ± 4.0	0.11 ± 0.01	0.95 ± 0.01~~4~~
$LGN_{T=63}$	4.2 x 10^{-2}	0.92± 0.03	1650	0.57 ± 0.00	105 ± 5	75.0 ± 5.4	0.13 ± 0.02	0.98 ± 0.01
$LGN_{T=67}$	2.4 x 10^{-2}	0.79± 0.11	2380	0.62 ± 0.03	104 ± 5	58.1 ± 3.4	0.14 ± 0.03	0.99 ± 0.00

Effects of vane speed on the formation of LGNs

The effect of vane speed during the structuring stage on the formation of lamellar structured liquids was explored for a range of shear rates of 50 $s^{-1,}$ 200 s^{-1}, 400 s^{-1}, and, 600 s^{-1}, respectively. The temperature and time for the structuring stage were maintained at the reference conditions of 60°C and 30 min. The viscosity profiles for these samples are given in Figure 3-5. To be able to directly compare samples which have been prepared at different rotation speeds and therefore different effective shear rates, it was necessary to transform the plots to show the apparent viscosity at the reference shear rate of 200 s^{-1}. This was achieved using the method outlined in Section 3.2.5. The viscosity-time plots before transformation can be found in Appendix 9-7.

Figure 3-5 shows the viscosity profile for $LGN_{\gamma=50}$ prepared at a shear rate of 50s^{-1}. The viscosity-time plot at this lower vane speed does not follow the same trend as the reference sample (*Fig. 5b*), in terms of an initial jump in viscosity when the solid BTAC is added at point *b*, followed an increase in viscosity up to a maximum at *d*. For $LGN_{\gamma=50}$, after the BTAC addition at point *b*, the viscosity value slightly reduces to a value near 0.0001 Pa s at t = 420s, before increasing to 0.004 Pa s at t = 900s. The viscosity of the system then remains at approximately 0.005 Pa s for the remainder of the structuring stage. This suggests the vane speed was not sufficient to induce mixing in the system, thus a structure did not develop.

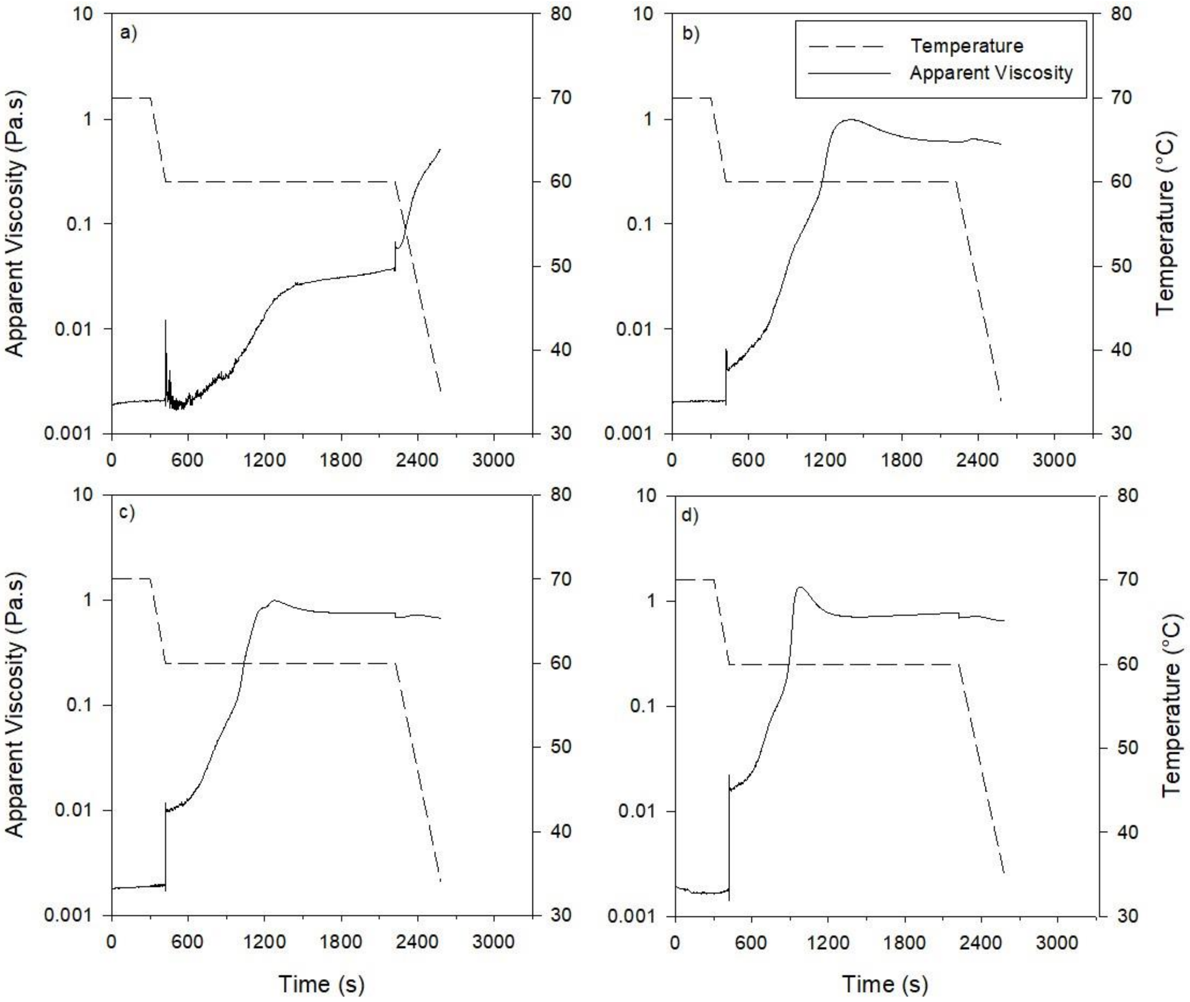

Figure 3-5. Viscosity-time plots for LGNs prepared at different structuring stage agitator speeds.
a)LGN$_{\gamma=50}$, b) LGN$_{ref}$, c) LGN$_{\gamma=400}$ d) LGN$_{\gamma=600}$
(dashed line = temperature profile; solid line = apparent viscosity)

Wunsch *et al.* (2016) prepared a ternary system of cetostearyl alcohol, CTAC and water in a DSC pan by performing DSC on a mixture of solid cetostearyl alcohol and CTAC solution. They also found that when no shear was applied, the lamellar structure was not formed in the same way that it is under normal production methods, highlighting that shear also affects the ability of the system to form a lamellar gel phase (Wunsch *et al.*, 2016). The viscosity of the system did increase during the cooling stage, however this was ascribed to the re-solidification of FA which had not been incorporated in to any lamellar structure (Yamagata and Senna, 1999). Increasing the shear rate to 400 s^{-1} does not significantly ($p > 0.05$) affect the viscosity gradient between *b* and *d*, nor the time and value of the maximum viscosity (Table 3-4). Increasing the vane speed further to 600s^{-1} increases viscosity gradient significantly to 1.5 x 10^{-1} Pa s.min^{-1}, leading to a the maximum viscosity (1.37 Pa s) being achieved around 360s earlier than for LGN_{ref}. The effects of increasing the vane speed to 600s^{-1} were also evident from the rheological properties of the final product. The average yield stress did not increase significantly between the samples prepared at 200s^{-1} and 400s^{-1} (108±3 Pa and 110±18 Pa, respectively), however when the vane speed was increased to 600s^{-1}, the yield stress of the final product was 136±10 Pa. When looking at the consistency index of the final LGNs, the samples follow a similar trend to yield stress, where the consistency index measured for LGN_{ref} and $LGN_{\gamma=400}$ were 75.5±5.5 Pa s^n and 79.3 Pa s^n respectively, and for $LGN_{\gamma=600}$ this increased to $K = 112.7$ Pa s^n. Neither the yield stress nor flow curve were able to be accurately measured for $LGN_{\gamma=50}$. Whilst there are no studies which have investigated the effect of energy input on the formation of lamellar gel networks, we can draw comparisons from emulsion formation and stability which has been more widely investigated. As expected, increasing the vane speed and thus the kinetic energy inputted to the system did improve the mixing in the system, evidenced by the increased rate of viscosity build during stage *c*, which thus improved the final structure of the product, evidenced by higher yield stress and consistency index (Liu and McGrath, 2005).

Table 3-4. Properties of LGNs prepared at different vane speeds

LGN	**Viscosity gradient *b* to *d* (Pa s min s^{-1})**	**Peak viscosity value, *d*, (Pa s)**	**Time of peak viscosity, *d*, (s)**	**Final Viscosity value (Pa s)**	**Yield stress (Pa)**	**Consistency index, K (Pa s^{n})**	**Flow index, n (-)**
$\text{LGN}_{\gamma=50}$	-	-	-	-	-	-	-
LGN_{ref}	6.1 x 10^{-2}	0.99 ± 0.03	1400	0.58 ± 0.02	108 ± 3	75.5 ± 4.0	0.11 ± 0.01
$\text{LGN}_{\gamma=400}$	6.9 x 10^{-2}	0.99 ± 0.31	1280	0.59 ± 0.08	110 ± 18	79.3 ± 0.2	0.13 ± 0.01
$\text{LGN}_{\gamma=600}$	2.4 x 10^{-2}	1.45 ± 0.02	1040	0.70 ± 0.04	136 ± 8	112.7 ± 4.8	0.03 ± 0.01

Effects of processing time on the formation of LGNs

The effects of varying time were investigated by varying the duration of the structuring stage for the following times: 10 min, 20 min, 30 min, and 40 min. The temperature and vane speed were maintained at the reference conditions, 60°C and 200s^{-1} respectively. Figure 3-6 shows the viscosity-time plots for $\text{LGN}_{t=10}$, $\text{LGN}_{t=20}$, LGN_{ref}, $\text{LGN}_{t=40}$.

Figure 3-6a shows the viscosity time-plot for $\text{LGN}_{t=10}$ where a structuring stage time of 10 mins was used. Reducing the structuring stage to 10 mins had the largest effect on the viscosity during the formation of the incipient LGN. For most of the samples prepared at other conditions, the maximum viscosity occurs during the structuring stage. However, for $\text{LGN}_{t=10}$, the viscosity has not reached a steady-state at the end of the structuring stage as it does for the reference conditions, and instead the viscosity continues to increase to a maximum viscosity (1.18 Pa s) during the cooling stage at a temperature of 43°C. The maximum viscosity for $\text{LGN}_{t=10}$ is the second highest maximum viscosity achieved ($\text{LGN}_{\gamma=600,t=10}$ being the highest at 1.36 Pa s).

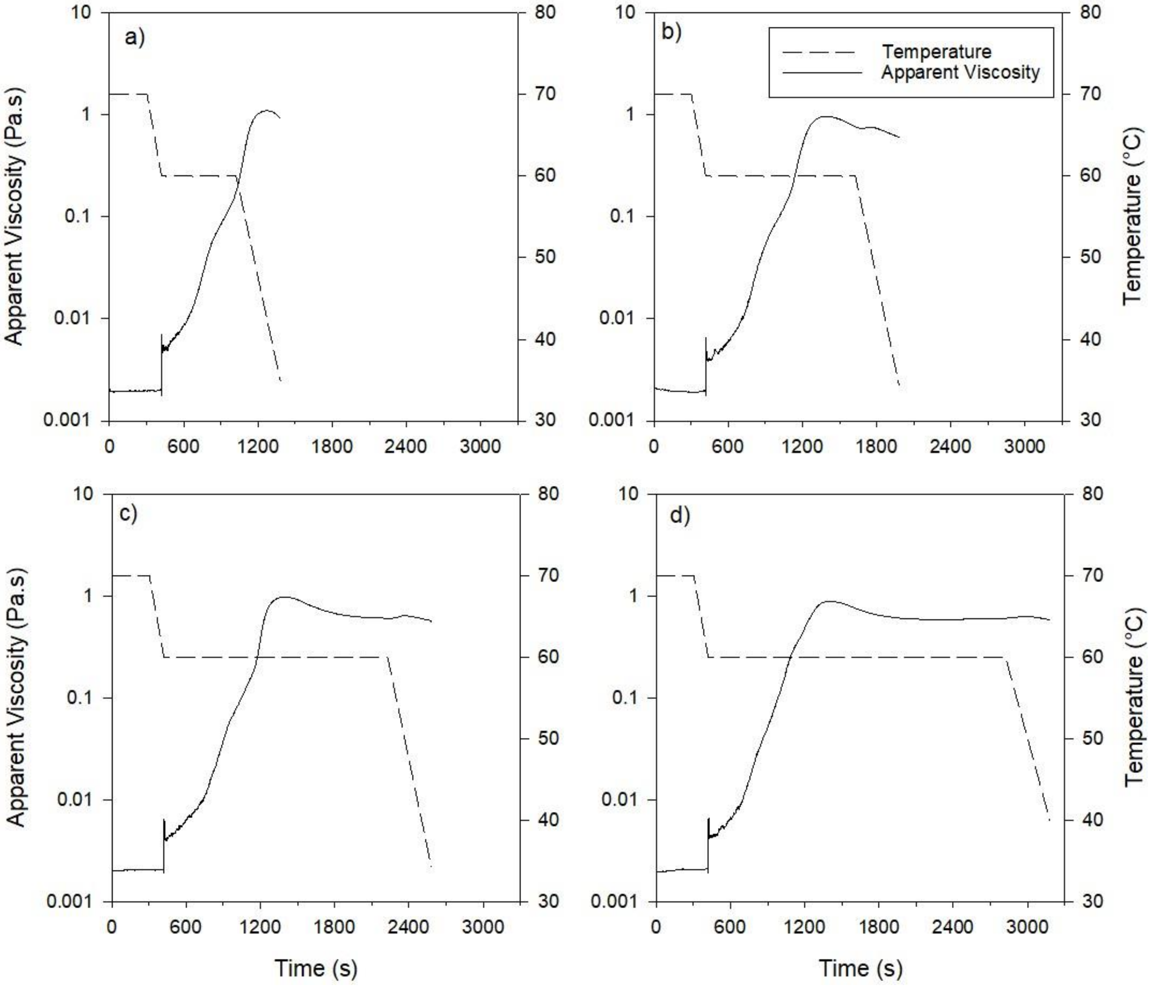

Figure 3-6. Viscosity-time plots for LGNs prepared at different structuring stage times.
a) $\text{LGN}_{t=10}$, b) $\text{LGN}_{t=20}$ c) LGN_{ref} (30 minutes) d) $\text{LGN}_{t=40}$
(dashed line = temperature profile; solid line = apparent viscosity)

This is reflected in the yield stress of the final product (139±8 Pa), which is the highest average yield stress value achieved. The higher yield stress and consistency of this sample suggest a well-connected and developed structure (Davies and Amin, 2020). Perhaps the reduced time at elevated temperatures provided less opportunity for the surfactant and FA to mix and form a lamellar liquid crystal, L_α, structure, followed by a transition to the lamellar gel phase accompanied by swelling, which is the predicted structure development (Wunsch *et al.*, 2016), and instead was able to immediately form a lamellar gel phase, $L_β$, at a temperature below the gel transition temperature during the cooling stage (Eccelston, 1997; Partal, *et al.*, 2001). The oscillatory amplitude sweeps for the LGNs can be interpreted to provide further information about the microstructure (Figure 3-7).

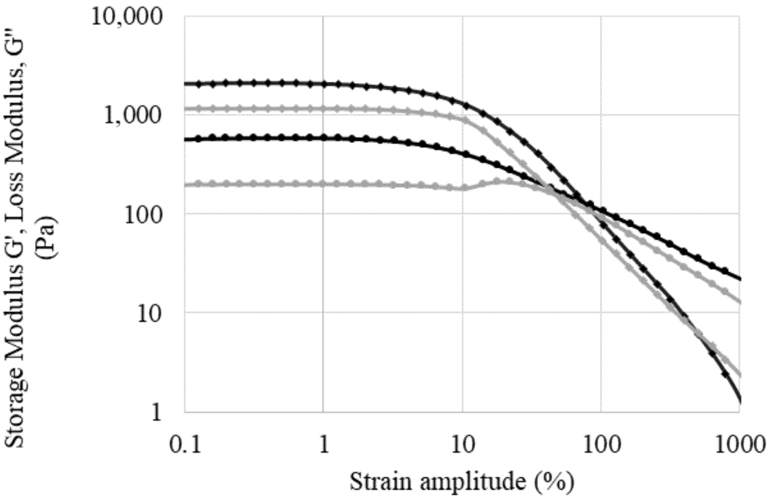

Figure 3-7. Oscillation amplitude strain sweep for LGNref and LGNt=10 (grey = LGNref; black = LGNt=10; diamond = G'; circle = G'')

Youssry *et al.* (2008) describe how a higher magnitude of the moduli can be attributed to stronger interactions between the flowing units – demonstrated by the slightly higher moduli for $LGN_{t=10}$ corresponding to a higher yield stress. Furthermore, the strain overshoot for the loss modulus (bump ~10% strain) is attributed to the formation of an intermediate structure which can resist strain up to a critical point (seen for LGN_{ref}). In this case, it is likely that MLVs are providing resistance to the strain. For $LGN_{t=10}$, the strain overshoot is absent, which suggests the lamellar phase is likely in a more swollen, planar state than LGN_{ref} which is more likely to have a higher proportion of MLVs present (Hyun *et al.*, 2002).

Figure 3-6b shows the viscosity time plot for $LGN_{t=20.}$ For this processing time (20 mins), the viscosity initially follows the same profile as samples prepared for longer times. The value of and time taken to achieve the maximum viscosity are comparable to the sample prepared at the reference conditions (Table 3-5). After point *d*, the reduced structuring stage time results in a reduction of the time from *d* to *e* , the beginning of the cooling stage. This is beneficial from a processing perspective, as the system is in steady state for this duration, so it is possible to reduce processing time without affecting product structure and quality. The yield stress value measured for $LGN_{t=20}$ (108±13 Pa) is comparable to the yield stress of LGN_{ref} and $LGN_{t=40}$ (Table 3-5), which further suggests that the majority of the structure formation occurs before point *d*, and any additional mixing has little effect on the structure. The variability in the yield stress values were slightly higher for $LGN_{t=20}$, which can be attributed to the proximity of the end of the 20 minute structuring time to the typical time of the maximum viscosity occurring (~1400 s). Figure 3-6c shows the viscosity time plot for LGN_{ref}, where a processing time of 30 min was used. Increasing the structuring stage time above the reference conditions to 40 min (Figure 3-6d) only increases the time between the peak viscosity at point *d* and the start of the cooling stage, *e,* where the viscosity of the system is not changing much as a function of time. This suggests that the structure of the system is also not changing, thus this increase in processing time is not conducive to improving the structuring of the incipient LGN. This is substantiated by the comparable time and value of the peak viscosity to the reference conditions (Table 3-5).

Table 3-5. Properties of LGNs prepared at different processing times

LGN	**Viscosity gradient *b* to *d* (Pa s min s^{-1})**	**Peak viscosity value, *d*, (Pa s)**	**Time of peak viscosity, *d*, (s)**	**Final Viscosity value (Pa s)**	**Yield stress (Pa)**	**Consistency index, K (Pa s^n)**	**Flow index, n (-)**
LGN$_{t=10}$	7.9×10^{-2}	1.18 ± 0.06	1040	0.93 ± 0.12	139 ± 7	44.33 ± 1.7	0.21 ± 0.01
LGN$_{t=20}$	5.9×10^{-2}	0.99 ± 0.07	1324	0.56 ± 0.04	101 ± 8	66.8 ± 0.6	0.21 ± 0.05
LGN$_{ref}$	6.1×10^{-2}	0.99 ± 0.03	1400	0.58 ± 0.02	108 ± 3	75.5 ± 4.0	0.11 ± 0.01
LGN$_{t=40}$	5.4×10^{-2}	0.95 ± 0.07	1400	0.59 ± 0.05	111 ± 11	88.5 ± 6.0	0.06 ± 0.02

As the greatest difference in microstructure formation and final product characteristics were observed from reducing the processing time and increasing the vane speed, it was decided to further investigate these characteristics by altering both conditions simultaneously. The conditions which were investigated were: a vane speed of 400s^{-1}, processing time of 20 minutes (LGN$_{\gamma=400,t=20}$) and a vane speed of 600s^{-1}, processing time of 10 minutes (LGN$_{\gamma=600,t=10}$). The samples were then compared against those prepared at the same shear rate, and reference processing time, and alternatively at the reference shear rate, and same processing time, to fully understand where the changes to the viscosity profile appear.

Figure 3-8 shows the viscosity profiles for LGN$_{\gamma=600,t=10}$, LGN$_{\gamma=600}$ and LGN$_{t=10}$. The samples prepared at the same shear rate (LGN$_{\gamma=600,t=10}$ and LGN$_{\gamma=600}$) initially follow a very similar profile, with peak *d* occurring at 1.37 Pa s, 980s for LGN$_{\gamma=600}$ and 1.40, 1020 Pa s for LGN$_{\gamma=600,t=10}$. The differences in the viscosity profile appear after the peak viscosity, *d*, in which the steady-state region is drastically reduced, and begins at the beginning of the cooling stage, *e*. Comparing the samples prepared at the same time but different shear rates, it is easy to see that increasing the shear rate to 600s^{-1} increases the apparent viscosity from point *b* where the BTAC surfactant is added and the maximum viscosity value occurs earlier in the process, as previously discussed *(c.f.* Figure 3-3*)*.

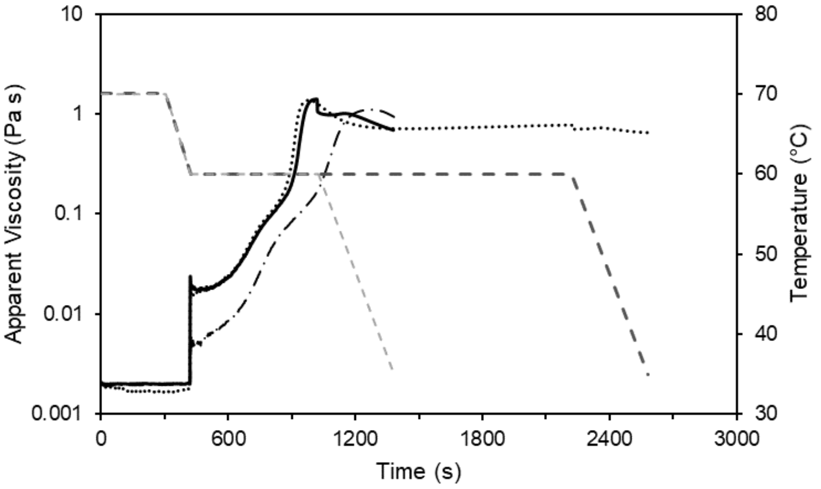

Figure 3-8. Viscosity-time plots for LGNs prepared at different times and agitator speeds (apparent viscosities: black solid line = LGN$_{\gamma=600,t=10}$, black dotted line = LGN$_{\gamma=600}$, black dot and dash line = LGN$_{t=10}$) (temperature profiles: dark grey dash line = 30 minute structuring stage (LGN$_{t=600}$), light grey dash line = 10 minute structuring stage (LGN$_{\gamma=600,t=10}$; LGN$_{t=10}$))

Interestingly, when looking at the final properties of the LGNs, combining the reduced processing time with the higher shear rate does not produce a LGN with a higher yield stress than each condition individually. The yield stress for LGN$_{\gamma=600,t=10}$ is 125 ± 3 Pa, compared to 136 ± 8 Pa for LGN$_{\gamma=600}$ and 139 ± 7 Pa for LGN$_{t=10}$. This could indicate that the vane speed is perhaps too high for short durations, and the effects of increased variability and fluctuations which often come with excessive mixing needs to be diminished by an increased processing time.

For LGN$_{\gamma=400,t=20}$, it was found that increasing the shear rate to 400s^{-1} and reducing the processing time to 20 min gave a profile which is initially similar to LGN$_{\gamma=400}$, with comparable times and values for the peak viscosity, *d*. However, for LGN$_{\gamma=400,t=20,}$ the time between *d* and the start of the cooling phase *e* is obviously reduced and shows the same trend as LGN$_{t=20,}$ *i.e.,* a reduction in the duration of the steady state phase. Comparing $LGN_{γ=400;t=20}$ to $LGN_{t=20,}$ which was prepared at the reference shear rate (200s^{-1}), the rate of viscosity increase is higher for $LGN_{γ=400;t=20}$ (8.22 x 10^{-2} Pa s.min^{-1}) from *b* to *d*, compared to 5.88 x 10^{-2} Pa s.min^{-1}. The value of the maximum viscosity also increased as a function of vane speed. The effects of increasing vane speed and reducing processing time increased the final yield stress of $LGN_{γ=400,t=20}$ (129 ± 5 Pa), higher than for both $LGN_{t=20}$ (*c.f. Table 3-5*) and $LGN_{γ=400}$ *(c.f. Table 3-4)*.

3.3.2 Effects of processing conditions on power consumption

As well as investigating the effects of varying process conditions on the rheological properties of the final LGN, it was also important to determine the process requirements for each set of conditions. Figure 3-9a shows a plot of the total mixing energy and energy input until the maximum viscosity was achieved as a function of temperature. At 57°C, there was no maximum viscosity so there is no value for this point. Above 60°C, as the temperature increases, the total mixing energy required reduces, as the system spends a longer portion of the process at a reduced viscosity (*cf.,* Figure 3-4). However, the power required to maintain the temperature of the system has not been considered in this work. This also explains why the energy required to achieve the maximum viscosity is higher for $LGN_{T=67}$ as the maximum viscosity is achieved ~1000s later than for LGN_{ref}. Figure 3-9b shows energy requirements as a function of vane speed (s^{-1}). The total energy input increases linearly as the vane speed is increased, whilst the energy required to achieve the maximum viscosity does not increase with vane speed; it is comparable amongst all the different speeds, 1.18 J/g for LGN_{ref}, 1.18 J/g for $LGN_{γ=400}$ and 1.63 J/g for $LGN_{γ=600}$.

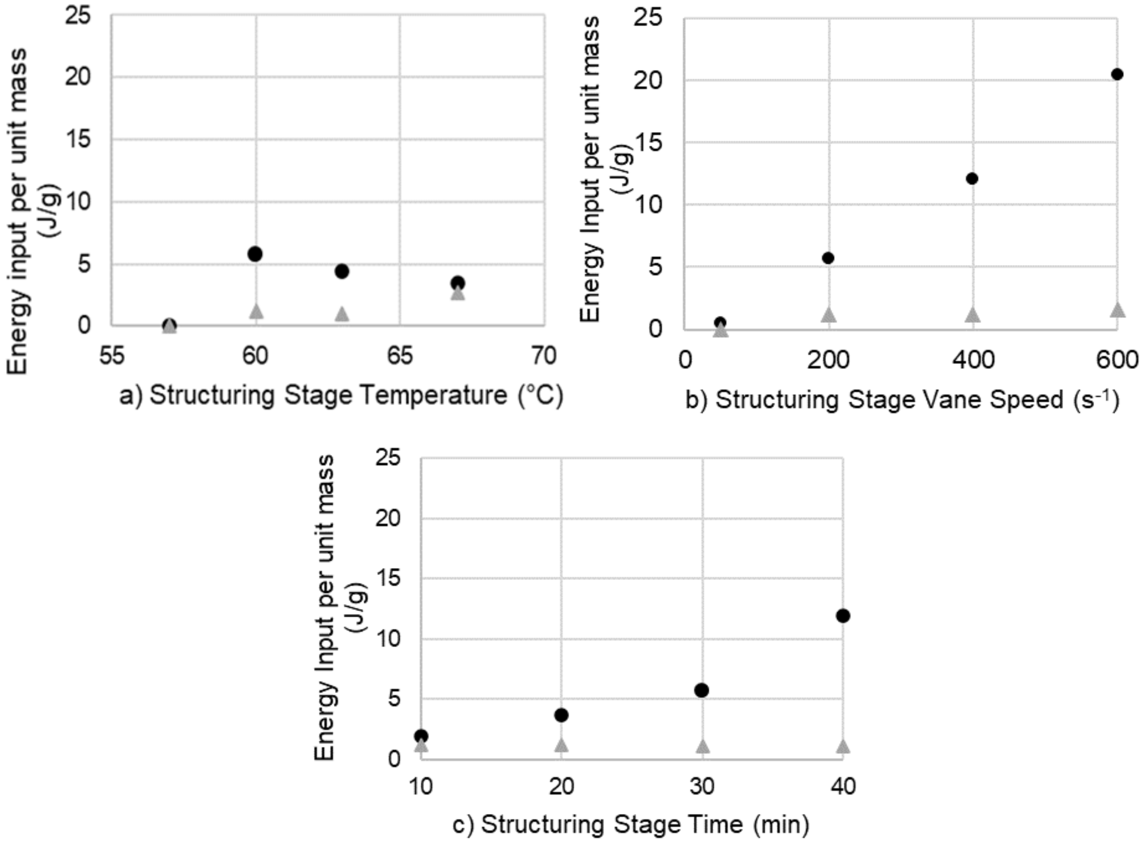

Figure 3-9. Total energy input per unit mass for different LGN processing conditions. a) different structuring stage temperatures, b) different structuring stage vane speeds , c) different structuring stage times (black circle = total energy input; grey triangle = energy input to maximum viscosity value.)

From Figure 3-9c, it can be seen that total energy input increases in an exponential manner as a function of structuring stage time. However, the energy required to achieve maximum viscosity is again comparable for all structuring times (1.18 J/g), which is logical as the maximum viscosity occurs at a similar time for samples prepared at the same vane speed. For $LGN_{\gamma=400,t=20}$, the energy input required to achieve the maximum viscosity was 1.18 J/g – again comparable to most of the other samples. However, for $LGN_{\gamma=600,t=10}$, the energy input required to achieve maximum viscosity was 2.29 J/g. Out of the samples with the highest yield stress, $LGN_{t=10}$ and $LGN_{t=600}$, $LGN_{t=10}$ had the lowest energy requirements. Reducing the processing time offers the most obvious option for reducing power consumption, whilst maintaining a high yield stress. This said, the total energy input for LGN$_{\gamma=600,t=10}$ (2.29 J/g) was one of the lowest which still produced a comparatively high yield stress.

3.4 Conclusions

The structure formation of a lamellar gel network system comprised of water, cetostearyl alcohol and BTAC has been followed through the use of a rheological mapping approach. A four-bladed vane and cup geometry rotational rheometer was utilised to follow the viscosity and power requirements of the system as a function of time. This work presents an insight into the kinetics of lamellar structure formation during processing, which has not been widely explored yet. Most other studies which have considered process conditions have only been able to focus on the properties of the sample after preparation. It was seen that the system typically followed a profile in which, after surfactant addition, the viscosity increased at a rate of 6.0 x $^{10-2}$ Pa s min^{-1} up to a maximum value which occurred around 1400 s (for LGN$_{ref}$). There was a slight secondary peak that occurred during the cooling stage, which was attributed to the swelling of the gel phase. The effects of process history on the final rheological characteristics were determined through traditional oscillatory and rotational rheometry techniques. The results provide information about how process conditions can be varied to improve final product quality, as well as reduce power consumption. An increase in temperature lead to an increased time to achieve a maximum viscosity but did not have a significant effect on the final yield stress of the samples. Variation of the vane speed proved the importance of shearing when producing a lamellar structure. At the lowest vane speed, a structure was not formed and the viscosity profile did not follow the anticipated pattern demonstrated for the reference conditions. Increasing the vane speed to the maximum speed tested here (600s^{-1}) led to an increase in the yield stress and consistency index of the final LGN, as well as an increase in the maximum viscosity seen during processing and a reduction in the time taken to achieve the maximum viscosity. However, the power requirements increased linearly with increased vane speed, meaning the total energy input for this sample was three times that for the reference conditions. Finally, it can be seen that increasing the structuring stage time past 30 minutes had minimal effect on the structure of the system, and only increased the steady-state phase of the process. Reducing the structuring stage time to 20 min provided the same yield stress, but reduced the power requirements. Reducing the time further to 10 min further increased the yield stress, and this is thought to be associated with the lamellar gel phase forming at a cooler temperature rather than first forming a lamellar liquid crystal and then transforming to gel when the system cools below the gel transition temperature. In the future it would be beneficial to investigate different formulations, such as different concentrations of the same components, or other surfactants to see if changing processing conditions has the same effect across formulations. Additionally, another aspect which would be interesting to explore is the use of a close clearance vane such as anchor or helical ribbon which would more commonly be used in larger scale processes to determine the suitability of this technique for scale-up considerations.

CHAPTER 4:INVESTIGATION OF INDUSTRIALLY RELEVANT RHEOMETER GEOMETRIES FOR IMPROVED SCALE-UP OF LAMELLAR STRUCTURED LIQUIDS

Adapted from Cunningham, G.E.; Deshpande, S.; Simmons, M.J.H., O'Sullivan, J.J. (2023). Investigation of Industrially Relevant Rheometer Geometries for Improved Scale-Up of Lamellar Structured Liquids. *IFSCC Magazine, 26, (March), pp. 55-62*

4.1 Introduction

The global beauty and personal care market is projected to continue growing to a value of around 758 billion USD by 2025, and in order to remain competitive, businesses must reduce their time to market for new products (Statista, 2022). Furthermore, with growing supply chain uncertainty due to global instabilities (*e.g.*, pandemics, global conflicts, climate change, *etc*.), it is ever more important to understand how feedstock flexibility (*i.e.*, material changes and variable quality) and process robustness could impact the formulation and properties of manufactured products (Hobbs, 2020; Jira and Toffel, 2013). When a formulated product is brought to market, it is first developed at a traditional laboratory scale (< 1 kg), before being progressed to a pilot plant environment (5-50 kg), and once the formulation and process conditions are confirmed, then deployed to factory-scale at a sourcing unit (> 1,000 kg). The scale of the process impacts both mixing and temperature profiles experienced by the raw materials, which affects the final product microstructure and physical properties (Wibowo and Ng, 2002). Having a representative scaled-down version of the manufacturing process would enable improved screening of new ingredients, a better understanding of the impact of process conditions on microstructure formation and aid the scale-up process by improving geometric similarity and understanding of power requirements.

In Chapter 3, a rheometer was employed to monitor the evolution of the structure of lamellar gel networks (LGNs) as a function of process conditions such as time, agitator speed, and temperature. However, one of the limitations of this work was the use of a vane geometry as the agitator. The vane geometry has gained popularity for measuring the yield stress and other rheological properties of complex fluids (*e.g.*, thixotropic, viscoelastic, plastic, *etc.*) due to its ability to inhibit slip, as the shape of the vane generates a cylindrical stress field around the rotating central axis, but the blades of the vane reduce slip compared to a cylindrical Couette geometry (Owens *et al.*, 2020). While it is known that in practice this is not always the case and that there can be mixing between the quadrants of the vane, it would be pertinent to utilise rheometer geometries that both promote mixing and possess geometric similarities to industrial mixing elements (Cullen *et al.*, 2003).

Therefore, the main objective of this chapter was to utilise custom-made rheometer geometries which more accurately reflect the geometric considerations of agitators employed at industrial scale. The study will aim to determine any differences in viscosity profile, mixing efficiencies, power requirements, and final product characteristics that arise from using different geometries to manufacture lamellar structured liquids. The effects of processing conditions on the final product structure have been characterised in terms of rheology, namely the yield stress of the product, which is known to strongly depend on the structure to distinguish between lamellar structures (bilayers and vesicles). The application of such capabilities at a rheometer scale could enable such tools to be used for broader process understanding, minimizing the number of pilot scale trials that are required, and reducing material and energy consumption.

4.2 Materials and Methods

4.2.1 Materials

This study focuses on the same formulation used in Chapter 3 (3.2.1) to enable direct comparison between results. The formulation is a ternary system of fatty alcohol, quaternary ammonium salt, and water; known to generate a lamellar structure under a range of process conditions and with rheological properties representative of a fully formulated cosmetic or personal cream product (Davies and Amin, 2020). The fatty alcohol (FA) used as part of this study was a commercially available blend of cetyl alcohol (30 wt. %) and stearyl alcohol (70 wt. %) (cetostearyl alcohol) sourced from Godrej Industries (Maharashtra, India). The surfactant used was behentrimonium trimethyl ammonium chloride (BTAC), supplied by Clariant International Ltd. (Munich, Germany). This surfactant is provided at 70 wt. % purity, where the remaining 30 wt. % is comprised of dipropyl glycol. Distilled water was used for all experiments.

4.2.2 Preparation of lamellar structured liquids

A Discovery HR-III stress-controlled rheometer (TA Instruments, Wilmslow, UK) was used to prepare the lamellar structured liquids according to the methods given in Chapter 3 (3.2.2), with some slight differences. In this work, three, new different geometries were investigated: TA helical rotor (TA Instruments, part no. 546018.901), 3D printed helical ribbon, and 3D printed anchor scraper (Figure 4-1) where the 3D printing process was direct metal laser sintering of titanium conducted by Laser Prototypes Europe Ltd (UK).

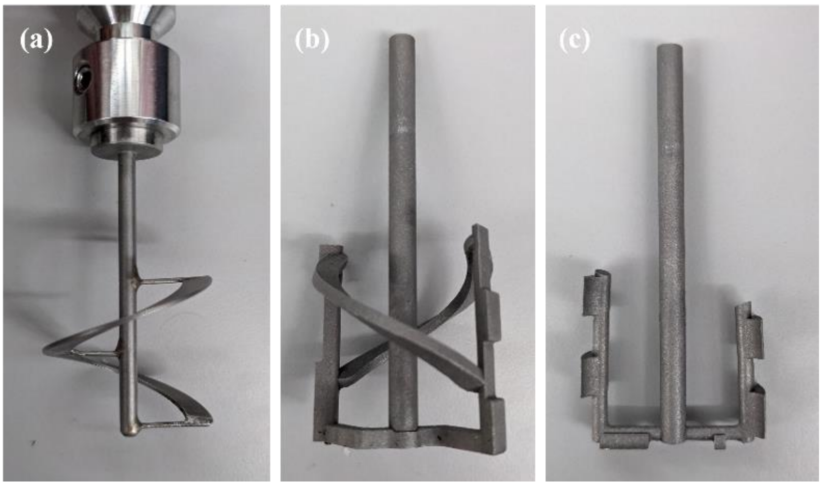

Figure 4-1. (a) TA Instruments helical rotor (TA-HR), (b) 3D printed helical ribbon (3D-HR), and (c) 3D printed anchor (3D-ANC)

The 3D printed helical ribbon and 3D printed anchor were based on mixing elements frequently used at larger scale. The helical ribbon is geometrically similar to the mixing geometry used in a 50L pilot scale mixer at Unilever which had torque measurement capability. Scaling this geometry down to rheometer and lab scale allowed for geometric similarity across scales in future experiments. The anchor was similar the mixing geometry on a 2L lab scale mixer. The TA helical ribbon is a commercially available geometry which was included to determine if geometry had an impact at this scale, and if the 3D printed, scaled—down geometries were necessary or if learning could be transferred from a generic helical ribbon type geometry. The geometric considerations for the custom-made mixing elements were based on representative pilot-scale examples.

Similarly to Chapter 3, variables were changed during the structuring stage of the process (addition of BTAC to a molten mix of FA and water). A fractional factorial design of experiments was used to investigate the effects of process temperature (T, °C), agitator speed (N, rad s^{-1}), mixing time (t, min), and rheometer geometry (Table 4-1). One additional experiment was added after completion of the design of experiments to fulfil a knowledge gap (3D-HR_60_16_30). Process conditions utilised in the previous chapter have been repeated in this work to enable direct comparison. Furthermore, it should be noted that angular velocity has been used to quantify agitator speed rather than shear rate, in order to directly compare differences in speed across different geometries.

Table 4-1. Fractional factorial design of experiments of process variables (geometry, temperature, agitator speed, and time) for the structuring stage of lamellar gel formation. Sample naming system is Geometry_Temperature_Speed_Time

Sample	**Rheometer geometry**	**Temperature (°C)**	**Speed (rad s^{-1})**	**Time (min)**
3D-HR_60_48_30	3D-HR	60	48	30
TA-HR_60_16_30	TA-HR	60	16	30
3D-ANC_60_16_30	3D-ANC	60	16	30
TA-HR_60_48_10	TA-HR	60	48	10
TA-HR_67_48_30	TA-HR	67	48	30
TA-HR_67_16_10	TA-HR	67	16	10
3D-ANC_67_48_10	3D-ANC	67	48	10
3D-ANC_60_48_10	3D-ANC	60	48	10
3D-HR_67_48_30	3D-HR	67	48	30
3D-ANC_67_16_30	3D-ANC	67	16	30
3D-HR_60_16_10	3D-HR	60	16	10
3D-HR_67_16_10	3D-HR	67	16	10
3D-HR_60_16_30	3D-HR	60	16	30

4.2.3 Calibration of Rheometer Geometries

The TA-HR, 3D-HR, and 3D-ANC were calibrated using the Couette analogy as recommended by the rheometer equipment supplier, TA Instruments (Franck), and described by Ait-Kadi *et al.* (2002). The calibration fluid was glycerine (Palmera G995E; > 99.5% purity; supplied by KLK Oleo; viscosity at 0.25 °C = 0.95 Pa s). The values calculated for the shear stress constant (k_τ) and the shear rate constant (k_γ) are given below in Table 4-2.

Table 4-2. Summary of shear rate and shear stress constants for the different geometries investigated

Geometry	**Shear stress constant (-)**	**Shear rate constant (-)**
Vane	16141	12.21
3D-ANC	23836	3.43
3D-HR	21891	4.51
TA-HR	26800	2.46

4.2.4 Rheological and Homogeneity Characterization of LGN Samples

The samples were characterised by measuring rheological properties and visual assessment of homogeneity, in addition to the in-situ process data that was captured during the manufacture of the LGN samples. Rheological characterization of all samples was carried out using the Discovery DHR-III stress-controlled rheometer (TA Instruments, UK) equipped with cross-hatched parallel plates to minimise slip effects. All measurements were carried out at 25 °C on samples aged for at least 24 h. The yield stress was measured using an oscillation amplitude sweep method described in Section 3.2.6 (Davies and Amin, 2020). A visual assessment of homogeneity was carried out by spreading a *ca.* 1 g sample of LGN to a thickness of *ca.* 1 mm onto a matte black tile and observing for both lumps of unincorporated FA or BTAC, and opacity.

4.2.5 Statistical Analysis

All samples were manufactured in triplicate, and an average of the viscosity profile is presented in this work. In addition, yield stress measurements were completed in triplicate (individual measures on samples prepared in triplicate) and an average and standard deviation are presented. ANOVA was used to determine the difference between single effects on single outputs, where a 95% confidence interval was employed, and data were considered statistically significant when $p < 0.05$.

4.3 Results & Discussion

4.3.1 Comparison of viscosity-time profiles of industrially relevant geometries to vane geometry

The impact of different rheometer geometries (vane, 3D-ANC, TA-HR, 3D-HR) on the formation of lamellar gel structure was initially investigated at the same processing conditions of T = 60°C, N = 16 rad s^{-1}, t = 30 min (*i.e.,* REF_16_30 according to the naming convention used). Figure 4-2 shows the viscosity profiles for these samples.

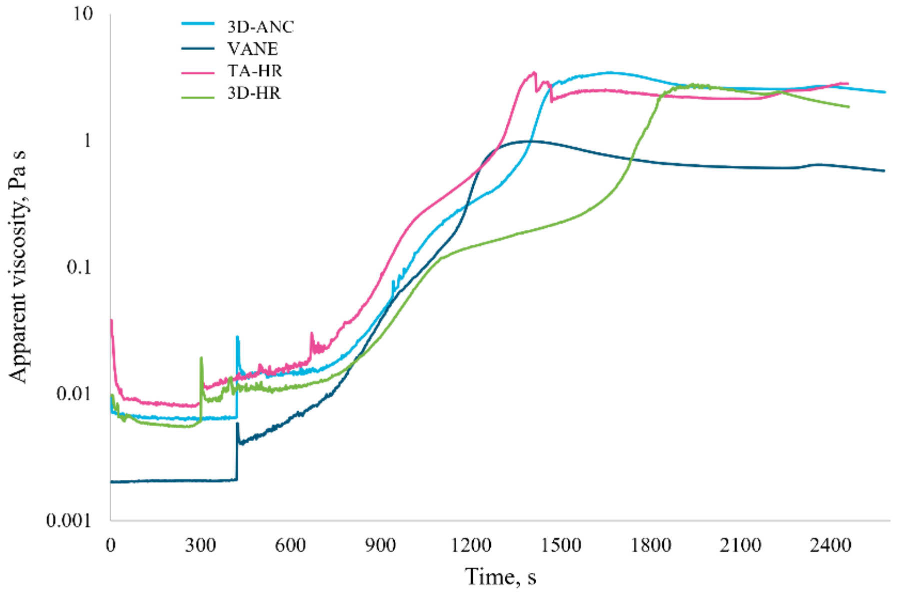

Figure 4-2. Viscosity-time profiles for samples prepared at reference conditions (T=60°C, N = 16 rad s-1, t = 30 min)

In general, the viscosity profiles predominantly follow the same trend of a slow initial increase in viscosity, followed by two changes in the rate of viscosity increase, before reaching a peak value. After this point, the viscosity plateaus until the cooling stage commences, where there is another slight peak. However, the rate of viscosity increases and the point at which the system reaches the peak viscosity varies between geometries. The relationship between viscosity and structure formation has been discussed previously in Chapter 3 (Section 3.3).

While they generally follow the same trend, the viscosity measurements for 3D-ANC and TA-HR were significantly greater than for the vane throughout the process, where this can be accounted for by the difference in shear rate constants for the different geometries (Table 4-2). The equivalent shear rate for the same speed was at least three times higher for the vane than the other investigated geometries; thus, for a shear thinning LGN system, the apparent viscosity was lower (Figure 4-2) (Datta *et al.*, 2020). However, it would be expected that the viscosity values for 3D-HR would also be similar to the 3D-ANC based on their similar shear rate constants. The viscosities start at similar values, but around 900 s, the rate of viscosity increase is much slower for the 3D-HR than the 3D-ANC, and the 3D-HR does not achieve the peak viscosity until much later than the rest of the samples (1942 s). The peak viscosities for the vane and TA-HR occur around the same time (1400 s, and 1414 s, respectively), while the peak viscosity for 3D-ANC occurs later (1670 s). If we consider the time of peak viscosity as an indicator of mixing efficiency, the vane and TA-HR are the most efficient, followed by 3D-ANC and then 3D-HR.

For the sample prepared using the TA-HR, after the peak viscosity (t = 1414 s), there are two perturbations in the curve. This behaviour is thought to be associated with when the system became too viscous at the peak viscosity for the TA-HR to mix the fluid properly, as it was visually observed that the material started moving as a solid body in the vessel and this was seen for the other investigated process conditions with the TA-HR geometry. This issue could potentially be resolved using a serrated or roughened cup to reduce slip effects. The shear rate constant for the TA-HR is the lowest for all the geometries investigated (Table 4-2) which means that for the same speed, the least power is inputted into the system in comparison to the other investigated geometries. Mihailova *et al.* (2018) noted a relationship between the torque and power requirements and the surface area of the agitator which is in contact with the liquid, where a larger surface area provides greater resistance to motion, and thus a higher torque response. A similar relationship has been seen in this work, in which the TA-HR has the smallest surface area and smallest power draw, and this is reflected in the value of the shear rate constant (Table 4-2).

The peak viscosity value was lowest for the sample prepared with the vane (0.99 Pa s), as expected due to the difference in shear rate constants previously discussed. However, when comparing the three industrially relevant geometries, the peak viscosity for 3D-HR (2.78 Pa s) was lower than that for 3D-ANC and TA-HR (3.43 Pa s and 3.45 Pa s, respectively). This, in addition to the longer time needed to achieve peak viscosity again, suggests poorer mixing by the 3D-HR geometry than by the 3D-ANC and TA-HR.

Nevertheless, the yield stress of the samples discussed here, prepared at the same processing conditions, were not significantly different ($p > 0.05$; vane = 108 ± 5 Pa; 3D-ANC = 111 ± 1 Pa, TA-HR = 106 ± 11 Pa, 3D-HR = 108 ± 3 Pa).

The energy required to achieve the peak viscosity is similar for the vane and the 3D-ANC, but not for TA-HR (vane = 1.18 J/g, 3D-ANC = 1.18 J/g, TA-HR = 0.327 J/g). Again, this suggests that the TA-HR promotes better mixing than the anchor and the vane and is able to achieve homogeneity with a smaller power input. For the process conditions discussed above, the geometry appears to have minimal effect on the type of structure formed, or the final rheological properties of the system (yield stress) but does affect the mixing characteristics, evidenced by the difference in times to achieve peak viscosity and the inflections in the viscosity-time profile for the TA-HR, in comparison to the other investigated geometries (Figure 4-2).

4.3.2 Effect of specific energy input on LGN formation

In Chapter 3, the conditions which provided the highest yield stress sample were T = 60°C, N = 16 rad s^{-1}, and t = 10 min. Thus, it was hypothesised that a shorter mixing time would also increase the yield stress for the geometries investigated in this study. For the geometries investigated in this study, 83.33% of samples prepared with a 10-min mixing time did not achieve homogeneity, while all samples prepared with a 30-min mixing time did (Figure 4-4). This behaviour was ascribed to insufficient time being provided to achieve adequate mixing of the system and achievement of a peak viscosity before cooling, which will be discussed in more detail later in this section.

Excluding the yield stress values for the inhomogeneous samples, mixing time did have a significant effect on the yield stress of the final samples ($p = 0.0058$), where the mean yield stress was higher for the samples produced with a 10-minute mixing time (149 Pa) than the 30-minute mixing time (114 Pa). This supports the hypothesis in Chapter 3 that a reduced processing time increases the final yield stress of the sample.

Figure 4-3 shows the viscosity profiles for three samples prepared with a 10-minute structuring stage time at two different speeds (vane and 3D-HR at 16 rad s^{-1} and 3D-ANC at 48 rad s^{-1}).

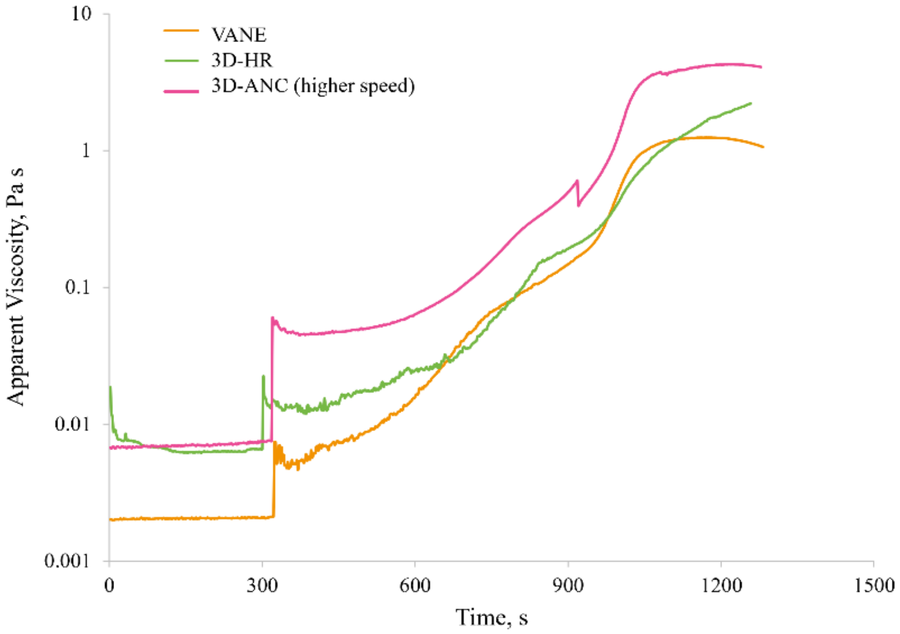

Figure 4-3. Viscosity-time profiles for samples with 10 minute mixing time and different agitator speeds (VANE_60_16_10, 3D-HR_60_16_10, 3D-ANC_60_48_10)

Firstly, examining the vane geometry, the system reached a peak viscosity before the end of the process and had started to plateau. However, for the 3D-HR, the viscosity of the system is still increasing at the end of the processing time and has not stabilised, resulting in inhomogeneous final samples (Figure 4-4). Thus, reducing the mixing time to 10 minutes at the reference speed of 16 rad s^{-1} did not provide increased yield stress as seen for the vane geometry. However, for the 3D-ANC, operated at a higher speed (48 rad s^{-1}), a homogenous sample was achieved, and the yield stress was significantly higher than the average (154 ± 13 Pa). The viscosity profile more closely resembles that of the vane, where the peak viscosity is achieved and has started to plateau before the end of the process. For the vane geometry, the energy input to the peak was 1.24 J/g, and similar for the 3D-ANC, 1.32 J/g (at 48 rad s^{-1}). However, for the 3D-HR, the total energy input is 0.71 J/g. Thus, it can be hypothesised that there is a minimum specific energy input required to achieve the peak viscosity, after which a homogeneous sample is formed. The closer the end of the process to the peak viscosity, the higher the yield stress of the sample. Due to the nature of the fractional factorial design of experiments, data for the 3D-ANC at lower processing speeds and 10-minute mixing time was not conducted. At other processing conditions, the 3D-ANC has outperformed the 3D-HR, however, it is thought that based on the results for the 3D-HR, which possesses a similar shear rate constant (Table 4-2) that the mixing would not be sufficient at 16 rad s^{-1}, 10 mins to produce a homogeneous sample (Figure 4-4). While the energy input is an important factor, it is known from the previous discussion of sample TA-HR_60_16_30 (*cf., 4.3.1*) that it cannot be used to quantify mixing efficiency in these geometries, as the TA-HR is capable of producing similar viscosity profiles and homogenous samples with lower energy inputs than the other investigated geometries. Examples of homogeneity of the samples are provided in Figure 4-4 using the methodology outlined in Section 4.2.4.

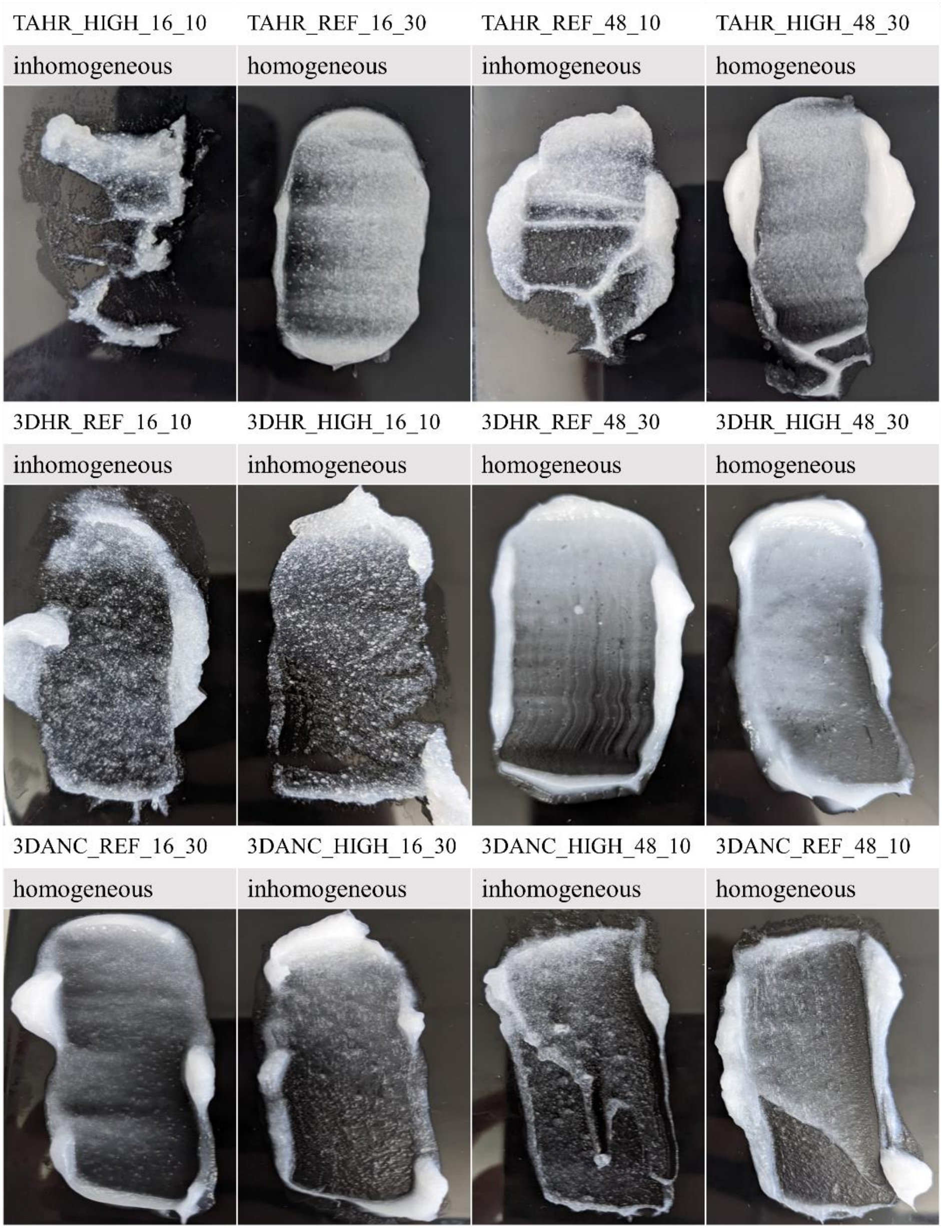
TAHR_HIGH_16_10 inhomogeneous
TAHR_REF_16_30 homogeneous
TAHR_REF_48_10 inhomogeneous
TAHR_HIGH_48_30 homogeneous
3DHR_REF_16_10 inhomogeneous
3DHR_HIGH_16_10 inhomogeneous
3DHR_REF_48_30 homogeneous
3DHR_HIGH_48_30 homogeneous
3DANC_REF_16_30 homogeneous
3DANC_HIGH_16_30 inhomogeneous
3DANC_HIGH_48_10 inhomogeneous
3DANC_REF_48_10 homogeneous

Figure 4-4. Images of samples detailed in Table 4-1 showing the degree of homogeneity, where each sample is categorised as homogenous or inhomogeneous based on number of particulates observed.

4.4 Effect of processing temperature on LGN formation

Viscosity profiles for the vane and 3D-ANC at two different temperatures (T = 60°C and T = 67°C) are shown in Figure 4-5, where the mixing time and agitator speed were the same for each trial, 30 min and 16 rad s^{-1}, respectively. Distinct differences were demonstrated in the rate of viscosity increase during the process due to the dual effect of temperature and mixer type.

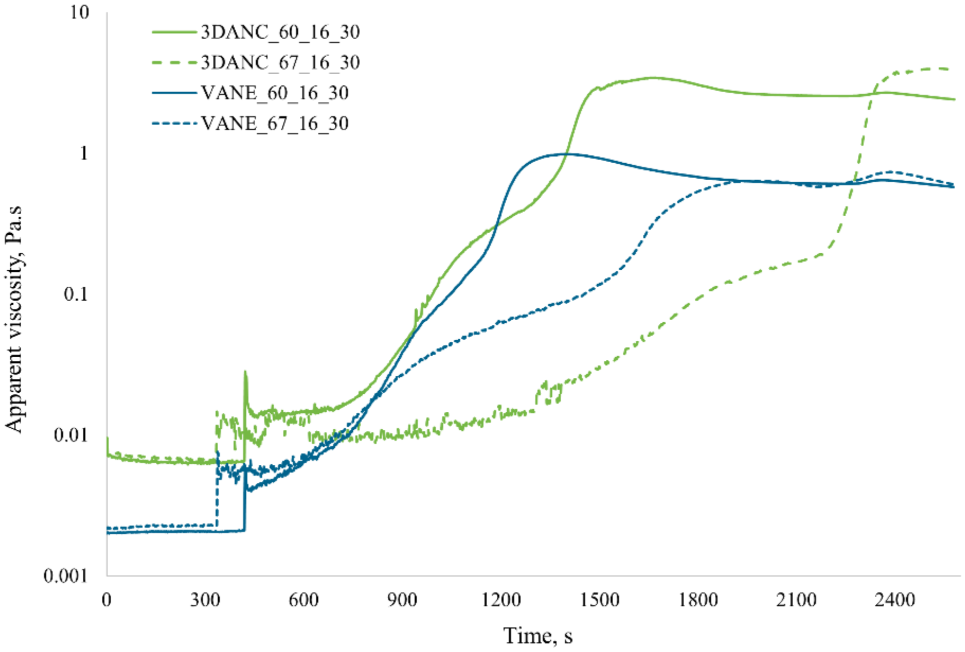

Figure 4-5. Viscosity-time profiles for samples prepared at different temperatures using the vane and 3D-ANC

It is difficult to decouple the temperature effects on the viscosity of the continuous phase vs. the differences in LGN microstructure that are formed. Typically, differences in yield stress of the final sample would give an indication of differences in microstructure formation. For the vane geometry, structure formation occurred at a faster rate when the temperature was at T = 60°C, however, ultimately the final viscosity of the samples was similar for both investigated temperatures (Figure 4-5). This was reflected in the final characteristics of the sample, where the yield stresses were not significantly different ($p > 0.05$; T = 60°C = 108 ± 3 Pa; T = 67°C = 104 ± 5 Pa). A comparison between the 3D-ANC and vane at T = 60°C has already been discussed (*cf., 4.3.1)*; while the apparent viscosity appeared higher for 3D-ANC, the samples had similar final yield stress values, suggesting that this is due to the lower shear rate constant for the 3D-ANC compared to the vane, and the peak viscosity for the 3D-ANC was achieved later, suggesting better mixing in the vane system.

Interesting behaviour was seen for the 3D-ANC at T = 67°C, which did not have repeatable viscosity profiles. In the sample shown here, initially, the apparent viscosity was lower for the 3D-ANC in comparison to the vane, and there were fluctuations in the data until the process achieved the cooling stage (*ca*. 2100 s). At this point, the viscosity of the system drastically increased, and the final apparent viscosity was higher than for the sample prepared at T = 60°C. This correlated with the yield stress of the final product, which was significantly higher for 3D-ANC_67_16_30 (153 Pa s) than the VANE_67_16_30 (104 ± 5 Pa) and 3D-ANC_60_16_30 (111 Pa). However, in another repeat of these conditions (data not shown here), the viscosity did not increase at ~ 2100 s and stayed within the same order of magnitude. This produced a sample, which was not homogeneous, and on visual inspection, a large lump of fats had collected around the central shaft of the agitator. Perhaps the lower viscosity of the system resulted in a tangentially or radially dominant mixing regime which meant the fats were not able to be incorporated properly (Ameur and Kamla, 2020).

4.5 Effect of processing variables on final product yield stress of LGNs

Figure 4-6 shows the range of yield stress measurements for the samples collected for each geometry type for all process conditions, including samples, which were not homogeneous. The differences in means of the yield stresses of the samples produced using each geometry were not significantly different (p = 0.645 using

ANOVA). However, this does not preclude the fact that the geometries perform differently at different process conditions, evidenced by the range of yield stresses, and the fact that the means have been compared across different process conditions.

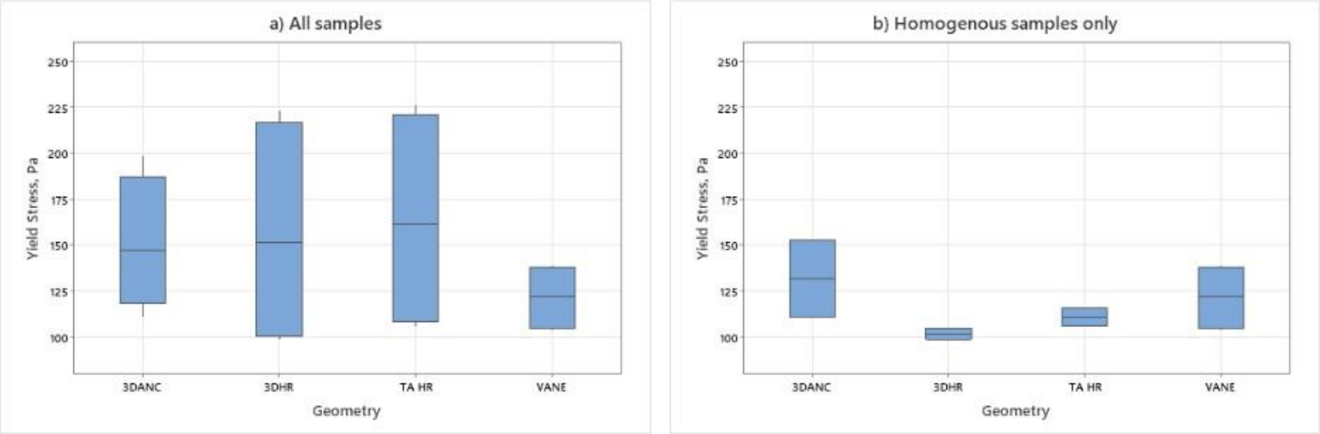

Figure 4-6. Box plot of yield stress measurements of final product samples by geometry type ((a) including heterogeneous samples; (b) excluding heterogeneous samples)

It should be noted that the majority of the high-yield stress measurements were for inhomogeneous samples, and the high value was likely, due to the fact that the LGN microstructure had not been fully formed. The presence of unincorporated solid fatty alcohol and surfactant in the sample causes jamming in the rheometer and affects the measurement. The rheological fingerprint can be used to confirm the lamellar structure of the sample. Figure 4-7 shows an oscillatory amplitude sweep for a homogeneous sample which was processed with a 30-min mixing time. At low strain rates, the storage modulus, G', is orders of magnitude higher than the loss modulus, showing a viscoelastic sample. As strain rate increases, both moduli decrease, showing a shear-thinning sample. The loss modulus, G", exhibits an overshoot prior to the cross-over-point of the moduli, which depicts the breakdown of a cross-linked gel structure. This strongly suggests the presence of lamellar vesicles within the structure (Figure 4-7a) (Youssry *et al.*, 2008; Hyun *et al.*, 2002). Conversely, in Figure 4-7b, there is a smaller difference in the linear region between the loss modulus and storage modulus, suggesting less viscoelasticity, and that the structure is less interconnected (Figure 4-7).

Further analysis of the effect of geometry on yield stress was conducted, excluding the inhomogeneous samples (Figure 4-6b) comparing the mean yield stress for each geometry when samples are prepared at a range of conditions, the 3D-ANC is highest (137 Pa), followed by the vane (122 Pa), TA-HR (111 Pa), 3D-HR (104 Pa). This could be due to the effects of the fractional factorial design, where optimal processing conditions have been randomly selected for certain geometries; but does suggest that generally, the 3D-ANC is capable of producing samples with higher yield stresses. Using a student's t-test, it was also shown that the yield stresses were significantly different for 3D-ANC and 3D-HR ($p = 0.0392$).

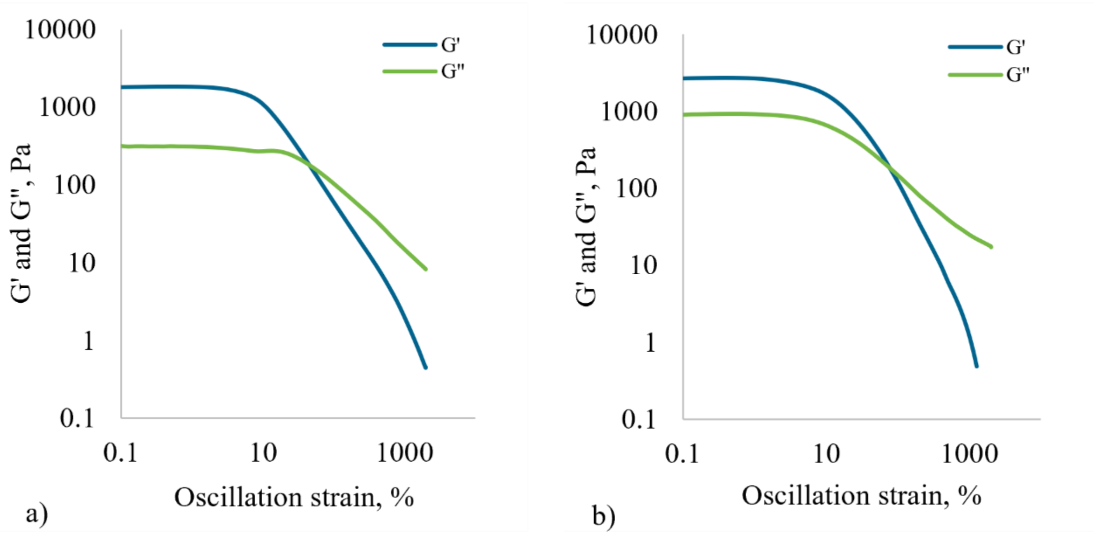

Figure 4-7. a) Oscillation amplitude sweep for 3D-HR_REF_16_30 b) Oscillation amplitude sweep for 3D-HR_REF_16_10

4.6 Conclusions

This study monitored the structure formation of lamellar gel liquids in-situ using a rheometer with different mixing rheometer geometries: conventional four-bladed vane, commercially available helical rotor (TA-HR), and two custom-made geometries, 3D printed in titanium, a helical ribbon (3D-HR) and an anchor scraper (3D-ANC). Viscosity-time profiles as a function of process variables and yield stress measurements on manufactured samples as per design of experiments were used to assess the impact of changing geometry. The results suggested that there were differences in the mixing capability of each investigated geometry, particularly for short processing times. For the 10-min samples prepared at 16 rad s^{-1}, the 3D-HR, and TA-HR were not capable of producing a homogeneous sample, whereas the vane was (3D-ANC was not tested at these conditions due to the nature of the fractional factorial design of experiments). This was likely due to differences in energy input into the system which was related to the shape, mass, and surface area of the rheometer geometry. The two samples with the highest yield stresses (which were homogeneous) were both produced using the 3D-ANC, yet at different process conditions (3D-ANC_67_16_30 = 153 Pa; 3D-ANC_60_48_10 = 141 Pa). The energy input to the peak viscosity for these samples was 1.15 J/g and 1.33 J/g, respectively. Hence, the longer mixing time at a lower speed was more energy efficient for this geometry. Overall, the industrially relevant geometries did not follow the same trends as the vane geometry, highlighting the importance of investigating how the mixing characteristics are affected by the interplay between geometry and processing conditions. The next steps for this work are to utilise the information collected to generate information around the power requirements of each type of geometry, and how this could be optimised to produce an LGN which is homogenous, achieves peak viscosity efficiently, and possessing a high-yield stress, with the lowest possible energy consumption. Power numbers for the geometries will be generated to determine the usefulness of this technique in scale-up. Overall, the application of industrially relevant geometries has provided a better insight into how the combination of processing conditions and geometry can result in different mixing characteristics within the vessel, and the resulting impact on the product characteristics.

CHAPTER 5: INVESTIGATING MIXER-VISCOMETER TECHNIQUES FOR PARTIALLY FILLED STIRRED TANKS

Adapted from Cunningham, G.E.; Deshpande, S.; Simmons, M.J.H.; O'Sullivan, J.J. (2023). Investigating mixer-viscometer techniques for partially filled stirred tanks. *Chemical Engineering Science, 282*, *119340.*

5.1 Introduction

The design and manufacture of formulated products is a major value-adding step, increasing the value of the constituent raw materials by up to two orders of magnitude. Furthermore, the estimated global market for formulated products is around €1.4 trillion (Centre for Process Innovation, 2018; Sunkle *et al.*, 2020). In efforts to make economic and environmental benefits, global manufacturers are driven to optimise resources such as raw materials and energy, where the manufacturing process plays a pivotal role.

The manufacture of formulated products typically involves a batch mixing stage, where raw materials are introduced to the vessel in a particular order and rate of addition, with controlled temperature profiles, mixing profiles, and other process conditions to attain optimal product structure. Mixing is a complex process which is not easily described, and many techniques have been developed to try and characterise mixing more meaningfully (Bowler *et al.*, 2020). With Industry 4.0 gaining more relevance in manufacturing settings, companies are looking for cost-effective, simple measurement techniques that can be implemented on existing processes to enable process optimisation. Novel sensing technologies, whilst promising, often pose challenges due to expense and implementation barriers, particularly in industrial applications. An alternative approach involves using well-established sensors to monitor variables such as temperature, torque, pressure and flowrate, and implementing these into physical and data-driven models to infer difficult to measure variables, referred to as 'soft sensors' (Vieira *et al.*, 2015). For example, Vieira *et al.* showed how temperature, flow rate and pressure sensor data can be inputted into a combination of physical models and artificial neural networks (ANNs) to model a spouted bed dryer to control the moisture content of milk powder during drying (Vieira *et al.*, 2015).

The measurement of the torque on the agitator shaft is an ideal candidate for use in mixing process models (Bowler *et al.*, 2020). For example, it enables the calculation of power per unit volume for use in scale-up, or in cases where a defined energy input is required to control product quality, power can be integrated with time (Xu *et al.*, 2017; Altuna *et al.*, 2016b). Furthermore, in the laminar mixing regime, torque-speed data can also be used to infer viscosity. This is particularly beneficial in systems where the rheology is evolving during the manufacturing process and is related to the product structure (Bowler *et al.*, 2020). However, there are limitations to the conditions where torque can be accurately measured, including sensitivity to changing environmental conditions which are inseparable from the manufacturing process, such as temperature, agitator speed, mixing regime, batch fill level and fluid rheology (Knight *et al.*, 2001). Nevertheless, as one of the most economical and simple techniques, researchers have developed numerous ways to characterise mixing systems and transform torque-speed data into viscosity-shear rate data, such as the power curve and torque curve method (Castell-Perez and Steffe, 1990), slope method (Rieger and Novak, 1973), and Couette analogy (Ait-Kadi *et al.*, 2002).

The basis of all mixer-viscometry techniques is to characterise the mixer in terms of the mixer constant, *k'*, which relates the impeller speed to the shear rate, and mixer coefficient, *k"*, which relates the torque to the viscosity - analogous to the shear rate constant and stress constant in rheometry. The characterisation of mixing systems can be simplified by developing correlations between dimensionless numbers. For Newtonian fluids in the laminar regime, the following relationship exists:

$$Po = K_P \, Re^{-1} \tag{5-1}$$

Where, Po is the dimensionless Power number (-), Re is the dimensionless impeller Reynolds number (-), and K_P *is the laminar power constant (-).*

Metzner and Otto expanded this relationship to non-Newtonian fluids by assuming the Newtonian viscosity term in the Reynolds number can be equated to the apparent non-Newtonian viscosity at a corresponding effective shear rate (Metzner and Otto, 1957). For example, for a power law fluid:

$$\mu = \eta = K(\dot{\gamma}_{av})^{(n-1)} \tag{5-2}$$

Where μ *is the Newtonian viscosity (Pa s),* η *is the apparent non-Newtonian viscosity (Pa s) at the effective shear rate,* $\dot{\gamma}_{av}$ *(s^{-1}), K is the consistency index (Pa s^n), n is the flow index (-).*

The effective shear rate is related to the impeller speed by:

$$\dot{\gamma}_{av} = k'N \tag{5-3}$$

Where N is the impeller speed and k' is the mixer constant, also known as the Metzner-Otto constant.

An alternative approach to the matching viscosity methods is the use of the Couette analogy (Ait-Kadi *et al.*, 2002). The method equates the rheometer mixing geometry and vessel to a coaxial cylindrical bob rotating inside another cylinder (a Couette geometry), where the Couette analogue gives the same torque measurement as the agitator when at the same speed (Ait-Kadi *et al.*, 2002).

Both the matching viscosity methods and the Couette analogy have been studied for various geometries and rheological properties. There is a lot of discussion in the literature about the effects of geometry, method, fluid rheology, and agitator speed on k'. The complexity of both the geometries utilised in mixer rheometry and the rheology of the fluids being measured leads to inconsistent conclusions. Despite the initial findings of Metzner and Otto suggesting k' might be independent of fluid rheology, it is now generally accepted that k' is dependent on the flow index of fluids when $n < 0.4$ (Bbosa *et al.*, 2017; Brito de la Fuente *et al.*, 1997; Mackey *et al.*, 1987). However, there are conflicting opinions on how k' changes with flow index as it is difficult to decouple the effects from other rheological properties, *e.g.,* viscoelasticity and agitator speed (Castell-Perez and Steffe, 1990; Carreau *et al.*, 1993).

Most attention has been focused on the effects of varying fluid rheology (Anne-Archard *et al.*, 2006), geometry (impeller to cup ratios) (Brito de la Fuente *et al.*, 1997), and rotational speed (Castell-Perez and Steffe, 1990); however little attention has been given to the effects of the fill level. Given that batch processes involve incremental ingredient additions, it would be useful to understand the effects of fill level on torque and viscosity. Sulaiman *et al.* (2012) investigated the effect of fill level when using the torque curve method when the fill level was higher than the height of the agitator but didn't consider partial fill levels. They found that the mixer coefficient, k'', and mixer constant, k', had a power-law relationship as a function of fill height, and that a fill height equal to 1.5 times the height of the impeller gave the most accurate results for estimations of K and n. The study only investigated one type of paddle type agitator, with a small gap between the agitator and the vessel (d_i, impeller diameter/ D_c, cup diameter = 0.98).

In order to successfully implement online viscosity measurement into batch mixing processes with evolving fill level and rheology, it would be interesting to see if traditional mixer-viscometer techniques are suitable for partial fill levels and fluids with a range of rheological behaviours. Therefore, in this work, a rheometer with a helical ribbon mixing geometry has been used to collect torque-speed data at different speeds, batch fill levels, and for fluids with different rheology. Two different approaches to determine the viscosity from torque-speed data have been selected to determine if a particular method has better suitability for low fill levels. A range of fluids with various rheological properties have been selected, with the aim of covering the range of properties which might be seen during the manufacture of formulated products. This includes a range of consistency indexes and flow indexes, as well as some fluids which show viscoelasticity and possess a yield stress. Similarly, the fill levels have been varied from 25% to 100% to represent the range seen during a batch manufacturing process. The novelty of this work is the extension of typical mixer-viscometer techniques to partial batch fill levels and correlating the success of these methods to the unprocessed torque-speed data to determine the limits for these methods in practical applications. Hence, the objectives of this study are (i) to study the effect of process variables, namely fluid rheology and batch fill level on torque measurement, and (ii) to determine how the mixer constant and mixer coefficient, and consistency index and flow index calculated using various mixer-viscometry techniques differ with the aforementioned variables. This will inform decisions on whether either of the methods investigated could be used in a practical application to infer viscosity from torque-speed data during a batch mixing process where the fill level is changing.

5.2 Materials and Methods

5.2.1 Materials

Three non-Newtonian fluids with distinct rheological behaviours were studied: Carbopol® solution (CP), xanthan gum, glycerine and water solution (XG), and a lamellar gel network (LGN). Formulations and rheological properties are given in Table 5-1. The flow and consistency indices of the non-Newtonian fluids were determined by measuring the steady state apparent viscosity over a range of shear rates (10 – 500 s^{-1}) using a Couette or cross-hatched parallel plate geometry and fitting the data to the Ostwald-de Waele power-law model (Eq. 5-4).

$$\tau = K\dot{\gamma}^{n} \text{ or } \eta = K\dot{\gamma}^{n-1} \tag{5-4}$$

This is a simplification which can be satisfactorily applied in the shear rate range investigated, as the mixer-viscometer techniques which have been applied are most commonly based on power-law fluids. However, it does not account for the other complex rheological properties of the fluids and this will be considered in the discussion. LGNs over a larger shear range are more typically fitted to a Herschel-Bulkley model, where the fluid possesses a yield stress. The XG solution was also found to demonstrate viscoelastic behaviour which has not been accounted for in any calculations. Glycerine was the Newtonian fluid used for calibrating geometries (Palmera G995E; 99.5% purity, supplied by KLK Oleo; viscosity 0.56 Pa s @ 30°C; density 1260 kg m^{-3} @ 30°C).

Table 5-1. Formulations, consistency indices and flow indices of non-Newtonian fluids investigated

Fluid	**Formulation (w/w%)**		**Consistency index, K (Pa s^n)**	**Flow behaviour index, n (-)**	**Density (kg m^{-3})**
Carbopol® solution (CP)	Carbomer powder[a]	1.5%	76.4±7.2	0.29±0.08	997
	Water	98.5%			
Xanthan gum solution (XG)	Xanthan Gum[b]	5%	36.6±7.7	0.25± 0.~~025~~03	1067
	Glycerine[c]	20%			
	Water	75%			
Lamellar gel network (LGN)	Cetearyl alcohol[d]	7.06%	186.0±6.6	0.135± 0.~~075~~08	880
	Behentrimonium Chloride (BTAC)[e]	2.35%			
	Water	90.59%			

a) Carbopol® 980 polymer (supplied by Lubrizol), b) Xanthan gum (supplied by Jungbunzlauer (Basel, Swizterland)), c) Palmera G995E; 99.5% purity, supplied by KLK Oleo, d) cetyl alcohol (30 wt%) and stearyl alcohol (70 wt%), (Godrej Industries (India)), e) behentrimonium trimethyl ammonium chloride (BTAC), supplied by Clairant International Ltd. (Germany). This surfactant is provided at 70 wt% purity, where the remaining 30 wt% is comprised of dipropyl glycol, which acts as a processing aid.

5.2.2 Experimental Design

A Discovery Hybrid Rheometer III (TA Instruments, UK) was used to collect torque data over a range of tip speeds, *i.e.,* the tangential velocity of the impeller at its outermost point (0.125 m/s – 1.5 m/s). The rheometer was operated at each speed for 2 min, and an average of the data from the final minute was used in calculations to ensure the system had achieved steady state. Temperature was maintained at 30°C. Three fluid fill levels were investigated (25%, 62.5%, 100%). ‘100% fill level’ signifies the fill height of the fluid in the vessel is equal to the height of the impeller. The mixer geometry used is a 3D printed helical ribbon (HR) printed using direct metal laser sintering of titanium conducted by Laser Prototypes Europe Ltd (UK). The geometric considerations for the bespoke mixing element were based on representative examples found within mixing equipment (Figure 5-1; Table 5-2).

Figure 5-1. 3D printed helical ribbon (HR)

Table 5-2. Dimensions of mixer rheometer geometries

Mixer geometry dimensions	
Height, mm	36
Diameter, mm	31
Rheometer cup dimensions	
Height, mm	50
Diameter, mm	34
Other dimensions	
Gap between bottom of agitator and cup, mm	0.5

As well as using a rheometer to measure torque, a transparent version of the vessel was set up to enable visualisation of the fluid (Figure 5-2). A vessel of the same diameter as the rheometer cup was constructed from PVC and placed inside a PVC cube, filled with water, to prevent any distortion. An overhead mixer (Heidolph RZR 2021, Heidolph Instruments GmbH & Co. KG, Schwabach, Germany) was used to rotate the agitators over the total range of speeds. Video at 60 fps was collected for 5 seconds at each speed. Still images were randomly collected from the videos in post-processing.

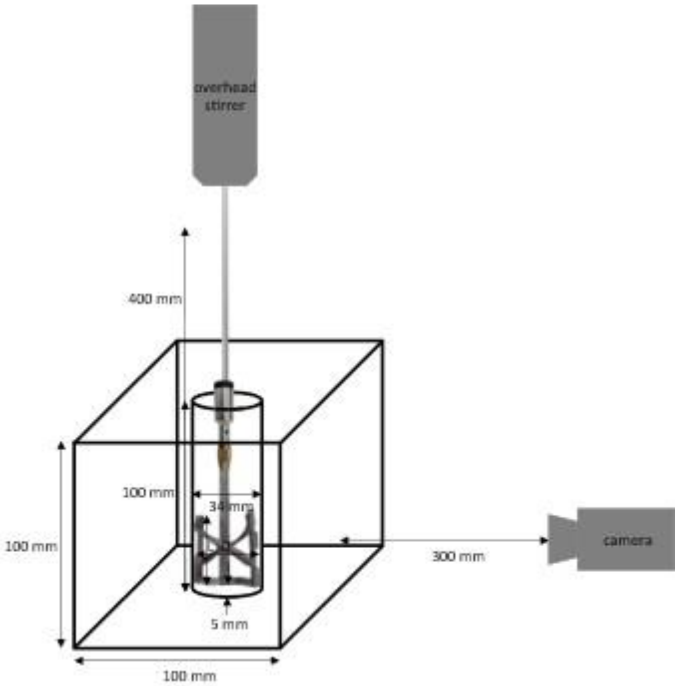

Figure 5-2. Schematic of transparent version of rheometer set up with overhead stirrer, vessel and mixer geometry

5.2.3 Mixer-Viscometer Methods

Torque Curve Method

The torque curve method was developed by Mackey *et al.* (1987) to investigate the effects of different factors on the mixer constant, *k'*. For example, Sulaiman *et al.*

(2012) used this method to find *k'* and *k"* as a function of fill height. By substituting in the definitions of the Power number and Reynolds number, Eq. 5-1 can also be expressed as:

$$\frac{P}{\rho\, D^5 N^3} = \frac{K_P \mu}{D^2 N \rho} \tag{5-5}$$

Where P is power consumption (W), ρ is the fluid density (kg m^{-3}*), D is diameter of the impeller (m), N is the impeller speed (rps), μ is viscosity (Pa s) and* K_p *is the laminar power constant.*

Given that power consumption, P, is a product of torque and angular velocity (P = M Ω), Eq. 5-5 can be further rearranged and simplified to give an equation for viscosity as a function of torque, speed and a constant, *k"*, the mixer coefficient:

$$\mu = \frac{M}{Ad^3 N} = \frac{k''M}{N} \tag{5-6}$$

Where M is torque (N m), A is a constant which is a product of the laminar power constant, K_P*, and 2π (which relate angular velocity rad s*$^{-1}$ *to impeller speed, s*$^{-1}$*).*

By measuring torque-speed data for Newtonian fluids of known viscosity, *k"* can be determined. To find the mixer constant, k_γ, the apparent shear rate is determined at several speeds using a reference non-Newtonian fluid, typically a power-law fluid which has been characterised using conventional measuring techniques. $\dot{\gamma}_{av}$ is plotted against speed (*angular velocity, Ω, or N, rps)* and the gradient of the plot gives a value for *k'*. First, the matching viscosity assumption is applied:

$$\mu = \eta = K(\dot{\gamma}_{av})^{(n-1)} \tag{5-7}$$

Combining Eq. 5-6 and Eq. 5-7 gives an expression for the shear rate in terms of the mixer coefficient, torque, and speed:

$$\frac{k''M}{\Omega} = K(\dot{\gamma}_{av})^{(n-1)} \tag{5-8}$$

Rearranging Eq. 5-8, the average shear rate can thus be expressed as:

$$\dot{\gamma}_{av} = \left(\frac{k''M}{\Omega K}\right)^{\frac{1}{n-1}} \tag{5-9}$$

Once *k'* and *k"* are determined, the apparent viscosity of new fluids can be determined from Eq. 5-7.

Couette Analogy

An alternative approach to the matching viscosity methods is the use of the Couette analogy (Ait-Kadi *et al.*, 2002). The method equates the rheometer mixing geometry and vessel to a coaxial cylindrical bob rotating inside another cylinder (a Couette geometry), where the Couette analogue gives the same torque measurement as the agitator when at the same speed (Choplin and Marchal, 2010). First, the equivalent Couette radius needs to be determined, using Eq. 5-10:

$$R_i = \frac{R_e}{\left(1 + \frac{4\pi N}{n}\left(\frac{2\pi\mu L R_e^2}{M}\right)^{1/n}\right)^{n/2}} \tag{5-10}$$

Where R_i is the equivalent Couette radius of the geometry (m), R_e is the radius of the vessel (m), and L is the length of the impeller (m). Ait-Kadi *et al.* (2002) found that the equivalent Couette radius was only slightly dependent on the flow index, *n*, thus it can be evaluated using a Newtonian fluid or well-characterised power law fluid. The shear rate and shear stress vary in the gap between the geometry and the cup as a function of radius, *r*, and fluid rheology, namely the flow index, *n*. At a given radius, the shear rate is nearly independent of the flow index of the fluid – the optimal radius, *r**. For geometries where there is a small gap between the equivalent Couette radius, R_i, and the radius of the cup, R_e, ($R_i/R_e > 0.9$), the optimal radius can be taken as $r^* = R_i + R_e/2$. However, in cases where the gap is large, *r** must be found through graphical or analytical methods, *e.g.,* plotting calculated shear rate at different radii for various values of the flow index, *n (Ait-Kadi et al., 2002; Novontá et al., 2001).* The radius at which the calculated shear rate values cross over, *i.e.,* are the same value for all flow indices is taken as *r** (Figure 5-3). If the range of flow indices that must be covered is large, as in the case of this study, (n = 0.05 – 0.3), there may not be a single point at which the shear rates are equal for all flow indices. Some authors have used different radii for different ranges of flow indices *e.g.*, 0.05-0.1, 0.1-0.3 (Novontá *et al.*, 2001). However, this is impractical in cases where the fluid rheology is not known. In this work, where there is not a single point, the cross-over value which was applicable over the largest range was used. The shear rate, $\dot{\gamma}_{av}$, and shear stress, τ (Pa), are then calculated from the below equations at the optimal radius, *r*, (Eq. 5-11 and 5-12).* Apparent viscosity is determined from a plot of shear rate *vs*. shear stress.

$$\dot{\gamma}_{av} = \frac{\frac{4\pi N}{n}\left(\frac{R_i}{r^*}\right)^{2/n}}{1-\left(\frac{R_i}{R_e}\right)^{2/n}}.N = k'N \tag{5-11}$$

$$\tau = \frac{M}{2\pi L {r^*}^2} \tag{5-12}$$

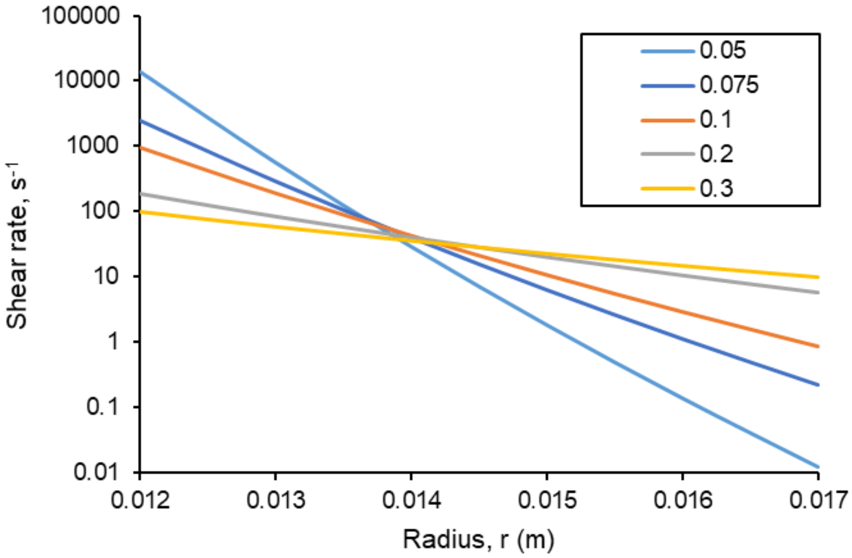

Figure 5-3. Shear rate as a function of radius, r, and flow index, n (when Ω = 1 rad s^{-1}). Using R_i = 0.01326m, calculated using CP as calibration fluid

5.2.4 Data Analysis

Torque values were studied as a factor of fluid fill level and rheology. In order to determine the suitability of mixer-viscometer techniques at fill levels less than 100%, two different methods were applied to convert torque-speed data to apparent viscosity – the torque curve method (TCM), (Mackey *et al.*, 1987; Castell-Perez and Steffe, 1990) and the Couette analogy (CA)(Ait-Kadi *et al.*, 2002). For the TCM, the mixer constant, *k'*, has first been found using each non-Newtonian fluid as the reference fluid to determine the impact of rheology for the systems studied here. Then, the constants for the CP fluid have been used to calculate the apparent viscosity and average shear rate for each fluid, as CP showed the least deviation in *k'* between methods at 100% fill level, and most closely follows the behaviour of power-law fluid. Plots of apparent viscosity versus average shear rate were used to determine the consistency and flow index (*K* and *n*). In the Couette analogy, the effects of fluid rheology on the equivalent Couette radius, R_i, optimal radius, r^*, and mixer constant, k', were first investigated by using each fluid to determine the values, and then compared to the findings of Ait-Kadi *et al.* for the 100% fill level (Ait-Kadi *et al.*, 2002). The values for the Newtonian fluid, glycerine, have been applied to find the apparent viscosity and shear rate for each fluid, and thus K and n.

5.3 Results and Discussion

5.3.1 Effects of fill level on torque measurement

Newtonian fluid

The average torque values for the Newtonian fluid, glycerine, at different tip speeds are given in Figure 5-5. Torque was measured across three fill levels: 25%, 62.5%, 100%. A linear increase in torque with tip speed was observed at all fill levels ($R^2 = 0.99$), aligning with anticipated Newtonian fluid behaviour (Bbosa *et al.*, 2017). Additionally, torque increased incrementally as a function of fill level, a trend congruent with results for granular high shear systems (Knight *et al.*, 2001). Greater variability in measurements was seen at lower fill levels, attributed to the increased void in the vessel, allowing greater variability in the fluid-impeller contact. Whilst the variability also appears larger at higher speeds, the percentage deviation was proportionate across all speeds.

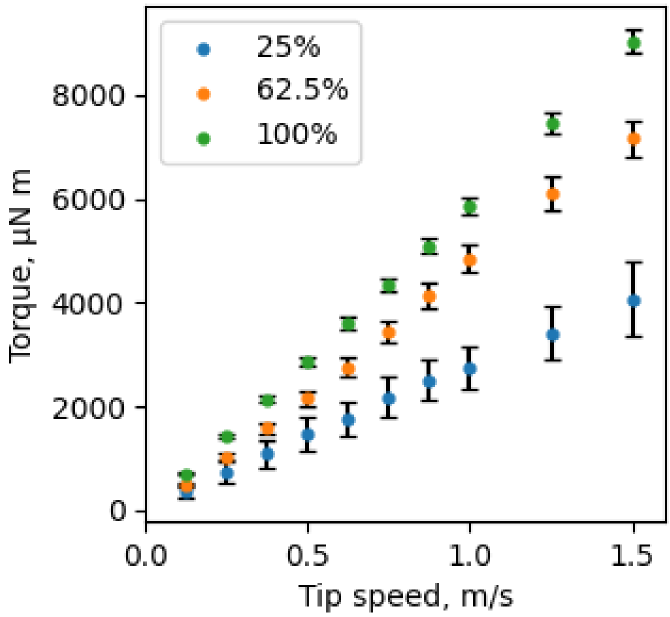

Figure 5-5. Torque as a function of tip speed for glycerine at three fill levels (25%, 62.5%, 100%)

Figure 5-4 shows the Power number calculated using the Newtonian torque data versus Reynolds number for all investigated fluid fill levels. The plots were fitted using regression to Eq. 5-1. to determine the power constant, *Kp*.

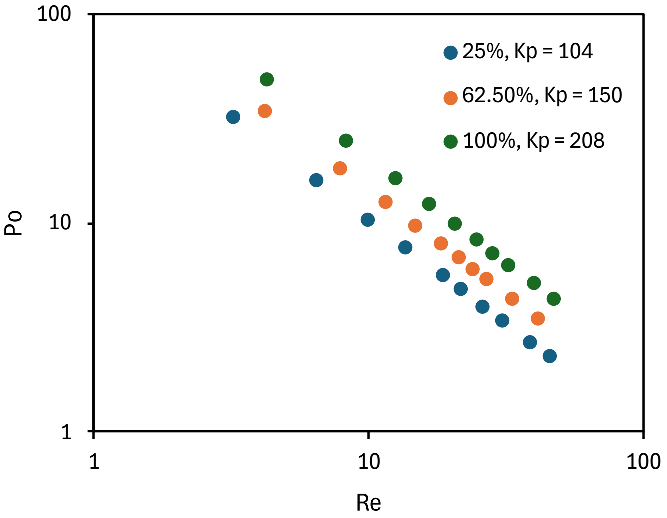

Figure 5-4. Power curves for investigated fill levels, 25%, 62.5%, 100% determined using glycerine

For the range of speeds investigated, corresponding to a maximum Reynolds number of ~33, glycerine remains in the laminar mixing regime for all fill levels, which is typical for close clearance scrapers operating up to these Reynolds numbers (Brito de la Fuente *et al.*, 1997). The laminar power constant, *Kp*, increases as a function of fill level, and is in the range of 104-208, which is in agreeance with literature values, which have been reported around 100-400 for close clearance scrapers at 100% fill level (Jo *et al.*, 2017; Rudolph *et al.*, 2009).

Non-Newtonian fluids

Figure 5-6 shows torque-speed plots for three non-Newtonian fluids across all investigated fill heights (25%, 62.5%, 100%). The degree of linearity between torque and tip speed for non-Newtonian fluids is less than for the Newtonian fluid (*c.f.,* Figure 5-5).

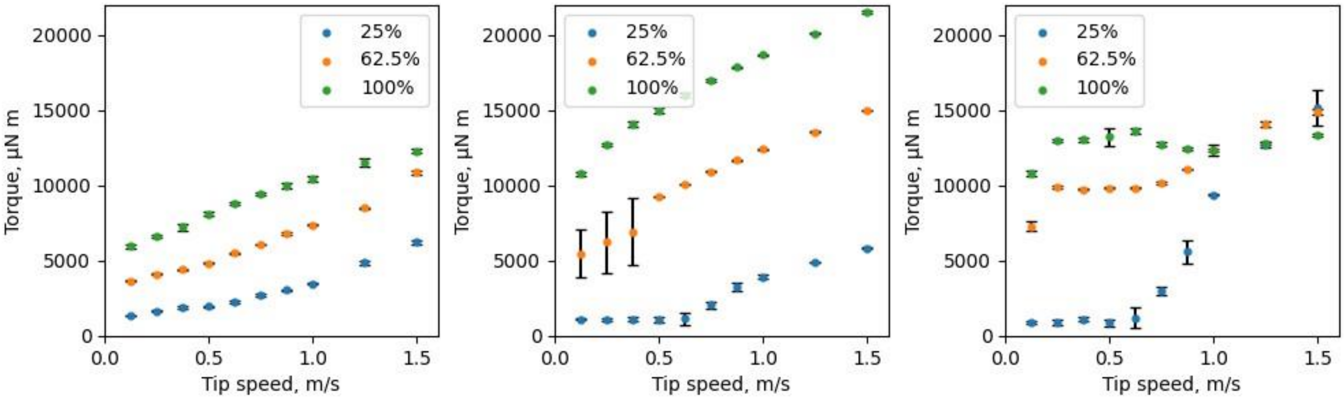

Figure 5-6. Plots of torque vs tip speed for non-Newtonian fluid. From left to right, fluids: a) XG, b) CP, c) LGN

Of the three non-Newtonian fluids, XG displayed behaviour most like the Newtonian fluid (Figure 5-6a). However, a notable difference is that the torque does not intercept at zero. This trend was observed across all non-Newtonian fluids and is attributed to factors such as the fluids approaching a zero-shear viscosity plateau at very low shear rates or possessing a true yield stress. Thus even at low tip speeds a significant torque response is measured (Larson, 1999; Castell-Perez and Steffe, 1990). XG exhibits the lowest torque values of the non-Newtonian fluids, corresponding with its lowest consistency index, *K.* In general, the higher viscosity of the non-Newtonian fluids reduced torque variability at each speed compared to the Newtonian fluid (*c.f.,* Figure 5-5).

In the cases of CP and LGN, the torque response exhibited more variability as a function of tip speed and fill level. For CP at 100% fill level (Figure 5-6b), the torque response generally increases linearly with speed, whilst for LGN (Figure 5-6c), a clear trend is absent. Torque initially increases to a maximum around 0.625 m/s, before decreasing and then slightly increasing again. The reduction in torque is attributed to air incorporation, reducing fluid density, whilst the subsequent rise potentially indicated a transition to turbulent or transitional regimes necessitating higher energy consumption due to increased radial and axial velocity flow components (Bbosa *et al.*, 2017; Rahimzadeh *et al.*, 2022).

For CP at 62.5% fill level, there is a large variation in the torque response recorded for the first three tip speeds, which could be related to the high viscosity of the fluid (Figure 5-6b). It is likely that at lower tip speeds, not all of the fluid is engaged in flow, evidenced by visual inspection of the fluid in the vessel (Figure 5-7)(Bbosa *et al.*, 2017). For LGN at 62.5%, again the torque does not follow the expected trend, and there is little change in torque with tip speed up until 0.5-0.625 m/s (Figure 5-6c). Above this speed, there is a steep increase in torque as a function of tip speed.

Similarly, for both CP and LGN at 25% fill level at lower tip speeds, the torque response remains steady up until 0.5-0.625 m/s, when torque starts to drastically increase with tip speed (Figure 5-6b and c). Analysis of images collected in the transparent system showed that at lower tip speeds, the fluid is mostly gathered centrally in the centre of to the agitator. Above 0.5 m/s, the velocity of the agitator causes the fluid to be propelled off the agitator and to the walls of the geometry, so less fluid is in contact with the agitator, and more fluid is located in the gap between the impeller and the wall. This increases the resistance of the impeller to force, increasing the torque required to achieve a given speed (Figure 5-7).

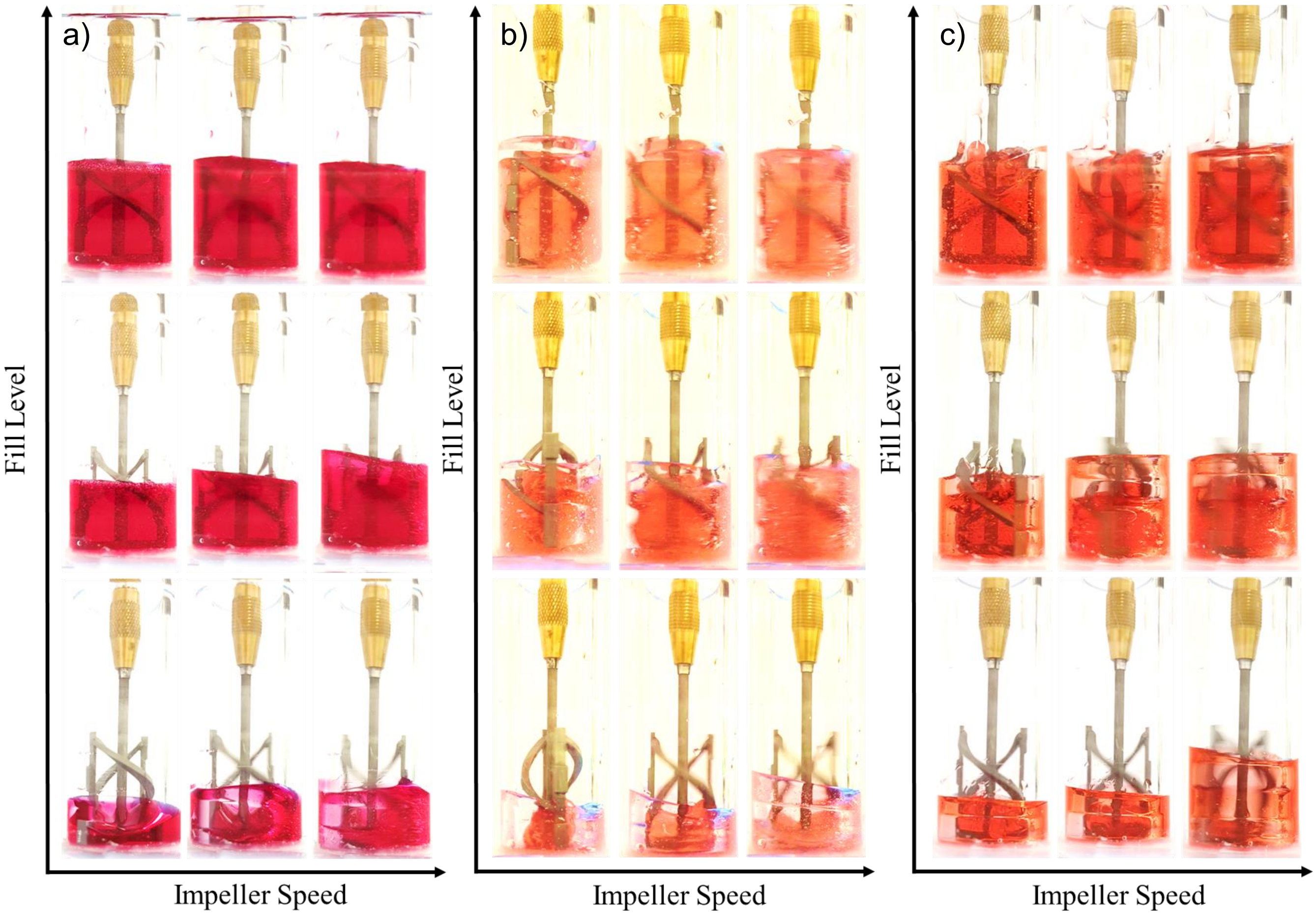

Figure 5-7. Images from transparent set up showing a) GLY, b) XG and c) CP being mixed at 0.125 m/s (Fr = 0.05), 0.5 m/s (Fr = 0.82), 1 m/s (Fr = 1.8) at three fill levels, 25%, 62.5%, 100% (LGN not included as non-transparent)

To attempt to quantify the point at which this transition from the 'bunched' flow regime to the 'centrifuged' state, the system was characterised by the Froude number. The Reynolds number was also considered to characterise the system but is difficult to determine at partial fill levels and requires knowledge of the apparent viscosity of the system. The Froude number was selected as it signifies the point at which vortex formation occurs. When Fr<1, flow is subcritical, and no vortex is present. At Fr=1, this signals the onset of vortex formation. When Fr>1, flow is supercritical, meaning that for a n unbaffled vessel, a vortex will form. The Froude number equation for a stirred tank is given in Eq. 5-13.

$$Fr = \frac{v^2}{g\ D} \tag{5-13}$$

Where, Fr is the dimensionless Froude number, v is the velocity of the fluid (m s^{-1}) (tip speed for stirred vessel), g is gravity (m s^{-2}), and D is the diameter of the impeller (m).

The Froude number was calculated for each speed and was found to first be greater than unity at 0.625 m/s (Fr at 0.5 m/s = 0.82, Fr at 0.625 m/s = 1.13). Figure 5-7 shows how the position of fluid in the vessel and the impeller-fluid contact changes with impeller speed, and therefore Froude number, for GLY, XG and CP. The difference in behaviour between the Newtonian fluid and non-Newtonian fluids is most apparent at the lower fill levels. For the Newtonian fluid, the fluid does not bunch around the centre of the impeller and maintains contact with more of the impeller even at greater speeds. Whilst for XG and CP, there is a transition from bunched to centrifuged when Fr<1, particularly at the lower fill levels. Using image analysis alone it is difficult to fully characterise the flow regimes. PIV or other flow visualisation techniques may be useful for further characterising the systems in the future. However, the purpose of this work is to determine the suitability of mixer-viscometer techniques to partial fill levels. When considering the suitability of mixer-viscometer techniques, the Froude number was considered as a possible limitation for where the techniques can be appropriately applied.

5.3.2 Comparison of techniques at 100% fill level

Effect of mixer-viscometry method and fluid rheology on mixer constant, k', at 100% fill level

The first step in assessing the suitability of mixer-viscometer techniques for partially filled vessels was to determine the effects of fluid rheology on the value of *k'* at 100% fill level. Other authors have previously investigated the impact of fluid rheology and mixer-viscometry method on *k'* at normal fill levels so a detailed analysis will not be provided here (Castell-Perez and Steffe, 1990; Ait-Kadi *et al.*, 2002; Bbosa *et al.*, 2017). However, previous work has shown that the effects are dependent on system geometry and rheology, so it is important to understand how *k'* varies for this system. *k'* was calculated using the two methods discussed: torque curve method (TCM), and Couette analogy (CA). Table 5-3 shows the mixer constant calculated using both methods.

Table 5-3. Mixer constant calculated using CA and TCM using different calibration fluids

Fluid	k'_{CA} (-)	k'_{TCM} (-)
GLY	3.90	-
XG	9.17	1.74
LGN	5.71	3.44
CP	5.79	3.13

It is not possible to calculate k'_{TCM} using only a Newtonian fluid, so no comparisons to k'_{CA} can be made for GLY. The largest difference in *k'* between the two methods was for XG, whilst the results for LGN and CP were in closer agreeance (CV =

25-30%, respectively). Furthermore, for each respective method, the values calculated for CP and LGN were similar to each other (Table 5-3). XG did exhibit viscoelastic behaviour, which helps to explain the discrepancies in k' compared to the other fluids. There have been several attempts to determine the impact of elasticity on the torque measured for complex geometries such as helical ribbons, but a consensus has not been reached. Carreau *et al.* (1993) and Collias and Prud'Homme (1985) found that elasticity increased the torque measurements, whilst Rieger and Novak and Ulbrecht and Carreau were incongruent (Rieger and Novak, 1974; Ulbrecht and Carreau, 1985). Ultimately, the effects of elasticity are dependent on the geometry, operating conditions and other fluid rheological behaviours (Carreau *et al.*, 1993; Jahangiri, 2008).

The values for k'_{TCM} determined using LGN and CP were closest to k'_{CA} determined using the Newtonian fluid. Considering all cases, there was greater variation in k' due to the method used than the calibration fluid used, which was also seen by Bbosa *et al.* (2017). Castell-Perez and Steffe found for the TCM that in general, higher values of n, and lower values of K, gave higher values of k' (Castell-Perez and Steffe, 1990). XG and LGN followed this trend, it would be expected that CP had a k' value between XG and LGN. This said, it was difficult to decouple other rheological properties, and the regression analysis required for the TCM contributes to errors. Furthermore, their study was based on paddle agitators, and the geometry also impacts the observed trends in k'.

Overall, at 100% fill level, both methods gave values for k' which were in agreement with literature values for similar geometries (Brito de la Fuente *et al.*, 1997), with the values for k' calculated using CP and LGN being in good agreement but using

XG showing discrepancies, likely due to its viscoelastic behaviour. Furthermore, the CA generally gave higher values for *k’* than the TCM, also seen by Bbosa *et al.* (2017).

Effect of mixer-viscometry method on determination of K and n

Using the methods described in 5.2.3, the mixer constant, *k’,* and mixer coefficient, *k’’,* were applied to the torque-speed data to approximate the shear rate and apparent viscosity for each fluid. For CA, *k′* and *k″* determined using the Newtonian fluid, GLY, were used. For TCM, where it is not possible to determine *k’* with a Newtonian fluid, the value determined using CP was used (Table 5-3). The consistency and flow index, *K* and *n*, respectively, are determined from fitting a plot of apparent viscosity as a function of shear rate to the Ostwald-de-Waele equation (Eq. 5-1). Therefore, the flow and consistency index can vary with the shear rate range over which they are (i) measured, and (ii) fitted to the Ostwald-de-Waele power law model (Chhabra, 2010). Table 5-4 shows the consistency indices, *K*, and flow indices, *n*, calculated for the investigated fluids for each method**.** The data in Table 5-4 shows that both the CA and TCM are suitable for determining the apparent viscosity and shear rates of the range of fluids investigated here when the fill level is at 100%. *K* and *n* are in good agreement to when measured using conventional geometries (cross-hatched parallel plates). Any discrepancies between the methods can be explained by the typical errors in measuring *K* and *n* using conventional methods (~5%) and in the methods themselves *e.g.,* due to regression fitting.

Table 5-4. Consistency index, K, and flow index, n, determined for all fluid and fill levels using conventional measurement, by CA and TCM

		Conventional		**All Data Points**				**Data limited to Fr<1**			
Fluid	**Fill Level**	**K**	**n**	**K_{CA}**	**K_{TCM}**	**n**	**R^2**	**K_{CA}**	**K_{TCM}**	**n**	**R^2**
XG	25%	36.6	0.25	7.89	20.19	0.59	0.86	25.54	164.49	0.29	0.99
	62.5%			17.54	17.63	0.42	0.96	44.19	43.44	0.19	0.99
	100%			33.88	38.08	0.31	0.99	-	-	-	-
LGN	25%	186	0.04	0.38	0.1	0.70	0.3	51.19	245.30	0.03	0.99
	62.5%			78.74	74.45	0.25	0.99	91.45	86.10	0.21	0.97
	100%			203.31	189.36	0.05	0.99	-	-	-	-
CP	25%	76.4	0.29	7.09	4.11	0.76	0.41	148.99	973.04	-0.03	0.99
	62.5%			38.1	28.9	0.44	0.97	55.08	41.97	0.35	0.97
	100%			90.65	79.48	0.28	0.99	-	-	-	-

5.3.3 Torque Curve Method (TCM) for fill levels less than 100%

The suitability of the chosen mixer-viscometer methods for determining apparent viscosity and shear rate has been demonstrated at 100% vessel fill level. Employing a single value of *k’* for each method allows the estimation of apparent viscosity across a range of rheological behaviours. The next step is extending these methods to partially filled vessels, *i.e.,* fill levels less than 100%.

For the TCM, the mixer constant, *k’*, was determined at each speed for each non-Newtonian fluid using Eq. 5-8. The results are presented in Figure 5-8. For 100% fill level, a linear relationship between the calculated shear rate and speed existed, thus a single value of *k’* is applicable across all speeds (Table 5-5). Similarly for 62.5% fill level, the relationship between calculated shear rate and speed is sufficiently linear to approximate a single value of *k’* (R^2 = 0.93-0.98) (Table 5-5).

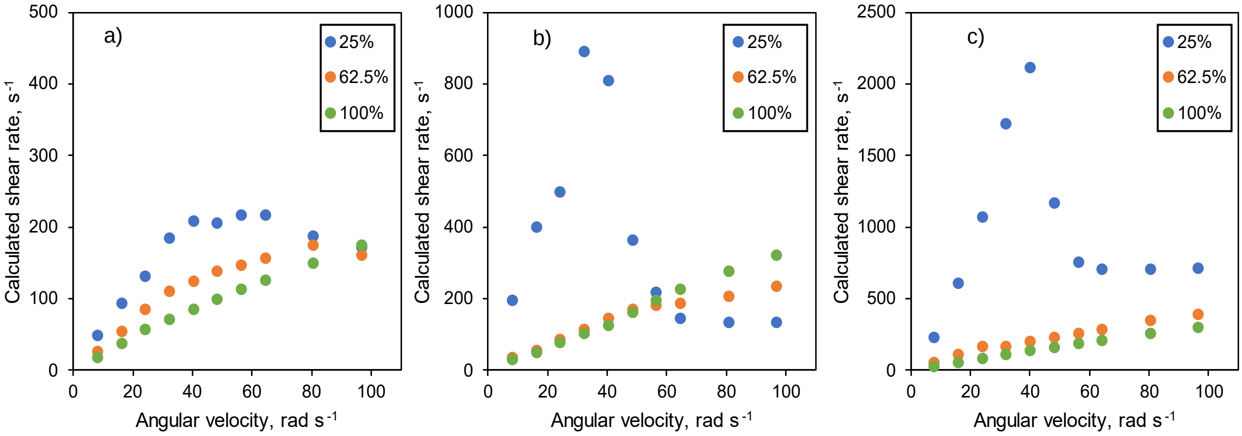

Figure 5-8. Average shear rate calculated for each speed using the TCM for XG, LGN, and CP at three fill levels, 25%, 62.5%, 100%

Table 5-5. Values determined for k' and k" using CA and TCM for all fill levels and using each fluid as the reference fluid

Fluid	**Fill Level**	**k' $_{TCM}$**	**k" $_{TCM}$**	**k' $_{CA}$**	**k" $_{CA}$**
CP	25%	61.4*	11905	1.96	62656
	62.5%	3.62	7155	3.93	8497
	100%	3.13	5945	5.79	3893
GLY	25%	-	11905	2.87	12746
	62.5%	-	7155	3.45	8072
	100%	-	5945	3.9	6224
LGN	25%	21.4*	11905	1.28	48800
	62.5%	2.27	7155	7.67	3165
	100%	3.44	5945	5.71	3537
XG	25%	5.08*	11905	3.92	11991
	62.5%	2.42	7155	5.35	4336
	100%	1.74	5945	9.17	1930

**Determined using only first 5 data points/speeds (Fr<1)*

However, at the lowest fill level, the plot of calculated shear rate versus speed shows significant deviations from linearity. Firstly, the calculated shear rates are orders of magnitude larger than for 62.5% and 100% fill levels. This can be attributed to the much lower torque values for this fill level. Up to a certain speed

(~40.27 rad s^{-1}, equivalent to tip speed of 0.625 m s^{-1}), the shear rate displayed some linearity, beyond which it either reduced or plateaued. This trend correlated directly with the torque-speed data (Figure 5-6). When the torque does not increase linearly with tip speed, corresponding to either a change in the mixing regime, incorporation of air into the system reducing the density, a change in the shape or position of the fluid in the vessel, or a change in the flow index of the fluid at higher tip speeds, then a single value of *k'* is not appropriate.

The Froude number was previously utilised to characterise the point at which the fluid transitioned from being mostly in contact with the agitator, to being centrifuged towards the walls (Figure 5-7). This principle was extended when determining *k'* at 25% fill level. When *Fr*<1, *i.e.,* below 0.625 m s^{-1}, the torque response is sufficiently linear to approximate a single value of *k'*. However, this still results in a value for *k'* orders of magnitude higher than that for 62.5% and 100% fill level (*c.f.,* Table 5-5). In general across all fluids, there was not much difference in k'_{TCM} determined at 62.5% and 100%, but the method did not extend well to 25% fill level, which gave considerably higher values for *k'*, even when data was limited to a linear region. To note, the mixer coefficient, *k",* is determined using Newtonian data, so is only a function of fill level and not fluid rheology.

Applying k'_{CP} across all fluids, the apparent viscosity and shear rate were estimated from the torque-speed data. At 100% fill level, k'_{CP} gave the smallest deviation in *K* and *n* compared to conventional geometries. However, for lower fill levels there is the largest variation in *k'* as a function of fill height, especially for 25% fill level. Figure 5-9 shows plots of apparent viscosity as a function of shear rate calculated using TCM for the three non-Newtonian fluids at different fill levels. The dotted line represents the power law line fitted to the data measured using conventional geometry.

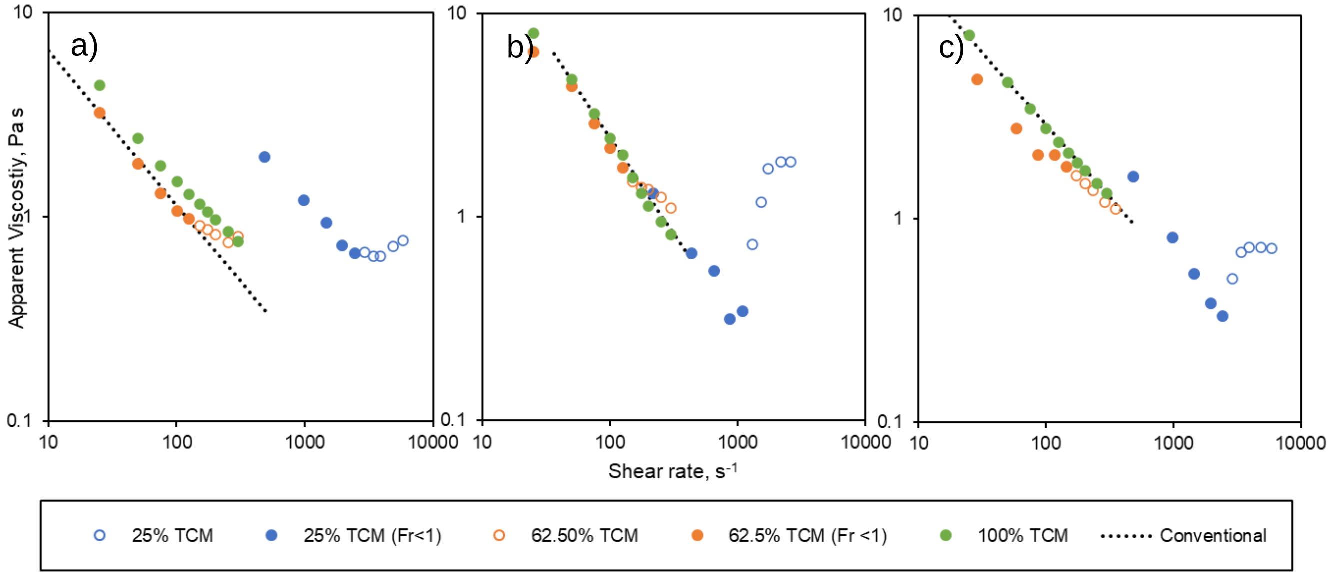

Figure 5-9. Plots of apparent viscosity versus shear rate determined using TCM for a) XG, b) LGN, c) CP at 25%, 62.5%, 100% fill level

As previously discussed, at 100% fill level, k'_{CP} effectively approximated the apparent viscosity and shear rate of the other fluids within acceptable error limits. At lower fill levels, applying a single value for the mixer constant and mixer coefficient (*i.e.,* for all speeds) data results in plots of apparent viscosity versus shear rate which reflect the shape of the torque-speed data (*cf.* Figure 5-6). The apparent viscosity initially follows a power law relationship with shear rate, up until the point at which the torque deviates from linear behaviour (~0.625 m s^{-1}). This marks the transition to supercritical flow and vortex formation, *i.e.,* Fr>1. Above this speed, the shape of the plot is related to the torque-speed data and follows a corresponding trend. For 25% and 62.5%, the flow and consistency indices (Table 5-4) were calculated using the full data, and data limited to Fr<1.

For 62.5% fill level, when the full data set is used, a power law model can be suitably fitted to the data, but the values for *K* and *n* are not in complete agreement with the conventional geometry (*c.f.,* Table 5-4). When the data is limited to *Fr*<1, most of the points sit on the curve fitted to the measurements taken with the conventional geometry. The estimates for *K* and *n* are also improved, in particular the gradient of the slope is now closer to the conventional flow curve, and therefore the flow index is more representative of conventional geometry. Overall, this suggests that *k'* estimated using the TCM could be suitable for predicting apparent viscosity and shear rate at fill levels as low as 62.5%, particularly if the data is limited to Fr<1.

For CP (Figure 5-9c), the first three data points do not follow the same gradient as the rest of the data. Referring to the torque-speed data, this is where large variability was seen due to not all of the fluid being engaged in flow. This suggests that whilst the Froude number can be useful in determining the limits of where a single value of *k'* can be applied for each fill level, in fact the success of the technique is reliant on the general flow regime.

For 25% fill level, the data initially follows a typical power law flow curve trend, up until shear rates equivalent to a speed of 0.625 m/s. Due to the higher value of *k'* calculated for 25% fill level, the plot is also shifted to higher shear rates for each speed. Using the whole dataset, it was not possible to determine *K* and *n* accurately, a power law model did not fit the data well (R^2 = 0.3-0.86) and the values significantly differed from those measured with conventional geometry. Limiting the data to Fr<1 again improved the fit of the power law model and gave values of *n* closer to the conventional geometry. However, due to the large value of *k'*, the consistency index *K* determined was much larger using the TCM than the conventional geometry.

Furthermore, when fitting the data to for CP at 25% fill level, the best fit of the data was when the flow index was negative. This typically suggests a shear-thickening fluid, which is not the case here, but instead shows the poor fitting of the data to the power law equation.

5.3.4 Couette Analogy (CA) for fill levels less than 100%

In the Couette analogy, the equivalent radius, R_i, is calculated using the torque (Eq. 5-10). As the torque decreases with fill level, intuitively so does the equivalent radius and optimal radius, r^*. The shear rate and mixer constant, k', are calculated using Eq. 5-11. In general, k' increased as a function of fill level across all fluids and showed less variability at lower fill levels than when applying the TCM. This appears to be related to the interdependency of k' *and* k''. In the TCM, the mixer coefficient is predetermined using the torque measured for a Newtonian fluid and is assumed to be independent of the fluid rheology. However, for the Couette analogy, the mixer coefficient is retrospectively calculated from the calculated apparent viscosity, the non-Newtonian torque measurement and the optimal radius (Eq. 5-10 & 5-11). This results in k'' varying with fluid rheology and fill level, where the trends follow the same pattern as k' calculated in the torque curve method (Figure 5-8), *i.e.,* for the lower fill levels for CP and LGN, the mixer coefficient is significantly higher (*c.f.*, Table 5-5). So, whilst k' varies much less with fill level and rheology using the CA method, k'' is consequently influenced. The final difference between TCM and CA is that for CA, only a single value for k' can be determined for all speeds, so it is not possible to determine the effects of speed on k' for this method. For the CA, k' determined using glycerine was applied to the other fluids and fill levels to approximate the apparent shear rate and viscosity from torque-speed data (Figure 5-10).

Similarly to the TCM, the method works well at 100% fill level for all three fluids. At partial fill levels, similar results to the TCM were seen, where the apparent viscosity and shear rate follow a power law model up until the point where flow enters the supercritical regime.

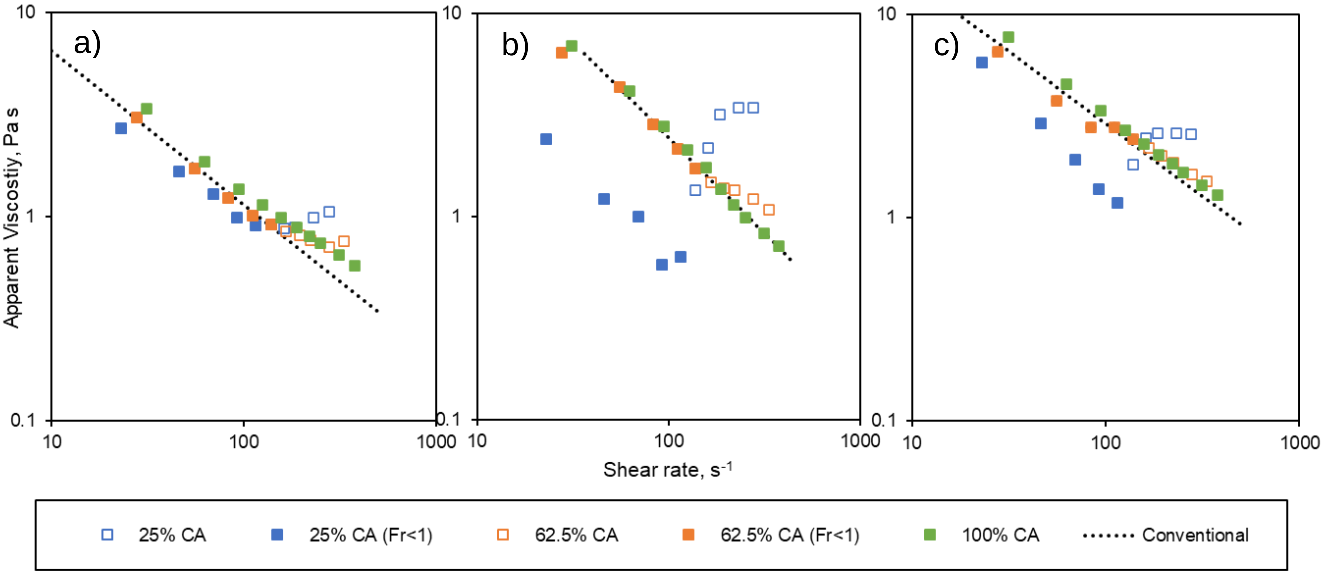

Figure 5-10. Plots of apparent viscosity versus shear rate determined using CA for a) XG, b) LGN, c) CP at 25%, 62.5%, 100% fill level

For all fluids, limiting the data to Fr<1 gave closer approximations for *K* and *n*, and the plots of apparent shear rate as a function of viscosity are much closer to the conventionally measure flow curve. As there was less difference in k'_{TCM} and k'_{CA} at 62.5%, there is less difference in *K* between the methods. However at 25%, the differences in *k'* (k'_{TCM} = 61.4, k'_{CA} = 3.9) were evident in the different values for *K*. This was more evident when the data was limited to Fr<1, and the power law model gave a better fit. Overall, the difference in *K* and *n* determined at 62.5% fill level compared to using a conventional geometry is much greater than any differences which might be encountered through measurement error.

In conclusion, the application of the Froude number to assess data viability for mixer-viscometer methods isn't universally suitable across fluid rheologies. For instance, the case of CP at 62.5% exhibited substantial torque variation for the first three data points, where the entire fluid wasn't engaged in flow, subsequently influencing apparent viscosity vs. shear rate plots. This underscores the need to comprehensively scrutinize torque-speed data and fluid flow, considering techniques like PIV or PEPT for improved insights into local flow velocities.

5.4 Conclusions

This study explored the impact of fill level, fluid rheology, and agitator speed on torque measurements. Subsequently, two mixer-viscometer methods—the Couette analogy and torque curve method—were employed to gauge their effect on *k’* calculation. Each method's ability to estimate apparent viscosity and shear rate using a single *k’* value at each fill level across the range of speeds was investigated. The primary objective was to assess whether typical mixer viscometer techniques could be employed in batch mixing scenarios, with evolving fill levels and fluid rheology, to develop a viscosity-based soft sensor from torque measurements.

In general, at 100% fill level, CA and TCM gave similar values for *k'* when CP and LGN were used as the calibration fluids, but varied slightly more using XG, where CA gave much higher values. This was attributed to the viscoelastic nature of XG. When k'_{CP} was applied for the TCM, and k'_{GLY} for the CA, the resulting values for *K* and *n* were in reasonable agreement with those measured using conventional geometries.

At lower fill levels, challenges arose in calculating *k’* for certain instances, due to non-linear torque-speed data. An attempt to constrain data to Fr < 1, a rheology-independent metric, improved results, but high *k’* values persisted for 25% fill levels in TCM, hindering the accurate prediction of shear rate and apparent viscosity. The observed vortex formation and torque changes were closely linked to fluid rheology attributes such as viscoelasticity or yield stress. Addressing this issue comprehensively for every fluid is impractical for potential online soft sensor applications. Further work could be done to provide approximation functions for the limitations of the mixer-viscometer techniques. This would require further data collection around the local fluid velocities and greater understanding of how the fluid-impeller contact changes as a function of fill height, fluid rheology and impeller speed.

In future studies, nonlinear modelling techniques or machine learning models like neural networks or random forest regression could prove more suitable for modelling viscosity from torque at partial fill levels. This research sets the stage for the incorporation of data-driven models in predicting apparent viscosity for partially filled vessels in larger-scale, industrial settings.

CHAPTER 6: IN PROCESS VISCOSITY PREDICTION FOR PARTIALLY FILLED ANCHOR AGITATED VESSELS

6.1 Introduction

6.1.1 Context

Formulated products are a mixture of components which have been combined in specific proportions, using specific processing methods to generate a process-sensitive microstructure which is critical to the performance, stability and efficacy of the final product (Edwards, 2006). For instance, the microstructural arrangement of air bubbles, ice crystals, and fat globules in ice-cream determines the texture and mouthfeel, melting behaviour, and flavour release (Amador *et al.*, 2017). Other examples include cosmetic and personal care products such as soaps, hair products, and toothpaste; household cleaning products such as laundry detergents and processed foods; such as ice cream, chocolate, and margarine (Hill, 2004).

Mixing is a critical unit operation in structured product manufacture and impacts other key unit operations such as heating and cooling, emulsification, and crystallisation (Hill, 2004). In batch mixing processes, raw materials are added to the vessel with defined rates and orders of addition. During this stage, the viscosity of the system evolves as a function of the microstructure generation (intermediate stages and final product) and key features of microstructure formation can take place before the vessel is fully charged (Hefft *et al.*, 2023). Close-clearance agitators such as anchors, and helical ribbons are typically employed to aid bulk mixing and heat transfer during high viscosity stages. As the rheology of the system is closely linked to the microstructure formation, monitoring viscosity during batch manufacture whilst the fill level changes within the vessel can provide a quantitative indication of product quality throughout the process (Cunningham *et al.*, 2023). Furthermore, it would allow for process optimisation by controlling the mixing time when a maximum or required viscosity is achieved (Altuna *et al.*, 2016a; Xu *et al.*, 2017; Hefft *et al.*, 2023).

Traditional offline viscosity measurement techniques are not easily transferred to online methods. This has resulted in the application of various novel sensor technologies, such as passive acoustic emissions (Hefft *et al.*, 2023), electrical resistance tomography (Machin *et al.*, 2018), and high frequency ultrasound (Awad *et al.*, 2012) being applied to predict either single-point viscosity or rheology. An alternative strategy involves developing a soft sensor, *i.e.,* a computational model or algorithm that estimates or predicts a physical or process variable in real-time based on available process data and mathematical techniques. This approach is particularly useful when physical sensors are expensive, difficult to install, unreliable or not available for a particular parameter of interest.

To predict online viscosity at partial fill levels, the use of machine learning algorithms harnessing available process data could be a useful approach (Ahmad and Benjamin, 2023). Artificial neural networks (ANN) and random forest regression models (RF) are amongst the most popular techniques in process engineering for predicting product performance from processing parameters. Ruan *et al.* (1995) investigated the suitability of ANNs to predict the rheological properties of dough (extensibility, maximum resistance and Farinograph peak), using 400 power-time points measured during the dough mixing stage as the input. They found they were able to accurately predict the rheological properties and the model showed promise for process optimisation. Kugler *et al.* (2014) used ANNs to model the viscosity at two different shear rates of a polymer melt exiting a screw extruder, using various sensor measurements along the length of the extruder (temperature, torque, pressure, strand diameter and extrudate swell). The model was able to predict viscosity changes relative to a 1% change in material proportions. Mowbray *et al.* (2022) investigated different modelling techniques (Gaussian processes, Bayesian neural networks and heteroscedastic noise neural networks) to predict the end viscosity of some cosmetic products manufactured in a batch process, using 28 different measured variables at a range of time steps across the process. Sun *et al.* (2023) utilised random forest regression to predict the strength and fresh (rheological) properties of alkali-activated concrete from the mixture properties and overall composition. Carou-Senra *et al.* (2023) compared different machine learning techniques (ANN, RF and SVM (support vector machines)) to separately predict the printability, type of droplet formation, and drug dosage of pharmaceutical inks.

Although the above studies show promise for a limited set of process parameters, thus far, no data-driven models have been applied to predict the viscosity of a system in-situ at intermediate process stages. Moreover, no robust methods exist for the prediction of viscosity in partially filled batch vessels, specifically with close-clearance impellers such as anchors and helical ribbons. Cunningham *et al.* (2023) investigated the suitability of traditional mixer-viscometer methods (Couette analogy and torque curve method) for determining the in-situ viscosity in partially filled vessels. Neither method was able to accurately predict viscosity, consistency index or flow index at fill levels less than 100% (25% and 62.5% were investigated), thus the use of data-driven models was recommended.

6.1.2 Machine Learning Models

In selecting an appropriate modelling approach, if a simple linear regression model is capable of accurately explaining the data, then that is the best option, due to its simplicity, interpretability and well-understood theory (Lunt, 2013). However, for more complex datasets, where the assumptions of linear regression are not met (linearity, homoscedasticity, multivariate normality, independence, lack of multicollinearity and reasonable outliers) other approaches are better suited. For example, multiple linear regression – using multiple variables to predict an output, non-linear regression – where a prediction expression is fitted to a curve function. For even more complex datasets, approaches such as Principal Components Analysis (PCA) and Partial Least Squares Regression (PLS), which aim to reduce the dimensionality of data which is dependent on multiple variables are often employed (James *et al.*, 2023). Common applications of these models include chemometrics *i.e.*, predicting concentrations of components within a mixture from spectroscopic data (Pottel, 1995; Ryder, 2002). However, there are limitations to both techniques: PCA still works best when the underlying relationships between the data are linear, and also assumes that the principal components (directions of maximum variance in the data) are perpendicular, which is not always the case (IBM, 2023; Bro and Smilde, 2014) . PLS is subject to overfitting, particularly because selection of the number of components in the model is subjective. It is also sensitive to outliers and cannot deal with multicollinearity in the input variables (Parastar and Shaye, 2015). Furthermore, both techniques are difficult to interpret and do not reveal much about the relationships between the data.

More recently, the combination of increased low-cost computing power and availability of large datasets has widened the use of more complex machine learning methods, such as decision trees, random forests, support vector machines, gradient boosting machines and neural networks (Pugliese *et al.*, 2021). Artificial neural networks (ANNs) operate on a principle based on the function of the human brain. The ANN consists of layers of interconnected nodes, where each node has its own function, with an input and output, weights and threshold. If the output of a node is above the specified threshold value, the node is activated and sends data forward on to the next layer of the network. Weights are determined at the input layer to determine the importance of a variable. Advantages of this model type are the ability to handle a wide range of data types, non-linear and missing data. However, ANNs require a large data set to initially train the model, have little interpretability, and can be prone to overfitting (IBM, 2024; Bonaccorso, 2018).

Decision trees are a non-parametric, supervised learning algorithm which make predictions by following a flow chart of questions about the data. At the initiating root, a feature of the data is selected, and the data evaluated against it so that it is split and follows one of two branches. This is repeated until the final leaf is reached. If a decision tree is not limited in any way, it could continue splitting branches until a very small sample size is present in every node. This causes the model to be overfitted and the model will not be suitable for making predictions about unseen data. Effective cross-validation and limiting the tree depth are two ways to manage this (Bonaccorso, 2018). Another way to overcome this is by combining a series of decision trees, known as a random forest. The robustness of the model is improved and has greater resistance to outliers (Beheshti, 2022; Cunha *et al.*, 2020). A bootstrapping technique is used to build each decision tree in the forest with a randomly different set of data. Random forest models have more interpretability than ANNs, can also handle non-linear relationships well and do not require as large an input dataset as ANNs.

6.1.3 Objectives

The objective of this work is to develop a model which can predict viscosity during the batch manufacture of formulated products across three different scales: a 0.045 L rheometer (Cunningham *et al.*, 2023) and 2 L and 50 L capacity stirred vessels. The three different scales have been combined in one model to introduce more datapoints into the model, and possibly allow for future interpolation at other scales. This will include estimation at partial fill levels, so that viscosity can be measured during filling or emptying of the vessel, and at points where key structure formation may be occurring. In addition, torque versus speed data across three different scales with comparable geometries and impellers is obtained. The modelling approach selected for this work is random forest regression, due to its suitability to the size and nature of the dataset. The output variable of the model is the 'flow curve viscosity'. This is apparent viscosity at a specific shear rate, where the shear rate constant has been determined by applying the Couette analogy to torque-speed data for a Newtonian fluid (glycerine) for each fill level and mixer. The input variables are determined during data exploration, however they are limited to the mixer scale, mixer diameter, impeller speed (RPS, tip speed or angular velocity), average torque, and fill level, as these are the only variables which can be measured. The model is intended to be used on fluids of unknown rheology, so any information about the fluid (consistency index, flow index, density, *etc.*) cannot be used as an input. Fluids with varying rheological behaviours will be investigated to represent the various rheological behaviours seen during personal care liquid manufacture. The random forest regression model will be built, tuned and evaluated using Scikit-learn machine learning Python library (Pedregosa, 2011).

6.2 Materials and Methods

6.2.1 Experimental Equipment

In this study, data was collected for a 2 L and a 50 L capacity mixing vessel equipped with helical-ribbon type impellers (IKA-Werke, Staufen, Germany, and Becomix – A. Berents GmbH & Co. KG, Bremen, Germany, respectively) (details in Table 6-1). Unprocessed torque-speed data was collected in a previous study for a 0.045 L vessel (Cunningham *et al.*, 2023) was also included and analysed using a new approach. The three mixing systems were geometrically similar, aside from subtle differences in the geometry of the PTFE scraper blades, and the shape of the bottom of the smallest scale mixer (Table 6-1).

Table 6-1. Dimensions of mixing vessels

	0.045 L	**2 L**	**50 L**
Impeller diameter, D (m)	0.031	0.135	0.41
Overall height, h (m)	0.036	0.15	0.45
Wall clearance, c (m)	0.0015 (~5%)	0.0075 (5%)	0.02 (5%)
Pitch (ribbon height in one 360° turn), p (m)	0.036	0.15	0.45
Width of the blade, w (m)	0.025	0.00675	0.0205
Number of blades, n_b	2	2	2
Vessel bottom shape	Flat	Torospherical	

The 2 L mixer was fitted with a TorqSense SGR510 strain gauge type torque transducer with a range from 0-6 N m (Sensor Technology Ltd., Banbury, Oxon, UK). Strain gauges work by converting torque measurement to electrical signal. The sensor normally consists of four strain gauges, affixed to the rotating shaft in a Wheatstone bridge circuit configuration. When torque is exerted on the shaft, the circuit twists in the direction of rotation, leading to shear strain. This causes one pair of strain gauges to elongate, whilst the other is compressed. The resistance of the circuit is affected, and the electrical output corresponds to the torque applied (Ascanio *et al.*, 2004; Schicker and Wegener, 2002).

The 50 L mixer was installed with a 0-100 N m TB1A reaction torque sensor supplied by HBK (Hottinger Brüel & Kjaer GmbH, Darmstadt, Germany). This sensor operates on a similar principle to a lever arm and load cell (HBM, 2024). For both measurement types, there are potential sources of error when measuring torque on the impeller shaft. For example, zero drift can occur after extended periods of operation (hours) but was not seen during these experiments. Zero errors can also be caused as the torque sensor measures bending moments on the impeller shaft, which makes it difficult to take a static zero measurement. Care was taken to install the torque transducer correctly (on the 2 L vessel) to reduce bending moments, whereas it was not a concern in the flange type sensor on the 50 L vessel which is permanently in place around the shaft. The torque measured on the shaft may also include losses to the system, e.g., shaft bearings. The impeller was run in an empty vessel at the same range of speeds to determine the system losses before being run with fluid present.

The internal temperature of the vessel/temperature of the material was measured with a temperature probe and controlled with a water bath and vessel jacket to 30°C ± 1 for all experiments.

6.2.2 Materials

The Newtonian fluids used were glycerine (Palmera G995E; 99.5 % purity, supplied by KLK Oleo; density 1260 kg m^{-3} @ 30°C) used at different temperatures and honey (blossom honey, supplied by Hilltop Honey, UK). They were used to generate power curves and estimate shear rate constants for the two mixers investigated (2 L and 50 L scale). Details of the viscosity of the fluids at the temperatures used can be found in Table 6-2.

Table 6-2. Viscosity of Newtonian calibration fluids at different temperatures

Fluid	Temperature (°C)	Viscosity (Pa s)
Glycerine	23	0.99
	30	0.59
Honey	30	1.98

Non-Newtonian fluids with rheological behaviours representative of those seen in personal care liquid manufacture were also used. Some of the materials and formulations were those also used in Cunningham *et al.* (2023), with the addition of another commercial lamellar gel network (LGN) structured personal care product. Details are given in Table 5-1. Flow curves were measured over a range of shear rates (0.1-500 s^{-1}) using a DHR-III rheometer (TA Instruments, Waters, UK) fitted with a 20mm diameter cross-hatched parallel plate geometry, using a 0.5mm gap. Over this shear rate range, the flow curves of the fluids could be reasonably fitted to the Ostwald-de Waele power law model:

$$\eta = K\dot{\gamma}^{n-1} \tag{6-1}$$

Where η is the apparent viscosity (Pa s), K is the consistency index, n is the flow index and γ is the shear rate (s^{-1}).

Table 6-3. Formulations, consistency indices and flow indices of non-Newtonian fluids investigated

Fluid	Formulation (w/w%)		Consistency index, K (Pa s^n)	Flow behaviour index, n (-)	Density (kg m^{-3})
Carbopol® solution (CP)	Carbomer powder[a]	1.5%	150.8 ± 2.5	0.13 ±0.~~005~~01	997
	Water	98.5%			
Xanthan gum solution (XG)	Xanthan Gum[b]	5%	51.9 ± 2.8	0.2 ± 0.~~025~~03	1067
	Glycerine[c]	20%			
	Water	75%			
Lamellar gel network (LGN 1)	Cetearyl alcohol[d]	7.06%	50.8 ±~~1~~2.~~95~~0	0.21 ± 0.~~005~~01	880
	Behentrimonium Chloride (BTAC)[e]	2.35%			
	Water	90.59%			
Commercial LGN (LGN 2)*	Not available		79 ± 3.0	0.06 ± 0.~~002~~00	880

a) Carbopol® 980 polymer (supplied by Lubrizol), b) Xanthan gum (supplied by Jungbunzlauer (Basel, Switzerland)), c) Palmera G995E; 99.5% purity, supplied by KLK Oleo, d) cetyl alcohol (30 wt%) and stearyl alcohol (70 wt%), (Godrej Industries (India)), e) behentrimonium trimethyl ammonium chloride (BTAC), supplied by Clairant International Ltd. (Germany). This surfactant is provided at 70 wt% purity, where the remaining 30 wt% is comprised of dipropyl glycol, which acts as a processing aid.

* Only measured for 2 L scale.

Flow curves for all the fluids used in this study can be found in Appendix 6.

6.2.3 Data Collection

At a 2 L scale, torque measurements were collected over a range of impeller tip speed from 0.25 – 2 m s^{-1}. Measurements were recorded using Torqview software (Sensory Technology Ltd., Banbury, Oxon, UK) 2 times per second for at least 30 seconds. An average torque value for each speed was used in calculations. At 50 L scale, torque measurements were collected over a range of tip speeds from 0.5 - 2.5 m s^{-1}. Measurements were collected over at least 30 seconds and again an average value was used. Further to this, torque-speed data for a rheometer scale (0.045 L) in a previous study by (Cunningham *et al.*, 2023) was also included in the random forest regression modelling. In all cases, torque-speed data was collected for each fluid (glycerine at 30°C and non-Newtonian fluids) across three fill levels ($h_l/h = 0.25, 0.625, 1$). Data was collected in triplicate and each repeat included as a data point in the random forest model. Where relevant, an average and standard deviation of the torque is presented. The corresponding ranges of Reynolds number used to build the power curve (*i.e.*, for the Newtonian fluids) and those included in the RF model (non-Newtonian fluids) are given in Table 6-4.

Table 6-4. Ranges of Reynolds number used for building the power curve and included in the RF model for each scale mixer

Scale	**Re used to build power curve (Newtonian fluids)**	**Re used in RF Model (non-Newtonian fluids)**
0.045 L	3 - 33	0.2 – 30
2 L	8 - 200	2 - 200
50 L	36 - 300	12 - 300

6.2.4 Data Analysis

Determining K_p

To determine similarities in the mixing systems across different scales and evaluate the limits of the laminar operating regime, the power curve for each mixing system was established. In the laminar mixing regime, the power number is proportional to the Reynolds number, Re, as follows:

$$Po = K_P Re^{-1} \tag{6-2}$$

where Po is Power number, Re is Reynolds number and K_P is the laminar power constant.

It is typically considered that flow in agitated vessels is in the laminar regime for Reynolds numbers up to 10, after which the flow moves into the transitional regime (10 < Re < 20 000), and finally the turbulent regime (Re < 20 000) (Dickey, 2015). However, for close clearance impellers, the laminar regime is still present at values of Reynolds numbers from 60 to 100 (Kamla *et al.*, 2021; Delaplace *et al.*, 2000b). To find K_P, Po and Re were fitted to Equation 6-2 using the Solver function in Microsoft Excel.

Determining k_γ

The shear rate constant, k_γ, was determined using the Couette analogy at h_l/h = 0.25, 0.625, and 1 using data from the Newtonian fluid, glycerine, at 30°C. The Couette analogy approximates the mixing geometry and vessel to a coaxial cylinder rotating inside another cylinder (Couette geometry), where the equivalent Couette gives the same torque measurement as the agitator when rotating at the same speed (Ait-Kadi *et al.*, 2002). The equivalent Couette radius first needs to be determined (Eq. 6-3):

$$R_i = \frac{R_e}{\left(1 + \frac{4\pi N}{n}\left(\frac{2\pi\mu L R_e^2}{M}\right)^{1/n}\right)^{n/2}} \tag{6-3}$$

where, R_i is the equivalent Couette radius of the geometry (m), R_e is the radius of the vessel (m), N is the angular rotational speed of the impeller (rad s^{-1}), n is the flow index (from Otswald de Waele power law), μ is fluid viscosity (Pa s), M is torque (N m) and L is the length of the impeller (m).

Next, the optimal radius, r^*, at which the shear rate is independent of the radius and fluid rheology is determined using a graphical method. The calculated shear rate is plotted against different radii for various values of the flow index, *n,* and the point at which the lines intersect is taken as the optimal radius (Ait-Kadi *et al.*, 2002; Novontá *et al.*, 2001).

The shear rate, $\dot{\gamma}_{av}$, is then calculated at the optimal radius, *r** (Eq. 6-4) (Ait-Kadi *et al.*, 2002).

$$\dot{\gamma}_{av} = \frac{\frac{4\pi N}{n}\left(\frac{R_i}{r^*}\right)^{2/n}}{1-\left(\frac{R_i}{R_e}\right)^{2/n}}.N = k_\gamma N \tag{6-4}$$

Where R_i is the equivalent Couette radius of the geometry (m), R_e is the radius of the vessel (m), r is the optimal radius (m), N is the angular rotational speed of the impeller (rad s^{-1}), n is the flow index (from Otswald de Waele power law) and k_γ is the shear rate constant.*

Once the shear rate is known, the apparent viscosity is then determined by applying the power law/Ostwald-de Waele equation (Eq. 6-1).

6.2.5 Random Forest Model Development

Data Exploration

To measure the strength of correlations between variables and to determine which to include in the model, Spearman's correlation coefficient was used, which determines the strength of correlation between two numerical values when relationships are non-linear.

Model Development

A Random Forest regression model was developed using Scikit Learn, an open-source machine learning Python library (Pedregosa, 2011). Its performance was evaluated using k-fold cross validation with 5 folds. In k-fold cross validation, the dataset is split into 'k' subsets of roughly equal size and the model is then trained and evaluated k times. Each time, k-1 subsets are used to train the model, and the remaining subset is used as the validation set, changing the validation subset on each iteration. The model is evaluated for each iteration (*e.g.*, by R^2), and then an average is taken. This improves the robustness of the model compared to a single train-test split (James *et al.*, 2023). A test-train split of 25-75 (187- 563 data points, respectively) was used, so that 75% of the data was used in training the model, including k-fold cross-validation, and further validated against the remaining 25% test data. The Python code used to develop the Scikit Learn model can be found in Appendix 5.

Hyperparameter tuning for the model was carried out using a randomised grid approach, *i.e.*, a range of hyperparameter variables were chosen, and the 'RandomizedSearchCV' function was used to search for the optimal hyperparameters of the model. The hyperparameters were selected based on previous preliminary studies on which variables had the largest impact on the model's performance. The selected hyperparameters and the values investigated for each are given in Table 6-5. Using the randomised grid, 30 different combinations of hyperparameters were selected.

The evaluation metrics used for assessing model performance were R^2 and MSE (mean squared error), with the best-performing model based on the highest R^2 and smallest MSE.

The 'flow curve viscosity' *i.e.*, the apparent viscosity at the calculated shear rate for each condition, when the fluid viscosity was measured using a conventional rheometer, was the target variable for prediction.

Table 6-5. Hyperparameter ranges included in randomised grid optimisation approach

Scikit-learn parameter	Description	Values
n_estimators	The total number of decision trees in the random forest.	10 – 500
max_depth	The maximum depth of a tree, *i.e.*, how many splits the tree can make. Too low = risk of underfitting data, too high = risk of overfitting data	5-50
min_samples_split	The minimum number of samples required to split an internal node. Values are inputted as fraction of total number of samples in the set.	4, 6, 8
max_features	The number of features to consider when looking for the best split. Reducing max number of features considered per split introduces further randomness and improves model generalisation. 1 = all features can be considered.	0.5, 1

6.3 Results

6.3.1 Torque-speed data

Figure 6-1 shows plots of torque-speed data for the 2 L (a-d) and 50 L (e-h) capacity mixer for glycerine (GLY), xanthan gum solution (XG), Carbopol solution (CP), and a lamellar gel network (LGN 1). At the 2 L scale, for the Newtonian fluid, GLY (Figure 6-1a), the torque increases linearly with speed, as expected (since $\Gamma \propto N$ in the laminar regime) and also as a function of fill height. There is more deviation in the torque at higher speeds (> 1 m s^{-1}), and also at the higher fill levels; this is likely due to the flow regime changing to transitional. The Reynolds number at 1 m s^{-1} is 106. In later analysis of the power curves for each mixer (Section 6.3.2), the critical Reynolds number, Re_{crit}, was found to be ~60, in line with previous results for helical ribbon type agitators (Brito de la Fuente *et al.*, 1997; Delaplace *et al.*, 2000c).

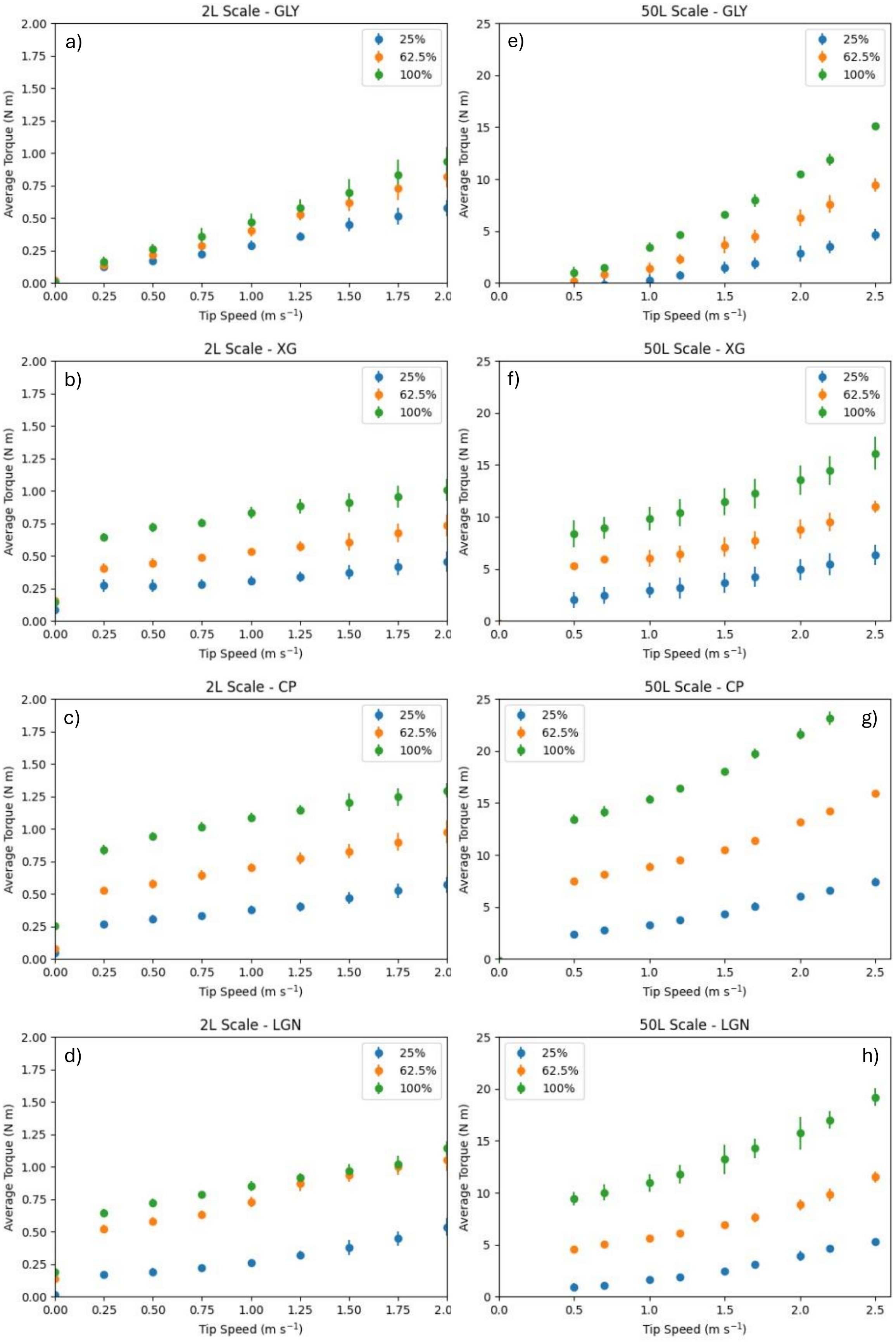

Figure 6-1. Torque-speed data for each fluid. Left top to bottom, 2 L scale. a) GLY b) XG c) CP d) LGN. Right top to bottom, 50 L scale. e) GLY f) XG g) CP h) LGN.

There is not much difference in torque for the three fill levels, particularly at the lower speeds, however a change in the gradient of the plot is seen ~1.5 m s^{-1}. This corresponds with the Froude number going over unity, signalling the formation of a vortex, however it was not possible to confirm this visually due to the opaque nature of the vessels. However, a noticeable change in the gradient of torque versus speed was also seen by Cunningham *et al.* (2023) for helical ribbon mixing systems at a much smaller scale (0.045 L) once Fr>1 was achieved.

For XG solution, the results are similar for both scales (Figure 6-1b, f). Speed does not have as great an impact on the torque values as for the other Newtonian and non-Newtonian fluids, as evidenced by the lower gradients of the torque-speed at each fill level. The XG solution showed viscoelastic properties. The effects of elasticity on torque have been previously discussed. Rieger and Novak and Ulbrecht and Carreau (Rieger and Novak, 1974; Ulbrecht and Carreau, 1985) found that elasticity reduced torque measurements. However, other authors have shown the opposite result (Carreau *et al.*, 1993; Collias and Prud'Homme, 1985). Similar results were obtained for CP at both 2 L and 50 L scale. There is a linear correlation between torque and speed at all three fill levels and a distinct separation between the fill levels. Finally, for LGN, the two scales showed some differences. At 2 L scale, the torque at 62.5% fill level is much closer to the torque at 100% fill level than for other fluids and converges with the torque at 100% fill level at higher speeds. This could suggest that the fluid spreads to the side of the vessel at higher speeds, and thus at 62.5% and 100%, the same amount of fluid is in contact with the impeller, resulting in similar torque responses. The same effects were not seen at larger scale, likely because the effects of vortexing are not as prominent, and the larger volume of fluid would not be centrifuged to the sides of the vessel in the same way.

6.3.2 Power curves and determination of Kp

The power curves of the mixers were characterised to determine the laminar operating range, and compare the systems, which were mostly geometrically similar (Table 6-1). Only slight differences existed in the scraper blades attached to the agitator, and the type of torque measurement, as highlighted in Section 6.2.1. Therefore, it is expected that the laminar power constants, K_p, should be similar. Hall (2012) found the following correlation gave a good estimation of K_p:

$$K_p = 82.8\frac{h}{D}\left(\frac{c}{D}\right)^{-0.38}\left(\frac{p}{D}\right)^{-0.35}\left(\frac{w}{D}\right)^{0.20} n_b^{0.78} \tag{6-5}$$

where h = overall height of helical ribbon impeller, m; c = wall clearance, m; p = pitch (ribbon height in one 360° turn), m; w = width of the blade, m and n_b *= number of blades.*

Using the dimensions in Table 6-1, the estimated values of K_p from Eq. 6-5 were found to be 288 for the 2 L vessel and 300 for the 50 L vessel, which are very close to each other. Maingonnat *et al.* (2008) calculated K_p for a similar impeller (Ekato Paravisc) at ~5 L scale to be 231. Iranshahi *et al.* (2016) found K_p to be 315 for a 30 L vessel. When determining K_p for the two different scale mixers, different fluids were used. At 2 L scale, honey was used as the Newtonian fluid (Table 6-2) to ensure flow was mostly in the laminar regime (Re<200). For the 50L vessel, it was not possible to use honey, and instead glycerine at a lower temperature was used (Table 6-2). Due to scale and the fluid viscosity, some of the data was in the transitional regime for both fluids. The critical Reynolds number, Re_{crit}, was found to be ~60, in line with previous results for helical ribbon type agitators (Brito de la Fuente *et al.*, 1997; Delaplace *et al.*, 2000c).

To confirm similarity between the scales, data collected for both mixers was plotted on the same graph (Figure 6-2) and the data was fitted to Eq. 6-2. The experimentally obtained value of K_p was thus determined to be 316, in line with expectations from literature and the theoretical values obtained using Eq. 6-5.

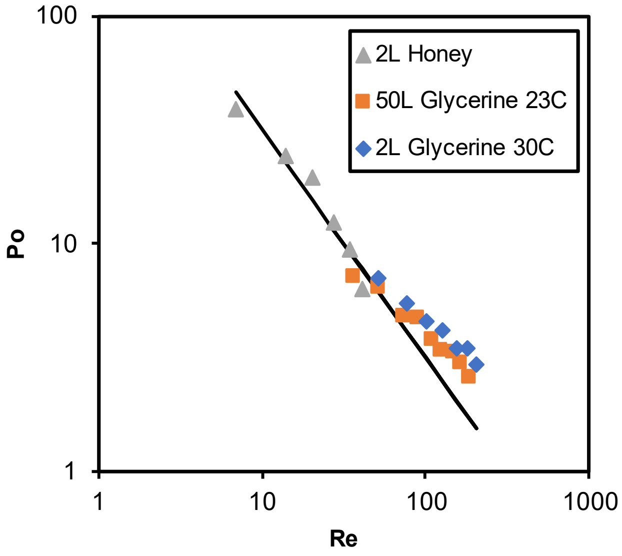

Figure 6-2. Power curve for 2 L scale calculated using Honey and Glycerine and 50 L scale using Glycerine

6.3.3 Determining k_γ

The Couette analogy was applied to both systems to determine the shear rate constant, k_γ, and process viscosity for both scales, using the data from the Newtonian fluid, glycerine. Results are given in Table 6-6 below. The shear rate was calculated using Eq. 6-4 and the apparent viscosity determined from the flow curve (Eq. 6-1).

Table 6-6. Shear rate constant using the Couette Analogy for 0.045 L, 2 L and 50 L mixing vessels for h_l/h = 0.25, 0.625, 1

	Shear rate constant, k_γ		
	Fill Level (h_l/h)		
Scale	**0.25**	**0.625**	**1**
0.045 L*	2.9	3.5	3.9
2 L	8.6	11.2	12.5
50 L	3.9	8.3	11.8

**Calculated previously in (Cunningham et al., 2023)*

6.3.4 Data Exploration

In this study, the variables which can be measured are limited to the impeller torque, impeller speed, mixing vessel maximum capacity (volume), impeller diameter, and the fluid fill level. As described above, the shear rate constant for each mixer has been calculated for each fill level and assumed to apply for all speeds and fluid rheology types. The shear rate at each speed was then used to determine apparent viscosity for different type of fluid across a range of rheological properties (*e.g.*, consistency and flow indices, elastic, thixotropic, yield stress). A limited data exploration was carried out by determining Spearman's correlation coefficient between relevant mixer and fluid attributes (Figure 6-3).

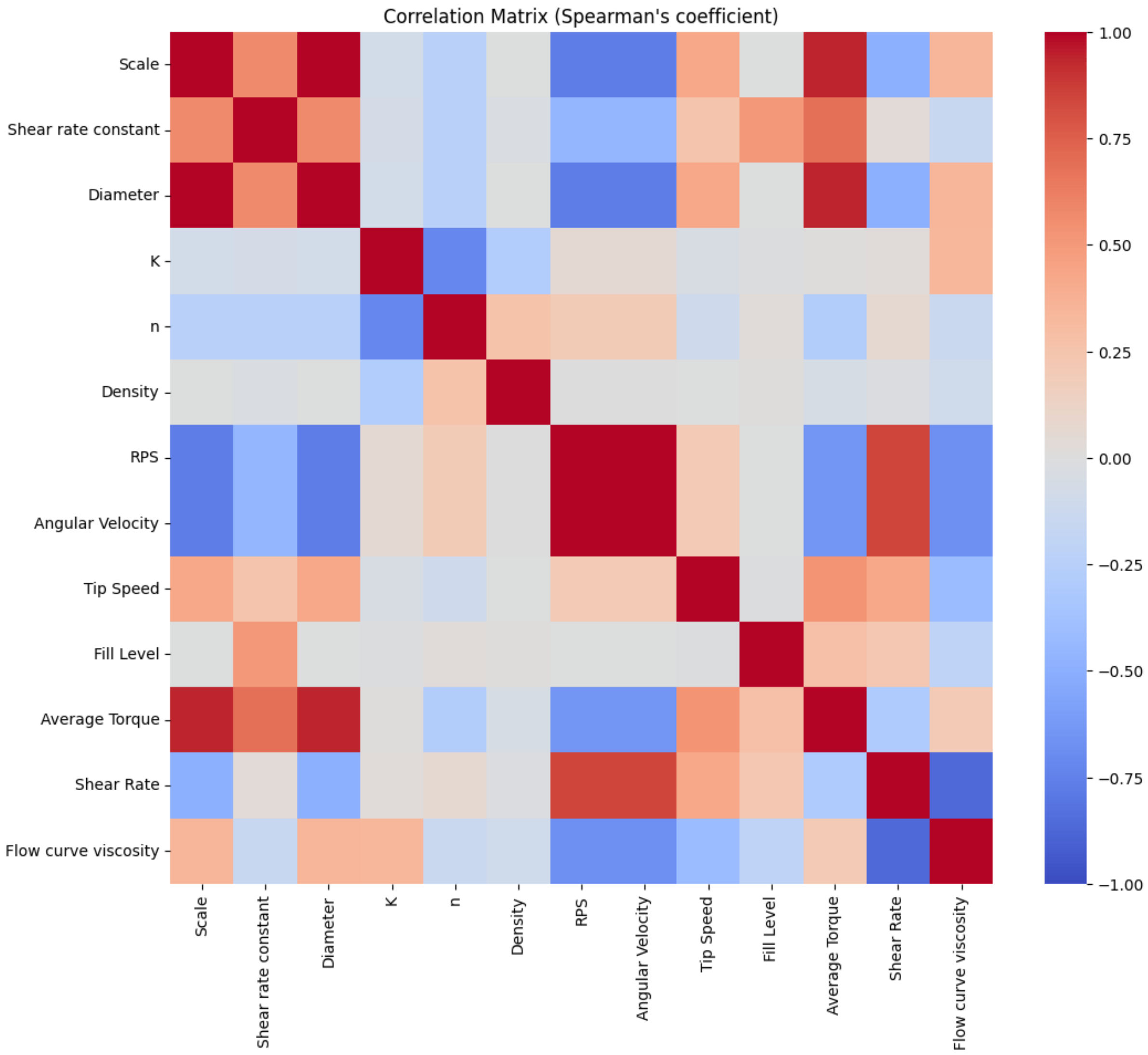

Figure 6-3. Correlation matrix using Spearman's correlation test

Based on the strengths of the correlations, the variables selected to be used in the RF model were: average torque, fill level, mixer diameter, and angular velocity. Whilst K_P and scale had a similar strength correlation to mixer diameter, only one attribute is required to describe the scale of the mixer, and diameter is easiest to measure. The consistency index, K, flow index, n, and density, ρ, will be unknown when measuring unknown/evolving fluids during manufacture so cannot be used. The Power number, Po, is related to the torque, angular velocity, fluid density, and diameter. Out of these, torque, angular velocity and diameter are all accounted for separately as inputs, and including Po would introduce density as a parameter about the fluid which the model may rely on to distinguish between the fluids. This could hinder the ability of the model to generalise when predicting the viscosity of unknown fluids. Finally, torque is dependent on fill level so has a moderate correlation with flow curve viscosity (Figure 6-1).

6.3.5 Random forest model

150 different fits, *i.e.*, 30 different combinations of hyperparameters with 5-fold cross-validation were fitted to the data to train the model. The models were then validated against the test set data and evaluated using the R^2 and MSE for the test data set. The best model was considered as that with the highest R^2 and the lowest MSE. The R^2 and MSE for the test and training data for each set of hyperparameters tested is given in Figure 6-4, ranked from highest scoring to worst. In general, the models with the highest R^2 and lowest MSE were larger/more complex, *i.e.,* had a higher number of trees, higher maximum depth, lower number of features considered when looking for the best split, and a lower minimum number of samples required to split an internal node. However, these larger, more complex models tended to show signs of overfitting. This is evident when the test set data R^2 is much lower than the training set R^2. Whilst the model with the best performance by the criteria given was: n_estimators, min_samples_split, max_features, max depth = 445, 4, 0.5, 35, respectively, reducing the number of trees to 227 and maximum depth of the tree to 20 gave comparable results. Thus, moving forward, the 3rd best model (n_estimators, min_samples_split, max_features, max depth = 227, 4, 0.5, 20, respectively) was

evaluated as it gave comparable results for less computing power and complexity (results in Table 6-7).

In order to achieve similarity in R^2 between the training and test datasets, the complexity of the model had to be notably reduced (n_estimators, min_samples_split, max_features, max depth = 10, 6, 0.5, 5, respectively) to give an R^2 of 0.78 and 0.74. Whilst this is an improvement in reducing overfitting, the MSE for this model was 1.28 for the training set and 1.46 for the test set, which is too large for the model to be useful. The typical viscosity range is 0 – 15 Pa s, and the majority of datapoints are less than 5 Pa s. Converting MSE to RMSE (root mean square error) so that it is the same units as the predicted variable, this would result in an error of approximately ± 1 Pa s. Thus it was decided to further evaluate the 3rd best model.

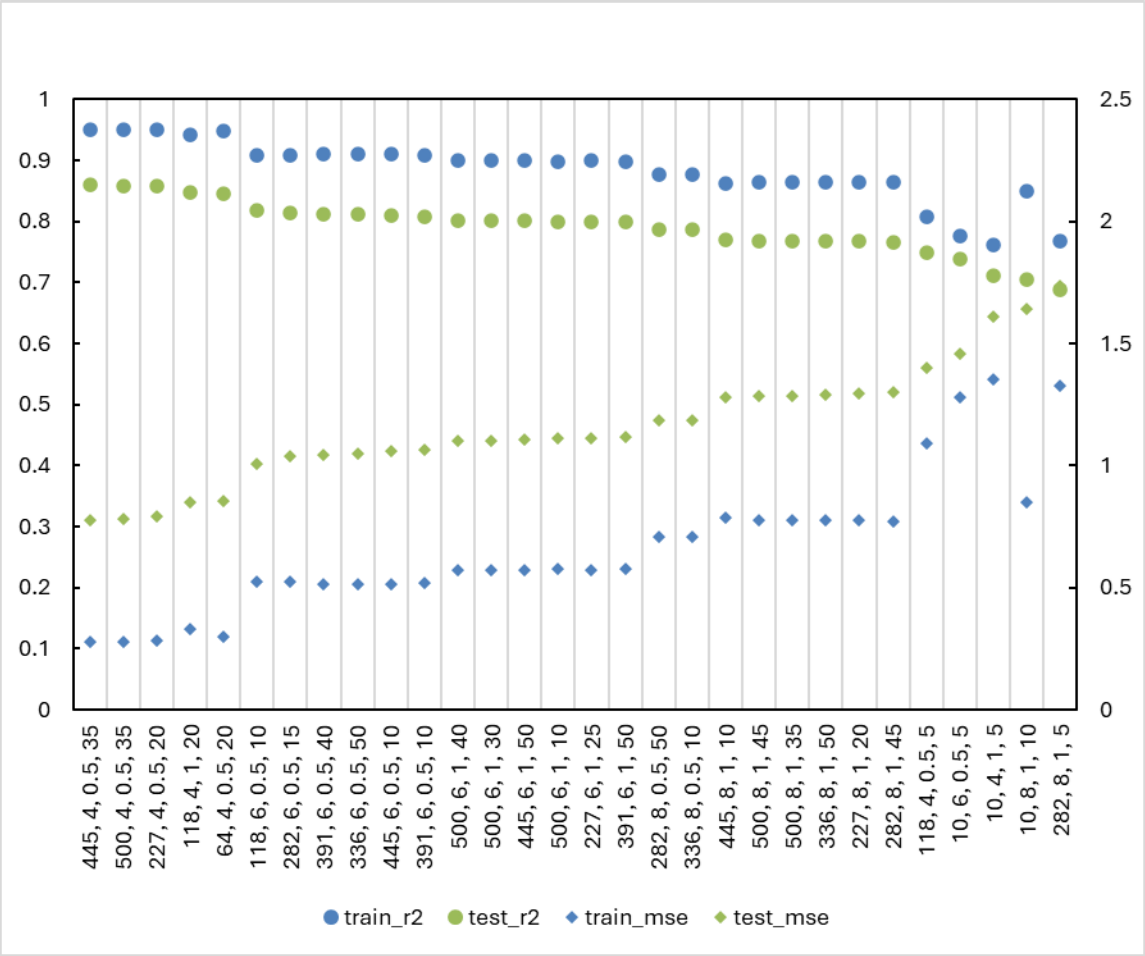

Figure 6-4. R^2 and MSE for training and test set data for each set of hyperparameter combinations tested, ranked by R^2_{test}. Where label represents n_estimators, min_samples_split, max_features, max depth.

Table 6-7. Results for best RF model

	R^2	**MSE**
Training data	0.95	0.28
Test data	0.86	0.79

The model has a high R^2 score on both the training and test sets, indicating that it explains a large portion of the variance in the data. However, the R^2 score is higher on the training set compared to the test set. The slight difference between the training R^2 (0.95) and test R^2 (0.86) suggests some degree of overfitting. The model fits the training data very well but not as well on the test data. However, the difference is not too large, indicating that overfitting is relatively controlled. The high R^2 and relatively low MSE on the test set indicate that the model performs well on unseen data. Overall, these results show that the model with the specified hyperparameters is a strong predictor for the dataset, with good generalisation to new, unseen data.

The parity plot of predicted values versus actual values for the training set data and test set data is given in Figure 6-5 a and b below.

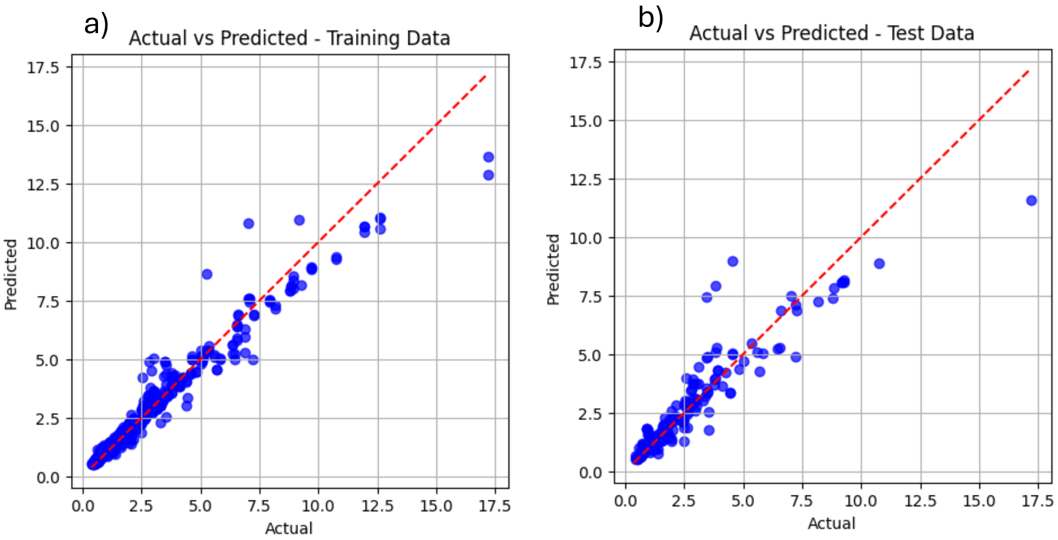

Figure 6-5. Parity plots of predicted viscosity vs actual viscosity for a) training data set and b) test data set

As can be seen from the parity plots, the majority of the viscosity data is under 5 Pa s, with some data points between 5 and 10 Pa s and only a small amount of data above 10 Pa s. Therefore, the model performs a lot better at the lower viscosity values where there is more data available. This is also reflected in plots of the residuals versus the predicted value which showed heteroscedastic features (Figure 6-6). Residuals for lower viscosity values (<5 Pa s) are mostly within ~1 Pa s, whilst higher values have much larger residuals.

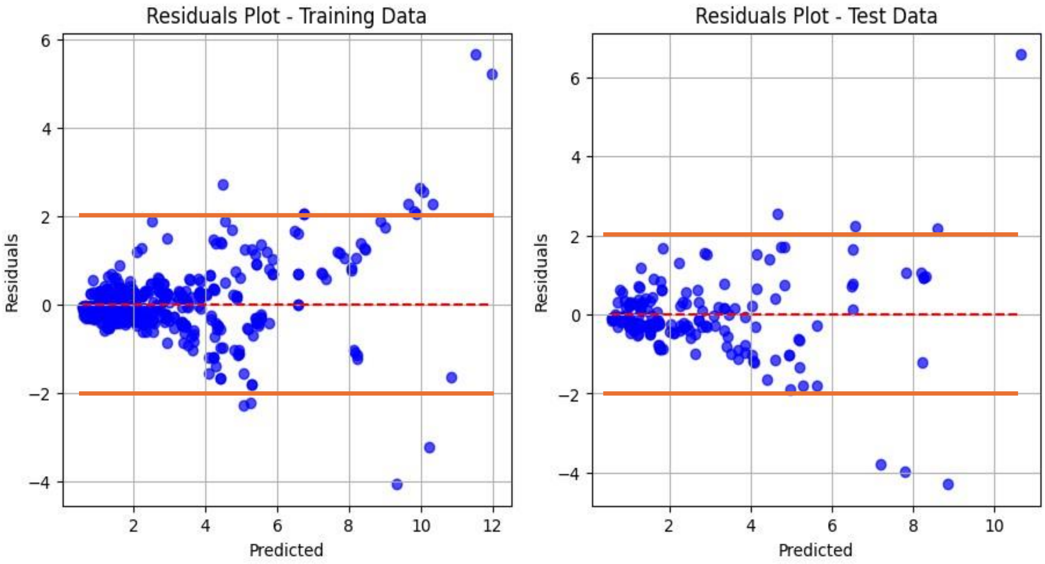

Figure 6-6. Plot of residuals versus predicted values for a) training set data b) test set data. Red dashed line = 0, orange solid line represent range of acceptable residuals.

The datapoints behind the outliers (considered as residuals greater than 2 and less than -2) were found to be for the CP fluid, and at lower fill levels (mostly 25%, sometimes 62.5%) at the minimum speeds investigated. This is when the apparent viscosity is at the very top of the range of data, as CP has the highest consistency index, and the mixer is at low speeds, thus low shear rates, resulting in the shear-thinning fluids being at higher viscosities on the flow curve.

It should be noted that the full range of data was initially used in the model, and not filtered to remove outliers. Figure 6-7 shows a box plot of the apparent viscosity shows the average, upper quartile, lower quartile and interquartile range of the data. Assuming that any data 1.5 times the interquartile range above the upper quartile is an outlier, any viscosity above 6.23 Pa s is considered an outlier. Excluding these outliers from the model may help to reduce large residuals at higher viscosity values. However, the nature of the shear-thinning fluids means that there will always be a higher proportion of data points at low viscosity than high viscosity, and it is practically difficult to collect more data points at higher viscosity. Ultimately for this reason, it was decided to include all of the data collected to determine how the random forest model manages an uneven dataset.

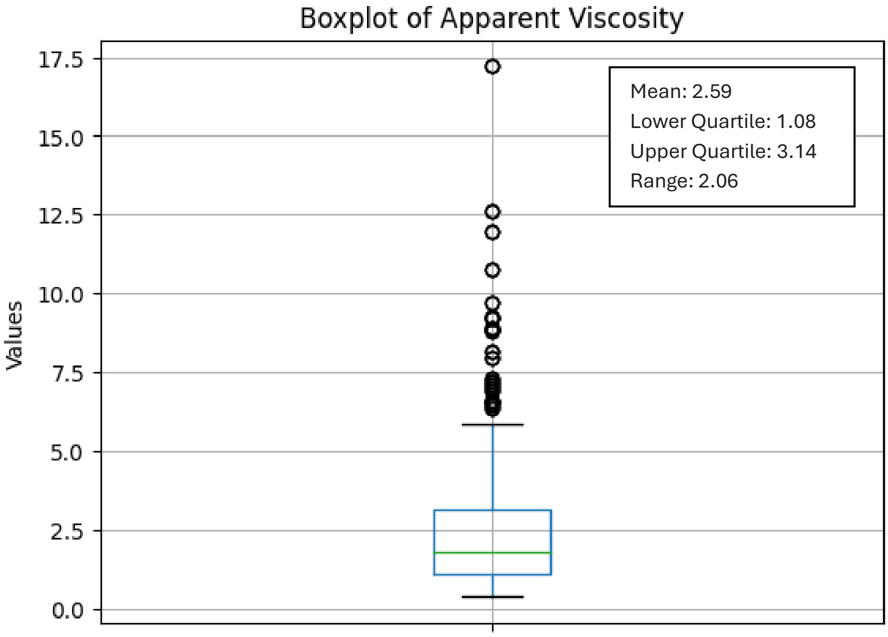

Figure 6-7. Box plot of apparent viscosity (predicted variable of RF model)

6.4 Conclusions

A random forest (RF) model for predicting the apparent viscosity of fluids of unknown rheology from torque, speed, fill level and vessel diameter was fitted using a randomised grid approach to hyperparameter tuning. A total of 150 different model fits were tested, comprised of 30 combinations of hyperparameters with 5-fold cross-validation. The performance of each model was evaluated using R^2 and mean squared error (MSE) metrics on both training and test datasets. The model with the highest R^2 and lowest MSE was initially identified as the best performer. However, it was observed that this model introduced unnecessary complexity, featuring a higher number of trees, greater maximum depth, fewer features considered per split, and a lower minimum number of samples required to split an internal node. Such complexity led to signs of overfitting, evident from the disparity between the high R^2 on the training set (0.95) and the lower R^2 on the test set (0.86). To reduce computational complexity, a third-best model with slightly fewer trees (227) and a reduced maximum depth (20) was selected. This model demonstrated comparable performance while being more efficient. Reduced complexity models which showed less tendency to overfit (similar R^2 values for the test and training set) but had a much larger MSE, which made them unsuitable. Therefore, the chosen model was the least complex option, whilst still maintaining the highest R^2 and lowest MSE. This model exhibited strong predictive capabilities, with an R^2 of 0.95 on the training data and 0.86 on the test data, indicating it effectively captured the underlying data variance. The relatively low MSE values further supported the model's accuracy. The slight difference in R^2 between the training and test sets suggested a manageable degree of overfitting, implying the model generalises well to new, unseen data.

Parity plots of predicted versus actual values showed that the model performed better for lower viscosity values, where more data was available. This was corroborated by residual plots, which displayed heteroscedasticity; residuals were smaller and more consistent at lower viscosities (<5 Pa s) but became larger at higher viscosities. The presence of outliers, particularly for CP at lower fill levels and minimum speeds, highlighted the model's limitations in certain scenarios. These outliers corresponded to higher apparent viscosities due to the fluid's high consistency index and low shear rates. Despite these outliers, it was decided to include the full dataset in the model to evaluate its performance on an uneven dataset, reflecting practical challenges in collecting high viscosity data.

Overall, the random forest model demonstrated high effectiveness in predicting viscosity for various fluids in different mixing scales. While some overfitting was observed, it was relatively controlled, and the model maintained strong generalisation capabilities. The inclusion of all data points, despite outliers, provided a realistic assessment of the model's performance across a range of viscosities. This study highlights the importance of balancing model complexity and computational efficiency while ensuring robust prediction accuracy, particularly in industrial applications involving non-Newtonian fluids.

The torque-speed data for the 2 L and 50 L mixers were analysed for various fluids. For the Newtonian fluid glycerine (GLY) at the 2 L scale, torque increased linearly with speed, as expected. Deviation at higher speeds and fill levels likely indicated a transition to the transitional flow regime. For XG, the torque was less affected by speed due to the viscoelastic properties of XG, which reduced the gradient of torque versus speed. CP showed a linear correlation between torque and speed at all fill levels. LGN demonstrated different behaviour at the two scales, thought to be related to vortexing of fluid to the walls at smaller scales.

The power curves were characterised to determine the laminar operating range and compare geometrically similar systems. Experimental values for K_p were close to values predicted using a geometry-related correlation and showed good agreeance with literature values for similar impellers, validating the torque measurements and methodology.

The shear rate constant, k_γ, and process viscosity were determined using the Couette analogy and data from glycerine. Individual values were calculated for each scale and fill level. The viscosity determined using k_γ was inputted into the RF model.

The analysis of torque-speed data, power curves, and shear rate constants provided a robust foundation for the RF model. Despite some challenges with overfitting and outliers, the model demonstrated strong predictive capabilities and generalisation across different fluid types and mixer scales. This study underscores the importance of thorough data exploration and model validation in developing reliable predictive models for industrial mixing processes. The study highlights the potential of data-driven models to be used for online prediction of viscosity during batch manufacture of formulated products.

CHAPTER 7: CONCLUSIONS & FUTURE WORK

7.1 Conclusions

This chapter consolidates the conclusions made in each results chapter, highlighting key insights and relevance to the overall aims of the project. The focus of this work was to further understanding of the manufacture and scale-up of lamellar structured liquids, particularly focusing on the role of evolving rheology and fill level on mixing efficiency and flow characteristics within the vessel. The project was split into four main objectives. The following paragraphs highlight the key conclusion made against each objective.

7.1.1 Lamellar gel network formation shows an initial viscosity peak post-surfactant addition, a cooling-induced secondary peak, and a stabilisation period after 30 minutes (Objective 1)

In Chapter 3, the formation kinetics of a lamellar gel network system comprising water, cetostearyl alcohol, and BTAC were investigated under various processing conditions (temperature, mixing time and mixing speed). By employing a rotational rheometer as the mixing vessel, the viscosity and power requirements of the system were monitored over time, revealing insights into the processing dynamics not explored before. A generic viscosity profile for the LGN formation was characterised by an initial rapid increase post-surfactant addition up to a peak value, followed by a secondary peak attributed to gel phase swelling during cooling. The values and timings of the peak viscosity values depended on time, temperature and speed. Furthermore, variations in temperature and speed significantly impacted the final rheological properties of the LGN, such as the yield stress and viscosity. Increasing the structuring stage mixing time beyond 30 minutes had minimal effect on the microstructure as the system had achieved steady-state and no further viscosity build was seen during this time.

7.1.2 Using 3D printed, scaled-down versions of factory representative mixer geometries highlighted the importance of mixing on structure formation. Regardless of mixer geometry, a minimum energy input was required to achieve a homogenous sample (Objective 2)

This work was expanded in Chapter 4 to look at the effect of mixing geometry as well. Pilot and industrial-scale agitators were scaled down and 3D-printed to produce novel rheometer geometries. Findings revealed that each geometry had distinct mixing capabilities, with differences especially notable for short processing times. Notably, the 3D-printed anchor geometry consistently produced homogeneous samples with high yield stresses, indicating its efficiency despite variations in processing conditions. However, the off-the-shelf helical rotor geometry did not exhibit the same trends as the conventional vane, underscoring the need to understand the interplay between geometry and processing conditions. Future steps involve exploring power requirements for each geometry to optimize homogeneity, viscosity, and yield stress while minimizing energy consumption, thereby facilitating potential scale-up applications.

7.1.3 The Torque Curve Method (TCM) and Couette Analogy (CA) provide effective viscosity and shear rate estimates at 100% fill level, but at

lower fill levels, particularly at 25%, significant differences arise due to variations in the mixer constant, requiring careful consideration of flow regimes and the use of techniques like the Froude number to improve accuracy (Objective 3)

Lamellar structured liquid manufacture involves the sequential addition of raw materials into the vessel, with important microstructure formation occurring when the vessel is not full. Torque and viscosity were proven to be a good indicator of completion of structure formation; thus it would be useful to measure viscosity online during manufacturing. Chapter 5 examined the influence of fill level, fluid rheology, and agitator speed on torque measurements, employing two mixer-viscometer methods (torque curve method and Couette analogy) to assess their applicability in mixing scenarios with partial fill levels. At H/T=1, both methods yielded similar *k'* values for Newtonian and power law fluids but differed for xanthan gum solution due to its viscoelastic nature. At lower fill levels, challenges in predicting shear rate and viscosity from torque-speed data arose due to the non-linearity of the data. Vortex formation and torque changes correlated closely with fluid rheology attributes. It was identified that further research is needed to address these challenges - potentially the use of non-linear modelling techniques or machine learning models for predicting viscosity in partially filled vessels in industrial settings.

7.1.4 Random forest models showed promise for use in industrial mixing processes to predict online viscosity of unknown fluids from torque, speed, fill level, and scale (Objective 4)

The final results chapter, Chapter 6, brings together ideas from the previous studies to investigate the use of random forest regression models for predicting viscosity from torque in partially filled vessels, across 3 different scales. Torque-speed data for mixing systems of similar geometry at three scales (rheometer – 45ml, lab -scale – 2L and pilot-scale, 50L) was inputted into a model which used a Metzner-Otto constant for each fill level and scale to predict shear rate and viscosity at different fill levels (25%, 62.5%, 100%). Random forest regression modelling proved somewhat useful in predicting viscosity at a given speed and shear rate for a fluid of unknown rheology, but the model did show some signs overfitting which could not be removed through hyperparameter tuning or removing outliers. The cause of this was higher data availability at lower viscosities, and less at higher viscosity (low speeds and higher viscosity fluids), which resulted in larger residuals for higher viscosity datapoints. However, overall the prediction capabilities of the model could prove useful across lab and pilot plant studies to predict the viscosity of a material during its manufacture, particularly when the vessel is partially filled.

7.2 Future Work

This section aims to explore further research areas that would enhance the outcomes of each study within this thesis, as well as future research topics/areas which have stemmed from the findings of this work.

7.2.1 Investigating Additional Processing Parameters and Complex Formulations

Further studies should explore the impact of additional processing parameters such as cooling rate and high shear homogenisation and extend the experiments to more complex formulations and ingredient ratios.

Chapter 3 only considered specific processing conditions, so future research should include cooling rate variations, high shear homogenisation stages, and adaptation of the rheometer to mimic industrial batch processes. Scaling up experiments would provide insights into more complex processes, and characterizing different formulations could reveal how these factors influence LGN properties.

7.2.2 Utilizing Advanced Characterization Methods for Enhanced Microstructure Analysis

Employing alternative techniques like DSC, x-ray tomography, or cryo-SEM could offer deeper insights into the microstructure and reveal differences undetected by current methods.

Microstructure analysis in this project was limited to oscillatory rheology and optical microscopy. Future studies could benefit from advanced methods to provide comprehensive measurements and improve understanding of LGN formation.

7.2.3 Investigating Scaling-Up and Energy Input Parameters

Chapter 4 showed that a peak viscosity value required a similar energy input (1.1 J/g) at 60°C, regardless of processing conditions. Future work should investigate whether this energy requirement is consistent at larger scales and assess its usefulness as a scale-up parameter for LGN manufacture.

7.2.4 Addressing Limitations in Mixer-Viscometer Techniques for Partial Fill Levels

Developing approximation functions and non-linear modelling techniques could expand mixer-viscometer applications for partial fills and complex fluid behaviours.

Chapter 5 highlighted the limitations of current mixer-viscometer methods at lower fill levels due to torque variations. Future studies should explore approximation models and flow visualisation techniques such as PIV, PEPT, or CFD to better understand local velocities and shear rates, addressing assumptions about fluid-impeller interactions.

7.2.5 Applying Advanced Machine Learning for Predicting Viscosity at Partial Fills

Implementing non-linear models or machine learning, such as neural networks or random forest regression, could improve predictions of viscosity from torque data. Developing machine learning approaches to predict viscosity at partial fill levels and applying these at larger scales could lead to an effective 'soft sensor' for online viscosity monitoring during manufacturing.

7.2.6 Expanding and Refining the Predictive Model

Enhancing the model from Chapter 6 with additional data inputs and improved shear rate constants could reduce overfitting and improve its predictive accuracy. Chapter 6's model showed signs of overfitting, so future work could involve using different modelling techniques and collecting more diverse data. Techniques like PIV, PEPT, or CFD could refine shear rate constants, enhancing model performance.

These future research areas aim to broaden the understanding of lamellar structured liquid manufacturing, improving process efficiency, scalability, and predictive capabilities.

References

ABATZOGLOU, N. 2015. Process Analytical Technology for Blending. *In:* CULLEN, P. J., ROMANACH, R. J., ABATZOGLOU, N. & RIELLY, C. D. (eds.) *Pharmaceutical Blending and Mixing*. John Wiley & Sons.

ADRIAN, R. J. 1991. Particle-Imaging Techniques for Experimental Fluid Mechanics. *Annual Review of Fluid Mechanics,* 23**,** 261-304.

AHMAD, I. & BENJAMIN, T.-A. 2023. Chapter 8 - Application of artifical intelligence and machine learning to food rheology. *In:* AHMED, J. & BASU, S. (eds.) *Advances in Food Rheology and Its Applications*. Woodhead Publishing.

AHMADI, D., MAHMOUDI, N., HEENAN, R. K., BARLOW, D. J. & LAWRENCE, M. J. 2020a. The Influence of Co-Surfactants on Lamellar Liquid Crystal Structures Formed in Creams. *Pharmaceutics,* 12**,** 864.

AHMADI, D., MAHMOUDI, N., LI, P., MA, K., DOUTCH, J., FOGLIA, F., HEENAN, R. K., BARLOW, D. & LAWRENCE, M. J. 2020b. Revealing the Hidden Details of Nanostructure in a Pharmaceutical Cream. *Nature Scientific Reports,* 10**,** 4082.

AHMED, U., MICHAEL, V., HOU, R., MOTHERSDALE, T., PROSSER, R., KOWALSKI, A. & MARTIN, P. 2018. An energy transport based evolving rheology in 2 high-shear rotor-stator mixers. *Chemical Engineering Research and Design,* 133**,** 398-406.

AIT-KADI, A., MARCHAL, P., CHOPLIN, L., CHRISSEMANT, A.-S. & BOUSMINA, M. 2002. Quantitative Analysis of Mixer-Type Rheometers using the Couette Analogy. *The Canadian Journal of Chemical Engineering,* 80**,** 1166-1174.

AJAYI, O., DAVIES, A. & AMIN, S. 2021. Impact of Processing Conditions on Rheology, Tribology and Wet Lubrication Performance of a Novel Amino Lipid Hair Conditioner. *Cosmetics,* 8**,** 77.

AL-SHEMMERI, M., WINDOW-YULE, K., LOPEZ-QUIROGA, E. & FRYER, P. J. 2021. Coffee bean particle motion in a spouted bed measured using Positron Emission Particle Tracking (PEPT). *Journal of Food Engineering,* 311**,** 110709.

ALBERINI, F., ALBANO, A., SINGH, P., CHRISTODOULOU, C., MONTANTE, G., MULATA, F. & PAGLIANTI, A. 2024. Fluid dynamics and power consumptions in a single use stirred tank adopted in the pharmaceutical industry. *Chemical Engineering Research & Design,* 204**,** 159-171.

ALBERINI, F., MALUTA, F., PAGLIANTI, A. & MONTANTE, G. 2023. Power Consumption and Fluid Mixing in a Scale-Down Geometry of a Stirred Digester for Biogas Production. *ACS Engineering AU,* 3**,** 102-113.

ALDERMAN, N. J. 1997. Non-Newtonian Fluids: Guide to Classification and Characteristics. ESDU International PLC.

ALESSANDRINI, A. & PIRACCINI, B. M. 2016. Essential of Hair Care Cosmetics. *Cosmetics,* 3**,** 34.

ALTUNA, L., ROMANO, R. C. O., PILEGGI, R. G., RIBOTTA, P. D. & TADINI, C. 2016a. Torque Measurement in Real Time during Mixing and Kneading of Bread Dough with High Content of Resistant Maize Starch Enzymes. *International Journal of Food Engineering,* 12**,** 719-728.

ALTUNA, L., ROMANO, R. C. O., PILEGGI, R. G., RIBOTTA, P. D. & TADINI, C. C. 2016b. Torque Measurement in Real Time during Mixing and Kneading of Bread Dough with High Content of Resistant Maize Starch and Enzymes. *International Journal of Food Engineering,* 12**,** 719-728.

AMADOR, J., HARTEL, R. & RANKIN, S. 2017. The Effects of Fat Structures and Ice Cream Mix Viscosity on Physical and Sensory Properties of Ice Cream. *Journal of Food Science,* 82**,** 1851-1860.

AMEUR, H. & KAMLA, Y. 2020. Geometrical modifications of the anchor impeller to enhance the overall performances in stirred tanks. *Instal,* 6**,** 42-45.

ANNE-ARCHARD, D., MAROUCHE, M. & BOISSON, H.-C. 2006. Hydrodynamics and Metzner-Otto correlation in stirred vessels for yield stress fluids. *Chemical Engineering Journal,* 125**,** 15-24.

ASCANIO, G., CASTRO, B. & GALINDO, E. 2004. Measurement of Power Consumption in Stirred Vessels - A Review. *Chemical Engineering Research and Design,* 92**,** 1282-1290.

AWAD, T. S., JOHNSON, E. S., BUREIKO, A. & OLSSON, U. 2011. Colloidal structure and physical properties of gel networks containing anoinic surfactant and fatty alcohol mixture. *Journal of Dispersion Science and Technology,* 32**,** 807-815.

AWAD, T. S., MOHARRAM, H. A., SHALTOUT, O. E., ASKER, D. & YOUSSEF, M. M. 2012. Applications of ultrasound in analysis, processing and quality control of food: A review. *Food Research International,* 48**,** 410-427.

BAKALIS, S., COX, P. W., RUSSELL, A. B., PARKER, D. J. & FRYER, P. J. 2006. Development and use of positron emitting particle tracking (PEPT) for velocity measurements in viscous fluids in pilot scale equipment. *Chemical Engineering Science,* 61**,** 1864-1877.

BALLMAN, C. & MUELLER, B. W. 2008. Stabilizing Effect of Cetostearyl Alcohol and Glycerylmonstearate as Co-emulsifiers on Hydrocarbon-free O/W Glyceride Creams. *Pharmaceutical Development and Technology,* 13**,** 433-445.

BANERJEE, A. 2013. *Power dissipation and mixing time in a partially filled pharmaceutical reactor equipped with a retreat-blade impeller at different fill ratios.* Master of Science in Chemical Engineering Master's Thesis, New Jersey Institute of Technology.

BARIGOU, M. 2004. PARTICLE TRACKING IN OPAQUE MIXING SYSTEMS: An Overview of the Capabilities of PET and PEPT. *Chemical Engineering Research and Design,* 82**,** 1258-1267.

BARNES, H. A. 1995. A review of the slip (wall depletion) of polymer solutions, emulsions and particle suspensions in viscometers: its cause, character and cure. *Journal of Non-Newtonian Fluid Mechanics,* 26**,** 221-231.

BARRY, B. W. & SAUNDERS, G. M. 1970. The Self-Bodying Action of the Mixed Emulsifier Cetrimide/Cetostearyl Alcohol. *Journal of Colloid and Interface Science,* 34**,** 300-315.

BBOSA, B., DELLECASE, E., VOLK, M. & OZBAYOGLU, E. 2017. Development of a mixer-viscometer for studying rheological behavior of settling and non-settling slurries. *Journal of Petroleum Exploration and Production Technology,* 7**,** 511-520.

BEHESHTI, N. 2022. *Random Forest Regression* [Online]. Medium. Available: https://towardsdatascience.com/random-forest-regression-5f605132d19d [Accessed December 10 2023].

BHUSHAN, B. 2008. Nanoscale characterization of human hair and hair conditioners. *Progress in Materials Science,* 53**,** 585-710.

BHUSHAN, B., WEI, G. & HADDAD, P. 2005. Friction and wear studies of human hair and skin. *Wear,* 259**,** 1012-1021.

BOLDUC, C. & SHAPIRO, J. 2001. Hair Care Products: Waving, Straightening, Conditioning, and Coloring. *Clinics in Dermatology,* 19**,** 431-436.

BOM, S., JORGE, J., RIBEIRO, H. M. & MARTO, J. 2019. A step forward on sustainability in the cosmetics industry: A review. *Journal of Cleaner Production,* 225**,** 270-290.

BONACCORSO, G. 2018. *Machine Learning Algorithms: Popular algorithms for data science and machine learning*, Packt Publishing Ltd.

BONNOT, S., CABARET, F., FRADETTE, L. & TANGUY, P. A. 2007. Characterization of Mixing Patterns in a Coaxial Mixer. *Chemical Engineering Research and Design,* 85**,** 1129-1135.

BOULLION, C. 1988. Shampoos and hair conditioners. *Clinics in Dermatology,* 6**,** 83-92.

BOWLER, A. L., BAKALIS, S. & WATSON, N. J. 2020. A review of in-line and on-line measurement techniques to monitor industrial mixing processes. *Chemical Engineering Research and Design,* 153**,** 463-495.

BRITO-DE LA FUENTE, E., L., C. & TANGUY, P. A. 1997. Mixing with helical ribbon impellers: Effect of Highly Shear Thinning Behaviour and Impeller Geometry. *Trans IChemE,* 75**,** 45-52.

BRITO DE LA FUENTE, E., CHOPLIN, L. & TANGUY, P. A. 1997. Mixing with helical ribbon impellers: effect of highly shear thinning behaviour and impeller geometry. *Chemical Engineering Research & Design,* 75**,** 45-52.

BRO, R. & SMILDE, A. K. 2014. Principal component analysis. *Analytical Methods,* 6.

BROWN, D. A. R., JONES, P. N. & MIDDLETON, J. C. 2004. Experimental Methods. Part A; Measuring Tools and Techniques for Mixing and Flow Visualization Studies. *In:* PAUL, E. L., ATIEMO-OBENG, V. A. & KRESTA, S. M. (eds.) *Handbook of Industrial Mixing.* Hoboken, New Jersey: John Wiley & Sons, Inc.

CAROU-SENRA, P., ONG, J. J., CASTRO, B. M., SEAONE-VIANO, I., RODRIGUEZ-POMBO, L., CABALAR, P., ALVAREZ-LORENZO, C., BASIT, A. W., PÉREZ, G. & GOYANES, A. 2023. Predicting pharmaceutical inkjet printing outcomes using machine learning. *International Journal of Pharmaceutics: X,* 5**,** 100181.

CARREAU, P. J., CHABRA, R. P. & CHENG, J. 1993. Effect of rheological properties on power consumption with helical ribbon agitators. *Am. Inst. Chem. Eng. J. ,* 39**,** 1421-1430.

CASTELL-PEREZ, M. E. & STEFFE, J. F. 1990. Evaluating shear rates for power law fluids in mixer viscometry. *Journal of Texture Studies,* 21**,** 439-453.

CAZACLIU, B. 2008. In-mixer measurements for describing mixture evolution during concrete mixing. *Chemical Engineering Research & Design,* 86**,** 1423-1433.

CENTRE FOR INDUSTRIAL RHEOLOGY. 2014. *Rheology Testing of Hair Conditioners* [Online]. Available: https://www.rheologylab.com/articles/cosmetic-personal-care/rheology-testing-conditioners/ [Accessed September 2023].

CENTRE FOR PROCESS INNOVATION. 2018. *Updated Common Vision and Roadmap for Formulated Products* [Online]. CPI. Available: https://www.formulation.org.uk/images/stories/FormulaX/Presentations/Formula%20X%20-%20Isabel%20Mira%20-%202030%20Formulation%20Roadmap.pdf [Accessed 10 January 2024].

CHAND, R., BREMNER, D. H., NAMKUNG, K. C., COLLIER, P. J. & GOGATE, P. R. 2007. Water disinfection using the novel approach of ozone and a liquid whistle reactor. *Biochemical Engineering Journal,* 35**,** 357-364.

CHARA, Z. & KYSELA, B. 2019. Comparison of saw tooth impeller and Rushton turbine. *AIP Conference Proceedings,* 2116.

CHAVEZ-MONTES, B. E., CHOPLIN, L. & SCHAER, E. 2003. Rheo-reactor for studying the processing and formulation effects on structural and rheological properties of ice cream mix, aerated mix and ice cream. *Polymer International,* 52**,** 572-575.

CHHABRA, R. P. 2010. Non-Newtonian Fluids: An Introduction. *In:* KRISHNAN, J. M., DESHPANDE, A. P. & KUMAR, P. B. S. (eds.) *Rheology of Complex Fluids.* New York, NY: Springer.

CHOPLIN, L. & MARCHAL, P. 2010. Mixer-Type Rheometry. *Rheology.* EOLSS Publications.

CHOPLIN, L., TORANDELL, S. & SERVOIN, J. 2009. In situ rheological monitoring in semi-batch emulsification process for cosmetic lotion production. *The Canadian Journal of Chemical Engineering,* 76**,** 506-510.

CLAIRANT CORPORATION 2018. Genamin BTLF Safety Data Sheet. Charlotte, NC: Clairant Corporation.

COLAFEMMINA, G., PALAZZO, G., MATEOS, H., AMIN, S., FAMEAU, A.-L., OLSSON, U. & GENTILE, L. 2020. The cooling process effect on the bilayer phase state of the CTAC/cetearyl alcohol/water surfactant gel. *Colloids and Surfaces A: Physicochemical and Engineering Aspects,* 587**,** 124821.

COLLIAS, D. J. & PRUD'HOMME, R. K. 1985. The Effect of Fluid Elasticity on Power Consumption and Mixing Times in Stirred Tanks. *Chemical Engineering Science,* 40**,** 1495-1505.

COPPOLA, L., NICOTERA, I. & OLIVIERO, C. 2005. Dynamic Rheological Analysis of MLVs and Lamellar Phases in the System C12E4/D2O. *Applied Rheology,* 15, 230-237.

CORTADA-GARCIA, M., DORE, V., MAZZEI, L. & ANGELI, P. 2017. Experimental and CFD studies of power consumption in the agitation of highly viscous shear thinning fluids. *Chemical Engineering Research and Design,* 119, 171-182.

CORTADA-GARCIA, M., WEHELIYE, W. H., DORE, V., MAZZEI, L. & ANGELI, P. 2018. Computational fluid dynamic studies of mixers for highly viscosu shear thinning fluids and PIV validation. *Chemical Engineering Science,* 179, 133-149.

CULLEN, P. J., O'DONNELL, C. P. & HOUSKA, M. 2003. Rotational Rheometry Using Complex Geometries - A Review. *Journal of Texture Studies,* 34, 1-20.

CUNHA, C. L., TORRES, A. R. & LUNA, A. S. 2020. Multivariate regression models obtained from nea-infrared spectroscopy data for prediction of the physical properties of biodiesel and its blends. *Fuel,* 261, 116344.

CUNNINGHAM, G. E., ALBERINI, F., SIMMONS, M. J. H. & O'SULLIVAN, J. J. 2021. Understanding the effects of processing conditions on the formation of lamellar gel networks using a rheological approach. *Chemical Engineering Science,* 242, 116752.

CUNNINGHAM, G. E., DESHPANDE, S., SIMMONS, M. J. H. & O'SULLIVAN, J. J. 2023. Investigating mixer-viscometer techniques for partially filled stirred tanks. *Chemical Engineering Science,* 282, 119340.

CYRIAC, F., LUGT, P. M. & BOSMAN, R. 2016. On a New Method to Determine the Yield Stress in Lubricating Greas. *Tribology & Lubrication Technology.* Taylor & Francis.

D'SOUZA, P. & RATHI, S. K. 2015. Shampoo and Conditioners: What A Dermatologist Should Know? *Indian Journal of Dermatology,* 60, 248-254.

DATTA, A., TANMAY, V. S., TAN, G. X., REYNOLDS, G., W., JAMADAGNI, S. N. & LARSON, R. G. 2020. Characterizing the rheology, slip, and velocity profiles of lamellar gel networks. *Journal of Rheology,* 64, 851-862.

DAVIES, A. R. & AMIN, S. 2020. Microstructure design of CTAC:FA and BTAC:FA lamellar gels for optimized rheological performance utilizing automated formulation platform. *International Journal of Cosmetic Science,* 42, 259-269.

DELAPLACE, G., LEUILET, J.-C. & RONSE, G. 2000a. Power Requirement when Mixing a Shear-Thickening Fluid with a Helical Ribbon Impeller Type. *Chemical Engineering & Technology,* 23, 329-335.

DELAPLACE, G., LEULIET, J. C. & RELANDEAU, V. 2000b. Circulation and mixing times for helical ribbon impellers. Review and Experiments. *Experiments in Fluids,* 28, 170-182.

DELAPLACE, G., TORREZ, C., ANDRÉ, C., LEULIET, J.-C. & FILLAUDEAU, L. CFD Simulation of Foodstuff Flows in an Agitated Vessel. 1st International Conference on simulation in food and bioindustries, 2000c Nantes, France. Society for Computer Simulation International.

DELBRIDGE, J. N., BARRETT, T. A., DUCCI, A. & MICHELETTI 2023. Power, mixing and flow dynamics of the novel Allegro stirred tank reactor. *Chemical Engineering Science,* 271, 118545.

DICKEY, D. S. 2015. Tackling Difficult Mixing Problems. *Chemical Engineering Process.*

DUERR-AUSTER, N., KOHLBRECHER, J., ZUERCHER, T., GUNDE, R., FISCHER, P. & WINDHAB 2007. Microstructure and Stability of a Lamellar Liquid Crystalline and Gel Phase Formed by a Polyglycerol Ester Mixture in Dilute Aqueous Solution. *Langmuir,* 23, 12827-12834.

ECCLESTON, G. M. 1985. Phase transitions in ternary systems and oil-in-water emulsions containing cetrimide and fatty alcohols. *International Journal of Pharmaceutics,* 27, 311-323.

ECCLESTON, G. M. 1989. Multiple-phase oil-in-water emulsions. *Journal of the Society of Cosmetic Chemists,* 41, 1-22.

ECCLESTON, G. M. 1997. Functions of mixed emulsifiers and emulsifying waxes in dermatological lotions and creams. *Colloids and Surfaces A: Physicochemical and Engineering Aspects,* 123-124**,** 169-182.

ECCLESTON, G. M., BEHAN-MARTIN, M. K., JONES, G. R. & TOWNS-ANDREWS, E. 2000. Synchotron X-ray investigations into the lamellar gel phase formed in pharmaceutical creams prepared with cetrimide and fatty alcohols. *International Journal of Pharmaceutics,* 203**,** 127-139.

EDWARDS, M. F. 2006. Product Engineering - Some Challenges for Chemical Engineers. *Trans IChemE,* 84**,** 255-260.

ESPINOSA-SOLARES, T., BRITO-DE LA FUENTE, E., TECANTE, A., MEDINA-TORRES, L. & TANGUY, P. A. 2002. Mixing Time in Rheologically Evolving Model Fluids by Hybrid Dual Mixing Systems. *Chemical Engineering Research and Design,* 80**,** 817-823.

ESPINOSA-SOLARES, T., BRITO-DE LA FUENTE, E., TECANTE, A. & TANGUY, P. A. 2001. Flow Patterns in Rheologically Evolving Model Fluids Produced by Hybrid Dual Mixing Systems. *Chemical Engineering & Technology,* 24**,** 913-918.

ESPINOZA, C. J. U., SIMMONS, M. J. H., ALBERINI, F., MIHAILOVA, O., ROTHMAN, D. & KOWALSKI, A. J. 2018. Flow studies in an in-line Silverson 150/250 high shear mixer using PIV. *Chemical Engineering Research and Design,* 132**,** 989-1004.

FAIRHURST, D. J., BAKER, M. E., SHAW, N. & EGELHAAF, S. U. 2008. Swelling and shrinking kinetics of a lamellar gel phase. *Applied Physics Letters,* 92**,** 174105.

FERNANDES, C., MEDRONHO, B., ALVES, L. & RASTEIRO, M. G. 2023. On Hair Care Physiochemistry: From Structure and Degredation to Novel Biobased Conditioning Agents. *Polymers (Basel),* 15**,** 608.

FORMULACTION. 2016. *Mimicking real life behaviour of common cosmetic products* [Online]. Available: https://www.microtrac.com/company/formulaction/ [Accessed January 25 2024].

FRANCK, A. *Non-standard geometries for rheological characterization of complex fluids* [Online]. Available: https://www.tainstruments.com/pdf/literature/AAN014e_V1_Non_standard_geometries_for_rheological_testing.pdf [Accessed 10 February 2022].

FRANCO, J. M., DELGADO, M. A., VALENCIA, C., SANCHEZ, M. C. & GALLEGOS, C. 2005. Mixing rheometry for studying the manufacture of lubricating greases. *Chemical Engineering Science,* 60**,** 2409-2418.

FUKUSHIMA, S. & YAMAGUCHI, M. 1983. The effect of cetostearyl alcohol in cosmetic emulsions. *Cosmetics & Toiletries,* 98**,** 89-102.

FUKUSHIMA, S., YAMAGUCHI, M. & HARUSAWA, F. 1977. Effect of Cetostearyl Alcohol on Stabilization of Oil-in-Wayter Emulsion II: Relation between Crystal Form of the Alcohol and Stability of the Emulsion. *Journal of Colloid and Interface Science,* 59**,** 159-165.

GAINI, C., SCHER, J., SCHUCK, P., HARDY, J., DESOBRY, S. & BANON, S. 2006. The dissolution behaviour of native phosphocaseinate as a function of concentration and temperature using a rheological approach. *International Dairy Journal,* 16**,** 1427-1434.

GAVAZZONI DIAS, M. F. R. 2015. Hair Cosmetics: An Overview. *International Journal of Trichology,* 7**,** 2-15.

GENTILE, L., BEHRENS, M. A., PORCAR, L., BUTLER, P., WAGNER, N. J. & OLSSON, U. 2014. Multilamellar Vesicle Formation from a Planar Lamellar Phase under Shear Flow. *Langmuir,* 30**,** 8316-8325.

GENTILE, L., SILVA, B. F. B., BALOG, S., MORTENSEN, K. & OLSSON, U. 2012. Strutural transitions induced by shear flow and temperature variation in a nonionic surfactant/water system. *Journal of Colloid and Interface Science,* 372**,** 32-39.

GERMANOTTA, S. & KHAYAT, N. 2011. Hair. Santa Monica, California: Interscope Records.

GHANEM, A., LEMENAND, T., DELLA VALLE, D. & PEERHOSSAINI, H. 2014. Static mixers: Mechanisms, applications and characterization methods - A review. *Chemical Engineering Research & Design,* 92**,** 205-228.

GHOSH, S., RAY, A., PRMANIK & NABAKUMAR 2020. Self-assembly of surfactants: An overview on general aspects of amphiphiles. *Biophysical Chemistry,* 265**,** 106429.

GOUSSARD, V., AUBRY, J.-M. & NARDELLO-RATAJ, V. 2022. Bio-based alternative to volatile silicones: Relationships between chemical structure, physiochemical properties and functional performances. *Advances in Colloid and Interface Science,* 304**,** 102679.

GRABENHOFER, R. 2022. Seven Top Trends in Sustainable Cosmetics R&D. *IFSCC Magazine,* 25**,** 141-146.

GROLLIER, J.-F. & RICHOUX, I. 1990. *Cosmetic preparation for th care of hair and use of the said composition*. United States patent application.

GUO, C., WANG, J., CAO, F., LEE, R. J. & ZHAI, G. 2010. Lyotropic liquid crystal systems in drug delivery. *Drug Discovery Today,* 15**,** 1032-1040.

HALL, S. 2012. 16 - Blending and Agitation. *In:* HALL, S. (ed.) *Branan's Rules of Thumb for Chemical Engineers*. Fifth ed.: Butterworth-Heinemann.

HALL, S., COOKE, M., EL-HAMOUZ, A. & KOWALSKI, A. 2011. Droplet break-up by in-line Silverson rotor-stator mixer. *Chemical Engineering Science,* 66**,** 2068-2079.

HAROON, K., ARAFEH, A., CUNLIFFE, S., MARTIN, P., RODGERS, T., MENDOZA, C. & BAKER, M. 2020. Comparison of Individual and Integrated Inline Raman, Near-Infrared, and Mid-Infrared Spectroscopic Models to Predict the Viscosity of Micellar Liquids. *Applied Spectroscopy,* 74**,** 819-831.

HATAKEYAMA, K., YAMAGATA, Y., TAKASAKI, Y., MIYAMOTO, K. & TAKASHI, T. 2023. Effects of temperature and shear conditions on lamellar-to-onion transition in nonionic surfactant/water systems. *Colloids and Surfaces A: Physicochemical and Engineering Aspects,* 659**,** 130755.

HBM. 2024. How to Select a Rotating Torque Sensor. Available: https://www.hbm.com/fileadmin/mediapool/files/technical-articles-technotes-white-papers/how_to_select_a_rotation_torque_sensor.pdf [Accessed February 2].

HEERTJE, I., ROIJERS, E. C. & HENDRICKX, H. A. C. M. 1998. Liquid Crystalline Phases in the Structuring of Food Products. *LWT - Food Science and Tehcnology,* 31**,** 387-396.

HEFFT, D. I., BLAKE, N. R., FARHOUD, A., FARRAR, E., O'SULLIVAN, J. J. & ALBERINI, F. 2023. Monitoring Rheological Changes Using Acoustic Emissons for Complex Formulated Fluids Manufacturing. *Chemical Engineering & Technology,* 46**,** 2245-2258.

HILL, M. 2004. Product and Process Design for Structured Products. *AIChE Journal,* 50**,** 1656-1661.

HOBBS, J. E. 2020. Food supply chains during the COVID-19 pandemic. *Canadian Journal of Agricultural Economics,* 68**,** 171-176.

HOFFMANN, M., SCHLÜTER, M. & RÄBIGER, N. 2006. Experimental investigation of liquid-liquid mixing in T-shaped micro-mixers using μ-LIF and μ-PIV. *Chemical Engineering Science,* 61**,** 2698-2976.

HOLLAND, F. A. & BRAGG, R. 1995. Pumping of Liquids. *In:* HOLLAND, F. A. & BRAGG, R. (eds.) *Fluid Flow for Chemical Engineers*. Butterworth-Heinemann.

HOUGH, J. A., CASUGBO, C., SERRIDGE, D., FLANAGAN, M. & NAUGHTON, J. M. 2013. *Process*. Global patent application.

HUANG, Y. & GUI, S. 2018. Factors affecting the structure of lyotropic liquid crystals and the correlation between structure and drug diffusion. *RSC Advances,* 8**,** 6978-6987.

HYUN, K., KIM, S. H., AHN, K. H. & LEE, S. J. 2002. Large amplitude oscillatory shear as a way to classify the complex fluids. *Journal of non-Newtonian Fluid Mechanics,* 107**,** 51-65.

IBM. 2023. *What is principal component analysis (PCA)?* [Online]. Available: https://www.ibm.com/topics/principal-component-analysis [Accessed 18th May 2024].

IBM. 2024. *What is a neural network?* [Online]. Available: https://www.ibm.com/topics/neural-networks [Accessed 6 June 2024].

IMARC GROUP. 2022. Hair Conditioner Market: Global Industry Trends, Share, Size, Growth, Opportunity and Forecast. Available: https://www.imarcgroup.com/hair-conditioner-market#:~:text=The%20global%20hair%20conditioner%20market,6.19%25%20during%202024%2D2032.&text=Hair%20conditioner%20is%20a%20hair,the%20texture%20of%20the%20hair.

INGRAM, A., HAUSARD, M., FAN, X., PARKER, D. J., SEVILLE, J. P. K., FINN, N. & EVANS, M. Portable Positron Emission Particle Tracking (PEPT) for Industrial Use. 2007 Vancouver. Engineering Conferences International Digital Archives.

IRANSHAHI, A., HENICHE, M., BERTRAND, F. & TANGUY, P. A. 2016. Numerical investigation of the mixing efficiency of the Ekato Paravisc impeller. *Chemical Engineering Science,* 61**,** 2609-2617.

ITO, M., KOSAKA, Y., KAWABATA, Y. & KATO, T. 2011. Transition processes from the lamellar to the onion state with increasing temperature under shear flow in a nonionic surfactant/water system studied by Rheo-SAXS. *Langmuir,* 27**,** 7400-7409.

IWATA, T. 2017a. Chapter 25 - Lamellar Gel Network. *In:* SAKAMOTO, K., LOCHHEAD, R. Y., MAIBACH, H. I. & YAMASHITA, Y. (eds.) *Cosmetic Science and Technology.* Kobe: Elsevier.

IWATA, T. 2017b. Stabilization of Emulsions by a-Gel. *Pharm. Tech. Japan,* 33**,** 75-82.

IWATA, T. & ARAMAKI, K. 2013. Effect of the Behenyl Trimethyl Ammonium Counterion on the Lamellar Gel Property. *International Federation of Societies of Cosmetic Chemists Magazine.*

JAHANGIRI, M. 2008. Shear Rates in Mixing of Viscoelastic Fluids by Helical Ribbon Impeller. *Iranian Polymer Journal,* 17**,** 831-841.

JAMES, G., WITTEN, D., HASTIE, T., TIBSHIRANI, R. & TAYLOR, J. 2023. *An Introduction to Statistical Learning : With Applications in Python,* Cham, SWITZERLAND, Springer International Publishing AG.

JIRA, C. & TOFFEL, M. W. 2013. Engaging Supply Chains in Climate Change. *Manufacturing & Service Operations Management,* 15**,** 1-19.

JO, H. J., JANG, H. K., KIM, Y. J. & HWANG, W. R. 2017. Process viscometry in flows of non-Newtonian fluids using an anchor agitator. *Korea-Australie Rheology Journal,* 29**,** 317-323.

JOHN, T. P., CARILLO DE HERT, S., REN, Z., KOWALSKI, A. & RODGERS, T. L. 2020. Predicting Droplet Size Distributions of Emulsions Produced in a Sonolator. *Industrial & Engineering Chemistry Research,* 59**,** 6681-6695.

JUNGINGER, H. E. 1984. Colloidal Structures of O/W Creams. *Pharmaceutisch Weekblad Scientific Edition,* 6**,** 141-149.

KAMLA, Y., AMEUR, H., ILIES ARAB, M. & AZEDDINE, B. 2021. Data on the hydrodynamics and power consumption induced by modified anchor impellers in cylindrical tanks. *Data in Brief,* 39**,** 107699.

KASPAREK, M. & NOVAKOVA, L. 2022. High optical quality models for flow visualization and PIV measurement. *Experimental Fluid Mechanics.* Czech Republic: EPJ Web of Conferences.

KAZEMZADEH, A., EIN-MOZAFFARI, F., LOHI, A. & PAKZAD, L. 2017. Intensification of mixing shear-thinning fluids possessing yield stress with coaxial mixers composed of two different central impellers and an anchor. *Chemical Engineering and Processing: Process Intensification,* 111**,** 101-114.

KHOPKAR, A. R., PANASKAR, S. S., PANDIT, A. B. & RANADE, V. V. 2005. Characterization of gas-liquid flows in stirred vessels using pressure and torque fluctuations. *Industrial & Engineering Chemistry Research,* 44**,** 3298-3311.

KNIGHT, P. C., SEVILLE, J. P. K., WELLM, A. B. & INSTONE, T. 2001. Prediction of impeller torque in high shear powder mixers. *Chemical Engineering Science,* 56**,** 4457-4471.

KOO, J. 2021. Batch Process vs Continuous Process for Food Manufacturers. *Tulip,* [Online]. Available: https://tulip.co/blog/batch-process-vs-continuous-process/ [Accessed July 14].

KUGLER, C., DIETL, K., HOCHREIN, T., HEIDEMEYER, P. & BASTIAN, M. 2014. Robust soft sensor based on an artifial neural network for real-time determination of the melt viscosity of polymers. *AIP Conference Proceedings,* 1593**,** 213-216.

LABA, D. 1997. An Introduction to Rheology. Weymouth, Dorset: International Federation of the Societies of Cosmetic Chemists.

LAI, K.-Y. 2005. *Liquid Detergents,* Boca Raton, CRC Press.

LAMBERTO, D. J., MUZZIO, F. J. & SWANSON, P. D. 1996. Using Time-Dependent RPM to Enhance Mixing in Stirred Vessels. *Chemical Engineering Science,* 51**,** 733-741.

LANGFORD, S., WIGGINS, C., TENPENNY, D. & RUGGLES, A. 2016. Positron Emission Particle Tracking (PEPT) for Fluid Flow Measurements. *Nuclear Engineering and Design,* 302**,** 81-89.

LARSON, R. G. 1999. *The Structure and Rheology of Complex Fluids,* New York, Oxford University Press.

LAURSEN, F. 2023. The Latest FMCG Sustainability Trends and Mounting Importance of ESG Data. *ADEC Marketplace,* [Online]. Available: https://marketplace.adec-innovations.com/blogs/the-latest-fmcg-sustainability-trends-and-mounting-importance-of-esg-data/ [Accessed May 16].

LEADBEATER, T. W. & PARKER, D. J. 2011. A modular positron camera for the study of industrial processes. *Nuclear Instruments and Methods in Physics Research Section A: Accelerators, Spectrometers, Detectors and Associated Equipment,* 652**,** 646-649.

LISTER, J. & BOGLE, I. D. L. 2019. Smart Process Manufacturing for Formulated Products. *Engineering,* 5**,** 1003-1009.

LIU, E.-H. & MCGRATH, K. M. 2005. Emulsion microstructure and energy input, roles in emulsion stability. *Colloids and Surfaces A: Physicochemical and Engineering Aspects,* 262**,** 101-112.

LUNT, M. 2013. Introduction to statistical modelling: linear regression. *Rheumatology,* 54**,** 1137-1140.

MAC NAMARA, C., GABRIELE, A., AMADOR, C. & BAKALIS, S. 2012. Dynamics of textile motion in a front-loading domestic washing machine. *Chemical Engineering Science,* 75**,** 14-27.

MACHIN, T. D., WEI, H.-Y., GREENWOOD, R. W. & SIMMONS, M. J. H. 2018. In-pipe rheology and mixing characterisation using electrical resistance sensing. *Chemical Engineering Science,* 187**,** 327-341.

MACKEY, K. L., MORGAN, R. G. & STEFFE, J. F. 1987. Effects of shear-thinning behaviour on mixer viscometry techniques. *Journal of Texture Studies,* 18**,** 231-240.

MAINGONNAT, J. F., DOUBLIER, J. L., LEFEBVRE, J. & DELAPLACE, G. 2008. Power consumption of a double helical ribbon impeller with Newtonian and shear-thinning fluids and during gelation of a iota-carrageenan solution. *Journal of Food Engineering,* 87**,** 82-90.

MARTIN, T. W., SEVILLE, J. P. K. & PARKER, D. J. 2007. A general method for quantifying dispersion in multiscale systems using trajectory analysis. *chemical Engineering Science,* 62**,** 3419-3428.

MARTINS, A. M. & MARTO, J. M. 2023. A sustainable life cycle for cosmetics: From design and development to post-use phase. *Sustainable Chemistry and Pharmacy,* 35.

MEACHUM, V. 2023. *Breaking Down Behentrimonium Methosulfate in Hair Products* [Online]. Available: https://themestizamuse.com/breaking-down-behentrimonium-methosulfate-in-hair-products/ [Accessed October 4 2023].

METZNER, A. B. & OTTO, R. E. 1957. Agitation of non-Newtonian fluids. *AIChE Journal,* 3.

MIHAILOVA, O., LIM, V., MCCARTHY, M. J., , M., KATHRYN L. & BAKALIS, S. 2015. Laminar mixing in a SMC static mixer evaluated by positron emission particle tracking (PEPT) and magnetics resonance imaging (MRI). *Chemical Engineering Science,* 137**,** 1014-1023.

MIHAILOVA, O., MOTHERSDALE, T., RODGERS, T., REN, Z., WATSON, S., LISTER, V. & KOWALSKI, A. 2018. Optimisation of mixing performance of helical ribbon mixers for high throughput applications using computational fluid dynamics. *Chemical Engineering Research and Design,* 132**,** 942-953.

MINGUET, M., SUBIRATS, N., CASTÁN, P. & SAKAI, T. 2010. Behenamidopropyl Dimethylamine: unique behaviour in solution and in hair care formulations. *International Journal of Cosmetic Science,* 32**,** 246-257.

MINTEL. 2023. A year of innovation in haircare, styling & colour, 2023. Available: https://clients.mintel.com/content/report/a-year-of-innovation-in-haircare-styling-colour-2023?fromSearch=%3Ffilters.category%3D5%26last_filter%3Dcategory%26resultPosition%3D1 [Accessed June 22].

MIYAKE, M. & YAMASHITA, Y. 2017. Chapter 24 - Molecular Structure and Phase Behaviour of Surfactants. *In:* SAKAMOTO, K., LOCHHEAD, R. Y., MAIBACH, H. I. & YAMASHITA, Y. (eds.) *Cosmetic Science and Technology: Theoretical Principles and Applications*. Elsevier.

MOKHEFI, A. 2024. Hydrodynamic and thermal performance analysis of an inclined anchor impeller designed for yield stress food mixing applications. *Food and Bioproducts Processing,* 143**,** 255-270.

MORAES, C., ANJOS, J. L. V., MARUNO, M., ALONSO, A. & ROCHA-FILHO 2018. Development of lamellar gel phase emulsion containing baru oil (Dipteryx alata Vog.) as a prospective delivery system for cutaneous application. *Asian Journal of Pharmaceutical Sciences,* 13**,** 183-190.

MORTENSEN, H. H., ARLOV, D., INNINGS, F. & HAKANSSON, A. 2018. A validation of commonly used CFD methods applied to rotor stator mixers using PIV measurements of fluid velocity and turbulence. *Chemical Engineering Science,* 177**,** 340-353.

MOSOROV, V. 2015. 19 - Applications of tomography in reaction engineering (mixing process). *In:* WANG, M. (ed.) *Industrial Tomography*. Woodhead Publishing.

MOTAMEDVAZIRI, S. 2012. Single and multiphase mixing in partially filled stirred vessels. New Jersey Institute of Technology.

MOWBRAY, M., KAY, H., KAY, S., CASTRO CAETANO, P., HICKS, A., MENDOZA, C., LANE, A., MARTIN, P. & ZHANG, D. 2022. Probablistic machine learning based soft-sensors for product quality prediction in batch processes. *Chemometrics and Intelligent Laboratory Systems,* 228.

MUELLER, J. 2023. Dove Launces Body Wash With 24-Hour Renewing MicroMoisture. *Cosmetics & Toiletries*.

MULLER, S., BORSCHIG, C., FRONSKI, W. & SCHMIDT, C. 1999. Shear-Induced States of Orientation of the Lamellar Phase of C12E4/Water. *Langmuir,* 15**,** 7558-7564.

NAGAHARA, Y., NISHIDA, Y., ISODA, M., YAMAGATA, Y., NISHIKAWA, N. & TAKADA, K. 2007. Structure and Performance of Cationic Assembly Dispersed in Amphoteric Surfactants Solution as a Shampoo for Hari Damaged by coloring. *Journal of Oleo Science,* 56**,** 289-295.

NAKAMA, Y. 2017. Chapter 15 - Surfactants. *Cosmetic Science and Technology: Theoretical Principles and Applications*. Kanagawa, Japan: Kishi Kasei Co., Ltd.

NAKARAPANICH, J., BARAMEESANGPET, T., SUKSAMRANCHIT, S., SIRIVAT, A. & JAMIESON, A. M. 2001. Rheological properties and structures of cationic surfactants and fatty alcohol emulsions: effect of surfactant chain length and concentration. *Colloid and Polymer Science,* 279**,** 671-677.

NG, D. J. W. & ASSIRELLI, M. 2007. Mixing Study in Batch Stirred Vessels using a Fibre-Optic UV-VIS Monitoring Technique: A Novel Method. *Chemical Engineering Research & Design,* 85**,** 1348-1354.

NIENOW, A. W., HARNBY, N. & EDWARDS, M. F. 1992. Introduction to mixing problems. *Mixing in the Process Industries.* Oxford, UK: Butterworth-Heinemann.

NIENOW, A. W. & MILES, D. 1969. A dynamometer for the accurate measurement of mixing torque. *Journal of Scientific Instruments* 2**,** 994-995.

NORTON, I. T., SPYROPOULOS, F. & COX, P. W. 2008. Rheological control and understanding necessary to formulate healthy everyday foods. *Annual Transactions of the Nordic Rheology Society,* 16.

NOVONTÁ, P., LANDFELD, A., KYHOS, K., HOUSKA, M. & STROHALM, J. 2001. Use of Helical Ribbon Mixer for Measurement of Rheological Properties of Fruit Pulps. *Czech Journal of Food Science,* 19**,** 148-153.

O'SULLIVAN, J. & LETT, A. 2015. Engineering food pleasure: Microstructure-function relationships for emulsion quality. *The Engineers Journal.*

O'SULLIVAN, J. J., ESPINOZA, C. J. U., MIHAILOVA, O. & ALBERINI, F. 2018. Characterisation of flow behaviour and velocity induced by ultrasound using particle image velocimetry (PIV): Effect of fluid rheology, acoustic intensity and transducer tip size. *Ultrasonics Sonochemistry,* 48**,** 218-230.

ÖHRLUND, Å. 2018. Evaluation of Rheometry Amplitude Sweep Cross-Over Point as an Index of Flexibility for HA Fillers. *Journal of Cosmetics, Dermatological Sciences and Applications,* 8.

OWENS, C. E., HART, A. J. & MCKINLEY, G. H. 2020. Improved rheometry of yield stress fluids using bespoke fractal 3D printed vanes. *Journal of Rheology,* 64.

OZKAN, S., ALONSO, C. & MCMULLEN, R. L. 2020. Rheological fingerprinting as an effective tool to guide development of personal care formulations. *International Journal of Cosmetic Science,* 42**,** 529-636.

PAKZAD, L., EIN-MOZAFFARI, F. & CHAN, P. 2008. Measuring Mixing Time in the Agitation of non-Newtonian Fluids through Electrical Resistance Tomography. *Chemical Engineering & Technology,* 31**,** 1838-1845.

PAKZAD, L., EIN-MOZAFFARI, F., UPRETI, S. R. & LOHI, A. 2013. Agitation of Herschel-Bulkley fluids with the Scaba-anchor coaxial mixers. *Chemical Engineering Research and Design,* 91**,** 761-777.

PARASTAR, H. & SHAYE, H. 2015. Comparitive study of partial least squares and multivariate curve resolution for simultaneous spectrophotmetric determination of pharmaceuticals in environmental samples. *RSC Advances,* 86.

PARKER, D. J., BROADBENT, C. J., FOWLES, P., HAWKSEWORTH, M. R. & MCNEIL, P. 1993. Positron emission particle tracking - a technique for studying flow within engineering equipment. *Nuclear Instruments and Methods in Physics Research Section A: Accelerators, Spectrometers, Detectors and Associated Equipment,* 326**,** 592-607.

PARKER, D. J. & FAN, X. 2008. Positron emission particle tracking - Application and labelling techniques. *Particuology,* 6**,** 16-23.

PARTAL, P., KOWALSKI, A. J., MACHIN, D., KIRATZIS, N., BERNI, M. G. & LAWRENCE, C. J. 2001. Rheology and Microstructural Transitions in the Lamellar Phase of a Cationic Surfactant. *Langmuir,* 17**,** 1331-1337.

PAUL, E. L., ATIEMO-OBENG, V. A. & KRESTA, S. M. 2003. *Handbook of Industrial Mixing: Science and Practice*, John Wiley & Sons, Inc.

PAWELCZYK, S., KNIEPKAMP, M., JESINGHAUSEN, S. & SCHMID, H.-J. 2020. Absolute Rheological Measurements of Model Suspensions: Influence and Correction of Wall Slip Prevention Measures. *Materials,* 13.

PAYNE, A. R. 1962. The dynamic properties of carbon black-loaded natural rubber vulcanizates. Part I. *Journal of Applied Polymer Science,* 6**,** 57-63.

PEDREGOSA, F. E. A. 2011. Scikit-learn: Machine Learning in Python. *Journal of Machine Learning Research,* 12**,** 2825-2830.

PEDROSA, S. M. C. P. & NUNHEZ, J. R. 2000. The behavior of stirred vessels with anchor type impellers. *Computers and Chemical Engineering,* 24**,** 1745-1751.

PEETERS, H. 2020. *Silicone alternatives*. Worldwide patent application.

PÉREZ-MOHEDANO, R., LETZELTER, N., AMADOR, C., VANDERROEST, C. T. & BAKALIS, S. 2015. Positron Emission Particle Tracking (PEPT) for the analysis of water motion in a domestic dishwasher. *Chemical Engineering Journal,* 259**,** 724-735.

PEREZ ALVARADO, F. A., HUSSEIN, M. A. & BECKER, T. 2016. A vision system for surface homogeneity analysis of dough based on the grey level co-occurence Matrix (GLCM) for optimum kneading time prediction. *Journal of Food Process Engineering,* 39**,** 166-177.

PIERALISI, I., MONTANTE, G. & PAGLIANTI, A. 2016. Prediction of fluid dynamic instabilities of low liquid height-to-tank diameter ratio stirredtanks. *Chemical Engineering Journal,* 295**,** 336-346.

PIZZINO, A., CATTÉ, M., VAN HECKE, E., SALAGER, J.-L. & AUBRY, J.-M. 2009. On-line light backscattering tracking of the transitional phase inversion of emulsions. *Colloids and Surfaces A: Physicochemical and Engineering Aspects,* 338.

POTTEL, H. 1995. The use of partial least squares (PLS) in quantitative FTIR: Determination of gas concentrations in smoke gases of burning textiles. *Fire and Materials,* 19**,** 221-231.

PUGLIESE, R., REGONDI, S. & MARINI, R. 2021. Machine learning-based approach: global trends, research directions, and regulatory standpoints. *Data Science and Management,* 4**,** 19-29.

RAGHAVA RAO, K. S. M. S., REWATKAR, V. B. & JOSHI, J. B. 1988. Critical impeller speed for solid suspension in mechanically agitated contactors. *AIChE Journal,* 34**,** 1332-1340.

RAHIMZADEH, A., EIN-MOZAFFARI, F. & LOHI, A. 2022. Investigation of power consumption, torque fluctuation, and local gas hold-up in coaxial mixers containing a shear-thinning fluid: Experimental and numerical approaches. *Chemical Engineering and Processing - Process Intensification,* 177.

REZENDE MACIEL, N., VARGAS OLIVEIRA, E. C., OKUMA, C. H., TOPAN, J. F., LIA, Q. A. & ROCHA-FILHO, P. 2016. A New System of Multiple Emulsions with Lamellar Gel Phases from Vegetable Oil. *Journal of Dispersion Science and Technology,* 37**,** 646-655.

RIBIERO, H. M., MORAIS, J. A. & ECCLESTON, G. M. 2004. Structure and rheology of semisolid o/w creams containing cetyl alcohol/non-ionic surfactant mixed emulsifier and different polymers. *International Journal of Cosmetic Science,* 26**,** 47-59.

RIEGER, F. & NOVAK, V. 1973. Power consumption of agitators in highly viscous non-Newtonian liquids. *Transactions of the Institution of Chemical Engineers,* 51**,** 105-111.

RIEGER, F. & NOVAK, V. 1974. Power Consumption for Agitating Viscoelastic Liquids in the Viscous Regime. *Transactions of the Institute of Chemical Engineers,* 52**,** 285-286.

ROBINSON, M. & CLEARY, P. W. 2012. Flow and mixing performance in helical ribbon mixers. *Chemical Engineering Science,* 84**,** 382-398.

ROCAFORT, C. M. 2017. Chapter 21 - Functional Materials for Hair. *Cosmetic Science and Technology.* Elsevier.

RUAN, R., ALMAER, S. & ZHANG, J. 1995. Prediction of Dough Rheological Properties Using Neural Networks. *Cereal Chemistry,* 72**,** 308-311.

RUDOLPH, L., ATIEMO-OBENG, V., SCHAEFER, M. & KRAUME, M. Power consumption and blend-time of co-axial tank mixing systems in non-Newtonian fluids. 13th European Conference on Mixing, 2009 London.

RYAN, D. J., BAKER, M. R., KOWALSKI, A. J. & SIMMONS, M. J. H. 2018. Emulsification using a "Sonolator" liquid whistle: A new correlation for droplet size from pilot-scale experiments. *Chemical Engineering Science,* 189**,** 369-379.

RYAN, D. J., SIMMONS, M. J. H. & BAKER, M. R. 2017. Determination of the flow field inside a Sonolator liquid whistle using PIV and CFD. *Chemical Engineering Science,* 163**,** 123-136.

RYDER, A. G. 2002. Classification of Narcotics in Solid Mixtures Using Principal Component Analysis and Raman Spectroscopy. *Journal of Forensic Sciences,* 47**,** 275-284.

SANDLER, E. 2022. *Shiny 'glass' hair becomes next focus of skinification trend* [Online]. Available: https://www.glossy.co/beauty/shiny-hair-becomes-next-big-focus-for-skinification-trend/ [Accessed December 2023].

SCARANO, F., GHAEMI, S., ALP CARIDI, G. C., BOSBACH, J., DIERKSHEIDE, U. & SCIACCHITANO, A. 2015. On the use of helium-filled soap bubbles for large-scale tomographic PIV in wind tunnel experiments. *Experiments in Fluids,* 56.

SCHICKER, R. & WEGENER, G. 2002. *Measuring Torque Correctly*, Hottinger Baldwin Messtechnik.

SIMMONS, M. J. H., ZHU, H., BUJALSKI, W., HEWITT, C. J. & NIENOW, A. W. 2007. Mixing in a Model Bioreactor Using Agitators with a High Solidity Ratio and Deep Blades. *Chemical Engineering Research and Design,* 85**,** 551-559.

SIMOES, A., VEIGA, F. & VITORINO, C. 2020. Progressing Towards the Sustainable Development of Cream Formulations. *Pharmaceutics,* 12**,** 647.

SINDALL, R. J., DAPELO, D., LEADBEATER, T. & BRIDGEMAN, J. 2017. Positron emission particle tracking (PEPT): A novel approach to flow visualisation in lab-scale anaerobic digesters. *Flow Measurement and Instrumentation,* 54**,** 250-264.

SIVAKUMAR, M., YING TANG, S. & WEI TAN, K. 2014. Cavitation technology - A greener processing technique for the generation of pharmaceutical nanoemulsions. *Ultrasonics Sonochemistry,* 21**,** 2069-2083.

STATISTA. 2022. Global value of the cosmetics market 2018-2025. *Statista* [Online]. Available: https://www.statista.com/statistics/585522/global-value-cosmetics-market/ [Accessed February 2].

STEFFE, J. F. 1996. *Rheological Methods in Food Process Engineering,* East Lansing, Michigan, Freeman Press.

STOKES, J. R. & TELFORD, J. H. 2004. Measuring the yield behaviours of structured fluids. *Journal of non-Newtonian Fluid Mechanics,* 124**,** 137-146.

SULAIMAN, R., DOLAN, K. D. & STEFFE, J., F. 2012. Effect of Fill Level in Mixer Viscometry. *Journal of Texture Studies,* 43**,** 319-325.

SUN, Y., CHENG, H., ZHANG, S., MOHAN, M. K., YE, G. & DE SCHUTTER, G. 2023. Prediction & optimization of alkali-activated concrete based on the random forest machine learning algorithm. *Construction and Building Materials,* 385.

SUNKLE, S., SAXENA, K., PATIL, A., KULKARNI, V., JAIN, D., CHACKO, R. & RAI, B. 2020. Information Extraction and Graph Representation for the Design of Formulated Products. *In:* DUSTDAR, S., YU, E., SALINESI, C., RIEU, D. & PANT, V. (eds.) *Lecture Notes in Computer Science*. Cham.: Springer.

SUZUKI, T. 2017. Chapter 30 - Effect of Molecular Assembly for Emulsion and Gel Formulations. *Cosmetic Science and Technology: Theoretical Principles and Applications*.

SWIFT, J. A. & BROWN, A. C. 1972. The critical determination of fine changes in the surface architecture of human hair due to cosmetic treatment. *Journal of the Society of Cosmetic Chemists,* 23**,** 695-702.

TAIFOURIS, M., MARTIN, M., MARTINEZ, A. & ESQUEJO, N. 2019. Challenges in te design of formulated products: multiscale process and product design. *Current Opinion in Chemical Engineering,* 27**,** 1-9.

THOMPSON, C. J., AINGER, N., STARCK, P., MYKHAYLYK, O. O. & J., R. A. 2023. Shampoo Science: A Review of the Physicochemical Processes behind the Function of a Shampoo. *Macromolecular Chemistry and Physics,* 224.

ULBRECHT, J. J. & CARREAU, P. J. 1985. Mixing of Viscous non-Newtonian Liquids. *In:* ULBRECHT, J. J. & PATTERSON, G. K. (eds.) *Mixing of Liquids by Mechanical Agitation.* New York, New York: Gordon and Breach Science Publications.

UNILEVER. 2023a. *Climate Action* [Online]. Available: https://www.unilever.com/planet-and-society/climate-action/ [Accessed July 8 2023].

UNILEVER. 2023b. The Formation of Unilever. Available: https://www.archives-unilever.com/discover/resources/the-formation-of-unilever-booklet/search/type:booklets/page/1/view_as/grid.

UNILEVER. 2023c. *Our Company | Unilever* [Online]. Unilever. Available: https://www.unilever.com/our-company/ [Accessed 6 March 2023].

UNILEVER. 2023d. *Our planet plans* [Online]. Available: https://www.unilever.com/suppliers/partner-with-purpose/our-planet-plans/ [Accessed January 11 2024].

UNILEVER 2024. Climate Transition Action Plan. Unilever.

VAN DER BURGH, A. 2023. Cosmetics manufacturing: Best practices for quality and consistency. *SkinConsult* [Online]. Available: https://skinconsult.com/en/blog/cosmetics-manufacturing-best-practices/ [Accessed October 31].

VIEIRA, G. N. A., FREIRE, F. B. & FREIRE, J. T. 2015. Control of the Moisture Content of Milk Powder Produced in a Spouted Bed Dryer Using a Grey-Box Inferential Controller. *Drying Technology,* 33**,** 1920-1928.

WAHL, P. R., TREFFER, D., MOHR, S., ROBLEGG, E., KOSCHER, G. & KHINAST, J. G. 2013. Inline monitoring and a PAT strategy for pharmaceutical hot melt extrusion. *International Journal of Pharmaceutics,* 455**,** 159-168.

WANG, F. & MARAGONI, A. G. 2014. Nature and dynamics of monostearin phase transitions in water: stability and the sub-a-gel phase. *RSC Advances,* 4**,** 50417-50425.

WIBOWO, C. & NG, K. M. 2002. Product-Centered Processing: Manufacture of Chemical-Based Consumer Products. *AIChE Journal,* 48**,** 1212-1230.

WINDOWS-YULE, C. R. K., HERALD, M. T., NICUŞAN, A. L., WIGGINS, C. S., PRATX, G., MANGER, S., ODO, A. E., LEADBEATER, T., PELLICO, J., DE ROSALES, R. T. M., RENAUD, A., GOVENDER, I., CARASIK, L. B., RUGGLES, A. E., KOKALOVA-WHELDON, T., SEVILLE, J. P. K. & PARKER, D. J. 2022. Recent advances in positron emission particle tracking: a comparitive review. *Reports on Progress in Physics,* 85**,** 016101.

WINDOWS-YULE, C. R. K., SEVILLE, J. P. K., INGRAM, A. & PARKER, D. J. 2020. Positron Emission Particle Tracking of Granular Flows. *Annual Review of Chemical And Biomolecular Engineering,* 11**,** 367-396.

WUNSCH, K., RELKIN, P., CUVELIER, G., CLÉMENT, F., NICOLAS-MORGANTINI, L., BENKHELIFA, H. & FLICK, D. 2016. Effect of surfactant on structure thermal behaviour of cetyl stearyl alcohols. *Journal of Thermal Analysis and Calorimetry,* 123**,** 1411-1417.

XU, S., HOSHAN, L., JIANG, R., GUPTA, B., BRODEAN, E., O'NEILL, J., SEAMANS, T. C., BOWERS, J. & CHEN, H. 2017. A practical approach in bioreactor scale-up and process transfer using a combination of constant P/V and vvm as the criterion. *Biotechnology Process,* 33**,** 1146-1159.

YAMAGATA, Y. & SENNA, M. 1999. Change in Viscoelastic Behaviors Due to Phase Transition of the Assembly Comprising Cetyltrimethylammonium Chloride/Cetyl Alcohol/Water. *Langmuir,* 15**,** 4388-4391.

YAMASHITA, Y. & SAKAMOTO, K. 2017. Chapter 38 - Structural Analysis of Formulations. *In:* SAKAMOTO, K., LOCHHEAD, R. Y., MAIBACH, H. I. & YAMASHITA, Y. (eds.) *Cosmetic Science and Technology: Theoretical Principles and Applications.* Elsevier.

YANG, J.-Z. & OKADA, T. 2012. *Hair conditioning composition having higher yield point and higher conversion rate of fatty compound to gel matrix*. EP2293765A2.

YANG, J. 2017. Hair Care Cosmetics. *In:* SAKAMOTO, K., LOCHHEAD, R. Y., MAIBACH, H. I. & YAMASHITA, Y. (eds.) *Cosmetic Science and Technology.* Elsevier.

YANG, K.-Z. & OKADA, T. 2014. *Hair conditioning composition containing behenyl trimethyl ammonium chloride, and having higher yield point*. United States patent application.

YANG, Y., YAN, S., YU, B., GAO, C., CHANG, K. & WANG, J. 2023. Lamellar gel containing emulsions as an effective carrier for stabilization and transdermal delivery of retinyl propionate. *Colloids and Surfaces A: Physiochemical and Engineering Aspects,* 674**,** 131834.

YOUSSRY, M., COPPOLA, L., NICOTERA, I. & MORÁN, C. 2008. Swollen and collapsed lyotropic lamellar rheology. *Journal of Colloids and Interface Science,* 321**,** 459-467.

ZILMAN, A. G. & GRANEK, R. 1999. Undulation instability of lamellar phases under shear: A mechanism for onion formation? *European Physical Journal B,* 11**,** 593-608.

ZOU, Y., YE, S.-S., WANG, Y.-D. & FEI, W.-Y. 2016. CFD Simulation and PIV measurment of liquid-liquid two-phase flow in pump-mix mixer. *Journal of the Taiwan Institute of Chemical Engineers,* 60**,** 15-25.

Appendices

9.1 Appendix 1 – Microscopy Images of LGNs prepared in Chapter 3

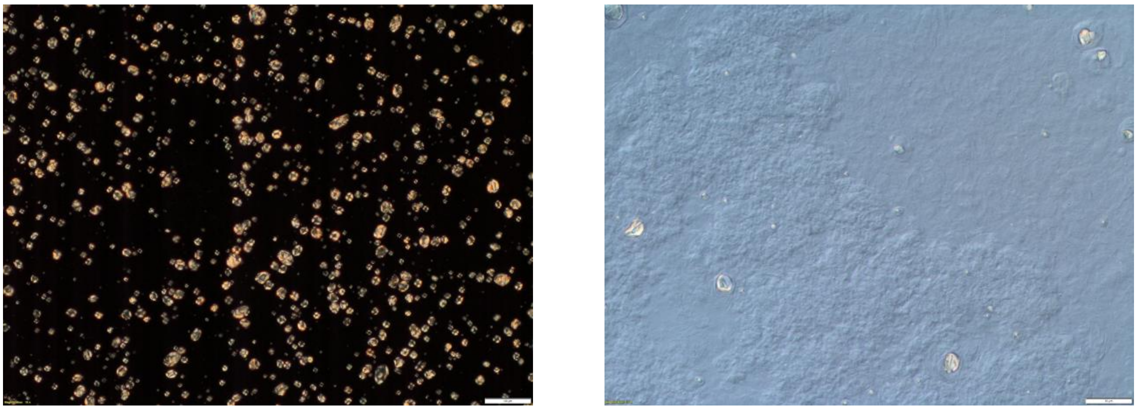

LGN$_{ref}$
10 x zoom
Polarized Light

LGN$_{t=10}$
20 x zoom
Differential Interference Contrast

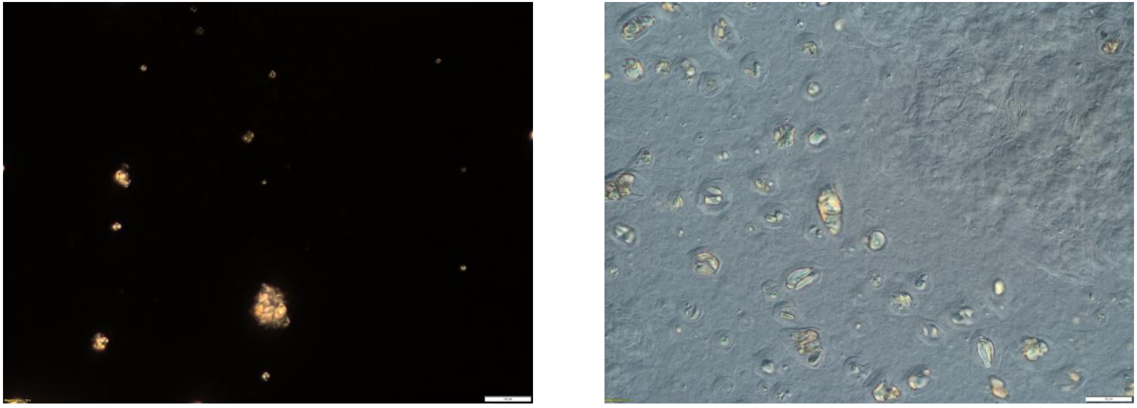

LGN$_{t=10}$
20 x zoom
Polarized light

LGN$_{T=67}$
20 x zoom
Differential Interference Contrast

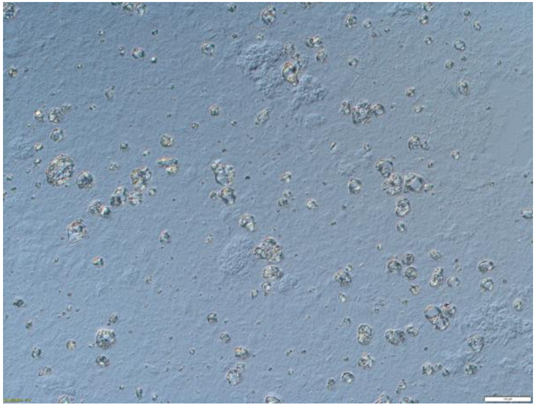

LGN$_{t=10, T=67}$
20 x zoom
Differential Interference Contrast

Figure 9-1. Microscope images collected for selected samples prepared in Chapter 3. Sample name and microscope settings provided underneath each image

9.2 Appendix 2 – Flow Curve and Yield Stress Measurements of LGN Samples prepared in Chapter 3

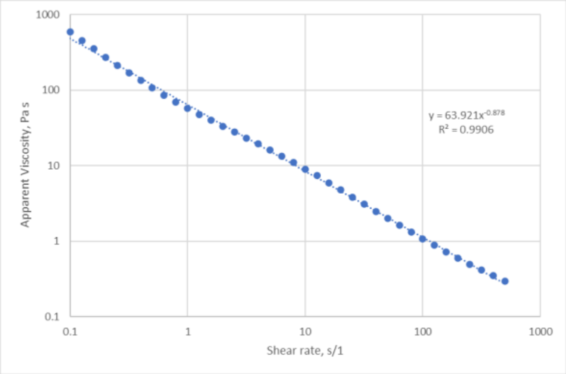

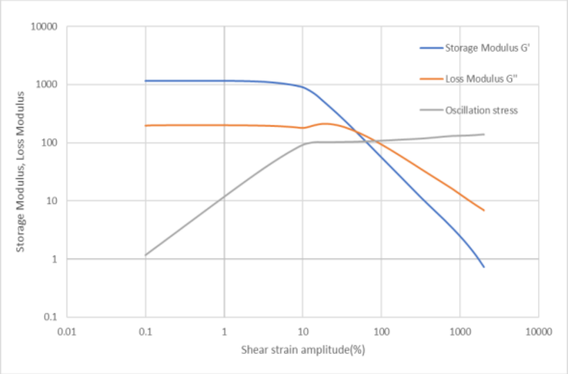

a) Flow curve measurement for LGN_{ref}

e) Yield stress measurement for LGN_{ref}

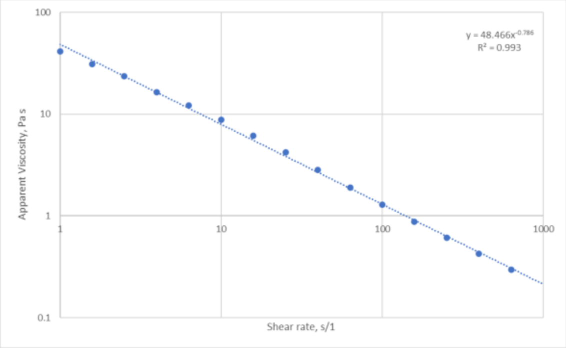

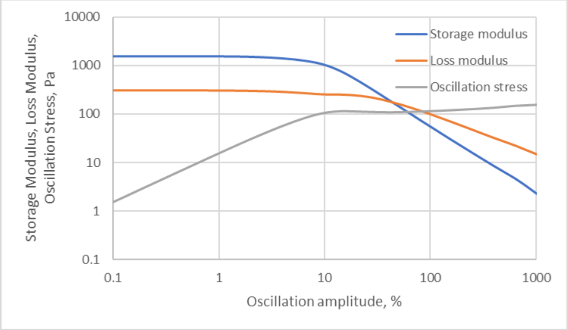

b) Flow curve measurement for $\text{LGN}_{\text{T=67}}$

f) Yield stress measurement for $\text{LGN}_{\text{T=67}}$

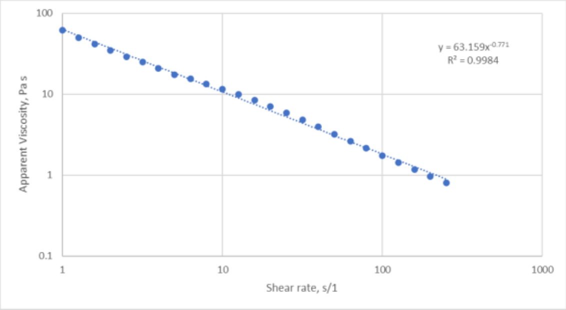

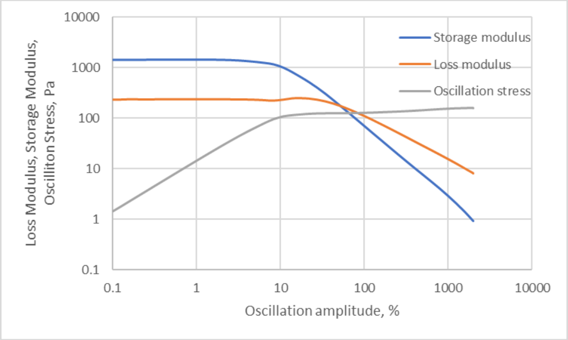

c) Flow curve measurement for $\text{LGN}_{\gamma=400}$

g) Yield stress measurement for $\text{LGN}_{\gamma=400}$

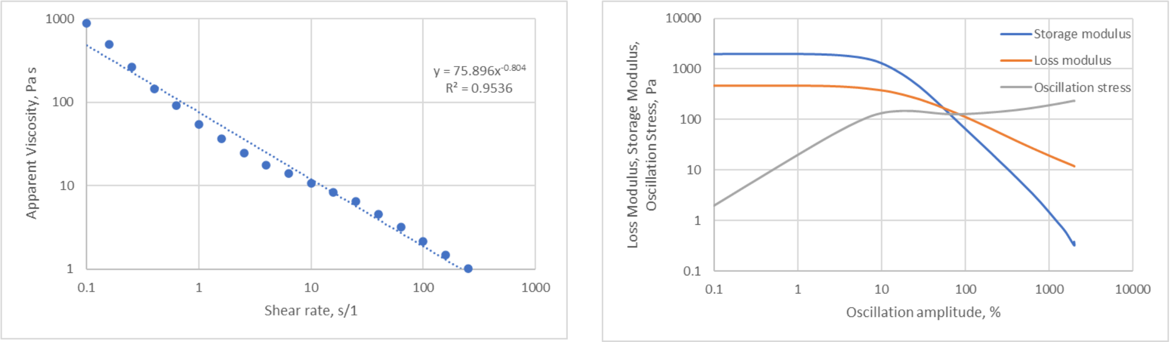

d) Flow curve measurement for LGN$_{t=20}$

h) Yield stress measurement for LGN$_{t=20}$

Figure 9-2. Flow Curve Measurements and Yield Stress Measurements for Selected Samples Prepared in Chapter 3. See Chapter 3.2.6 for measurement details a,d) LGN$_{ref}$, b,f) LGN$_{T=67}$, c,g)LGN$_{y=400}$, d,h) LGN$_{t=200}$

9.3 Appenix 3 – Torque-speed data for other rheometer geometries

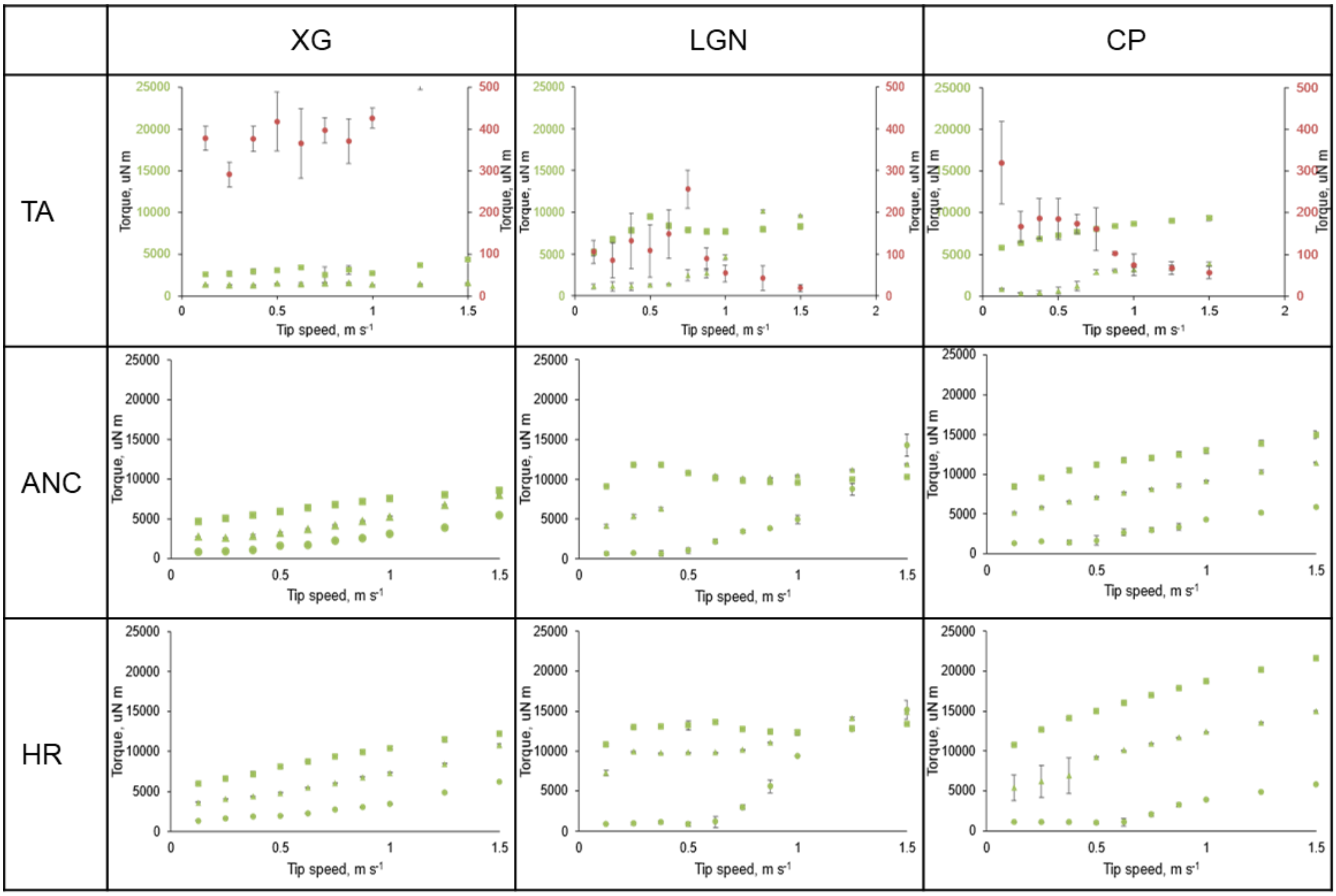

Figure 9-3. Torque-speed data for other rheometer geometries collected as part of Chapter 5 (TA Helical Ribbon, 3D printed anchor, 3D printed helical ribbon). Details of geometries are given in Figure 4-1.

Appendix 4 – Images of TA Helical Ribbon at different fill levels and speeds with XG solution

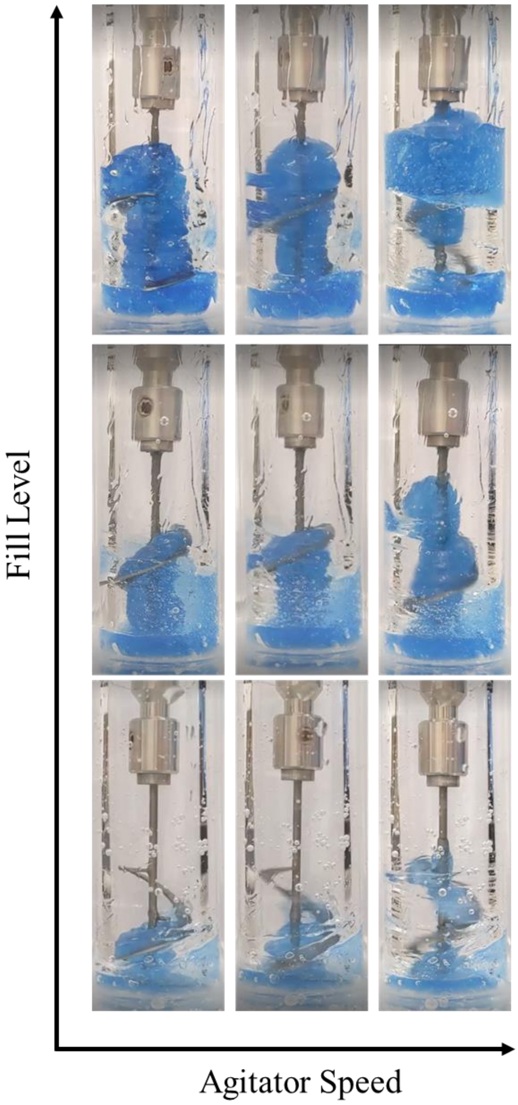

Figure 9-4. Images of XG solution being mixed by TA helical ribbon at increasing speeds along the x-axis (0.125 m/s (Fr = 0.05), 0.5 m/s (Fr = 0.82), 1 m/s (Fr = 1.8)) and increasing fill levels along the y-axis (25%, 62.5%, 100%)

9.4 Appendix 5 – Python Code to produce Random Forest Regression Model (Chapter 6)

```
import pandas as pd
import numpy as np
from sklearn.model_selection import train_test_split,
RandomizedSearchCV
from sklearn.ensemble import RandomForestRegressor
from sklearn.metrics import mean_squared_error, r2_score, make_scorer
from openpyxl import Workbook
import openpyxl

# Load the data
data = pd.read_excel("RF Data 1.6.25.xlsx", sheet_name="Sheet1 (2)")

# Define input and output columns
inputs = ['Average Torque', 'Angular Velocity', 'Diameter', 'Fill
Level']
output = 'Flow curve viscosity'

# Extract features (X) and target (y)
X = data[inputs]
y = data[output]

# Split the data into training and testing sets
X_train, X_test, y_train, y_test = train_test_split(X, y,
test_size=0.25, random_state=42)

# Define the parameter grid for RandomizedSearchCV
param_grid = {
    'n_estimators': [int(x) for x in np.linspace(start=10, stop=500,
num=10)],
    'max_features': [0.5, 1],
    'max_depth': [int(x) for x in np.linspace(5, 50, num=10)],
    'min_samples_split': [4, 6, 8],
}

# Initialize the model
rf = RandomForestRegressor(random_state=42, bootstrap=True)

scorers = {
    'r2': 'r2',
    'mse': make_scorer(mean_squared_error, greater_is_better=False)
}
```

```
random_search = RandomizedSearchCV(estimator=rf,
param_distributions=param_grid,
                                          n_iter=30, cv=5, verbose=2,
random_state=42, n_jobs=-1,
                                              return_train_score=True,
scoring=scorers, refit='r2')

random_search.fit(X_train, y_train)

results = []

# Iterate through each set of hyperparameters tested
for i in range(len(random_search.cv_results_['params'])):
    params = random_search.cv_results_['params'][i]


    model = RandomForestRegressor(**params, random_state=42)
    model.fit(X_train, y_train)

    y_train_pred = model.predict(X_train)
    train_r2 = r2_score(y_train, y_train_pred)
    train_mse = mean_squared_error(y_train, y_train_pred)

    y_test_pred = model.predict(X_test)
    test_r2 = r2_score(y_test, y_test_pred)
    test_mse = mean_squared_error(y_test, y_test_pred)

    results.append({
        'params': params,
        'train_r2': train_r2,
        'train_mse': train_mse,
        'test_r2': test_r2,
        'test_mse': test_mse
    })

results_df = pd.DataFrame(results)

# Save the results to an Excel file
with pd.ExcelWriter('results.xlsx') as writer:
    results_df.to_excel(writer, sheet_name='Hyperparameter Results',
index=False)

# best parameters based on test set R²
best_result = max(results, key=lambda x: x['test_r2'])
print(f"Best Parameters: {best_result['params']}")
print(f"Train R²: {best_result['train_r2']}, Train MSE:
{best_result['train_mse']}")
print(f"Test R²: {best_result['test_r2']}, Test MSE:
{best_result['test_mse']}")
```

9.5 Appendix 6 – Flow curves of fluids used in Chapter 5

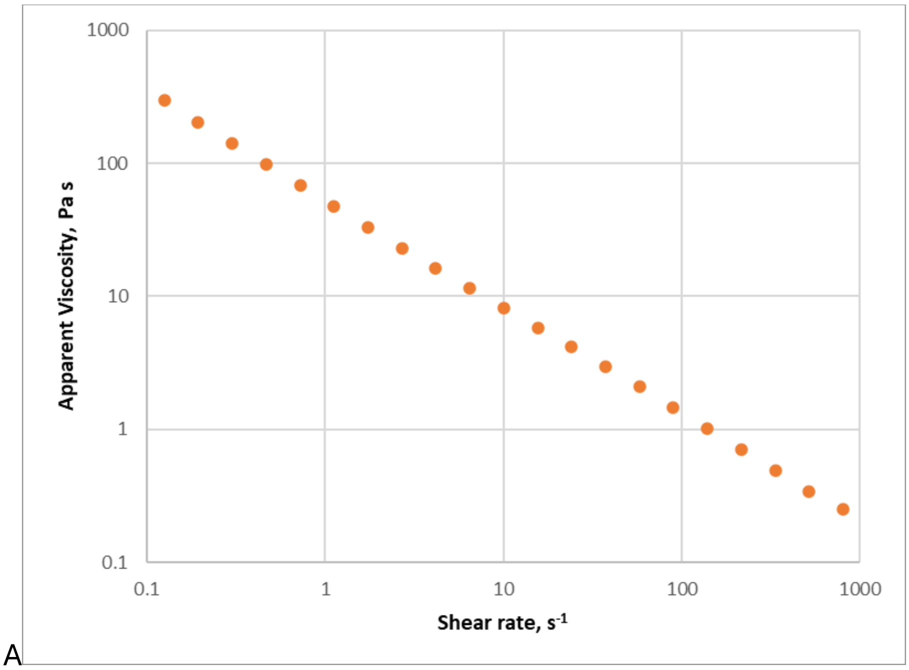

Figure 9-5. Flow curve measured for XG solution used in Chapter 5 using conventional rotational plate geometry

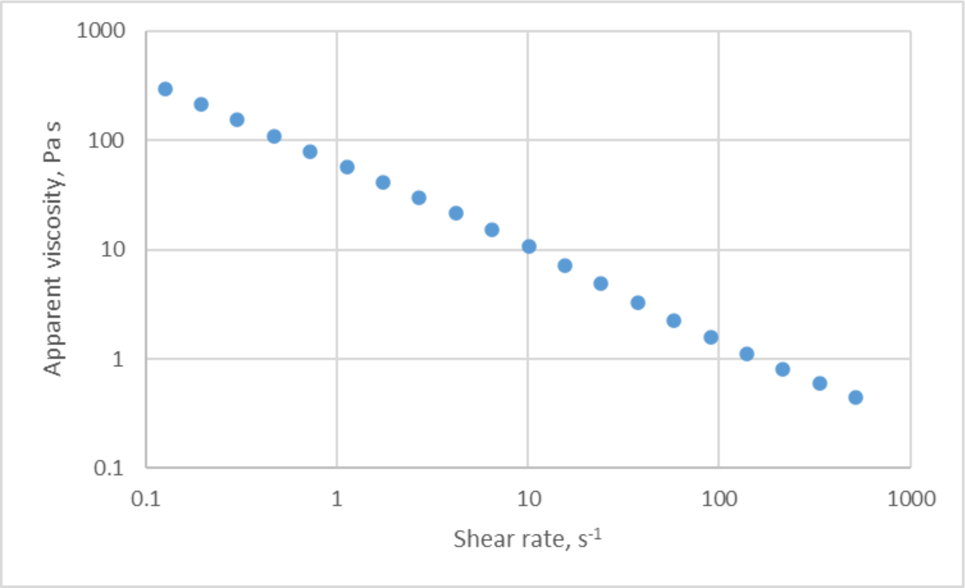

Figure 9-6. Flow curve measured for CP solution used in Chapter 5 using conventional rotational plate geometry

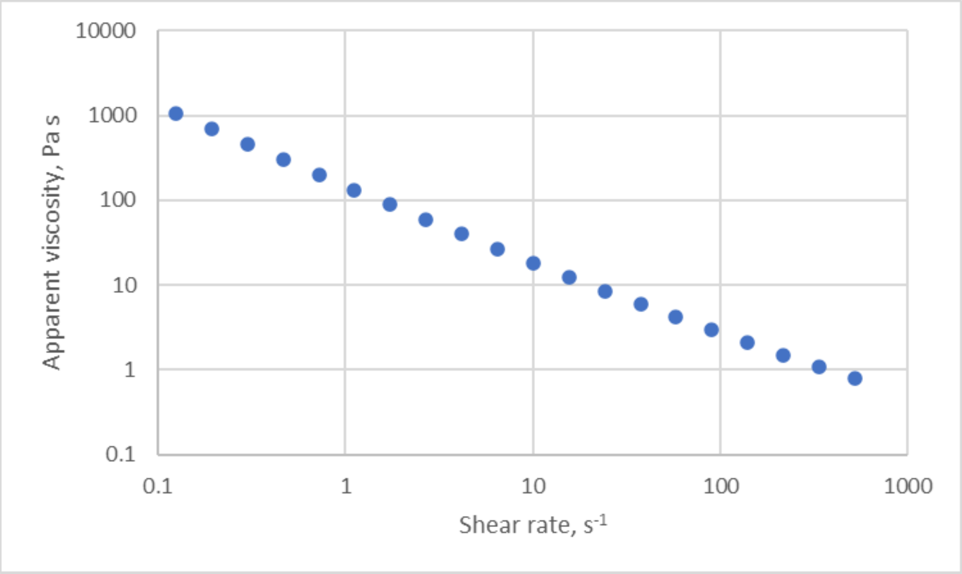

Figure 9-7. Flow curve measured for LGN1 solution used in Chapter 5 using conventional rotational plate geometry

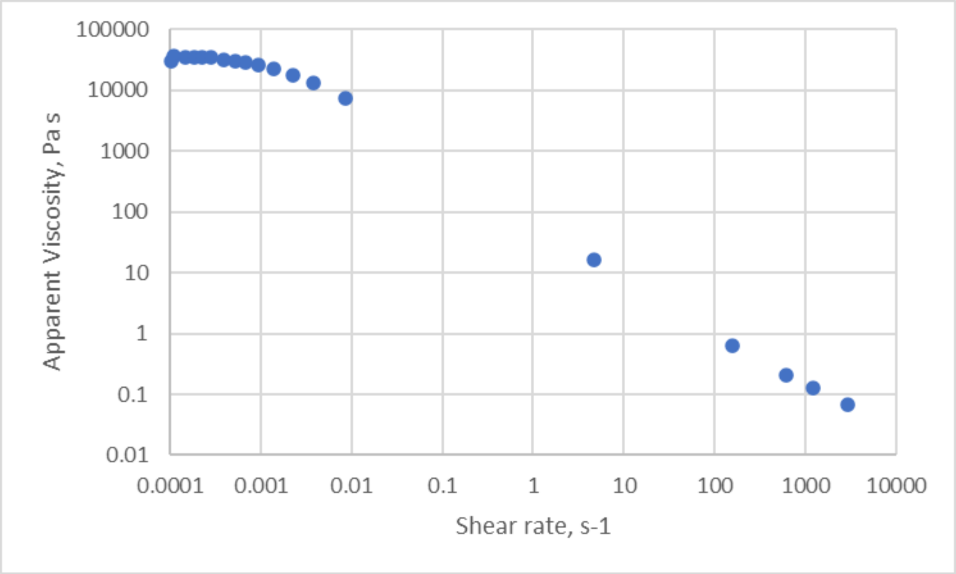

Figure 9-8. Flow curve measured for LGN2 solution used in Chapter 5 using conventional rotational plate geometry

9.6 Appendix 7 – Untransformed Data Apparent Viscosity-Time Plots from Chapter 3

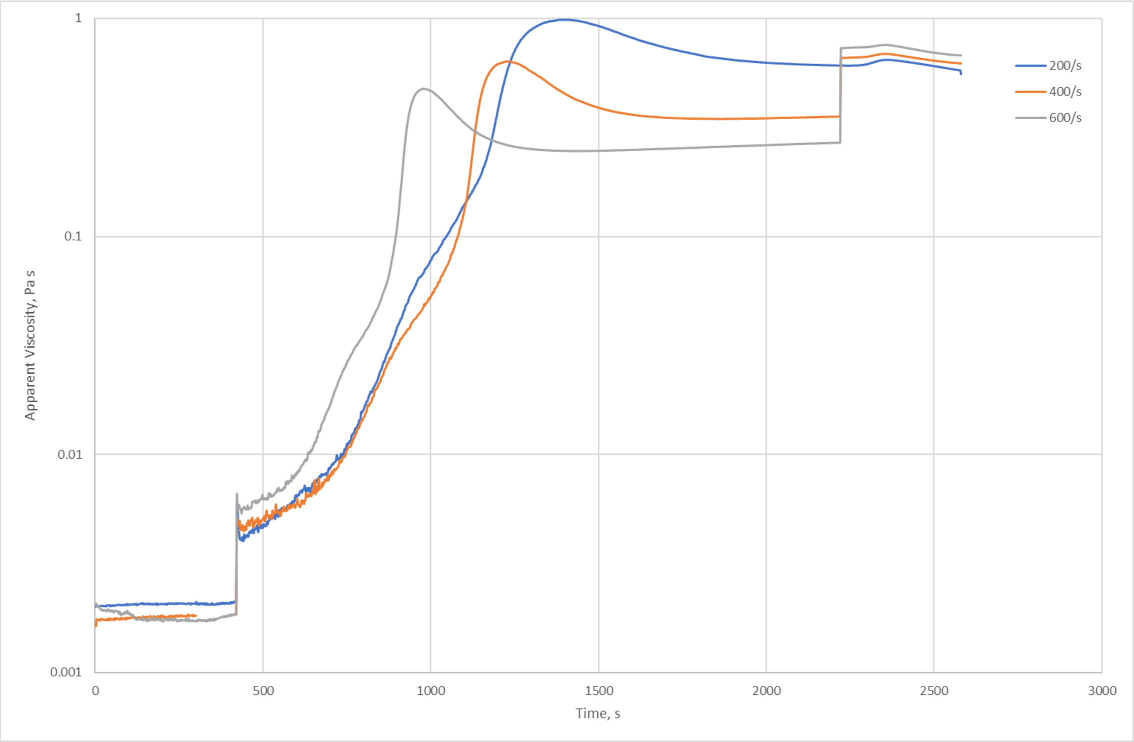

Figure 9-9. Raw measured apparent viscosity-time for samples prepared at different shear rates (200/s, 400/s, 600/s) with no transformation to account for different shear rates. Corresponding to Figure 3-5 for transformed data.